TECHNISCHE UNIVERSITÄT WIEN
Vienna University of Technology

GEOWISSENSCHAFTLICHE MITTEILUNGEN

Heft Nr. 91, 2013

Estimation of solid Earth tidal parameters and FCN with VLBI

Hana Krásná

Veröffentlichung des Departments für Geodäsie und Geoinformation
ISSN 1811-8380

Schriftenreihe der Studienrichtung VERMESSUNG UND GEOINFORMATION

TECHNISCHE UNIVERSITÄT WIEN
Vienna University of Technology

GEOWISSENSCHAFTLICHE MITTEILUNGEN

Heft Nr. 91, 2013

Estimation of solid Earth tidal parameters and FCN with VLBI

Hana Krásná

Veröffentlichung des Departments für Geodäsie und Geoinformation
ISSN 1811-8380

Schriftenreihe der Studienrichtung VERMESSUNG UND GEOINFORMATION

2013
Published by the Department of Geodesy and Geoinformation
of the Vienna University of Technology
Gußhausstraße 27-29
1040 Vienna, Austria

Responsible for this issue: Prof. Dr. Johannes Böhm
Printed by: Grafisches Zentrum HTU GmbH

The digital version of the full document with colored figures is available online:
http://www.ub.tuwien.ac.at/diss/AC07814900.pdf

Die Kosten für den Druck wurden vom Department für Geodäsie und Geoinformation übernommen.

Diese Arbeit wurde an der Fakultät für Mathematik und Geoinformation der Technischen Universität Wien zur Erlangung des akademischen Grades einer Doktorin der technischen Wissenschaften eingereicht.

Begutachter:

Prof. Dr. Harald Schuh
Department für Geodäsie und Geoinformation der Technischen Universität Wien
Gußhausstraße 27-29, 1040 Wien, Österreich
Department 1 „Geodäsie und Fernerkundung", Deutsches Geoforschungszentrum GFZ
Telegrafenberg, 14473 Potsdam, Deutschland

Assoc.Prof. Dr. Rüdiger Haas
Department of Earth and Space Sciences, Chalmers University of Technology
41296 Göteborg, Schweden
Onsala Space Observatory
43992 Onsala, Schweden

Tag der mündlichen Prüfung: 31.01.2013

Auflage: 100 Stück

ISSN 1811-8380

Prüfungssenat:

Prof. Dr. Georg Gartner
Vienna University of Technology

Prof. Dr. Harald Schuh
GFZ German Research Centre for Geosciences

Assoc.Prof. Dr. Rüdiger Haas
Chalmers University of Technology

Prof. Dr. Johannes Böhm
Vienna University of Technology

Dr. Jan Vondrák
Academy of Sciences of the Czech Republic

Zusammenfassung

Die Very Long Baseline Interferometry (VLBI) ist das einzige geodätische Weltraumverfahren, das die direkte Verknüpfung zwischen dem terrestrischen Referenzrahmen (realisiert durch die Positionen von erdfesten Stationen), und dem himmelsfesten Referenzrahmen (realisiert durch Positionen von extragalaktischen Radioquellen) gestattet. Beide Referenzrahmen sind durch die sog. Erdrotationsparameter verbunden. Die VLBI-Beobachtungen werden durch verschiedene Prozesse beeinflusst, die a priori modelliert werden müssen. Weiterhin enthalten die VLBI-Beobachtungen Informationen über eine Vielzahl geodynamischer Parameter und ermöglichen so die Validierung der Modelle.

Die Gravitationswirkung der Sonne und des Mondes auf die Erde verursacht eine Deformation der Erdoberfläche, die täglich bis zu mehreren Dezimetern in radialer Richtung betragen kann. Die Verschiebung der Erdoberfläche ist eine Funktion der sog. Love Zahlen (radiale Richtung) und der Shida Zahlen (horizontale Richtung). Bei den heutigen hohen Genauigkeitsanforderungen der VLBI müssen die Love und Shida Zahlen in komplexer Form angegeben werden, wobei der imaginäre Teil die Anelastizität des Erdmantels ausdrückt. Außerdem muss man die einzelnen Tiden innerhalb der verschiedenen Frequenzbänder unterscheiden. In der vorliegenden Arbeit werden die Love und Shida Zahlen der zwölf täglichen und fünf langperiodischen Tiden bei der Datenauswertung geschätzt und mit denen die theoretischen Modelle verglichen. Die Gezeitenparameter werden aus einer Gesamtlösung aller geeigneten VLBI-Daten aus den letzten 27 Jahre (1984.0 - 2011.0) gerechnet. Die Differenzen zwischen den Verschiebungsamplituden, wie sie aus den theoretischen und gerechneten Love und Shida Zahlen bestimmt werden, sind kleiner als 0.3 mm. Der Gesamtunterschied zu den theoretischen Werten, der als eine Summe der absoluten Beiträge aller zwölf täglichen Tiden gerechnet wird, erreicht 1.73 $\pm$ 0.29 mm in vertikaler Richtung und 1.15 $\pm$ 0.15 mm in horizontaler Richtung. Die zonalen Love Zahlen für die halbjährliche Tide (S_{sa}, theoretischer Wert: 0.6182) und die monatliche (M_m, theoretischer Wert: 0.6126) werden als 0.5584 $\pm$ 0.0095 und 0.5896 $\pm$ 0.0080 bestimmt, was einem Unterschied von 1.17 $\pm$ 0.19 mm und 0.51 $\pm$ 0.18 mm in den vertikalen Amplituden entspricht. Ebenso wird

ein etwas zu niedriger Wert für die Love Zahl der Polgezeiten aufgrund der Chandler-Periode (433 Tagen) bestimmt (0.5495 ± 0.0109) im Vergleich zu dem theoretisch prädizierten Wert von 0.6206. Der Grund dafür könnte in den Ungenauigkeiten der a priori Stationsmodellierung auf längeren Zeitperioden liegen, die sich dann in anderen Parameter wiederfinden.

In dieser Arbeit wird auch die Periode der Free Core Nutation (FCN) bestimmt, die sowohl in den frequenzabhängigen Deformationen der festen Erde wie auch im Nutationsmodell erscheint. Sie wird in einem konsistenten globalen Ausgleich der VLBI-Daten als gemeinsamer Parameter bestimmt. Der erhaltene Wert von -431.18 ± 0.10 Sterntagen unterscheidet sich gering von dem konventionellen Wert von -431.39 siderischen Tagen, der in Petit and Luzum (2010) angegeben wird. Des Weiteren wird ein empirisches Modell der FCN gerechnet, das eine variable Amplitude und Phase beinhaltet. Die Parameterbestimmung wird mit globalen Lösungen der VLBI-Daten durchgeführt und die gerechneten Amplituden und Phasen werden in jährlichen Schritten berechnet.

Abstract

Very Long Baseline Interferometry (VLBI) is a space-geodetic technique directly connecting the Terrestrial Reference Frame (TRF) realized by positions of Earth-based stations, with the Celestial Reference Frame (CRF) which is a set of extragalactic radio sources distributed throughout the sky. The link between the TRF and CRF is provided by the Earth orientation parameters. The geodetic measurements are influenced by a variety of processes which have to be modelled and put as a priori information into the analysis of the space-geodetic data. The increasing accuracy of the VLBI measurements allows access to these parameters and provides possibilities to validate them directly from the measured data.

The gravitational attraction of the Moon and the Sun causes deformation of the Earth's surface which can reach several decimetres in radial direction during a day. The displacement is a function of the so-called Love and Shida numbers. Due to the present accuracy of the VLBI measurements the parameters have to be specified as complex numbers, where the imaginary parts describe the anelasticity of the Earth's mantle. Moreover, it is necessary to distinguish between the single tides within the various frequency bands. In this thesis, complex Love and Shida numbers of twelve diurnal and five long-period tides included in the solid Earth tidal displacement modelling are estimated directly from the 27 years of VLBI measurements (1984.0 - 2011.0). The differences in the individual displacement amplitudes as determined with the theoretical and estimated diurnal Love and Shida numbers do not exceed 0.3 mm. The total difference to the theoretical displacement summed over the absolute values of all twelve diurnal waves reaches 1.73 $\pm$ 0.29 mm in vertical direction and 1.15 $\pm$ 0.15 mm in horizontal direction. The zonal Love numbers for semi-annual (S_{sa}, theoretical value: 0.6182) and monthly (M_m, theoretical value: 0.6126) tides are estimated as 0.5584 $\pm$ 0.0095 and 0.5896 $\pm$ 0.0080, which correspond to 1.17 $\pm$ 0.19 mm and 0.51 $\pm$ 0.18 mm difference in the vertical amplitudes, respectively. Similarly, a lower estimate of the pole tide Love number determined at the Chandler period (i.e. 433 days) (0.5495 $\pm$ 0.0109) than expected from the theory (0.6206) is obtained. The reason for this could be due to deficiencies in the a priori station modelling at longer time periods which

then propagate to other parameters.

In this work, the period of the Free Core Nutation (FCN) is estimated which shows up in the frequency-dependent solid Earth tidal displacement as well as in a nutation model describing the motion of the Earth's axis in space. The FCN period in both models is treated as a single parameter and it is estimated in a rigorous global adjustment of the VLBI data. The obtained value of -431.18 ± 0.10 sidereal days differs slightly from the conventional value -431.39 sidereal days given in Petit and Luzum (2010). An empirical FCN model based on variable amplitude and phase is determined, whose parameters are estimated in yearly steps directly within VLBI global solutions.

Acknowledgements

I wish to express my thanks to all who have helped me and supported me during the writing of this work.

I am grateful to Mondi Austria Privatstiftung for their scholarship and financial support during my first three years of Ph.D. studies. Further I would like to thank the Austrian Science Fund (FWF) for their follow-up support of my work within the project Integrated VLBI (P23143-N21).

I express my gratitude to my principal supervisor Prof. Dr. Harald Schuh who accepted me as a Ph.D. student and gave me the possibility to stay at the Institute of Geodesy and Geophysics at the Vienna University of Technology to do research here, and to participate in many scientific meetings. My sincere thanks go to my second supervisor Prof. Dr. Rüdiger Haas for his interest and remarks on the Ph.D. topic.

My very special thanks belong to Prof. Dr. Johannes Böhm for helping me at any time, giving me constant guidance and encouragement for the further work, and for involving me in several international projects. I am very happy that I was involved in the birth of the new VLBI analysis software VieVS together with Dr. Tobias Nilsson, DI Lucia Plank, and Dr. Kamil Teke. The helpfulness and cooperativeness which were presented in our small developer team persist till today, when more colleagues in the VieVS team are included. To all of them goes a big thank you. I am grateful to all my colleagues for the friendly atmosphere which is present at the Institute.

My sincere thanks go to my family, to my brother-in-law John for proofreading this Ph.D. thesis, and especially to my husband Karel for giving me so much love, patience and understanding, and for being with me when it was most needed.

Contents

Zusammenfassung v

Abstract vii

Acknowledgements ix

Contents x

1 Introduction 1

1.1 Research objectives 1

1.2 Thesis outlines 2

2 Very Long Baseline Interferometry 4

2.1 VLBI principle 4

2.2 Reduced observed delay 6

2.3 VLBI delay model 7

2.4 Estimation of parameters 11

2.5 Vienna VLBI Software (VieVS) 11

2.5.1 Vie_GLOB 13

2.6 International VLBI Service for Geodesy and Astrometry 14

2.6.1 VLBI2010 15

3 Least Squares Adjustment 18

3.1 Least Squares Adjustment - Basics 18

3.2 Reduction and stacking of parameters 20

3.3 Constraining of parameters 23

4 Station displacement 28

4.1 Solid Earth tides 29

4.2 Ocean loading 29

4.3 Atmospheric pressure loading . . . 31
4.4 Pole tide loading . . . 34
4.5 Ocean pole tide loading . . . 36
4.6 Hydrology loading . . . 38

5 Solid Earth tides **42**
5.1 Tidal potential . . . 42
5.2 Harmonic expansion of the tidal potential . . . 46
5.3 Tidal waves . . . 48
5.4 Deformation of the crust . . . 51

6 TRF and CRF **53**
6.1 Introduction . . . 53
6.2 Terrestrial Reference Frame . . . 54
6.2.1 Comparison of VieTRF10a with VTRF2008 . . . 61
6.3 Celestial Reference Frame . . . 63
6.3.1 Comparison of VieCRF10a with ICRF2 and other CRF catalogues . . . 67
6.4 Annual and semi-annual harmonic signal in TRF . . . 71

7 Love and Shida numbers **76**
7.1 Love and Shida numbers for the diurnal tides . . . 77
7.1.1 Estimates of Love and Shida numbers for the diurnal tides . . . 79
7.1.2 Two models for ocean tidal loading . . . 85
7.2 Love and Shida numbers for the long-period tides . . . 88
7.3 Love and Shida number for the pole tide . . . 93

8 Free Core Nutation **97**
8.1 FCN in solid Earth tides . . . 98
8.2 FICN in solid Earth tides . . . 99
8.3 FCN in celestial pole offsets . . . 100
8.3.1 Motion of CIP in celestial reference system . . . 100
8.3.2 Description of FCN in celestial pole offsets . . . 103
8.3.3 Spectral analysis of CPO . . . 106
8.3.4 Model for CPO with two periods . . . 108
8.3.5 Estimation of a constant FCN period . . . 110
8.3.6 Estimation of a constant FCN period from CIP motion . . . 112

8.4 Empirical FCN model with globally estimated varying amplitude 115
8.5 Simultaneous estimation of FCN period from solid Earth tides and nutation . . . 118

9 Conclusions **119**

Bibliography **121**

List of Figures **131**

List of Tables **138**

Curriculum vitae **141**

Appendices **142**

A Appendices **142**
A.1 VieTRF10a - coordinate and velocity residuals 142
A.2 Tropospheric effects on TRF and CRF 147
A.2.1 Impact of tropospheric gradient estimation 147
A.2.2 Impact of two different mapping functions 156

1. Introduction

Geodesy is a science describing and measuring our planet Earth in terms of its shape, rotation and mass distribution. In my Ph.D. thesis I use measurement data obtained by a geodetic space technique called Very Long Baseline Interferometry (VLBI) to access several interesting geophysical and geodynamic parameters, and to compare them with their theoretical values resulting from models. VLBI is a unique technique which connects Earth-based stations with extragalactic objects through the Earth orientation parameters. It contributes significantly to a realization of terrestrial reference frames through the determination of baseline lengths between two antennas, particularly to its scale which is directly connected to the speed of light. It is the only technique which has access to the extragalactic radio sources whose estimated positions realize a celestial reference frame. Such global frames of reference are fundamental backbones for measuring and consistently interpreting key global change processes on the Earth and for many other scientific and societal applications (Plag and Pearlman, 2009).

1.1. Research objectives

The increasing precision and quality of the VLBI measurements allow access to parameters describing the Earth and its interior which were put into the analysis process as a priori information from theoretical models needed to describe changes occurring in the Earth's shape and motion. Together with my colleagues at the Institute of Geodesy and Geophysics at the Vienna University of Technology, during my Ph.D. studies, we developed VLBI analysis software called VieVS (Böhm et al., 2012) which allows the analysis of VLBI measurements with a special focus on the specific parameters of concern. I investigate the accuracy and consistency of terrestrial and celestial reference frames with a simultaneous estimation of Earth orientation parameters. One of my key research objectives is to determine the solid Earth tidal parameters (Love and Shida numbers) which describe the Earth's elastic response to the tidal potential caused by

the Moon and the Sun and to compare them to theoretically estimated values (Mathews et al., 1995) presently recommended in the IERS Conventions 2010 (Petit and Luzum, 2010). Another objective is to concentrate on the free core nutation which yields information related to the deep Earth's interior. Its presence is reflected simultaneously in the solid Earth tides and Earth rotation, i.e. in celestial pole offsets. Investigation of such parameters contributes to a better understanding of the Earth system.

1.2. Thesis outlines

- The very long baseline interferometry technique is introduced in chapter 2. An overview of its basic principles with a focus on modelling and analysis is given. The newly developed analysis software VieVS is described concentrating on the module Vie_GLOB (Spicakova et al., 2010) which was developed in connection with this Ph.D. thesis. It has the capability to estimate parameters in a so-called global solution, i.e. from a common adjustment of all available observations.

- Chapter 3 summarizes the basic computational strategy used in the software VieVS to adjust the measurements with the method of least squares. Procedures required to reduce and to stack the parameters in large data volumes are introduced together with the necessary constraining of certain parameters.

- Modelling of station displacement is discussed in chapter 4. Crustal deformation models accounting for solid Earth tides, ocean and atmospheric tidal loading, pole tide and ocean pole tide loading, together with models describing non-tidal loading caused by the atmosphere and hydrology are introduced. Their influence on reliable station coordinates estimation, i.e. on the estimation of TRF, is thoroughly shown.

- Chapter 5 gives a detailed explanation of solid Earth tides. The relationship between tidal potential and Earth deformation is shown giving the background to the research of Love and Shida numbers.

- Consistent determination of terrestrial and celestial reference frame is a basic requirement for a reliable estimation of geophysical parameters. Therefore I devote chapter 6 to investigations on TRF and CRF. A clear understanding of the required handling of respective

groups of stations and sources in terms of their involvement in the measurements during the entire included time span is crucial for the delivery of stable reference frames. A comprehensive study on the handling of tropospheric gradients and mapping functions on the reference frames is given in appendix A.2.

- Estimation of Love and Shida numbers from diurnal and long-period frequency bands is introduced in chapter 7. A detailed presentation of the results with an investigation on the influence of the a priori chosen ocean tide model on the Love and Shida estimates is given.

- In chapter 8 a comprehensive study on free core nutation is made. Its presence influences the displacement of stations through the solid Earth tides and also the rotation of the Earth where it is visible in the nutation motion of the Earth rotation axis. I compute the period of free core nutation in a rigorous least squares adjustment of VLBI data from both phenomena simultaneously which assures a reliable estimation. Furthermore, I provide an empirical model of the free core nutation based on variable amplitude and phase where the coefficients of the model (cosine and sine amplitude terms) are determined within global solutions and tabulated in yearly steps.

2. Very Long Baseline Interferometry

Very Long Baseline Interferometry (VLBI) is a space-geodetic technique which plays a unique role in geodesy by allowing the determination and maintenance of the quasi-inertial Celestial Reference Frame (CRF) realized by positions of extragalactic quasi-stellar radio sources, so-called quasars. Furthermore, as the only available technique it allows the monitoring of the full set of Earth Orientation Parameters (EOP) at regular intervals and in particular it is uniquely skilled at giving direct measurements of Universal Time (UT1) and precession-nutation over longer time spans. It essentially contributes to the Terrestrial Reference Frame (TRF) by enabling the determination of station positions, in particular the baseline lengths between the stations. Due to the long intercontinental baselines it supports the keeping of a stable scale. Moreover, in this work I make use of the information about geodynamic parameters contained in the VLBI observations and determine these parameters (such as Love and Shida numbers or free core nutation period) from the long history of the VLBI data records starting in the year 1984.

2.1. VLBI principle

The principle of VLBI is that at least two Earth-fixed antennas receive extragalactic microwave signals simultaneously. The received signals are pairwise combined in the so-called correlators where the output of the cross correlation is time delay (τ), i.e. the difference between the reception times of the signal (t_1, t_2) at stations No. 1 and No. 2, which is the primary observable of the VLBI technique. As can be seen in Figure 2.1 the time delay of the signal is caused by a difference in the ray paths (green line). The right-angled triangle provides a direct relationship between the baseline vector $\boldsymbol{b}$ and the direction to the radio source $\boldsymbol{k}$, where the observed time delay is represented by the scalar product of these two vectors (Campbell, 2000). This

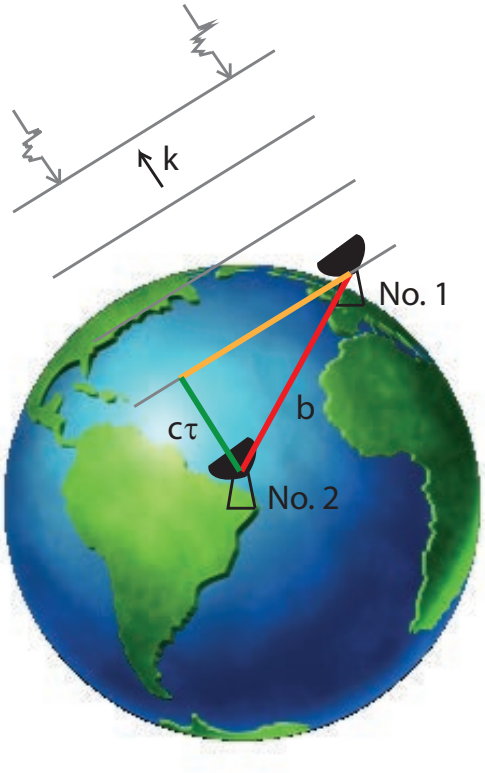

Figure 2.1.: VLBI observation principle. Wavefronts emitted by a quasar from the direction $\boldsymbol{k}$ reach stations No. 1 and No. 2 separated by a baseline $\boldsymbol{b}$. The green line represents the spatial distance which equals the time delay τ multiplied by the velocity of light c.

fundamental VLBI model can be written as:

$$\tau = -\frac{\boldsymbol{b} \cdot \boldsymbol{k}}{\mathrm{c}} = t_2 - t_1. \tag{2.1}$$

In equation (2.1) the baseline vector and the unit source vector are given in a geocentric system. In practical computation, the time delay is modelled in a barycentric frame. Transformations have to therefore be introduced in accordance with the Earth rotation and the change of the origin. A detailed description is given in section 2.3. In the real world before the arrival at the stations the wave front is affected differently by the gravitational fields presented along its journey in the Solar system (details follow in section 2.3) and also by the Earth's atmosphere. Between the time of the arrival of the signal at stations No. 1 and No. 2 it comes to the shift of the second station caused by the rotational motion of the Earth. All these aspects have to be considered during the analysis of VLBI data.

2.2. Reduced observed delay

In Figure 2.2 a schematic flow diagram describing the VLBI data analysis is introduced. On the upper left hand side of the figure the reduction of the observed time delay provided by the correlator is described. The raw time delay coming from the correlator is affected by instrumental effects, troposphere, ionosphere and also radio source structure. The instrumental effects include e.g. systematic clock instabilities, electronic delay in cables and circuitry, and deformation of the telescope structure (Campbell, 2000; Schuh, 2000). The effect of the troposphere is currently recognized as the most serious problem. During a VLBI scan the globally distributed antennas are pointed towards the same source through different meteorological conditions at different elevation angles. The content of the water vapour can cause an extra delay of about 0.4 metres in zenith direction (Campbell, 2000; Schuh, 2000). The monitoring of the rapid changes of the wet part of the troposphere can be done by water vapour radiometers by measuring the fluctuations in the line-of-sight path delay at radio wavelengths (Resch, 2000). The differing delays of the radio signal exhibited by the ionized part of the atmosphere (the ionosphere) can be corrected rather easily with the information from the measurements at two frequencies. In the standard geodetic VLBI two different observing frequencies are used. One in S-band on 2.3 GHz and the second one in X-band on 8.4 GHz where the wavelengths correspond to

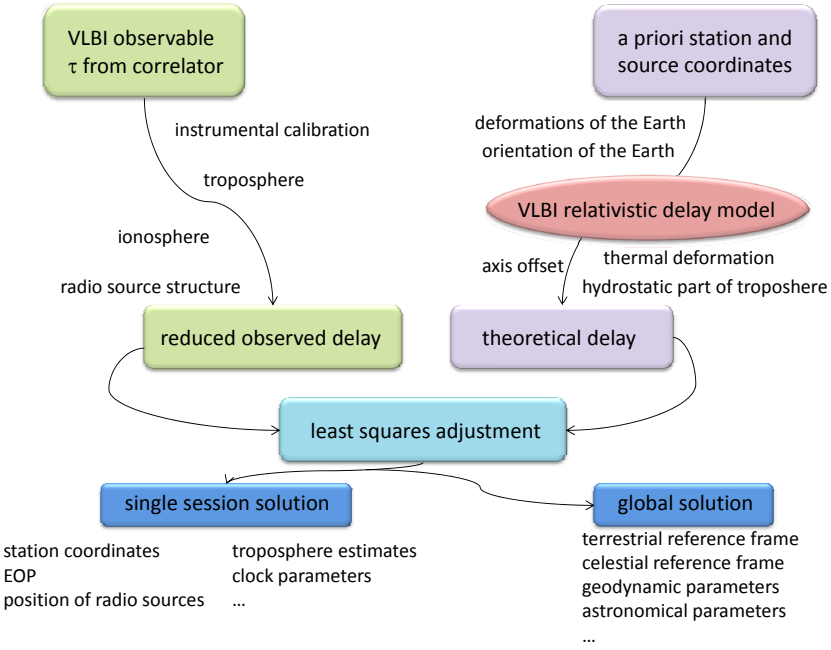

Figure 2.2.: Schematic flow diagram describing the VLBI data analysis. Based on Schuh (1987).

13 and 3.5 cm, respectively. For further analysis, the X-band observations are used, where the ionospheric correction is computed from the difference between the X-band and S-band measurements utilizing the characteristic of the ionosphere as a dispersive medium for the radio frequencies. Another limiting factor of VLBI is the apparent motion of the radio sources caused by their intrinsic structure. Nowadays a large amount of imaging data is available which is used to filter out the most extended sources and also to identify the most compact sources for defining a celestial reference frame (Fey et al., 2009). In order to describe the astrometric quality of the radio sources a structure index was established by Fey and Charlot (1997). The sources are divided into four categories based on the predicted magnitude of the effects of the intrinsic source structure on VLBI delay observations. In Fey et al. (2009) the structure index was changed to a continuous scale and derived for 701 different sources by using a total of 3046 X-band VLBI images.

2.3. VLBI delay model

The theoretical VLBI delay, i.e. the time difference between the arrival of the plane wave from quasar at station No. 1 and No. 2 (always in the sense arrival time at station No. 2 minus at station No. 1), is computed by analysis software and then compared to the reduced observed delay coming originally from the correlator. In the analysis software VieVS (Böhm et al., 2012) we follow by computing of the theoretical VLBI delay the "consensus model" which was published in Eubanks (1991) and is recommended in the IERS Conventions 2010 (Petit and Luzum, 2010). In this section an introduction into the modelling of the VLBI time delay is given.

The modelling of the theoretical delay can be divided into the following steps:

Step 1

Location of the two stations in an Earth fixed frame

The position of the two stations in an Earth fixed frame is computed at the time t, when the wave from quasar arises at station No. 1. The coordinates and velocities are taken from a TRF catalogue and are modified according to models of station displacement such as Earth solid tides, ocean and atmospheric loading, pole tide and others. A comprehensive overview of models describing the station movements is given in chapter 4.

Step 2

Transformation of station positions into GCRS

The Geocentric Celestial Reference System (GCRS) is a kinematically non-rotating system with its origin in the geocenter. In order to follow the currently valid IERS Conventions 2010 (Petit and Luzum, 2010) and IAU 2000/2006 (Capitaine et al., 2003; Mathews et al., 2002) resolutions, the relationship of the ITRS to the GCRS at the date t of the observation is expressed by

$$[GCRS] = \boldsymbol{Q}(t) \cdot \boldsymbol{R}(t) \cdot \boldsymbol{W}(t) \cdot [ITRS] \tag{2.2}$$

where matrix $\boldsymbol{Q}$ represents the motion of the Celestial Intermediate Pole (CIP) in the celestial system, matrix $\boldsymbol{R}$ arises from the rotation of the Earth around the CIP axis, and matrix $\boldsymbol{W}$ from the polar motion. With this transformation we obtain the baseline vector $\boldsymbol{b}$ in GCRS.

Step 3

Estimation of the gravitational delay ΔT_{grav}

The gravitational delay arises due to the fact that the parallel signals from a quasar passing near a massive celestial body are deflected with a different intensity and thus, the radio signal further away from the celestial body has a shorter path than the other one. The difference in the delay is called the gravitational delay. Following the present requirements on the VLBI accuracy summarized in the project VLBI2010 (Niell et al., 2005) a positional accuracy is expected to achieve 1 mm, which forces the modelling to be precise to one order of magnitude, i.e. 0.1 mm (0.3 ps). For such requirements the gravitational delay due to the Earth, the Sun, Jupiter, Saturn, the Moon and Venus has to be considered as shown e.g. by Soja (2011). The general equation for the gravitational delay caused by the celestial body "J" reads:

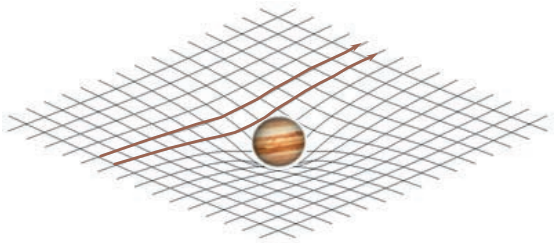

Figure 2.3.: Deflection of two parallel radio signals near a massive gravitating body.

$$\Delta T_{grav_J} = (1+\gamma)\frac{GM_J}{\mathrm{c}^3} \ln \frac{|\boldsymbol{R}_{1J}| + \boldsymbol{K} \cdot \boldsymbol{R}_{1J}}{|\boldsymbol{R}_{2J}| + \boldsymbol{K} \cdot \boldsymbol{R}_{2J}}, \tag{2.3}$$

with the post-Newtonian parameter γ equal to 1 in the general relativity theory, the gravitational constant G, the mass M_J of the J^{th} gravitating body, the barycentric unit source vector $\boldsymbol{K}$ and the vectors $\boldsymbol{R}_{1J}$, $\boldsymbol{R}_{2J}$ from the gravitating body to the stations No. 1 and No. 2, respectively.

As mentioned in Step 1, the reference time for all quantities is the time t, when the wave from a quasar arrives at station No. 1. Therefore the vector $\boldsymbol{R}_{2J}$ has to be corrected for the movement of station No. 2 caused by the Earth's velocity $\boldsymbol{V}_\oplus$ between the arrivals of the signal at stations No. 1 and No. 2:

$$\boldsymbol{R}_{2J} = \boldsymbol{X}_2(t) - \frac{\boldsymbol{V}_\oplus}{\mathrm{c}}(\boldsymbol{K}\cdot\boldsymbol{b}) - \boldsymbol{X}_J(t_J), \tag{2.4}$$

where $\boldsymbol{X}_2$ is the barycentric radius vector of station No. 2 and $\boldsymbol{X}_J$ is the barycentric vector of the J^{th} gravitating body at the time t_J of closest approach of the signal. Vector $\boldsymbol{R}_{1J}$ is computed simply as a difference between $\boldsymbol{X}_J$ and $\boldsymbol{X}_1$:

$$\boldsymbol{R}_{1J}(t) = \boldsymbol{X}_1(t) - \boldsymbol{X}_J(t_J). \tag{2.5}$$

The station's position in the Barycentric Celestial Reference System (BCRS) with accuracy sufficient for equations (2.4) and (2.5) is obtained by:

$$\boldsymbol{X}_i(t) = \boldsymbol{X}_\oplus(t) + \boldsymbol{x}_i(t), \tag{2.6}$$

with $i = 1, 2$ for station No. 1 and No. 2. Station vector $\boldsymbol{x}_i$ in GCRS comes from the equation (2.2).

For the gravitational delay due to the Earth, a simplified delay with geocentric station radius vector is computed:

$$\Delta T_{grav\oplus} = (1+\gamma)\frac{GM_\oplus}{\mathrm{c}^3}\ln\frac{|\boldsymbol{x}_1| + \boldsymbol{K}\cdot\boldsymbol{x}_1}{|\boldsymbol{x}_2| + \boldsymbol{K}\cdot\boldsymbol{x}_2}, \tag{2.7}$$

which is precise to picosecond accuracy (Petit and Luzum, 2010).

The total gravitational delay ΔT_{grav} is obtained with a summation over all ΔT_{grav_J} together with the Earth's contribution.

Step 4

Vacuum geometric delay

The modelling of the vacuum geometric delay is defined in the Barycentric Reference System. The difference between the time of arrival of the wave front at station No. 1 (T_1^{vac}) and station No. 2 (T_2^{vac}) is generally given as the multiplication of the unit source vector with the baseline vector corrected for the gravitational delay:

$$T_2^{vac} - T_1^{vac} = -\frac{\boldsymbol{K}\cdot\left(\boldsymbol{X}_{2(T_2^{vac})} - \boldsymbol{X}_{1(T_1^{vac})}\right)}{\mathrm{c}} + \Delta T_{grav}. \tag{2.8}$$

For the practical computation the barycentric station vectors $\boldsymbol{X}_i$ have to be transformed into geocentric ones $\boldsymbol{x}_i$ by using the relativistic transformations. The problems of time transformation

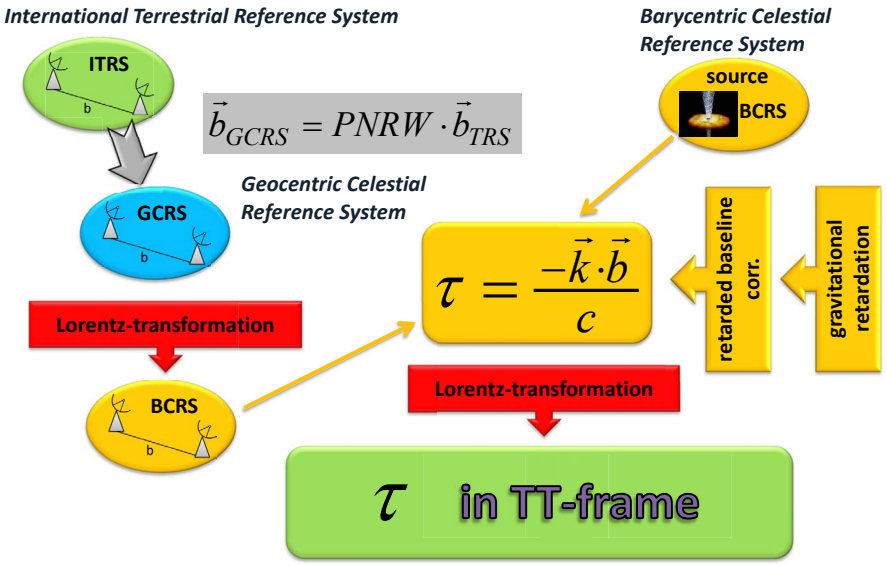

Figure 2.4.: Symbolic illustration of the transformation of station positions (baseline vector) into GCRS (Step 2) and the following calculation of the time delay in BCRS (Step 4). (Courtesy of Lucia Plank.)

will be not discussed here, it can be read e.g. in Petit and Luzum (2010). The resulting equation (2.9) is given for the difference of the geocentric times t_1^{vac} and t_2^{vac}:

$$t_2^{vac} - t_1^{vac} = \frac{\Delta T_{grav} - \frac{\boldsymbol{K}\cdot\boldsymbol{b}}{\mathrm{c}}\left[1 - \frac{(1+\gamma)\cdot U}{\mathrm{c}^2} - \frac{|\boldsymbol{V}_\oplus|^2}{2\mathrm{c}^2} - \frac{\boldsymbol{V}_\oplus\cdot\boldsymbol{v}_2}{\mathrm{c}^2}\right] - \frac{\boldsymbol{V}_\oplus\cdot\boldsymbol{b}}{\mathrm{c}^2}\left(1 + \frac{\boldsymbol{K}\cdot\boldsymbol{V}_\oplus}{2\mathrm{c}}\right)}{1 + \frac{\boldsymbol{K}\cdot(\boldsymbol{V}_\oplus + \boldsymbol{v}_2)}{\mathrm{c}}} \tag{2.9}$$

with gravitational potential U at the geocenter, barycentric velocity of the geocenter $\boldsymbol{V}_\oplus$ and the geocentric velocity $\boldsymbol{v}_2$ of the station No. 2.

Step 5

Total delay

To obtain the total theoretical delay several corrections have to be added to the vacuum geometric delay. These are the hydrostatic part of the tropospheric delay t_{hydro}(dependent on the pressure, height and latitude of the station), delay caused by the thermal deformation of the antenna $\tau_{thermdef}$, and axis offsets corrections τ_{ao}:

$$t_2 - t_1 = t_2^{vac} - t_1^{vac} + \left(t_{hydro2} - t_{hydro1} + t_{hydro1}\frac{\boldsymbol{K}\cdot(\boldsymbol{v}_2 - \boldsymbol{v}_1)}{\mathrm{c}}\right) + \tau_{thermdef} + \tau_{ao}. \tag{2.10}$$

2.4. Estimation of parameters

As illustrated in Figure 2.2 the reduced observed delay and the theoretical delay go into a least squares solution where they build a vector with reduced observations "o − c" (observed minus computed). In principle two kinds of parameters can be estimated by the VLBI technique. The first group involves parameters which are connected only with one observation session and are changing in time. These are e.g. clock parameters, atmospheric parameters, Earth orientation parameters or station positions which refer to the time within the session. The second group are so-called global parameters which are constant in time and are determined from all measured sessions. The terrestrial reference frame (station coordinates and velocities referring to a certain reference epoch), celestial reference frame (time-independent coordinates), and constant geophysical or astronomic parameters are estimated in this way.

2.5. Vienna VLBI Software (VieVS)

The Vienna VLBI Software (VieVS) has been developed at the Institute of Geodesy and Geophysics of TU Vienna since 2008 (Böhm et al., 2009, 2012). It is analysis software written in Matlab programming language. In its basic form it is capable of estimating parameters from the measured VLBI time delay. The potential of VieVS has grown and nowadays it consists of several add-on modules which considerably extends its capabilities (see Figure 2.5). The software is controlled by a user via a graphical interface where analysis options can be chosen. The core of the software consists of three separate modules: Vie_INIT (Nilsson et al., 2011), Vie_MOD (Plank et al., 2013) and Vie_LSM (Teke et al., 2009). In Vie_INIT the input data is read in, e.g. the station coordinates and velocities from a TRF catalogue, quasar coordinates from a CRF catalogue, and the observed time delay presently from an NGS file. At this stage the outlier observations can be removed and it is also possible to exclude stations, sources or baselines. In the module Vie_MOD the theoretical time delay is computed and partial derivatives of the delay with respect to the parameters of interest are built. The modelling currently follows the IERS Conventions 2010 (Petit and Luzum, 2010) with their electronic updates. The adjustment of observations and estimation of the parameters take place in Vie_LSM using the classical Gauss-Markov least squares method. The parameters are estimated as piecewise linear offsets at intervals chosen by the analyst. Three kinds of the intervals can be chosen: 1) integer hours (e.g. 17:00 UTC, 18:00 UTC, ...), 2) integer fractions of integer hours (17:20 UTC,

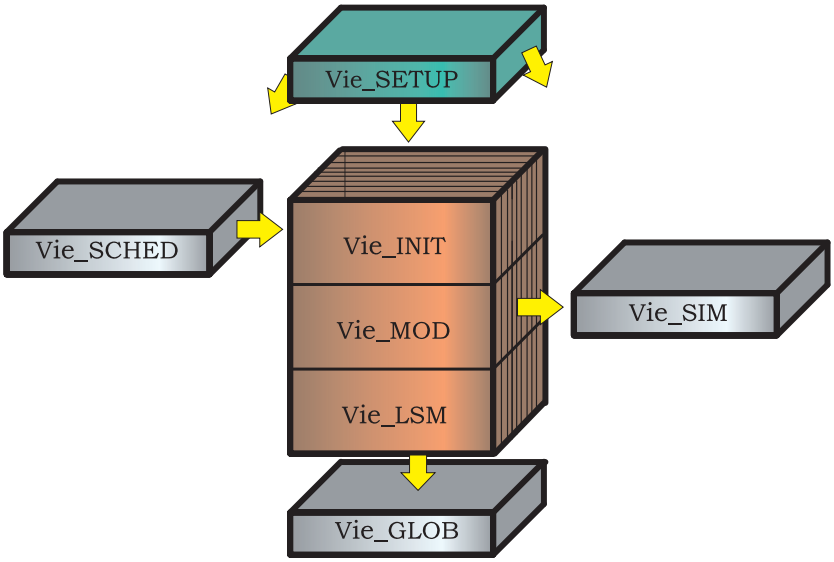

Figure 2.5.: Internal structure of VieVS Version 2.0. Adapted from Spicakova et al. (2009)

17:40 UTC, ...), or 3) integer multiplies of integer hours (00:00 UTC, 03:00 UTC, ...). This allows a following combination of parameters or a comparison of results obtained from other space-geodetic techniques very easy and straightforward.

In addition to these basic features of VieVS, i.e. to analyze one measured VLBI session, the version 2.0 of VieVS allows simulations of VLBI observations (Vie_SIM (Pany et al., 2011)), to create an observation schedule for a whole session (Vie_SCHED (Sun et al., 2011)), and to estimate global parameters from several sessions simultaneously (Vie_GLOB (Spicakova et al., 2010)). The simulation tool in Vie_SIM simulates three major error sources in the VLBI: the tropospheric delay using the method of Nilsson and Haas (2010), the station clock errors as a sum of random walk and integrated random walk process according to Herring et al. (1990), and white noise per baseline. The simulated observations can be used to generate artificial observations of the planned VLBI stations which do not yet exist, or to research investigations because the distribution of the errors in the measurement is known from the simulated observations. The scheduling package Vie_SCHED has the capability to create an observation schedule for a VLBI session, i.e. instructions for each VLBI station detailing which radio source should be observed at the specified time. The module takes into account the specific characterizations of each VLBI antenna such as its slew rate in azimuth and elevation, and a structure model for each source to predict the observed flux on each baseline of a scan (Sun et al., 2011).

The module Vie_GLOB offers the option to stack observations from multiple VLBI sessions and

to estimate parameters from the whole history of VLBI measurements. It has been designed and created in connection with this Ph.D. thesis.

2.5.1. Vie_GLOB

Module Vie_GLOB has the capability to estimate parameters which are common to all VLBI sessions from a so-called global solution, i.e. from a common adjustment of many VLBI sessions. The input data for Vie_GLOB are datum-free normal equations (NEQ) prepared by the module Vie_LSM. The global solution is typically used to determine TRF in terms of station positions and velocities, and the CRF in terms of radio source coordinates. Figure 2.6 shows one of the graphical user interfaces where several options for estimating the new TRF and CRF can be chosen by an analyst. The computational strategy of Vie_GLOB follows several steps. First, information from all sessions is read to detect all parameters which are contained in the input normal equations. Because of limited computer memory capacity, and due to time consumption, it is essential to keep the equation system small. Therefore only parameters of interest for the global solution are kept in the session-wise NEQ and the remaining parameters are either fixed to their a priori values or reduced from the equations. The reduction takes place for parameters which appear in only a single session and are dependent on a finite amount of time. These

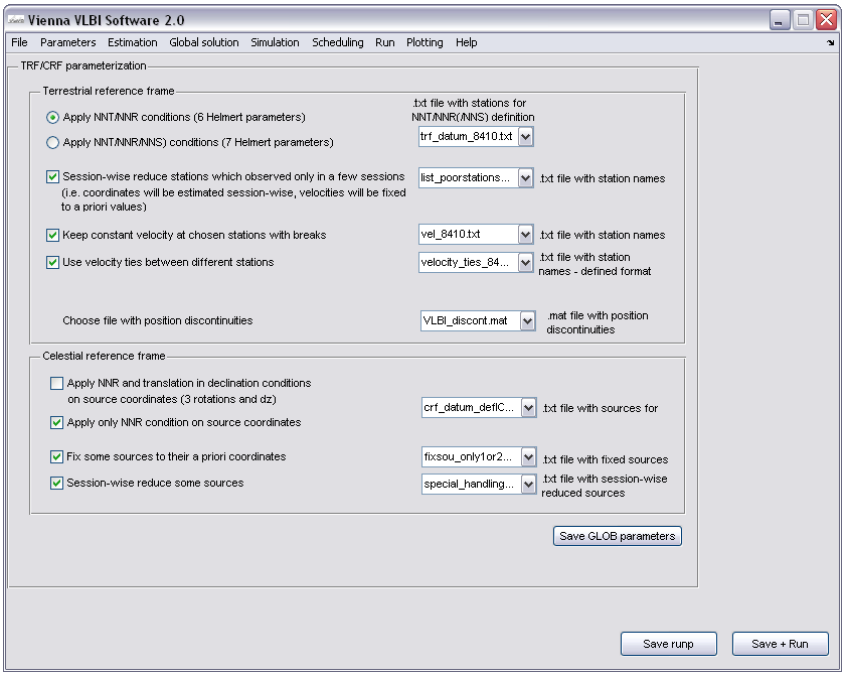

Figure 2.6.: One of the graphical user interfaces of VieVS 2.0 controlling the module Vie_GLOB.

are, for example, the clock parameters, zenith wet delays or tropospheric gradients which can vary by several hours. The reduction means an implicit estimation of such parameters from the session-wise NEQ by a least squares adjustment. The global parameters are detected in the NEQ taken from single sessions, and a new reference number is assigned to each parameter. In the second step of Vie_GLOB the NEQ are reorganized following the new order of parameters (columns/rows in normal matrix and rows in normal vector) and stacked together with the reorganized NEQ from other sessions. This leads to one common global normal matrix which consists of the global parameters only. In the third step conditions (like no-net-rotation and no-net-translation on TRF or no-net-rotation on CRF) and eventually constraints are applied, and by a final inversion of the NEQ system the estimates of the global parameters are obtained. In a usual run of Vie_GLOB where we are only interested in the global parameters (e.g. in a new reference frame) the analysis stops at this stage. However, if we are also interested in the solution for parameters which have been session-wise reduced, a backward solution has to be carried out. This means that the residuals estimated for the global parameters are taken and substituted into the reduced equation going step by step always one level up. Details concerning the least squares adjustment and the computational procedure applied in Vie_GLOB is described in chapter 3. In this thesis I concentrate mainly on the estimation of TRF, CRF and of geophysical parameters such as Love and Shida numbers or free core nutation parameters.

2.6. International VLBI Service for Geodesy and Astrometry

The International VLBI Service for Geodesy and Astrometry (IVS) is an official service of the International Association of Geodesy (IAG) and supports geodetic and astrometric work on reference systems, Earth science research, and operational activities (Schlüter, 2000). It was established in 1999 and from that time it has coordinated the globally distributed VLBI components (see Figure 2.7) consisting presently of a total of 79 permanent components, representing 41 institutions in 19 countries with ca. 280 associate members (Behrend and Baver, 2011a). Before the establishment of IVS the cooperation between organizations was on a voluntary basis, but now from the time that an organization is accepted as a member of the IVS its contribution to the service is an obligation. Therefore IVS can guarantee the delivery of high quality products for scientific and also operational applications (Schlüter, 2000). The VLBI products are the foundation of many scientific and practical applications requiring the use of an accurate inertial reference frame, such as high-precision navigation and positioning (Behrend and Baver,

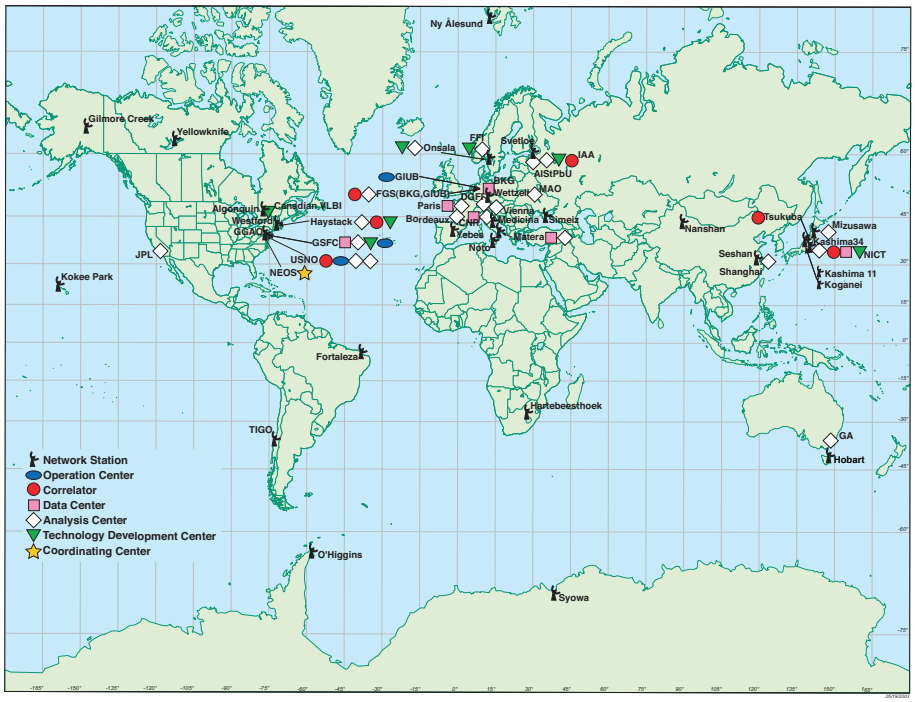

Figure 2.7.: Map with the global distribution of IVS components.

2011b). In Figure 2.8 an overview of the current main IVS products is given. VLBI data products currently available are the full set of Earth orientation parameters, the TRF, the CRF, and tropospheric parameters (Schuh and Behrend, 2012). All IVS data and products are archived in data centres and are publicly available for research in related areas of geodesy, geophysics, and astrometry.

2.6.1. VLBI2010

In 2005 a key report called "VLBI2010: Current and Future Requirements for Geodetic VLBI Systems" (Niell et al., 2005) was accepted by the IVS directing board. It consists of a revision of the current and future requirements for geodetic VLBI, including all components from antennas to analysis. The report also states recommendations for a new generation of VLBI systems to ensure new criteria for future IVS products defined by the requirements of the Global Geodetic Observing System (GGOS). These criteria are:

- 1 mm measurement accuracy on global baselines,
- continuous measurements for time series of station positions and EOP,
- turnaround time to initial geodetic results of less than 24 hours (near real-time).

PRODUCTS	SPECIFICATION	STATUS (2010)
Polar motion x_p, y_p	Accuracy	50-80 µas
	Product delivery	8-10 days
	Resolution	1 day
	Frequency of solution	~3 days/week
UT1 − UTC	Accuracy	3-5 µs
	Product delivery	8-10 day
	Resolution	1 day
	Frequency of solution	~3 days/week
UT1 − UTC (Intensives)	Accuracy	15-20 µas
	Product delivery	1 day
	Resolution	1 day
	Frequency of solution	7 days/week
Celestial pole dX, dY	Accuracy	50 µas
	Product delivery	8-10 days
	Resolution	1 day
	Frequency of solution	~3 days/week
TRF (x, y, z)	Accuracy	5 mm
CRF (α, δ)	Accuracy	40-250 µas
	Frequency of solution	1 year
	Product delivery	3 months

Figure 2.8.: Main IVS products with their current accuracies. Based on Schlüter (2000) and Schuh and Böhm (2013).

Following the acceptance of the report, the IVS established the VLBI2010 Committee to carry out a series of studies recommended by Niell et al. (2005) and to encourage the realization of the new vision for geodetic VLBI. The results and achievements of the VLBI2010 Committee have been summarized in the VLBI2010 Progress Report called "Design Aspects of the VLBI2010 System" (Petrachenko et al., 2009). The impact of new strategies on the quality of VLBI products was investigated with Monte Carlo simulations (Pany et al., 2011). The effect of the three dominant VLBI random error processes (reference clock, troposphere, and the delay measurement noise) was studied, and it was confirmed that the dominant error source is the atmosphere. Concerning the requirements for the new VLBI2010 antennas, a single 12-m diameter antenna with a slew rate of 12 deg/s in azimuth or twin-antennas with slew rates of minimal 5 deg/s in azimuth, are desired to allow a reduction in the time required for slewing between sources and also to decrease the on-source time needed to make a precise delay measurement (Petrachenko et al., 2009). The concept of VLBI2010 includes a new observable which ensures a requisite precision with the shortened on-source time. This is the broadband delay with a recommended four-band system that uses a broadband feed to span the entire frequency range from 2 to

14 GHz (Petrachenko et al., 2009). To ensure the third criterion for the future IVS products (i.e. the results' availability in near real-time) at least a subset of antennas has to have access to high-speed optical fibre networks to ensure fast delivery of the initial IVS products. There are high expectations of the automation systems at the stations and of the remote control technologies. The operator would have full access to the antenna remotely and should also be able to control several antennas from an arbitrary distance (Neidhardt et al., 2011).

After the publication of the VLBI2010 Progress Report (Petrachenko et al., 2009) the IVS Directing Board established the VLBI2010 Project Executive Group "to provide strategic leadership to the VLBI2010 project and guide the transition from the VLBI2010 development phase to the VLBI2010 implementation phase" (Hase et al., 2011). It serves as a primary contact inside IVS for institutions which plan to upgrade their equipment according to the VLBI2010 requirements. Presently it is expected that the VLBI network will be fully implemented until the end of 2020, and the new broadband observations will be carried out within a regular operation from 2015. The existing global S/X network stations will be maintained in parallel to support data continuity, astrometry, and space applications (Hase et al., 2011).

3. Least Squares Adjustment

In geodesy the method of least squares is the common method to find "the best" estimate of the measured components of an observation vector. With the best estimate a unique solution with a minimal sum of squared residuals in an overdetermined system is meant, i.e. system in which there are less unknowns than equations. In this chapter a brief overview of this method is given, based mainly on publications from Hampacher and Radouch (2003), Perović (2005) and Angermann et al. (2004). Attention is paid only to issues relevant to this thesis.

3.1. Least Squares Adjustment - Basics

From a series of measurements one gets an observation vector $\boldsymbol{l'}$ which differs from the real value $\boldsymbol{L}$ which is due to the various error sources $\boldsymbol{\varepsilon}$, which influence the measurement

$$\boldsymbol{L} = \boldsymbol{l'} + \boldsymbol{\varepsilon}. \tag{3.1}$$

It is not possible to estimate $\boldsymbol{\varepsilon}$ and $\boldsymbol{L}$ from the measurement, therefore it is searching for an approximation of $\boldsymbol{L}$, which is called the adjusted value $\bar{\boldsymbol{l}}(\boldsymbol{x})$. The adjusted value is often a function of more unknown values $\boldsymbol{x}$.

$$\bar{\boldsymbol{l}}(\boldsymbol{x}) = \boldsymbol{l'} + \boldsymbol{v}. \tag{3.2}$$

The equation of residuals $\boldsymbol{v}$ giving the difference between the adjusted value and the measurements can be written as

$$\boldsymbol{v} = \bar{\boldsymbol{l}}(\boldsymbol{x}) - \boldsymbol{l'}. \tag{3.3}$$

The least squares method can be used under two assumptions:

1. linearity, and
2. unbiasedness.

The unbiasedness of observational errors means the absence of systematic measuring errors. Because of the difficulty to fulfil this condition in the praxis, it is sufficient to realize such conditions in the measurements that the systematic influences in the measurements are negligible compared to random errors.

The linearity of the equation (3.3) has to be achieved by a Taylor series expansion of $\bar{\boldsymbol{l}}(\boldsymbol{x})$ restricted to the terms of first order. Therefore if possible, approximate a priori values $\boldsymbol{x_0}$ of the unknown parameters are introduced and within the least squares method only small corrections $\boldsymbol{dx}$ in the neighbourhood of these values are estimated. After the introduction of $\boldsymbol{x} = \boldsymbol{x_0} + \boldsymbol{dx}$ into the equation (3.3) and the Taylor expansion one gets:

$$\boldsymbol{v} = \bar{\boldsymbol{l}}(\boldsymbol{x_0}) + \frac{\boldsymbol{\partial}\bar{\boldsymbol{l}}(\boldsymbol{x})}{\boldsymbol{\partial x}} \mid_{\boldsymbol{x}=\boldsymbol{x_0}} \cdot \boldsymbol{dx} - \boldsymbol{l'}. \tag{3.4}$$

The equation of residuals can be expressed as:

$$\boldsymbol{v} = \boldsymbol{A} \cdot \boldsymbol{dx} - \boldsymbol{l}, \tag{3.5}$$

with $\boldsymbol{A}$ as design matrix, i.e. matrix containing partial derivatives of $\bar{\boldsymbol{l}}(\boldsymbol{x})$ for n independent observations w.r.t. u estimated parameters:

$$\boldsymbol{A} = \frac{\boldsymbol{\partial}\bar{\boldsymbol{l}}(\boldsymbol{x})}{\boldsymbol{\partial x}} \mid_{\boldsymbol{x}=\boldsymbol{x_0}} = \begin{bmatrix} \frac{\partial \bar{l}_1(\boldsymbol{x})}{\partial x_1} & \cdots & \frac{\partial \bar{l}_1(\boldsymbol{x})}{\partial x_u} \\ \vdots & \vdots & \vdots \\ \frac{\partial \bar{l}_n(\boldsymbol{x})}{\partial x_1} & \cdots & \frac{\partial \bar{l}_n(\boldsymbol{x})}{\partial x_u} \end{bmatrix}, \tag{3.6}$$

and reduced observation vector $\boldsymbol{l}$, referred also as "o − c" vector, meaning "observed minus computed":

$$\boldsymbol{l} = \boldsymbol{l'} - \bar{\boldsymbol{l}}(\boldsymbol{x_0}). \tag{3.7}$$

The least squares method seeks a vector $\boldsymbol{dx}$ which will be unique and where the weighted square sum of residuals will be minimized:

$$\begin{aligned} \boldsymbol{\Omega} = \boldsymbol{v}^T\boldsymbol{P}\boldsymbol{v} = minimum \quad \Rightarrow \quad \frac{\partial \boldsymbol{\Omega}}{\partial \boldsymbol{dx}} = 0 \quad \text{and} \quad \frac{\partial^2 \boldsymbol{\Omega}}{\partial \boldsymbol{dx}^2} > 0 \\ \frac{\partial \boldsymbol{v}^T\boldsymbol{P}\boldsymbol{v}}{\partial \boldsymbol{dx}} = (\frac{\partial \boldsymbol{v}}{\partial \boldsymbol{dx}^T})2\boldsymbol{P}\boldsymbol{v} = \boldsymbol{A}^T 2\boldsymbol{P}\boldsymbol{v} = 0. \end{aligned} \tag{3.8}$$

$\boldsymbol{P}$ is the weight matrix of the observation vector. In case of uncorrelated observations the weight matrix $\boldsymbol{P}$ is a diagonal matrix with weights p_i for each observation

$$p_i = \frac{\sigma_0^2}{\sigma_i^2}. \tag{3.9}$$

The weights are proportional numbers giving a higher importance to more accurate observations to ensure a higher influence on the adjusted values. Therefore the weights are defined by the

standard deviation of observation σ_i and by a constant value called a priori standard deviation of unit weight σ_0 to which corresponds an observation with the weight $p_i = 1$. Substitution of $\boldsymbol{v}$ from equation (3.5) into equation (3.8) yields the system of normal equations

$$\begin{aligned} \boldsymbol{A}^T\boldsymbol{P}(\boldsymbol{A}\cdot\boldsymbol{dx}-\boldsymbol{l}) = \boldsymbol{A}^T\boldsymbol{P}\boldsymbol{A}\cdot\boldsymbol{dx} - \boldsymbol{A}^T\boldsymbol{P}\boldsymbol{l} = 0 \\ \boldsymbol{N}\cdot\boldsymbol{dx}-\boldsymbol{b}=0. \end{aligned} \tag{3.10}$$

The solution for $\boldsymbol{dx}$ is

$$\boldsymbol{dx} = \boldsymbol{N}^{-1}\boldsymbol{b} = (\boldsymbol{A}^T\boldsymbol{P}\boldsymbol{A})^{-1}\boldsymbol{A}^T\boldsymbol{P}\boldsymbol{l} \tag{3.11}$$

and the unknown parameters are gained by

$$\boldsymbol{x} = \boldsymbol{x_0} + \boldsymbol{dx}. \tag{3.12}$$

A covariance matrix $\boldsymbol{M_{dx}}$ of estimated parameters is a matrix where the diagonal elements are variances and the non-diagonal ones are covariances of $\boldsymbol{dx}$. It can be obtained by multiplying a corresponding cofactor matrix $\boldsymbol{Q_{dx}}$ with a dimensionless squared a posteriori variance of unit weight σ_0^2.

$$\boldsymbol{M_{dx}} = \sigma_0^2\cdot\boldsymbol{Q_{dx}}, \text{with} \tag{3.13}$$

$$\boldsymbol{Q_{dx}} = \boldsymbol{N^{-1}}, \text{and} \tag{3.14}$$

$$\sigma_0^2 = \frac{\boldsymbol{v}^T\boldsymbol{P}\boldsymbol{v}}{dof}, \tag{3.15}$$

where dof denotes "degree of freedom" of the adjusted system, i.e. $dof = n - u$.
In view of equation (3.12) for the covariance matrix $\boldsymbol{M_x}$ of the unknown parameters follows:

$$\boldsymbol{M_x} = \boldsymbol{M_{dx}}. \tag{3.16}$$

3.2. Reduction and stacking of parameters

The VLBI measurements are carried out nowadays in so-called sessions, i.e. in a certain time period (from one hour to one day) a network of a few stations observes extragalactic sources and the measurements are recorded. The analyst will then get a file containing the prime observable (time delay). In the least squares adjustment the N matrix contains only measurements from this actual time period.
In this work I am mainly interested in estimating the parameters that need a long time span

(several years) for their determination. In this case it is necessary to combine the N matrices from single sessions into one common N matrix and estimate the concerned parameters in one adjustment. There are two main features which have to be dealt with when using this procedure and which can be solved by a session-wise reduction of selected parameters. The first problem is the limited computer memory. In cases where one would involve all parameters from the single session N matrices into one N matrix, the size of this new N matrix would be too huge to be processed using a standard PC. The second reason for a parameter reduction is that some parameters are not suitable for a global adjustment. They can either describe time-varying events (e.g. Earth rotation) or not enough data is collected to estimate them globally (e.g. short data time span for station velocity estimation).

The reduction of parameters is based on a division of the normal equation system into two parts. In the first part those parameters are concentrated, which will be kept in the global matrix, and in the second part parameters are ordered, which will be estimated only from a single session:

$$\begin{bmatrix} \boldsymbol{N_{11}} & \boldsymbol{N_{12}} \\ \boldsymbol{N_{21}} & \boldsymbol{N_{22}} \end{bmatrix} \cdot \begin{bmatrix} \boldsymbol{dx_1} \\ \boldsymbol{dx_2} \end{bmatrix} = \begin{bmatrix} \boldsymbol{b_1} \\ \boldsymbol{b_2} \end{bmatrix}. \tag{3.17}$$

The matrix equation (3.17) corresponds to the following two coupled equations:

$$\boldsymbol{N_{11}} \cdot \boldsymbol{dx_1} + \boldsymbol{N_{12}} \cdot \boldsymbol{dx_2} = \boldsymbol{b_1}, \tag{3.18}$$

$$\boldsymbol{N_{21}} \cdot \boldsymbol{dx_1} + \boldsymbol{N_{22}} \cdot \boldsymbol{dx_2} = \boldsymbol{b_2}. \tag{3.19}$$

From equation (3.19) vector $\boldsymbol{dx_2}$ can be expressed containing the reduced parameters:

$$\boldsymbol{dx_2} = \boldsymbol{N_{22}^{-1}} \cdot \boldsymbol{b_2} - \boldsymbol{N_{22}^{-1}} \boldsymbol{N_{21}} \cdot \boldsymbol{dx_1} \tag{3.20}$$

and substituted into equation (3.18):

$$\boldsymbol{N_{11}} \cdot \boldsymbol{dx_1} + \boldsymbol{N_{12}} \boldsymbol{N_{22}^{-1}} \cdot \boldsymbol{b_2} - \boldsymbol{N_{12}} \boldsymbol{N_{22}^{-1}} \boldsymbol{N_{21}} \cdot \boldsymbol{dx_1} = \boldsymbol{b_1}, \tag{3.21}$$

$$(\boldsymbol{N_{11}} - \boldsymbol{N_{12}} \boldsymbol{N_{22}^{-1}} \boldsymbol{N_{21}}) \cdot \boldsymbol{dx_1} = \boldsymbol{b_1} - \boldsymbol{N_{12}} \boldsymbol{N_{22}^{-1}} \cdot \boldsymbol{b_2}, \qquad \Longrightarrow \tag{3.22}$$

$$\boldsymbol{N_R} \cdot \boldsymbol{dx_1} = \boldsymbol{b_R}. \tag{3.23}$$

The reduced N matrix $\boldsymbol{N_R}$ and the reduced b vector $\boldsymbol{b_R}$ are than "stacked" with reduced normal equation systems from other sessions and a global N matrix $\boldsymbol{N_G}$ and a global b vector $\boldsymbol{b_G}$ is created. Attention has to be paid so that the order of parameters is identical in the reduced normal equation systems:

$$\begin{aligned} \boldsymbol{N_G} &= \boldsymbol{N_{R1}} + \boldsymbol{N_{R2}} + \boldsymbol{N_{R3}} + \cdots, \\ \boldsymbol{b_G} &= \boldsymbol{b_{R1}} + \boldsymbol{b_{R2}} + \boldsymbol{b_{R3}} + \cdots. \end{aligned} \tag{3.24}$$

The final solution for the global parameters is done using an inversion of the global normal equation system:

$$\boldsymbol{dx_G} = \boldsymbol{N_G^{-1}} \cdot \boldsymbol{b_G}. \tag{3.25}$$

The estimates of the session-wise reduced parameters can be obtained by substituting the vector $\boldsymbol{dx_G}$ into the equation (3.20), where $\boldsymbol{dx_1} = \boldsymbol{dx_G}$ and thus contains the globally adjusted parameters. It is obvious that one has to store the matrices $\boldsymbol{N_{22}}$, $\boldsymbol{N_{21}}$ and vectors $\boldsymbol{b_2}$ of each session. To obtain the time series of the reduced parameters from all sessions it should be started with the reduced normal equation of the last session and then continued in a "backward direction" always one level up (Gipson, 1998).

For derivation of the covariance information for global and session-wise parameters, the equations for $\boldsymbol{dx_G}$ and $\boldsymbol{dx_2}$ are transformed back to the matrix notation. With a substitution of $\boldsymbol{dx_G}$ from equation (3.22) into the equation (3.20) one gets the following matrix system:

$$\begin{bmatrix} \boldsymbol{dx_G} \\ \boldsymbol{dx_2} \end{bmatrix} = \begin{bmatrix} \boldsymbol{N_G^{-1}} & \boldsymbol{N_G^{-1} \cdot N_{12} \cdot N_{22}^{-1}} \\ \boldsymbol{N_{22}^{-1} \cdot N_{21} \cdot N_G^{-1}} & \boldsymbol{N_{22}^{-1} + N_{22}^{-1} \cdot N_{21} \cdot N_G^{-1} N_{12} \cdot N_{22}^{-1}} \end{bmatrix} \cdot \begin{bmatrix} \boldsymbol{b_G} \\ \boldsymbol{b_2} \end{bmatrix}, \tag{3.26}$$

where the cofactor matrices are those on the diagonal, i.e.

$$\boldsymbol{Q_G} = \boldsymbol{N_G^{-1}}, \tag{3.27}$$

$$\boldsymbol{Q_{22}} = \boldsymbol{N_{22}^{-1}} + \boldsymbol{N_{22}^{-1} \cdot N_{21} \cdot N_G^{-1} N_{12} \cdot N_{22}^{-1}}. \tag{3.28}$$

By a substitution of $\boldsymbol{Q_{dx}}$ in equation (3.13) with $\boldsymbol{Q_G}$ and $\boldsymbol{Q_{22}}$ the variance matrix for global and session-wise parameters, respectively, is obtained. Concerning the σ_0 in the equation (3.15), $\boldsymbol{v^T P v}$ has to be divided into two parts. The first part of the general division reading

$$\begin{aligned} \boldsymbol{v^T P v} = (\boldsymbol{A \cdot dx - l})^T \boldsymbol{P}(\boldsymbol{A \cdot dx - l}) = (\boldsymbol{dx^T \cdot A^T - l^T})\boldsymbol{P}(\boldsymbol{A \cdot dx - l}) = \cdots \\ = \boldsymbol{l^T P l - dx^T \cdot A^T P l} = \boldsymbol{l^T P l - dx^T \cdot b}, \end{aligned} \tag{3.29}$$

depends on the single-session analysis and the second part can be evaluated only after the global adjustment. In the case of the session-wise reduction it is necessary to subtract for each session the session-wise matrix $\boldsymbol{N_{22}}$ and vector $\boldsymbol{b_2}$ from the $\boldsymbol{l^T P l}$ value and after the final solution subtract the product of $\boldsymbol{dx_G}^T$ and $\boldsymbol{b_R}$:

$$\boldsymbol{v^T P v} = (\boldsymbol{l^T P l} - \boldsymbol{b_2^T N_{22}^{-1} b_2}) - \boldsymbol{dx_G}^T \cdot \boldsymbol{b_R}. \tag{3.30}$$

3.3. Constraining of parameters

During the VLBI analysis it often happens that the observations do not contain all the necessary information needed for creating a solution, or that the observations are not homogeneously distributed in time. Introduction of external limits is essential to avoid the normal equation system being singular. It can be done by installing fictitious observations, so-called "pseudo-observations", and including them into the adjustment.
The linearized system of conditions is introduced as

$$\boldsymbol{B} \cdot \boldsymbol{dx} = \boldsymbol{b_c}, \tag{3.31}$$

if $\boldsymbol{b_c}$ is a stochastic vector, then instead of equation (3.31) one can write

$$\boldsymbol{v_b} = \boldsymbol{B} \cdot \boldsymbol{dx} - \boldsymbol{b_c}. \tag{3.32}$$

After applying the least squares condition (equation (3.8)) on equations (3.5) and (3.31) one can derive the normal equation system. The method of Lagrange where the condition equation is multiplied by $-2\boldsymbol{k}^T$ with $\boldsymbol{k}$ being so-called Lagrange correlates allows one to rewrite the equations as:

$$\begin{gathered}
\overline{\boldsymbol{\Omega}} = \boldsymbol{v}^T\boldsymbol{P}\boldsymbol{v} - 2\boldsymbol{k}^{\boldsymbol{T}}(\boldsymbol{B} \cdot \boldsymbol{dx} - \boldsymbol{b_c}) = minimum \\
\frac{\partial\overline{\boldsymbol{\Omega}}}{\partial \boldsymbol{dx}} = (\frac{\partial \boldsymbol{v}}{\partial \boldsymbol{dx}^{\boldsymbol{T}}}) \cdot 2\boldsymbol{P}\boldsymbol{v} - 2\boldsymbol{B}^T\boldsymbol{k} = 0; \qquad \frac{\partial\overline{\boldsymbol{\Omega}}}{\partial \boldsymbol{k}} = \boldsymbol{B} \cdot \boldsymbol{dx} - \boldsymbol{b_c} = 0, \\
\boldsymbol{A}^T 2\boldsymbol{P}(\boldsymbol{A} \cdot \boldsymbol{dx} - \boldsymbol{l}) - 2\boldsymbol{B}^T\boldsymbol{k} = 0, \\
\boldsymbol{A}^T\boldsymbol{P}\boldsymbol{A}\boldsymbol{dx} - \boldsymbol{B}^T\boldsymbol{k} - \boldsymbol{A}^T\boldsymbol{P}\boldsymbol{l} = 0,
\end{gathered} \tag{3.33}$$

$$\begin{aligned}
&\boldsymbol{A}^T\boldsymbol{P}\boldsymbol{A}\boldsymbol{dx} - \boldsymbol{B}^T\boldsymbol{k} - \boldsymbol{A}^T\boldsymbol{P}\boldsymbol{l} = 0, \\
&\boldsymbol{B} \cdot \boldsymbol{dx} \qquad\qquad\quad - \boldsymbol{b_c} = 0.
\end{aligned} \tag{3.34}$$

In a matrix form the normal equation system with conditions can be written as:

$$\begin{bmatrix} \boldsymbol{A}^T\boldsymbol{P}\boldsymbol{A} & \boldsymbol{B}^T \\ \boldsymbol{B} & 0 \end{bmatrix} \cdot \begin{bmatrix} \boldsymbol{dx} \\ -\boldsymbol{k} \end{bmatrix} = \begin{bmatrix} \boldsymbol{A}^T\boldsymbol{P}\boldsymbol{l} \\ \boldsymbol{b_c} \end{bmatrix}. \tag{3.35}$$

Relative constraints

The parameters are constrained to each other by a known value. In case the parameter estimation is done for certain intervals (e.g. parameterisation by piece-wise linear offsets every 30 minutes) there can be two following intervals without any observation. In such a case constraints have to be applied to connect the parameter estimates, referring to the time before the data dropout, to the parameter estimates from time intervals after the data dropout. In this work I use relative

constraints also e.g. to estimate an equal velocity of antennas being located at the same place. In this case the value in vector $\boldsymbol{b_c}$ is zero. If one uses the relative constraints to define the so-called "local ties", i.e. known coordinates' differences at one site between two antennas, the vector $\boldsymbol{b_c}$ would contain the known value (measured by a terrestrial technique). The condition equation for relative constraints between parameter $p1$ and $p2$ is

$$x_{p1} - x_{p2} = b_c \tag{3.36}$$

and following the equation (3.32) one gets:

$$v_b = x_{p1} - x_{p2} - b_c, \tag{3.37}$$

$$v_b = \begin{bmatrix} 1 & -1 \end{bmatrix} \cdot \begin{bmatrix} x_{p1} \\ x_{p2} \end{bmatrix} - b_c. \tag{3.38}$$

The impact of constraints on the solution can be regulated by introducing a weight matrix P_c.

$$\begin{aligned} \boldsymbol{B}^T\boldsymbol{B} \cdot \boldsymbol{dx} - \boldsymbol{B}^T\boldsymbol{b_c} &= 0, \\ \boldsymbol{dx} &= (\boldsymbol{B}^T\boldsymbol{B})^{-1}\boldsymbol{B}^T\boldsymbol{b_c}, \\ \text{where} \quad \boldsymbol{H} &= (\boldsymbol{B}^T\boldsymbol{B})^{-1}\boldsymbol{B}^T. \end{aligned} \tag{3.39}$$

By adding the normal equation system of the pseudo-observations to the unconstrained normal equation system it can be written:

$$(\boldsymbol{A}^T\boldsymbol{P}\boldsymbol{A} + \boldsymbol{H}^T\boldsymbol{P_c}\boldsymbol{H}) \cdot \boldsymbol{dx} = \boldsymbol{A}^T\boldsymbol{P}\boldsymbol{l} + \boldsymbol{H}^T\boldsymbol{P_c}\boldsymbol{b_c}. \tag{3.40}$$

Minimum constraints - TRF

VLBI is a relative technique, therefore to obtain absolute locations of the antennas certain conditions on the network have to be introduced. One way is to introduce so-called "free network" conditions. These are based on a similarity transformation between the a priori and the new adjusted reference frame. These two frames are, in general, related to each other by seven Helmert parameters, i.e. three translations, three rotations and one scale factor, which fix the TRF at a given epoch and by their time derivatives to define the TRF time evolution. Free network conditions mean that some of the parameters are set to zero. If the three translation parameters $\boldsymbol{T}_{TRF}$ are set to zero it results in a no-net-translation (NNT) condition imposed on the new adjusted coordinates w.r.t. the a priori reference frame. Setting the three rotation angles $\boldsymbol{R}_{TRF}$ to zero implies a no-net-rotation (NNR) condition. In the case of a global VLBI adjustment, the NNT condition together with the NNR condition is applied. In the VLBI analysis there is no constraining of the scale employed.

The transformation of a coordinate vector $\boldsymbol{X_1}$ in reference system 1 into coordinate vector $\boldsymbol{X_2}$ in reference system 2 is thus given by

$$\boldsymbol{X_2} = \boldsymbol{X_1} + \boldsymbol{T}_{TRF} + \boldsymbol{R}_{TRF}\boldsymbol{X_1}. \tag{3.41}$$

The transformation for a velocity vector is got by the differentiating equation (3.41) w.r.t. time:

$$\partial\boldsymbol{X_2} = \partial\boldsymbol{X_1} + \partial\boldsymbol{T}_{TRF} + \partial\boldsymbol{R}_{TRF}\boldsymbol{X_1} + \boldsymbol{R}_{TRF}\partial\boldsymbol{X_1}. \tag{3.42}$$

Between the reference frame 1 and 2 only small rotations are assumed, so it holds

$$\boldsymbol{T}_{TRF} = \begin{bmatrix} T_x \\ T_y \\ T_z \end{bmatrix}, \qquad \boldsymbol{R}_{TRF} = \begin{bmatrix} 0 & -\omega_z & \omega_y \\ \omega_z & 0 & -\omega_x \\ -\omega_y & \omega_x & 0 \end{bmatrix} \tag{3.43}$$

where the sign of rotation follows the IERS Conventions 2010 (Petit and Luzum, 2010).
The vector of Helmert parameters is denoted as $\boldsymbol{\chi}$:

$$\boldsymbol{\chi}^T = \begin{bmatrix} T_x & T_y & T_z & \omega_x & \omega_y & \omega_z & \partial T_x & \partial T_y & \partial T_z & \partial\omega_x & \partial\omega_y & \partial\omega_z \end{bmatrix} \tag{3.44}$$

and the equations (3.41) and (3.42) can be rewritten as

$$\Delta\boldsymbol{X} = \boldsymbol{B} \cdot \boldsymbol{\chi} \tag{3.45}$$

with

$$\Delta\boldsymbol{X} = \begin{bmatrix} \boldsymbol{X_2} - \boldsymbol{X_1} \\ \partial\boldsymbol{X_2} - \partial\boldsymbol{X_1} \end{bmatrix} \tag{3.46}$$

and

$$\boldsymbol{B} = \begin{bmatrix} & \vdots & \\ \boldsymbol{B1} & & 0 \\ \boldsymbol{B2} & & \boldsymbol{B1} \\ & \vdots & \end{bmatrix} \tag{3.47}$$

, where

$$\boldsymbol{B1} = \begin{bmatrix} 1 & 0 & 0 & 0 & Z_1^i & -Y_1^i \\ 0 & 1 & 0 & -Z_1^i & 0 & X_1^i \\ 0 & 0 & 1 & Y_1^i & -X_1^i & 0 \end{bmatrix} \tag{3.48}$$

and

$$\boldsymbol{B2} = \begin{bmatrix} 0 & 0 & 0 & 0 & \dot{Z}_1^i & -\dot{Y}_1^i \\ 0 & 0 & 0 & -\dot{Z}_1^i & 0 & \dot{X}_1^i \\ 0 & 0 & 0 & \dot{Y}_1^i & -\dot{X}_1^i & 0 \end{bmatrix}. \tag{3.49}$$

According to Petit and Luzum (2010) the term $\boldsymbol{R}_{TRF}\partial\boldsymbol{X_1}$ in equation (3.42) is about 0.1 mm over 100 years and can therefore be omitted. This leads to an approximation of $\boldsymbol{B2}$ to a zero matrix.

Analogously to equation (3.32) the equation of residuals for the Helmert parameters reads

$$\boldsymbol{v_b} = \boldsymbol{B} \cdot \boldsymbol{\chi} - \Delta\boldsymbol{X} \tag{3.50}$$

and following the equation (3.39) one can write for the Helmert parameter estimates

$$\boldsymbol{\chi} = (\boldsymbol{B}^T\boldsymbol{B})^{-1}\boldsymbol{B}^T \cdot \Delta\boldsymbol{X}. \tag{3.51}$$

As already mentioned, the NNT + NNR conditions request the zero for the sum over the coordinate differences, i.e. $\Delta\boldsymbol{X} = 0$, which leads to a simplified form of the normal equation system (3.40) which is then used in the adjustment:

$$(\boldsymbol{A}^T\boldsymbol{P}\boldsymbol{A} + \boldsymbol{H}^T\boldsymbol{P_c}\boldsymbol{H}) \cdot \boldsymbol{dx} = \boldsymbol{A}^T\boldsymbol{P}\boldsymbol{l}. \tag{3.52}$$

Minimum constraints - CRF

To estimate the celestial reference frame, similarly to the terrestrial reference frame, one can also use free network conditions but only to constrain the orientation of the CRF. The relationship between the a priori CRF (1) and the estimated one (2) can be realized with a rotation matrix $\boldsymbol{R}_{CRF}$ containing three rotation angles. Alternatively an additional parameter dz accounting for a global translation of the source coordinates in declination can be introduced, which reflects systematic differences caused, e.g. by inaccuracy of the tropospheric propagation correction for sources observed at low elevations. If in the VLBI analysis a gradient estimation is applied, the parameter dz is expected to be negligible. Following Feissel-Vernier et al. (2006) the differences in coordinates for one source in the two reference frames are:

$$\alpha_2 - \alpha_1 = A_1 \tan\delta_1 \cos\alpha_1 + A_2 \tan\delta_1 \sin\alpha_1 - A_3, \tag{3.53}$$

$$\delta_2 - \delta_1 = -A_1 \sin\alpha_1 + A_2 \cos\alpha_1 + dz. \tag{3.54}$$

In matrix notation one gets

$$\boldsymbol{B} = \begin{bmatrix} & \vdots & & \\ \tan\delta_1\cos\alpha_1 & \tan\delta_1\sin\alpha_1 & -1 & 0 \\ -\sin\alpha_1 & \cos\alpha_1 & 0 & 1 \\ & \vdots & & \end{bmatrix} \tag{3.55}$$

and the $\boldsymbol{\chi}$ vector with free network parameters

$$\boldsymbol{\chi}^T = \begin{bmatrix} A_1 & A_2 & A_3 & dz \end{bmatrix}. \tag{3.56}$$

With this annotation the procedure of TRF constraints can be followed and the final equation (3.52) for constraining the normal equation system with the VLBI observations can be applied.

4. Station displacement

In this chapter an overview of phenomena causing station displacements is given. Conventional models dealing with crust deformation are described in the IERS Conventions. The recent version 2010 (Petit and Luzum, 2010) recommends corrections of station catalogue coordinates for the effect of solid Earth tides and loading due to ocean tides, atmospheric tides, pole tide, and ocean pole tide. The corrected station coordinates are used then as a priori instantaneous positions into the adjustment of observational data. The influence of single events on the vertical displacement is shown in Figure 4.1 whereas deformation in the horizontal plane is typically nearly one order of magnitude smaller. The displacement caused by non-tidal atmospheric loading and hydrology loading (two bars on the right-hand side in the Figure 4.1) are not included in the recommendations of the IERS Conventions. Nevertheless it is stated in the document that some recommended models to correct the crustal displacement caused by these non-tidal effects are envisioned for the next edition of the IERS Conventions.

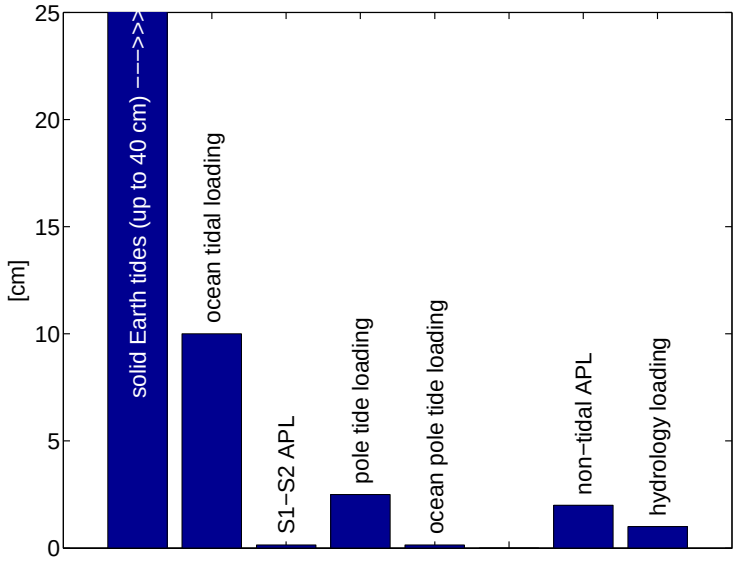

Figure 4.1.: Maximal vertical crustal deformation that can be caused by these particular phenomena.

4.1. Solid Earth tides

As visible in Figure 4.1 the effect of solid Earth tides on the station displacement clearly dominates over all other phenomena. The deformation arises from the direct effect of the external tidal potential caused by the Moon and the Sun. In Figure 4.2 the motion of station Wettzell during one month is shown. The peak-to-peak variation in the vertical direction reaches up to 40 cm, in the horizontal plane the deformation varies by several centimetres. A comprehensive description of this surface displacement is given in a following chapter 5 as this is one of the key issues relevant to my work.

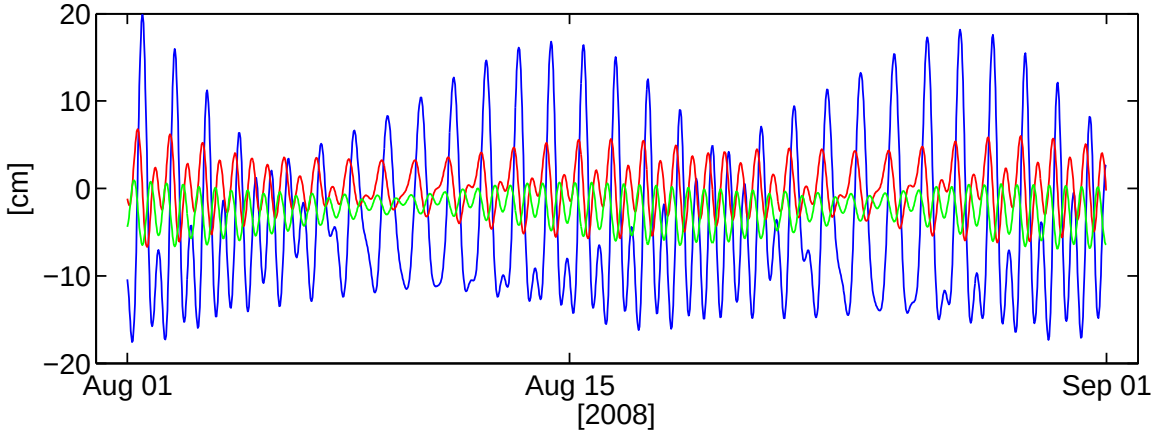

Figure 4.2.: Modelled displacement (in local REN system - blue, red, green) at station Wettzell caused by solid Earth tides during August 2008.

4.2. Ocean loading

Similar to solid Earth tides, ocean tides are caused by the tide generating potential due to the gravitational attraction of the Moon and Sun. They redistribute water mass and cause an associated load on the oceanic crust. The response of the oceans is dependent on their location and the local regional conditions that affect the water flow, therefore models with gridded formulations are needed (Petit and Luzum, 2010). The IERS Conventions 2010 provide a table with several global ocean tidal models, but recommend using the two most recent ones: TPXO7.2 (Egbert and Erofeeva, 2002) which was derived using tide gauge and TOPEX/Poseidon data, and FES2004 (Letellier, 2004) computed as a hydrodynamic solution with altimetry data. The amplitudes and phases for eleven main tides (M_2, S_2, N_2, K_2, K_1, O_1, P_1, Q_1, M_f, M_m, and S_{sa}) can be obtained

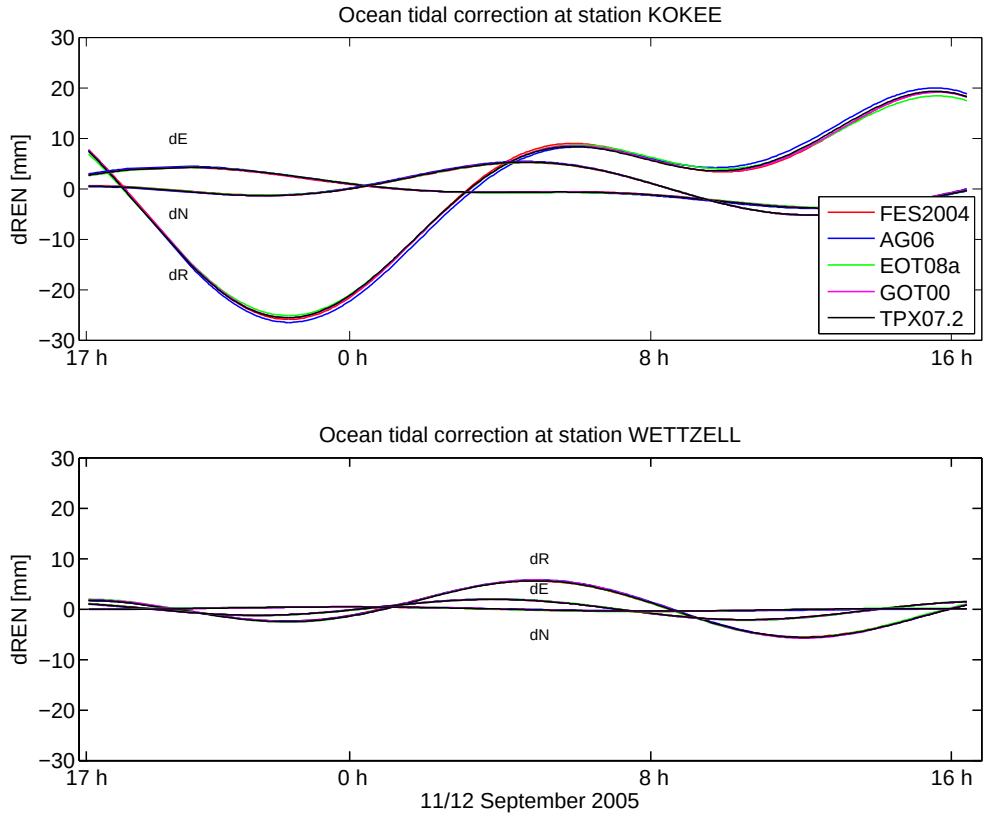

Figure 4.3.: Comparison of five ocean tidal models providing ocean loading corrections during one 24-hour VLBI session on September 12, 2005. The upper plot shows the differences at station Kokee Park exceeding 2 mm. On the lower plot the ocean loading corrections for station Wettzell are plotted.

for each VLBI site from the ocean loading service site at http://froste.oso.chalmers.se/loading/ maintained by M. S. Bos and H.-G. Scherneck. In addition recent IERS Conventions 2010 require an implementation of 342 constituent waves whose amplitudes and phases are found by an interpolation of the tidal admittances based on the eleven main tides. In the VLBI analysis software VieVS ocean loading corrections based on five different ocean tide models are implemented. In Figure 4.3 a comparison of these different loading corrections for stations Kokee Park (Hawaiian Islands) and Wettzell (Germany) during one 24-hour session is shown. At station Kokee Park where the effect of ocean tidal loading is large (about 5 cm in vertical component during this particular day), the corrections in the vertical direction differ in their maximum amplitudes by about 2 mm. For the inland station Wettzell, where the ocean loading effect reaches about 1 cm in the vertical during one day, the differences are negligible (a few tenths of a millimetre).

4.3. Atmospheric pressure loading

The redistribution of the air masses in the atmosphere causes displacement of geodetic sites of up to several millimetres, and in the regions of strong variability of pressure systems (e.g. mid-latitude regions) the amplitudes of vertical displacement can reach up to 1-2 cm. The non-tidal atmospheric loading corrections are provided as a time series, usually with a six hour resolution. Nowadays time series from three different atmospheric pressure loading (APL) services are implemented in VieVS. These are a) APL time series provided by the Goddard (GSFC) VLBI group which are available on the web at http://gemini.gsfc.nasa.gov/aplo (Petrov and Boy, 2004); b) APL time series determined at the University of Luxembourg (http://geophy.uni.lu/ncep-loading.html (van Dam, 2010)); and c) APL time series provided by the Vienna group ((Wijaya et al., 2012) http://ggosatm.hg.tuwien.ac.at/LOADING/). The a) and b) series are derived from the NCEP (National Center for Environmental Prediction) reanalysis surface pressure field given

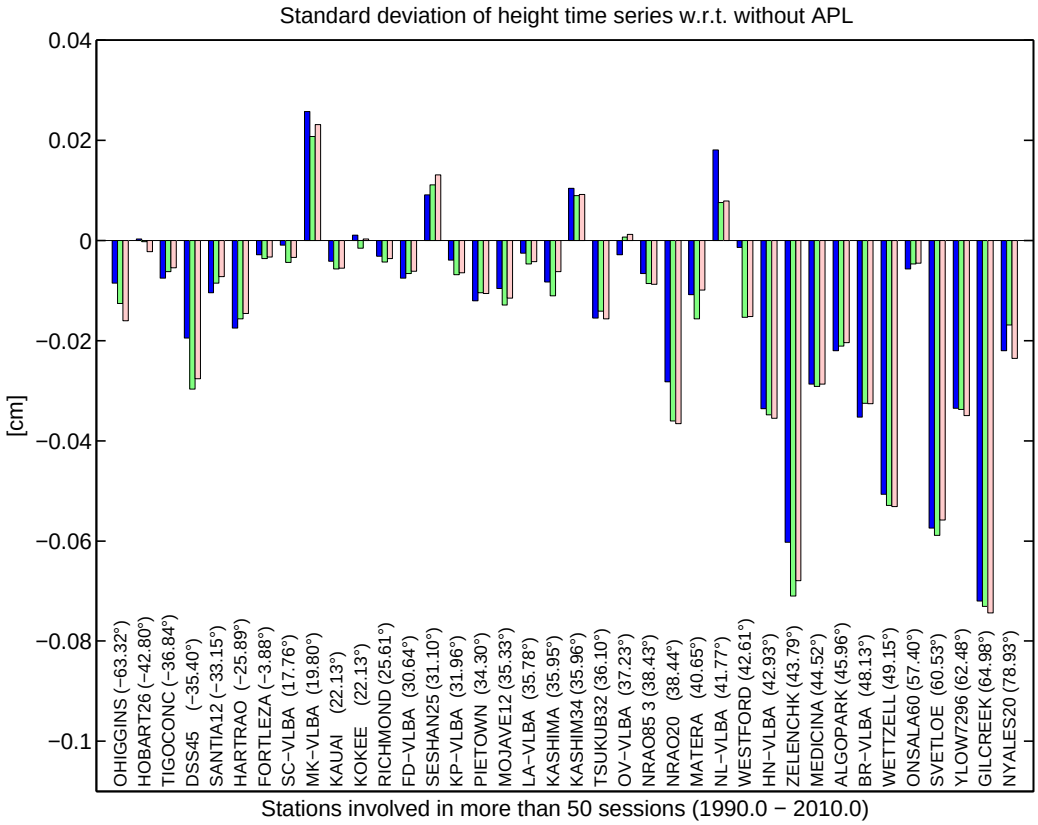

Figure 4.4.: Standard deviations of height time series from three VLBI solutions with different APL corrections: Vienna group (blue), GSFC group (light green) and University of Luxembourg (light pink). The differences are with respect to the solution where no APL corrections were applied.

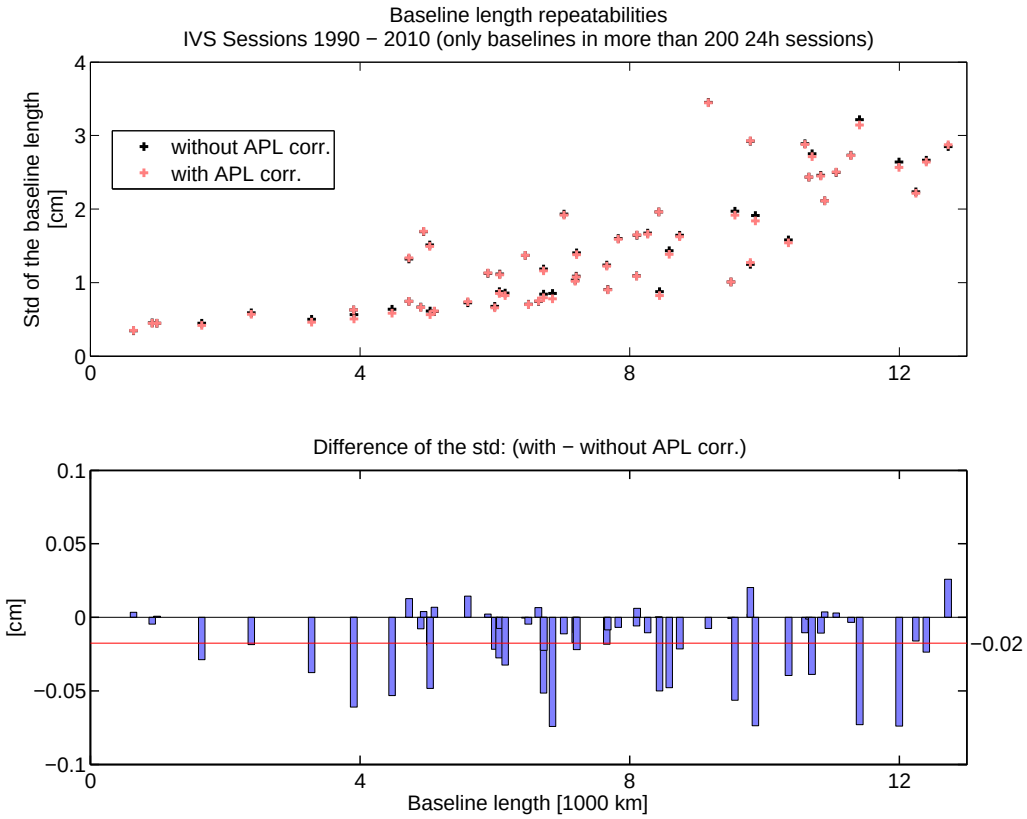

Figure 4.5.: Baseline length repeatabilities from VLBI solution with applying APL as a priori corrections (black) and from solution without applying APL (light red). The lower plot shows differences in the standard deviation (std) of the baseline length (with minus without APL). The mean std is plotted with the red line.

on a global grid of 2.5° x 2.5° spatial resolution. The c) series are calculated using the reference pressure derived from ECMWF (European Centre for Medium-Range Weather Forecasts) reanalysed data with 1.0° x 1.0° spatial resolution. The pressure data for calculating the time series contains signals associated with the diurnal (S1) and semi-diurnal (S2) atmospheric tides. Since the data is provided with a six hour resolution, the representation of the tidal signals cannot be done with an accurate resolution (van den Dool et al., 1997). The tidal signals have to be removed from the pressure data and a separate model describing only the tidal (S1 and S2) loading corrections is introduced. The IERS Conventions 2010 recommend applying only the tidal atmospheric pressure loading for a diurnal tide S1 and a semi-diurnal tide S2 on the measured data in the analysis. For the non-tidal part of the loading no conventions are adopted. I did several tests to investigate the impact of applying APL on the station coordinates, in terms of baseline length and station height repeatabilities.

The VLBI data was processed following the standard parameterisations described in chapter 6, where one reference solution was computed without applying any APL corrections. Three other

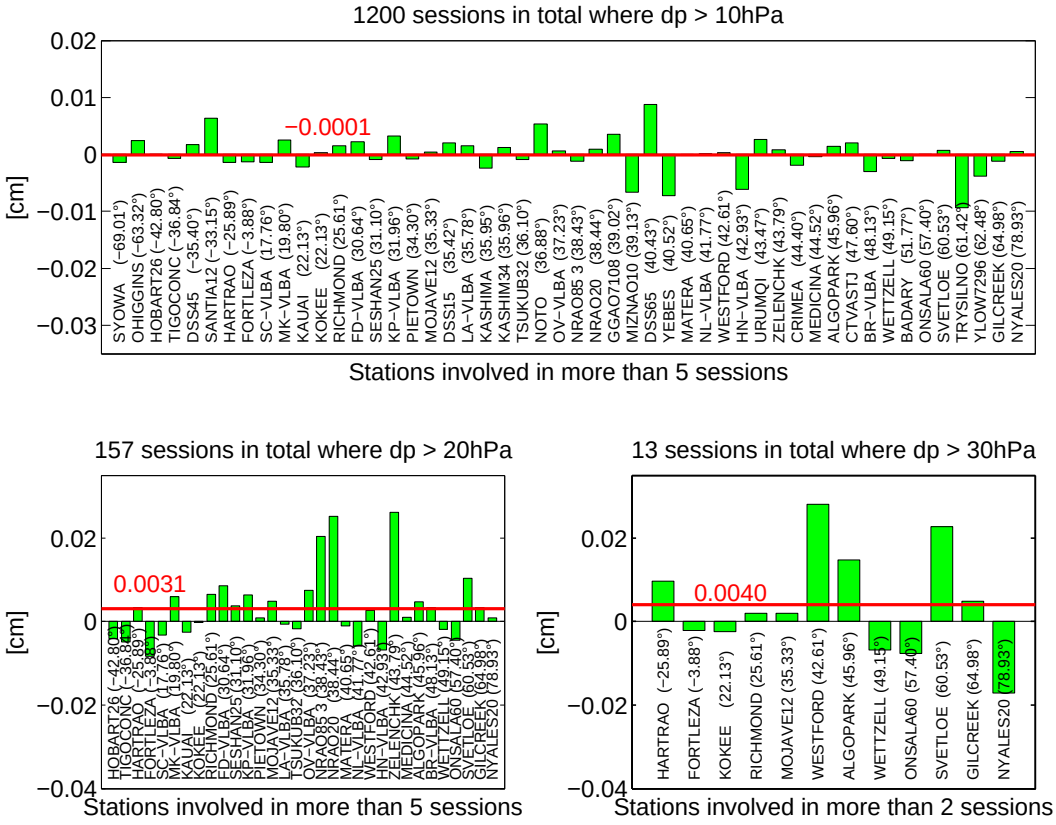

Figure 4.6.: Standard deviations of the height time series. In the upper figure std from sessions with a pressure difference of more than 10 hPa at one station are plotted. In the lower left and right figures the std are computed from sessions with a pressure difference of more than 20 hPa and 30 hPa respectively. The red lines show the mean std of the height time series.

solutions were carried out by applying the three different APL series a priori on the station coordinates. In Figure 4.4 the differences in the standard deviations of height time series between the reference solution and the solution with APL provided by Vienna group (blue), GSFC group (light green) and University of Luxembourg (light pink) are plotted. It can be seen that there are no big differences between applying any of the three APL corrections. Each of them provides, at most of the stations, a better standard deviation of the height time series compared to the solution with neglected APL. The stations are sorted by latitude in the x-axis and it is obvious that the largest improvement after applying APL corrections appears at mid-latitude sites (around $40° - 60°$N) where the APL effect is largest. In Figure 4.5 the baseline length repeatabilities for baselines which were included in more than 200 sessions are plotted. The reference solution (without APL corrections) is compared to the baseline estimates where the APL time series provided by van Dam (2010) were applied. An improvement in terms of standard deviation of the baseline length can be seen at 74% of the baselines with a mean difference of -0.2 mm.

There is a question whether applying APL corrections to the measured data is necessary at observation level (i.e. a priori) or if it would be sufficient to apply an averaged correction to each station at the stage of normal equations. Therefore I divided the sessions into three groups. The first group involves sessions in which at least one station showed the measured pressure difference during the session exceeding 10 hPa. The second group contains sessions with a pressure difference of 20 hPa and the third group of 30 hPa and more. The differences in the standard deviation of the height time series are plotted in Figure 4.6 (in the sense APL applied at normal equation level minus at observation level). The first group of sessions contained about 1200 sessions and there is no visible difference in the standard deviations between these two solutions. In the second group (pressure difference $>$ 20 hPa) the standard deviation is clearly smaller for the solution with APL corrections applied at observation level with a mean difference of 0.03 mm. The sessions with an extreme pressure difference at one side during a day (i.e. 30 hPa and more) show better standard deviation when the APL corrections were applied a priori with an interpolated value for each observation. From this follows that for "saving" sessions where one antenna was observing under extreme weather conditions, application of APL corrections at the observation level is appropriate.

4.4. Pole tide loading

The displacement of the antennas is also caused by the Earth rotation variations. Polar motion causes variations in the station coordinates which can reach a few centimetres. The Earth's mean rotation pole has a secular variation, which is a long-term drift of the pole with respect to the Earth's surface. In previous IERS Conventions 2003 (McCarthy and Petit, 2004) a linear model for describing the secular trend was adopted. In the recent IERS Conventions 2010 the mean pole is modelled with a cubic function (over the period 1976.0 - 2010.0). In Figure 4.7 both approximations are plotted, in light red the linear model and in blue the cubic one. The instantaneous pole coordinates have to be corrected for the secular pole wander.

In Plank et al. (2013) we simulated VLBI observations to investigate the effect of the mean pole modelling on the change of the TRF scale component. We used schedules corresponding to R1 and R4 sessions, which are rapid turnaround experiments regularly performed on Mondays and Thursdays, consisting of about eight globally distributed stations. The IVS started to perform these sessions in 2002. The geometry of R1 and R4 differs. Normally the networks consist of six core stations each with the addition of about two other stations observing in the network.

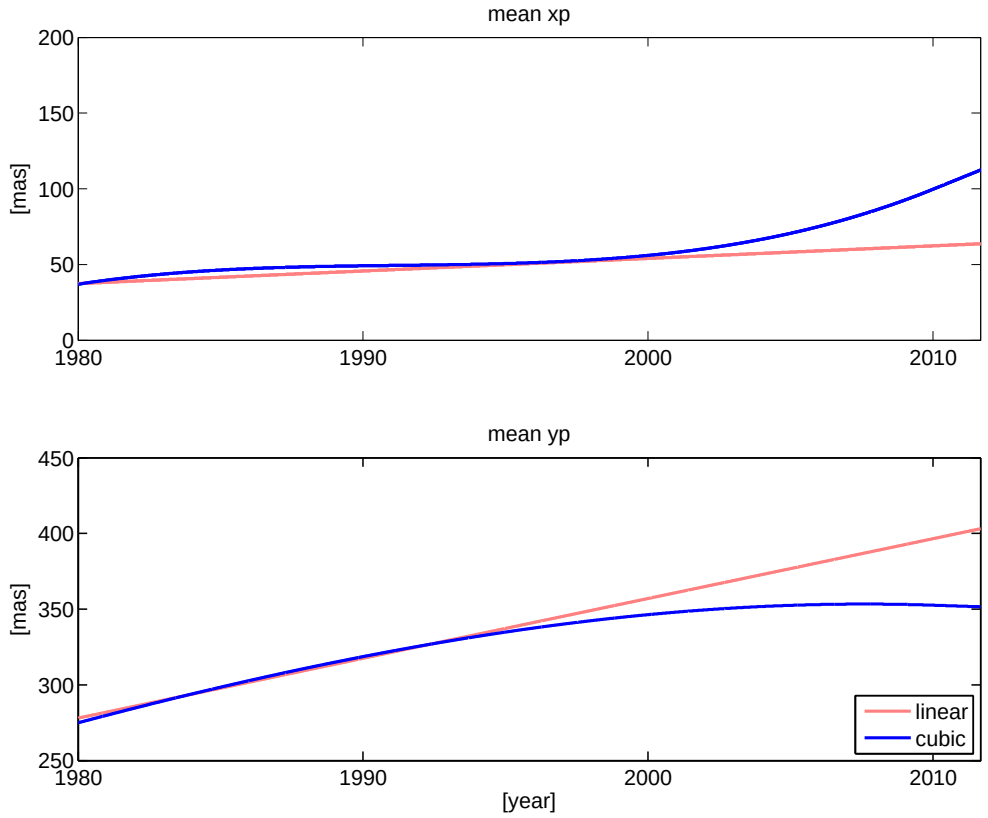

Figure 4.7.: Models for secular variation of the Earth's mean rotation pole.

In the Figures 4.8 and 4.9 the session-wise change in the scale component of the TRF is shown. Figure 4.8 shows the session-wise scale change in the estimated TRF between a solution where the mean pole path was approximated by the linear model and a solution where the secular variation was totally neglected. The results for sessions R1 (left) and R4 (right) are divided into separate plots. The colour bars represent the volume of the station network [in $10^{18}\mathrm{m}^3$] involved in the particular session. The scale offset caused by the omission of the mean pole derived from R1 sessions reaches 2 mm over 8.5 years, and about 4 mm over 8.5 years if derived from R4 sessions. The difference between these two results is caused by the diverse network geometry. The denser network of stations (R1) and large volume networks (red/yellow dots) absorb the impact on the scale from a mismodelled effect better. In Figure 4.9 the corresponding change in the scale of the TRF is shown, where the new cubic model was applied instead of the former linear one. The sessions with a large volume confirm again that the mismodeling is not critical for them as they can absorb the effect during the adjustment. Especially for the R4 networks a scale change of 0.6 mm for the time span investigated is visible.

Further investigation of the pole tide is given in chapter 7.3 which is focused on the related Love and Shida numbers.

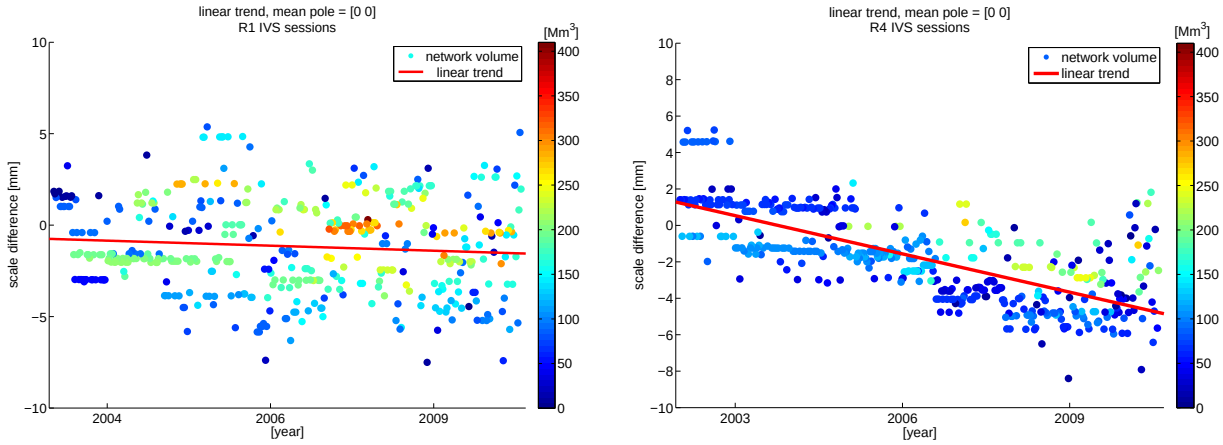

Figure 4.8.: Change of the TRF scale caused by disregarding the linear mean pole path model. On the left hand side results arising from R1 networks are plotted and on the right hand side from the R4 networks. The R1 networks (denser and with a large volume) balance the impact on the scale from the mismodelled effect better than R4, where the scale change corresponds to 0.47 mm/yr.

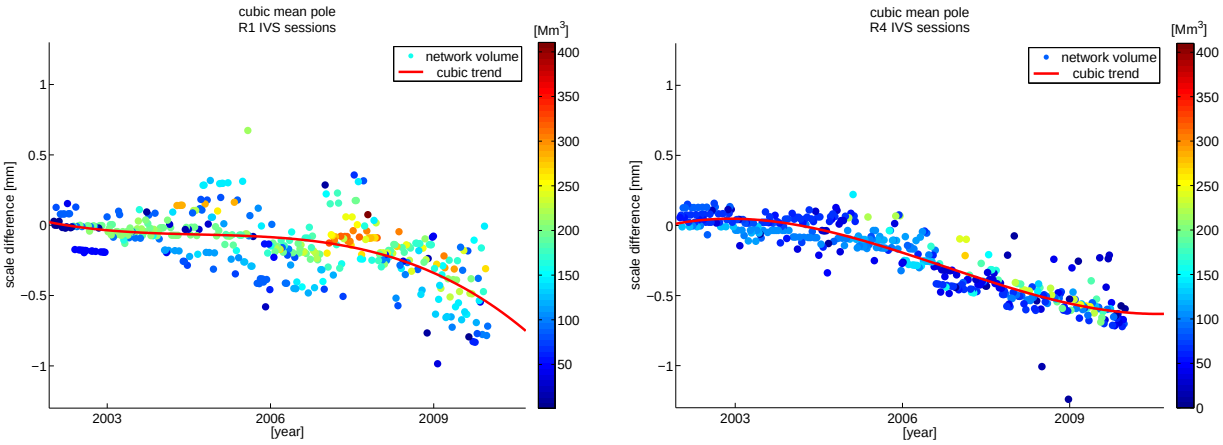

Figure 4.9.: Change in the scale of the TRF where the new cubic model, rather than the linear one, was applied. The scale change after 8.5 years exceeds 0.6 mm.

4.5. Ocean pole tide loading

The loading caused by the ocean pole tide is recommended to apply to a priori station coordinates since the latest IERS Conventions 2010. As shown in Figure 4.1 the maximum displacement which can be caused by this load reaches a maximum of 2 mm vertically. The ocean pole tide is

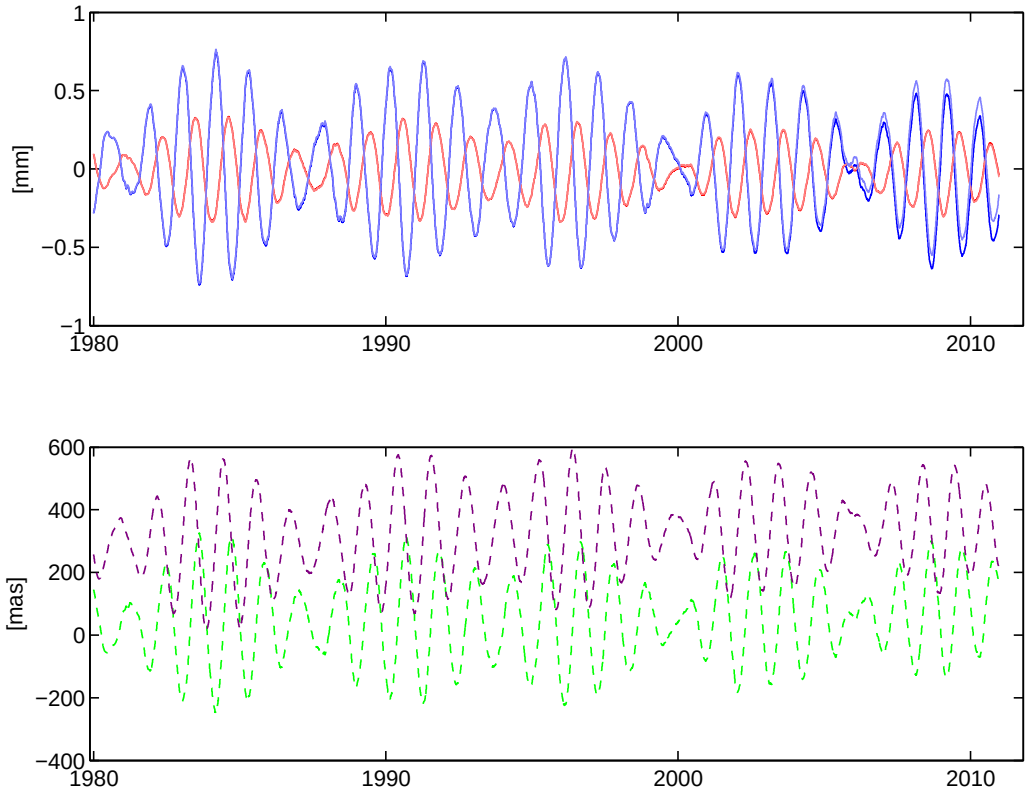

Figure 4.10.: Upper plot: ocean pole tide loading in vertical direction at station Wettzell (red) and Kokee Park (blue). In light colour shades the displacement computed with cubic mean pole function is plotted, in dark colour shades the corrections resulting from the linear mean pole approximation. Lower plot: instantaneous rotation pole components (C04 08 time series), x-pole is shown in green and y-pole in dark violet.

generated by the centrifugal effect of polar motion on the oceans (Petit and Luzum, 2010) and a recommended model for the description of the ocean pole tide is from Desai (2002). The vector of the station displacement is obtained from the ocean pole tide model as a function of the wobble parameters (m_1, m_2). These are time-dependent offsets of the instantaneous rotation pole (x_p, y_p) from the mean rotation pole $(\bar{x}_p, \bar{y}_p)$: $m_1 = x_p - \bar{x}_p$ and $m_2 = y_p - \bar{y}_p$. In the lower plot of Figure 4.10 the coordinates of the instantaneous rotation pole (x_p in green, and y_p in dark violet) for the time period from 1980.0 to 2012.0 are plotted taken from the C04 08 time series. As noted in the previous section, the mean rotation pole can be modelled by two functions: a linear one and a cubic one, and this path is shown in Figure 4.7. For this whole time span of 32 years, displacement caused by the ocean pole tide is modelled for two stations: Kokee Park and Wettzell. For each station both approximations of the mean pole tide are taken into account. The ocean pole tide loading resulting from the linear mean pole is plotted in dark colour shades and the station corrections computed with the cubic mean pole are shown in light

colour shades in the upper plot of Figure 4.10. The displacement of station Wettzell is plotted in red, and of station Kokee Park in blue. From the plot it can be seen that there is no significant difference between the calculated ocean tidal loading corrections with linear or cubic mean pole approximation during the investigated time span ca. till the year 2005. As the Figure 4.7 shows the growing difference between the linear and cubic function starting after the year 2000, the differences in the displacement become visible at the sub-millimetre level especially at the island station Kokee Park in the last investigated years where the peak difference around the year 2010 reaches 0.1 mm.

4.6. Hydrology loading

The effect of hydrological variations influences the surface deformation of the Earth. The usual vertical displacement at stations caused by the hydrology loading reaches a few millimetres, but at some areas with strong hydrological variations (South America, Asia, Central Europe) it can be up to 2 - 3 cm. The horizontal variations are smaller and do not exceed one centimetre. In the software VieVS the hydrology loading corrections provided by the NASA GSFC VLBI group are implemented (available at http://lacerta.gsfc.nasa.gov/hydlo/ (Eriksson & MacMillan)). These displacement series are computed from the GLDAS NOAH hydrology model provided by the NASA GSFC GLDAS team on a global grid map with a spatial resolution of 1 x 1 degree. The model accounts for soil moisture, snow water equivalent, and canopy water, i.e. water contained in the foliage canopy. The loading time series for each station (with respect to the centre of mass of the total Earth) is given with a monthly time resolution always to the 15^{th} day of the month. In the VLBI analysis with VieVS the hydrology loading corrections to the time of the scan are gained with Lagrange interpolation. In the Figure 4.11 hydrology loading corrections in the vertical direction for stations Zelenchukskaya (blue line) and Kokee Park (light red line) are plotted. At Zelenchukskaya, which is situated east of the Black Sea, the peak to peak vertical variations reach up to 2 cm and the maximum positive corrections appear during the summer months. The strong yearly variation of the hydrology at this site is expressed with a clearly dominant signal with the amplitude of 4 mm gained by the Fourier transformation of the time series (Figure 4.12, blue line). The station Kokee Park is located on the Hawaiian Islands where the hydrological conditions are relatively stable during the whole year. In Figure 4.12 the yearly signal in the vertical corrections detected by the Fourier transformation is shown with an amplitude of 0.4 mm and is then ten times smaller than yearly signals at mid-latitude inland stations

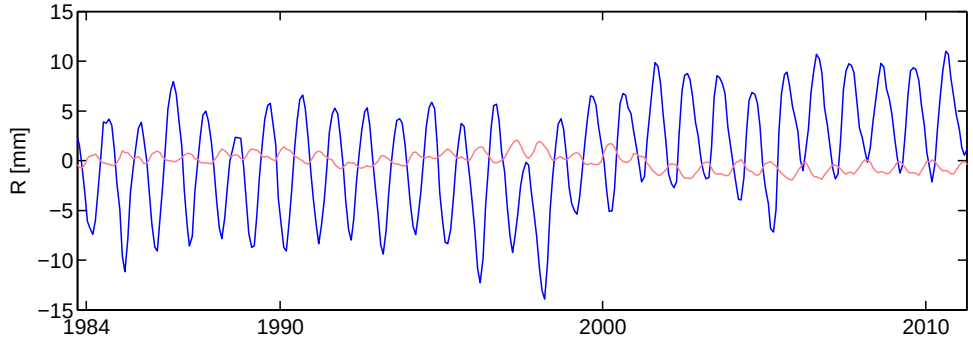

Figure 4.11.: Vertical hydrology loading corrections provided by the NASA GSFC VLBI group for station Zelenchukskaya (blue) and Kokee Park (light red).

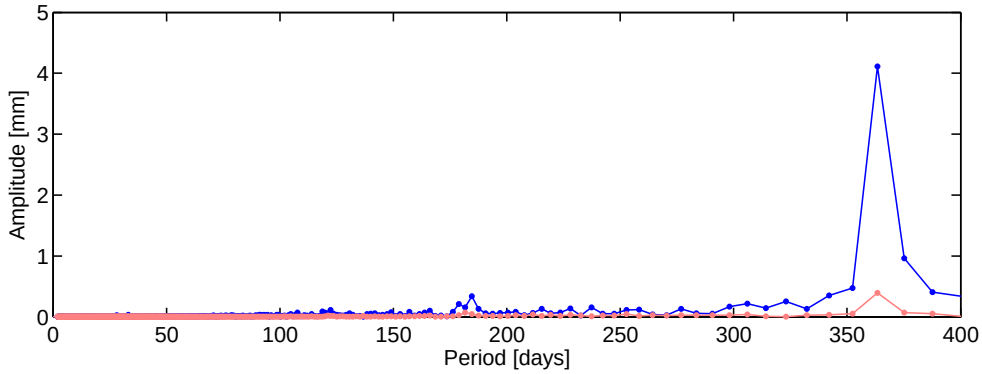

Figure 4.12.: Fourier spectrum obtained for the vertical hydrology loading corrections at station Zelenchukskaya (blue) and Kokee Park (light red).

like Zelenchukskaya.

The performance of the hydrology loading model provided by the NASA GSFC GLDAS team was examined in terms of the standard deviations of the height time series and baseline length repeatabilities. Two analyses of the VLBI data were carried out following the parameterisation and models described in chapter 6. The only difference came when applying the a priori hydrology loading corrections to the station coordinates in the second solution. In the reference solution the hydrology loading was neglected which is in accordance with the IERS Conventions 2010 where no model for hydrology loading corrections is recommended. In Figure 4.13 differences between the standard deviations of the height time series at particular stations (weighted according to the formal errors of the height estimates) between the two solutions are plotted. The stations were chosen according to the number of their participation in the VLBI sessions where the minimum was set to 50. From this group of 39 stations, at 22 stations (i.e. at 56% of the stations) a lower standard deviation of the height time series was achieved after applying the hydrology loading as a priori correction on the station coordinates. The differences in the standard deviations at all stations are under 0.5 mm with the only exception at the VLBA

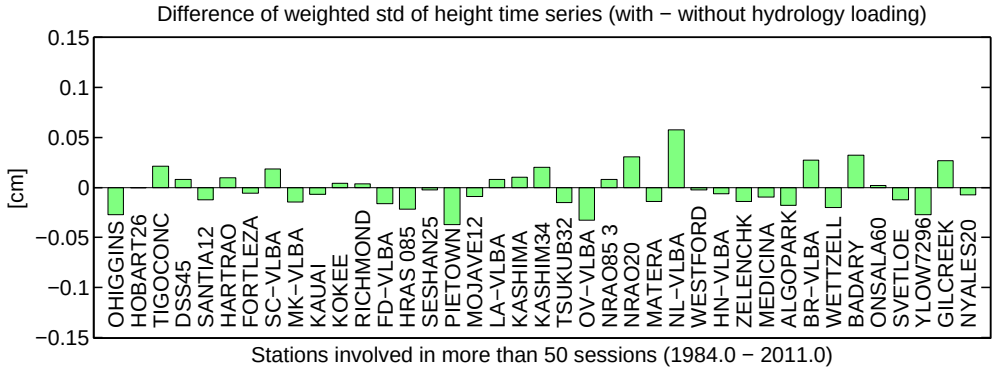

Figure 4.13.: Differences between the standard deviations of the height time series (with minus without hydrology loading).

station at North Liberty in Iowa where the difference reached 0.58 mm.

Figure 4.14 shows the time series of the height residuals at station Wettzell. Shown in the upper plot (in blue) are estimates from the solution when not applying the hydrological loading and the estimates when hydrology loading is applied are shown in red. In the lower plot differences

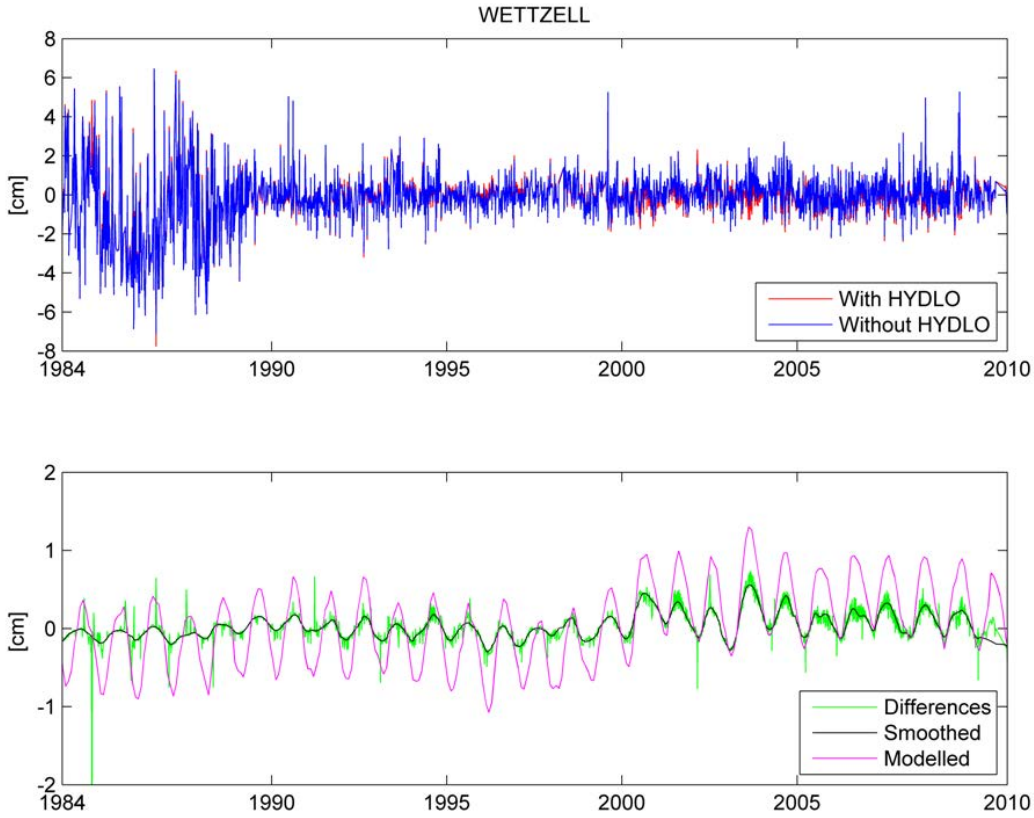

Figure 4.14.: Session-wise station height residuals at Wettzell (upper plot) with applied hydrology loading corrections (red) and without (blue). The lower plot shows the differences between these two solutions (without minus with) and the smoothed values over 50 days which are compared to the modelled values shown in pink.

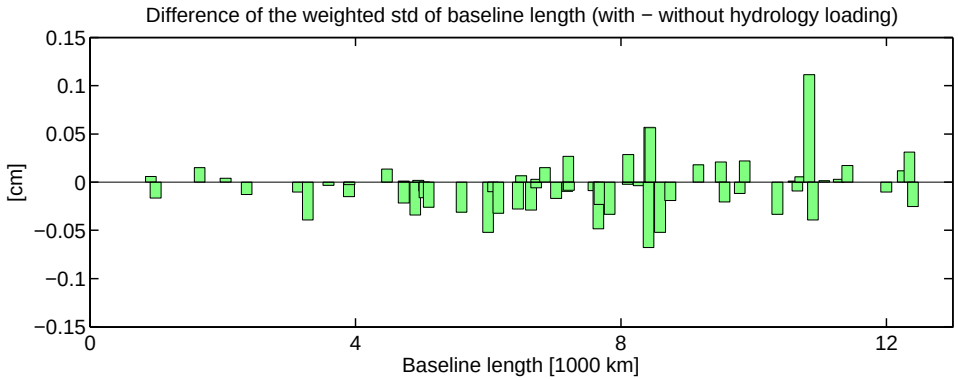

Figure 4.15.: Differences between the standard deviations of the baseline length (with minus without hydrology loading).

between these two solutions are plotted (green line) and smoothed over 50 days (black line). In the same plot the respective hydrology loading corrections are shown (pink line). It can be seen that the difference between the two solutions does not exceed the original model. This is caused by the fact that in the analysis of VLBI measurements, where the network consists of a relatively small number of stations, the applied NNT/NNR conditions on the station network absorb (i.e. distribute to other sites) a significant part of the unmodelled phenomenon.
In Figure 4.15 the comparison of the baseline length repeatabilities is given. Plotted are 62 baselines which were included in more than 200 sessions over the 27 years. The improvement in terms of a lower standard deviation after applying hydrology loading occurs at 36 baselines (i.e. at 61% of the baselines). The three baselines where the application of the hydrology loading increases the standard deviation for more than 0.5 mm are TIGO at Concepcion - Hartebeesthoek (8431 km), 32 m at Tsukuba - Wettzell (8445 km) and TIGO at Concepcion - Gilmore Creek (10837 km). The mean value of the differences in the baseline length repeatabilities is -0.006 mm. After excluding the three baselines mentioned above as outliers the mean value changes to -0.010 mm. The increase of the standard deviation for the baseline Tsukuba - Wettzell (8445 km) after applying the hydrology loading corrections, while the standard deviation of the height component of these two stations decreased, can be observed also by other baselines built by the 32 m antenna at Tsukuba. These are the baselines Tsukuba - Ny Alesund (6498 km) and Tsukuba - Westford (9506 km). The possible explanation being the redistribution of the mis-modelled effect from the 32 m antenna at Tsukuba to other sites in the network by applying the NNT/NNR condition in order to compute the station position. The length of a baseline is invariant to the NNT/NNR conditions on station coordinates. Therefore the standard deviation of the baseline length reflects the quality of the solution better than the standard deviation of the station height estimates.

5. Solid Earth tides

Research of solid Earth tides goes back to 1876 when Lord Kelvin drew attention to the deformations of the Earth and stated that it was no longer acceptable to consider the Earth as being completely rigid (Melchior, 1978). Deformation of the Earth due to solid Earth tides is caused by tidal forces arising from the gravitation attraction of celestial bodies surrounding the Earth. The tidal force at a point on the surface of, or within the Earth is the difference between the gravitation force of an attracting celestial body and forces coming up from the Earth's orbital acceleration which is constant in the whole Earth. The resulting tidal forces and the Earth deformation are shown in a sketch in Figure 5.1. At the point directly underneath the attracting body and at its antipode the tidal force is directed away from the geocentre. This causes two opposite tidal bulges which deform the Earth.

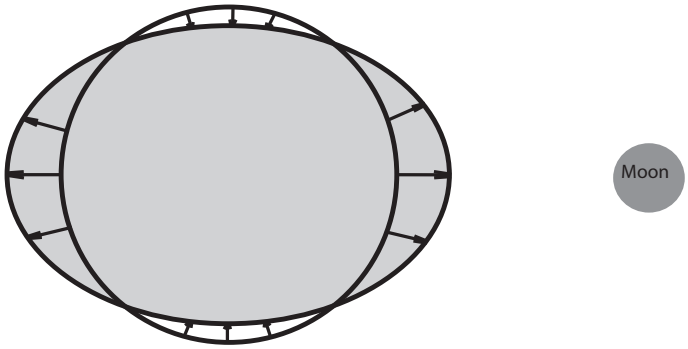

Figure 5.1.: Field of resulting tidal forces

5.1. Tidal potential

Since force is defined as a gradient of potential, the expression for the deformation caused by tidal forces is based on the description of tidal potential. Let's start with the gravitation potential V^g. It is defined as a product of the gravitational constant G with the mass M_j of the perturbing body divided by the distance ρ from the perturbing body to the considered point. The distance ρ can be interpreted as the topocentric distance to the perturbing body and can be expressed

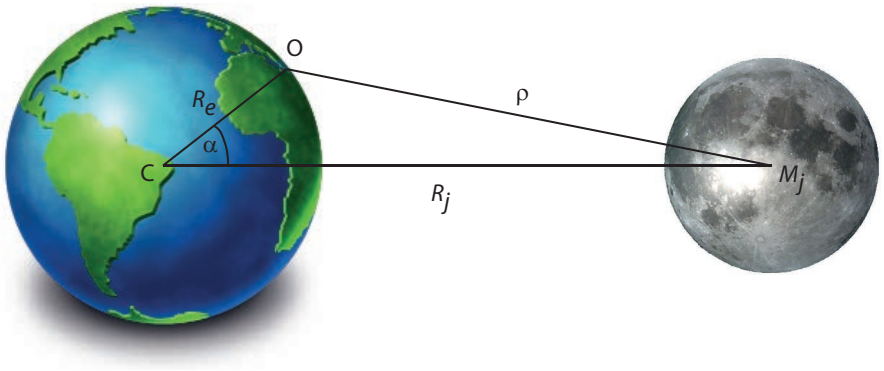

Figure 5.2.: Geometry of the two-body problem needed for the expression of a tidal force produced by the Moon at an Earth-based point O.

using the trigonometric cosine rule by the geocentric distance to the attracting body R_j, the Earth's radius R_e and a geocentric zenith distance α of the attracting body (see Figure 5.2):

$$V^g = \frac{GM_j}{\rho} = \frac{GM_j}{\sqrt{R_j^2 + R_e^2 - 2R_eR_j\cos\alpha}} = \frac{GM_j}{R_j}\frac{1}{\sqrt{1 + \frac{R_e^2}{R_j^2} - 2\frac{R_e}{R_j}\cos\alpha}}. \tag{5.1}$$

The square-root term in equation (5.1) is in practice expressed as a sum of Legendre polynomials with the argument $\cos\alpha$:

$$V^g = \frac{GM_j}{R_j}\sum_{n=0}^{\infty}\left(\frac{Re}{R_j}\right)^n P_n\big(\cos\alpha\big). \tag{5.2}$$

Legendre polynomial of degree zero equals to one, thus its gradient (i.e. the force) is zero and it can be removed from the summation. Legendre polynomial of degree one equals to its argument, i.e. $\cos\alpha$ and the whole term for the degree one potential reads:

$$V_1^g = \frac{GM_j}{R_j}\left(\frac{Re\cos\alpha}{R_j}\right). \tag{5.3}$$

Since the gradient of $Re\cos\alpha$ describes a constant force along the connection line of the geocentre and centre of the perturbing body it equals to the Earth's orbital acceleration. As noted above, this force has to actually be subtracted to get the tidal force. From this follows that tidal potential V^t is the gravitation potential starting with degree two (e.g. in Wahr (1995)):

$$V^t = \frac{GM_j}{R_j}\sum_{n=2}^{\infty}\left(\frac{Re}{R_j}\right)^n P_n\big(\cos\alpha\big). \tag{5.4}$$

In Table 5.1 the comparison of magnitudes of the second degree tidal potential produced by the Moon, the Sun, Venus, and Jupiter is shown. The magnitude is proportional to the mass of the perturbing body divided by the power of three of the geocentric distance to the body. In the first column the distances between the Earth and the celestial bodies are given. Due to

Table 5.1.: Geocentric distance R_j and the mass M_j of the Moon, the Sun, Jupiter, and Venus as input parameters for a comparison of second degree tidal potential.

	R_j **[km]**	M_j **[kg]**	$\frac{GM_j}{R_j^3}$ w.r.t. the Moon **[-]**
Moon	$0.38 \cdot 10^6$	$7.35 \cdot 10^{22}$	1
Sun	$149.6 \cdot 10^6$	$1.99 \cdot 10^{30}$	0.44
Jupiter	$800 \cdot 10^6$	$1.90 \cdot 10^{27}$	$3 \cdot 10^{-6}$
Venus	$200 \cdot 10^6$	$4.87 \cdot 10^{24}$	$5 \cdot 10^{-7}$

the ever-changing constellations between the Earth and Jupiter, and the Earth and Venus, the distances given in the table are approximate averages. In the second column the mass of the celestial bodies can be seen and in the third column the second degree potential generated by the bodies relative to the Moon's value is given. The largest second degree tidal potential on the Earth comes from the Moon and about half of its strength is generated by the Sun. The values for Jupiter and Venus are considerably smaller and can be ignored, which is also recommended by the IERS Conventions 2010 (Petit and Luzum, 2010).

Since the tidal potential is computed as a sum of Legendre polynomials one has to decide on to which degree it is necessary to do the summation. It is obvious that the influence of the polynomials decreases with the increasing degree hence the geocentric distance to the perturbing body is a denominator in the fraction $\left(\frac{Re}{R_j}\right)^n$. In Table 5.2 the values of this fraction for the degree two, three, and four for the Moon and the Sun are given. From the computed values and according to the IERS Conventions 2010 (Petit and Luzum, 2010) only the tidal potential of the second and third degree generated by the Moon and of second degree generated by the Sun is taken into consideration when the displacement on the Earth caused by the tidal forces is calculated to achieve the one millimetre accuracy. Earth deformation caused by these components of tidal potential is plotted in Figure 5.3.

Table 5.2.: Ratio between the Earth's radius and the geocentric distance to the Moon and the Sun in the second, third, and fourth degree of the tidal potential.

		n = 2	**n = 3**	**n = 4**
Moon	$\left(\frac{Re}{R_j}\right)^n$	$\frac{1}{3600}$	$\frac{1}{2 \cdot 10^5}$	$\frac{1}{1 \cdot 10^7}$
Sun	$\left(\frac{Re}{R_j}\right)^n$	$\frac{1}{6 \cdot 10^8}$	$\frac{1}{1 \cdot 10^{13}}$	$\frac{1}{3 \cdot 10^{17}}$

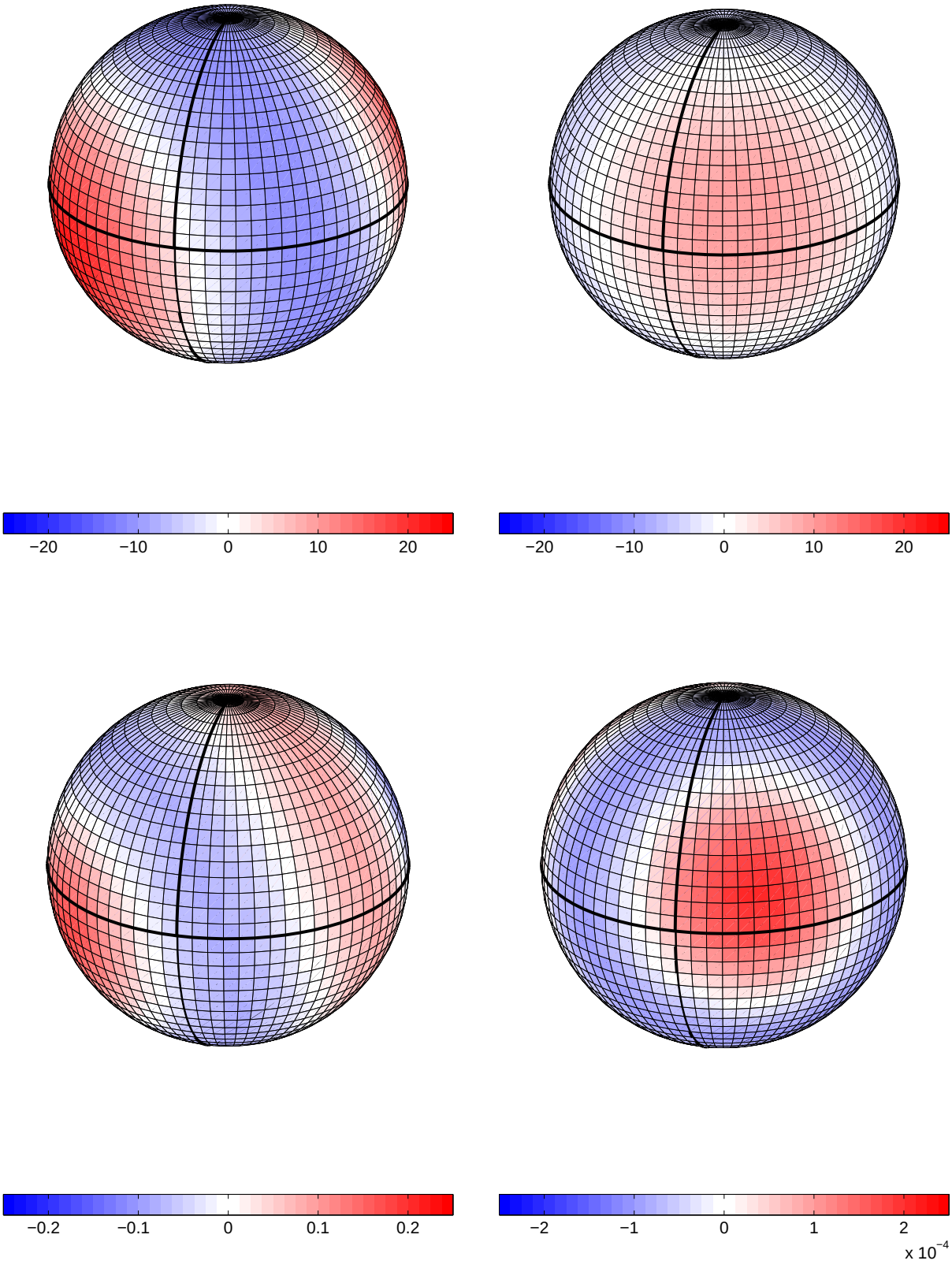

Figure 5.3.: Vertical displacement due to degree two (upper plots) and three (lower plots) tides caused by the Moon (left-hand side) and the Sun (right-hand side) on April 14^{th}, 2012 at 12 UT. The thick black lines highlight the equator and the zero meridian. Units of all colour bars are centimetres.

To find the Earth's response to the tidal potential the following Love and Shida numbers were used: $h_2 = 0.6078, l_2 = 0.0847, h_3 = 0.292, l_3 = 0.015$ as the nominal values adopted in IERS Conventions 2010. The constellation of the Earth-Moon-Sun system is taken for April 14^{th}, 2012 at 12 UT. In the plots the displacement for the whole Earth is shown caused by the tidal potential of second degree (upper plots) and of the third degree (lower plots) produced by the Moon (left-hand side) and the Sun (right-hand side). The units in the colour bars are centimetres for all plots. The largest displacement is caused by the Moon's second degree potential. The limits of the deformation go up to ± 25 cm. In red the uplift of the Earth's crust is plotted showing the two oppositely directed bulges. The second order displacement caused by the Sun reaches ± 10 cm. The bulge at the northern hemisphere near the zero meridian generated by the Sun nicely agrees with the Sun's expected position during the spring months at 12 UT together with the accounted Earth rotation. From the colour bar of the third degree Moon's tidal potential it can be seen that it leads to Earth deformation which is 100 times smaller (± 0.25 cm) than that caused by the second degree. The displacement caused by the third degree potential of the Sun is totally negligible, as can be seen from the limits not exceeding $\pm\, 2.5 \cdot 10^{-3}$ mm.

5.2. Harmonic expansion of the tidal potential

For a further analytical description it is desirable to express the geocentric zenith distance of the perturbing body α in equation (5.4) with coordinates of the celestial body and of the station O on the Earth's surface (see Figure 5.2). This can be done by using a basic formula of spherical law of cosines which includes geocentric coordinates of the station O (co-latitude Θ and longitude Λ) and the equatorial coordinates of the perturbing body (declination De expressed as a geocentric polar distance $\Psi = 90° - De$ and right ascension RA) (e.g. in Melchior (1978)):

$$\cos\alpha = \cos\Theta\cos\Psi + \sin\Theta\sin\Psi\cos H. \tag{5.5}$$

The local hour angle H is a difference between the meridian of the celestial object and the meridian of the station O which can be expressed with the hour angle of the conventional Greenwich zero meridian GH as $GH - \Lambda$.

Applying the addition theorem of spherical functions (Hobson, 1931) on $P_n\big(\cos\alpha\big)$ one gets:

$$P_n\big(\cos\alpha\big) = P_{n0}\big(\cos\Theta\big)P_{n0}\big(\cos\Psi\big) + 2\sum_{m=1}^{n}\frac{(n-m)!}{(n+m)!}P_{nm}\big(\cos\Theta\big)P_{nm}\big(\cos\Psi\big)\cos\big(m(GH-\Lambda)\big). \tag{5.6}$$

Definition of the second degree associated Legendre functions for the order m equal to zero, one and two is (with $\cos\alpha = x$):

$$\begin{aligned} P_{20}(x) &= \frac{1}{2}\Big(3x^2 - 1\Big), \\ P_{21}(x) &= -3x\sqrt{1-x^2}, \\ P_{22}(x) &= 3\big(1-x^2\big). \end{aligned} \tag{5.7}$$

The second degree Legendre polynomial for $P_2\big(\cos\alpha\big)$ can then be written as:

$$P_2\big(\cos\alpha\big) = P_{20}\big(\cos\Theta\big)P_{20}\big(\cos\Psi\big) + 2\sum_{m=1}^{2}\frac{(2-m)!}{(2+m)!}P_{2m}\big(\cos\Theta\big)P_{2m}\big(\cos\Psi\big)\cos(m(GH-\Lambda)) =$$

$$\begin{aligned} =&\frac{1}{2}\Big(3\cos^2\Theta - 1\Big)\frac{1}{2}\Big(3\cos^2\Psi - 1\Big) \\ &+ 2\left(\frac{1!}{3!}\Big(-3(\cos\Theta)\sqrt{1-\cos^2\Theta}\Big)\Big(-3(\cos\Psi)\sqrt{1-\cos^2\Psi}\Big)\cos(GH-\Lambda)\right. \\ &\left.+ \frac{0!}{4!}3\Big(1-\cos^2\Theta\Big)3\Big(1-\cos^2\Psi\Big)\cos\Big(2(GH-\Lambda)\Big)\right) = \end{aligned}$$

$$\begin{aligned} =&\frac{9}{4}\Big(\cos^2\Theta - \frac{1}{3}\Big)\Big(\cos^2\Psi - \frac{1}{3}\Big) \\ &+ 2\left(\frac{1}{6}\Big(-3\cos\Theta\sin\Theta\Big)\Big(-3\cos\Psi\sin\Psi\Big)\cos(GH-\Lambda)\right. \\ &\left.+ \frac{9}{24}\sin^2\Theta\sin^2\Psi\cos\Big(2(GH-\Lambda)\Big)\right) = \end{aligned} \tag{5.8}$$

$$\begin{aligned} =&\frac{3}{4}\left(3\Big(\cos^2\Theta - \frac{1}{3}\Big)\Big(\cos^2\Psi - \frac{1}{3}\Big)\right. \\ &+ \sin 2\Theta\sin 2\Psi\cos(GH-\Lambda) \\ &\left.+ \sin^2\Theta\sin^2\Psi\cos\Big(2(GH-\Lambda)\Big)\right). \end{aligned} \tag{5.9}$$

As follows from equation (5.4) the tidal potential of second degree is obtained by a multiplication of equation (5.9) by $\frac{GM_j}{R_j}\left(\frac{Re}{R_j}\right)^2$ for the j^{th} celestial perturbing body. Having the tidal potential in the form of equation (5.9) one can distinguish between the so-called terms of Laplace. The three terms (separated by lines) represent the three types of spherical harmonic functions. Laplace called attention to their meaning and geometric characterization (described e.g. in Melchior (1978), or in Beutler (2005)). In Figure 5.4 the three kinds of spherical harmonics are plotted. On the left plot the so-called zonal function is shown. This function does not depend on longitude. The latitude dependence is defined by the Legendre polynomials $P_{20}\big(\cos\Theta\big)$ and

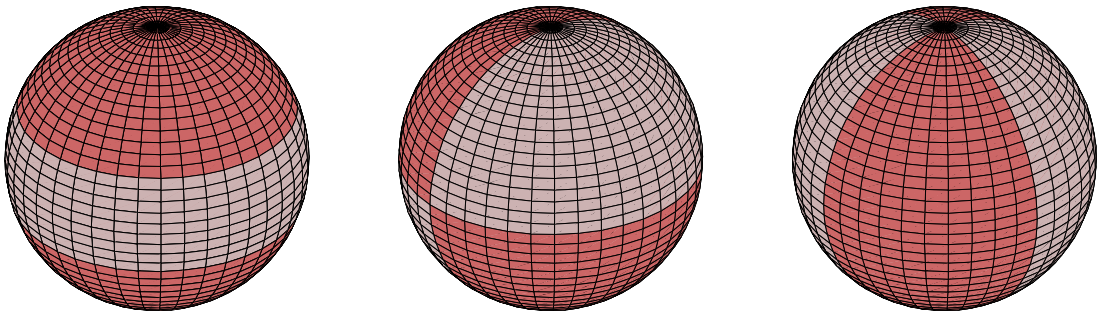

Figure 5.4.: Graphical illustration of second degree spherical harmonics of order zero (zonal, left plot), one (tesseral, middle plot), and two (sectorial, right plot).

$P_{20}\big(\cos\Psi\big)$ as can be seen on the first line of equation (5.9). In the interval from -1 to 1 the Legendre polynomial of second degree has two different roots therefore there are three latitude zones on the unit sphere with a sign change at the borders and positive values at the poles. Since it is a squared cosine function of the polar distance $(90° - De)$ of the perturbing body, its fundamental period for the Moon will be fourteen days and six months for the Sun. The middle line in equation (5.9) describes so-called tesseral functions (middle plot in Figure 5.4). These are in this case Legendre associated functions of degree two and order one. They divide the sphere into regions which change sign with the declination of the perturbing body. The corresponding tidal period is diurnal. The right plot in Figure 5.4 shows the Legendre associated function of degree and order two which corresponds to the last line in equation (5.9). As can be seen there is a multiplication of squared sine functions of co-latitude and polar distance which always yields a positive value. The term $\cos\big(2(GH - \Lambda)\big)$ makes this function dependent on longitude with a sign change at four equally spaced meridians and it's name is sectorial function. The period of corresponding tides is semi-diurnal, and their maximum amplitudes are at the equator when the declination of the perturbing body is zero.

5.3. Tidal waves

As noted above the tidal terms in the tidal potential are divided into three main frequency bands according to the length of their periods, i.e. long periodical, diurnal, and semidiurnal. Within each group there are tides with different amplitudes and strength. To get a description of tidal potential as a pure sum of sinusoidal waves one uses the notation published by Doodson. Each tidal wave is described by its amplitude and a phase angle, called astronomical tide argument θ_f.

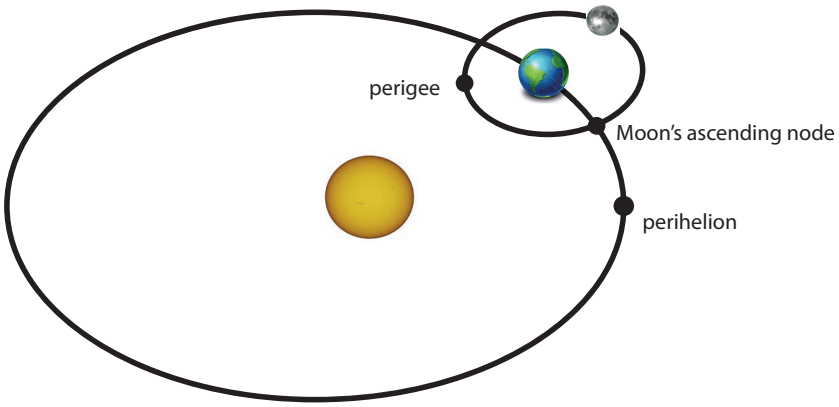

Figure 5.5.: Graphic to Doodson variables (Table 5.3).

This argument is a linear combination of six variables β (mean sidereal time and five fundamental angular arguments of the nutation series (mean longitudes)) which are over a century practically linear increasing functions of the time (described e.g. in Melchior (1978)):

$$\theta_f = \sum_{i=1}^{6} n_i \beta_i, \tag{5.10}$$

where n there are six integers separated by a dot in the middle with a certain sequence which defines one tide and is called Doodson argument number:

$$n_1(n_2+5)(n_3+5).(n_4+5)(n_5+5)(n_6+5). \tag{5.11}$$

The Doodson variables β are related to the fundamental arguments of nutation so-called Delaunay variables (see e.g. IERS Conventions 1992). Their description is given in Table 5.3.

Table 5.3.: Doodson variables and their relation to the fundamental arguments of nutation, i.e. to the Delaunay variables.

Doodson variables	Delaunay variables	
τ	$\theta_{MG} + \pi - s$	mean lunar time (θ_{MG} mean sidereal time of Greenwich meridian)
s	$F + \Omega$	mean longitude of the Moon
h	$s - D$	mean longitude of the Sun
p	$s - l$	longitude of the Moon's mean perigee
N'	$-\Omega$	negative longitude of the Moon's mean ascending node
p_1	$s - D - l'$	longitude of the Sun's mean perigee (perihelion)

Mean solar time t can be expressed from the relationship $\tau + s = t + h$ as:

$$t = \tau + s - h. \tag{5.12}$$

For each tide is n_1 equal to m, i.e. to the order of the Legendre function. Therefore the description of all diurnal tidal waves starts with 1 and of semidiurnal with 2. The first three variables have the greatest velocity. The first two digits of the argument number are called the group number and characterise the tidal waves separable from each other by one month's observations. The first three digits are called the constituent number where the tidal waves inside this group are separable after one year of data. The last three indices represent effects with only slow variations (change in latitude of lunar perigee, ascending lunar node, and perihelion).

Table 5.4.: Tidal waves selected for this work. The amplitudes are taken from Cartwright and Tayler (1971).

Name	Doodson number	Tide argument θ_f	Frequency [cpsd]	Cartwright-Tayler amplitude [mm]
Q_1	135.655	$(\tau - s) - (s - p)$	0.890804	-50.21
O_1	145.555	$\tau - s$	0.926996	-262.25
M_1	155.655	$(\tau + s) - (s - p)$	0.963806	20.62
π_1	162.556	$(t - h) - (h - p_1)$	0.991807	-7.16
P_1	163.555	$t - h$	0.994537	-122.35
K_1	165.555	$(\tau + s)$	0.999998	369.14
K_1'	165.565	$(\tau + s) + N'$	1.000145	49.97
ψ_1	166.554	$(t + h) + (h - p_1)$	1.002728	2.94
ϕ_1	167.555	$t + 3h$	1.005459	5.26
θ_1	173.655	$t + s + p$	1.031347	3.94
J_1	175.455	$(\tau + s) + (s - p)$	1.036191	20.62
Oo_1	185.555	$\tau + 3s$	1.073000	11.29
Ω_1	55.565	N'	0.000147	27.9
S_{sa}	57.555	$3h$	0.005461	-30.9
M_m	65.455	$s - p$	0.036193	-35.2
M_f	75.555	$2s$	0.073002	-66.7
M_f'	75.565	$2s + N'$	0.073149	-27.6

5.4. Deformation of the crust

The displacement of the Earth is proportional to the tidal potential by factors which reflect the amount by which the surface of the Earth responds to the tidal forces. If the Earth was an incompressible rigid body there would be no deformations of its surface. But in 1863 Lord Kelvin (Thomson, 1863) pointed out the Earth's rigidity is approximately that of steel. The proportionality numbers which link the tidal potential to the surface displacement are so-called Love and Shida numbers. The Love number h was introduced by A. E. Love in Love (1909) and it describes the displacement in a vertical direction. The deformation in the horizontal plane is linked by the Shida number l which holds its name from T. Shida and was published in 1912 (Melchior, 1978). For a basic Earth model where the Earth is considered to be spherical, non-rotating, elastic and isotropic the Love and Shida numbers are dependent on the degree of the tidal potential. The displacement vector Δd induced by the tidal potential in the local coordinate system (radial ($\hat{r}$), east($\hat{e}$), north ($\hat{n}$) (REN)) is then written as:

$$\begin{aligned}\Delta d =& \frac{1}{g}\sum_{n=2}^{\infty} h_n \cdot V_n^t \, \hat{r} \\ &+ \frac{1}{g\cos\Phi}\sum_{n=2}^{\infty} l_n \cdot \frac{\partial V_n^t}{\partial \Lambda} \, \hat{e} \\ &+ \frac{1}{g}\sum_{n=2}^{\infty} l_n \cdot \frac{\partial V_n^t}{\partial \Phi} \, \hat{n},\end{aligned} \tag{5.13}$$

where Φ and Λ are geocentric coordinates of the station and g is gravitational acceleration. The deformation of the Earth's surface caused by the degree two and three tidal potential was shown in Figure 5.3.

In the conventional model (Petit and Luzum, 2010; Wahr, 1981) for solid Earth tides the Earth is elliptic, rotating, elastic and isotropic. The Earth's ellipticity and Coriolis force due to Earth rotation cause the latitude dependence and small interband variations. Furthermore, due to a resonance of nearly diurnal free wobble in the diurnal band it leads to a strong frequency dependence of the respective Love and Shida numbers. The displacement vector is then based on a sum of tidal potential with spherical harmonic degrees n and orders m, where the effective values of Love and Shida numbers additionally depend on station latitude and tidal frequency f (Wahr,

1981):

$$\begin{aligned}\Delta d =& \frac{1}{g}\sum_{n=2}^{3}\sum_{m=0}^{n}\sum_{f} h_{nmf}\cdot V^t_{nmf}\ \hat{r} \\ &+ \frac{1}{g\cos\Phi}\sum_{n=2}^{3}\sum_{m=0}^{n}\sum_{f} l_{nmf}\cdot\frac{\partial V^t_{nmf}}{\partial\Lambda}\ \hat{e} \\ &+ \frac{1}{g}\sum_{n=2}^{3}\sum_{m=0}^{n}\sum_{f} l_{nmf}\cdot\frac{\partial V^t_{nmf}}{\partial\Phi}\ \hat{n}.\end{aligned} \tag{5.14}$$

When accounting for the anelasticity of the Earth, Love and Shida numbers become complex numbers where the imaginary part causes a phase lag of the displacement w.r.t. the tidal potential. The displacement vector due to a certain tidal wave results from equations given in Mathews et al. (1995). More details follow and are discussed in chapter 7.

6. TRF and CRF

6.1. Introduction

A reliable estimation of geophysical and geodynamic parameters requires consistent and accurate reference frames. Therefore, in this chapter, I concentrate on the determination of a Terrestrial (TRF) and a Celestial (CRF) Reference Frame. The TRF and CRF are computed simultaneously within a rigorous least squares adjustment which assures their compatibility. The analysis of the VLBI data is done by the software VieVS using 4.6 million observations from 1984.0 to 2011.0 included in 3360 24-hour IVS sessions which fulfil two criteria: 1) more than two stations were observing, and 2) the a posteriori sigma of unit weight obtained from a single-session adjustment does not exceed the value of 2. The a priori models and parameterisation of the default TRF and CRF designed as VieTRF10a and VieCRF10a are summarized in Table 6.1 and the reference frames have been published by Krásná et al. (2012b). In this paper a special focus on atmospheric effects is given, which could cause some systematic errors in the estimated station and source positions. The findings of the paper, containing some additional investigations that could not be included there because of the page limit, can be found in the appendix (A.2) of this thesis.

For each session a normal equation (NEQ) system is set up using a classical least squares method. It includes the station coordinates and velocities, source coordinates, Earth orientation parameters, zenith wet delays, tropospheric gradients, and clock parameters. The local parameters (connected only to a single session) are session-wise reduced from the normal equations. These parameters are the EOP, zenith wet delays, tropospheric gradients and clock parameters. The number of parameters included in the NEQ which enters the global adjustment then decreases significantly and makes the matrix easy to handle in terms of the computer memory capacity. In the global solution the NEQ system contains only the station coordinates, station velocities and source coordinates. The time series of EOP, zenith wet delays and tropospheric gradients

of each station are obtained by a backward solution using a substitution of estimates of the global parameters. A detailed description of the parameter reduction and retrieving them by the backward solution was described in chapter 3.2.

6.2. Terrestrial Reference Frame

During the 27 years of VLBI observations (1984.0 - 2011.0), which are included in this analysis, 94 stations took part in the measurements (see Table 6.2). In the second and third column of the table, the first and last year of the provided data is given and in the fourth column the time period in years is computed. The fifth column gives a total number of sessions in which each respective station was observing. Due to disruptions, such as an earthquake or antenna repairs, there is displacement of the antenna and a change in its a priori coordinates. In such cases the estimation of the antenna coordinates proceeds for the time before the event and after it. The

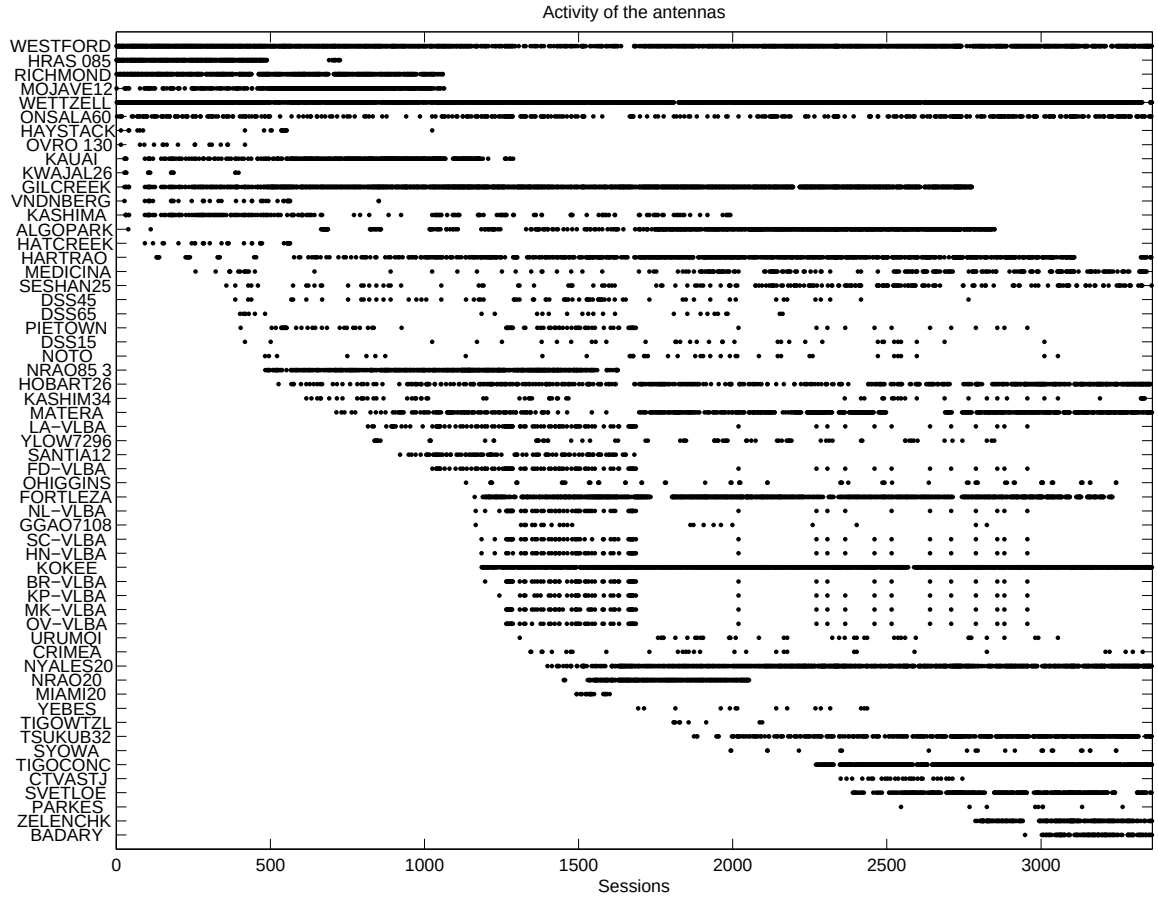

Figure 6.1.: Involvement of VLBI antennas in single sessions (1984.0 - 2011.0) included in the global adjustment.

Table 6.1.: Overview of a priori models and parameterisation options used to analyze VLBI data for estimation of the VieTRF10a and VieCRF10a.

	some a priori modelling options
TRF	VTRF2008 (Böckmann et al., 2010)
CRF	ICRF2 (Fey et al., 2009)
EOP	C04 08 + effect of ocean tides and libration on ERP according to IERS2010 (Petit and Luzum, 2010)
precession/nutation model	IAU 2006/2000A (Capitaine et al., 2003; Mathews et al., 2002)
solid Earth tides	IERS2010
pole tides	cubic model, IERS2010
ocean tidal loading	FES2004 (Lyard et al., 2004)
atmosphere loading	APL series and S1/S2 tides (Petrov and Boy, 2004)
a priori tropospheric gradients	DAO (MacMillan and Ma, 1997)
mapping functions	VMF1 (Böhm et al., 2006b)
	some parameterisation options
clock parameters	60 min piece-wise linear (pwl) offsets (relative constraints: 42 ps) + rate + quadratic term
zenith wet delays	30 min pwl offsets (relative constraints: 35 ps)
tropospheric gradients	6 h pwl offsets (relative constraints: 0.5 mm + absolute constraints: 1 mm)
EOP	24 h offsets for polar motion, UT1 and precession/nutation)

number of sessions in the respective intervals with the station involved is given in column six. Particular attention has to be paid to the strong heterogeneity in the quality and quantity of data gained at the stations. VLBI antennas such as the mobile ones, the ones used primarily by astronomers, or the very new ones, only take part very sporadically in the experiments which are included in this analysis. From the columns of Table 6.2 it is obvious that the observation time spans range from several months to 27 years. As the strategy is to prefer quality rather than quantity, the stations with a poor observation history were excluded from computation of the new TRF. The applied key for choosing stations for the new TRF was to take a minimum number of ten observations and to use the entire time span of the data greater than one year. These two conditions assure a stable estimation of station velocities. The exclusion of the stations from

the normal equation systems is done by a second reduction, which includes their coordinates. The affected VLBI antennas are: Aira (Japan), 10-m at Chichijima (Japan), CTVA 3.6-m at Shirley's Bay (Canada), DSS65A 34-m HEF at Madrid (Spain), mobile Fortords (California, USA), GORF7102 (Greenbelt, Maryland, USA), 12-m at Hobart (Tasmania), 11-m Keystone at Kashima (Japan), mobile Kodiak (Alaska, USA), 11-m Keystone at Koganei (Japan), Marcus (Japan), Maryland Point (Maryland, USA), 13.7-m astronomy antenna at Metsahovi (Finland), mobile Metsahovi (Finland), 11-m Keystone at Miura (Japan), NAO 10-m antenna at Mizusawa (Japan), mobile Monument Peak (California, USA), 6-m at Nobeyama (Japan), 140-ft NRAO Green Bank (West Virginia, USA), 85-1 NRAO Green Bank (West Virginia, USA), mobile Quincy (California, USA), mobile Platteville (Colorado, USA), mobile Point Reyes (California, USA), mobile San Francisco (California, USA), mobile Sand Point (Alaska, USA), SEST (Chile), mobile Sourdough (Alaska, USA), 11-m Keystone at Tateyama (Japan), 70-m DSS43 at Tidbinbilla (Australia), mobile Tromso (Norway), mobile Trysil (Norway), 20-m NAOJ VERA at Ishigakijima (Japan), VLA-N8 (Socorro, New Mexico, USA), mobile Whitehorse (Canada), mobile Yakataga (Alaska, USA), and 40-m at Yebes (Spain). The remark for these stations is in the seventh column of Table 6.2 as session-wise adjusted.

Table 6.2.: All VLBI antennas in the analysed sessions. .

VLBI antenna	**data span**			**no. of sessions**		**adjustment**	**datum of**
	start	**end**	**Δt [yr]**	**all**	**interv.**		**ref. frame**
WESTFORD	1984.0	2011.0	27.0	1615		global	yes
RICHMOND	1984.0	1992.6	8.6	611		global	yes
HRAS 085	1984.0	1990.8	6.8	393		global	no
MOJAVE12	1984.0	1992.7	8.7	423	415/8	global	no
WETTZELL	1984.0	2011.0	27.0	2348		global	yes
ONSALA60	1984.1	2011.0	26.9	434		global	yes
OVRO 130	1984.3	1988.9	4.6	16		global	no
HAYSTACK	1984.3	1992.5	8.2	23		global	no
GILCREEK	1984.5	2006.0	21.5	1556	1262/294	global	no
KAUAI	1984.5	1994.1	9.5	328		global	no
KWAJAL26	1984.5	1988.6	4.1	15		global	no
VNDNBERG	1984.5	1991.6	7.1	40		global	no
KASHIMA	1984.6	1999.8	15.3	173		global	yes
ALGOPARK	1984.7	2006.6	21.9	643		global	yes
HATCREEK	1985.4	1989.9	4.5	31		global	no
HARTRAO	1986.0	2011.0	24.9	664		global	yes

Continued on next page...

Table 6.2 – Continued

VLBI antenna	data span			no. of sessions		adjustment	datum of
	start	end	Δt [yr]	all	interv.		ref. frame
PLATTVIL	1986.2	1989.3	3.1	7		session-wise	no
MEDICINA	1987.3	2010.8	23.4	213	26/187	global	no
SESHAN25	1988.3	2011.0	22.7	186		global	yes
DSS45	1988.5	2005.9	17.4	71		global	yes
YAKATAGA	1988.6	1989.6	1.0	3		session-wise	no
SOURDOGH	1988.6	1989.6	1.0	6		session-wise	no
DSS65	1988.7	2001.5	12.8	27	17/10	global	no
PIETOWN	1988.7	2007.5	18.8	91		global	no
DSS15	1988.9	2007.9	19.1	35	2/33	global	no
MON PEAK	1989.1	1989.1	0.0	2		session-wise	no
QUINCY	1989.3	1989.3	0.0	1		session-wise	no
NOTO	1989.4	2007.9	18.5	39		global	no
NRAO85 3	1989.4	1996.6	7.2	431		global	yes
MARPOINT	1989.4	1989.6	0.2	5		session-wise	no
METSHOVI	1989.5	1989.5	0.0	2		session-wise	no
WHTHORSE	1989.6	1989.6	0.0	3		session-wise	no
HOBART26	1989.7	2010.9	21.2	500		global	yes
PRESIDIO	1989.8	1991.5	1.7	6		session-wise	no
FORTORDS	1989.8	1991.6	1.7	9		session-wise	no
PT REYES	1989.8	1991.5	1.7	6		session-wise	no
NOBEY 6M	1990.1	1991.5	1.5	4		session-wise	no
KASHIM34	1990.2	2010.7	20.5	64		global	yes
SEST	1990.3	1990.4	0.1	2		session-wise	no
MARCUS	1990.5	1990.5	0.0	1		session-wise	no
KODIAK	1990.5	1990.5	0.0	3		session-wise	no
SNDPOINT	1990.5	1990.5	0.0	3		session-wise	no
NRAO 140	1990.7	1994.8	4.1	3		session-wise	no
MATERA	1990.8	2011.0	20.2	580		global	yes
LA-VLBA	1991.4	2007.5	16.1	107		global	yes
YLOW7296	1991.5	2006.6	15.1	72		global	no
TRYSILNO	1991.9	1993.2	1.4	12		session-wise	no
SANTIA12	1991.9	1996.9	5.0	92		global	no
GORF7102	1991.9	1992.5	0.6	2		session-wise	no

Continued on next page...

Table 6.2 – Continued

VLBI antenna	data span			no. of sessions		adjustment	datum of
	start	end	Δt [yr]	all	interv.		ref. frame
FD-VLBA	1992.5	2007.5	15.0	92		global	yes
TROMSONO	1992.7	1992.7	0.0	1		session-wise	no
OHIGGINS	1993.1	2009.9	16.8	65		global	no
FORTLEZA	1993.3	2009.8	16.5	1001		global	yes
NL-VLBA	1993.3	2007.5	14.2	64		global	yes
GGAO7108	1993.3	2006.4	13.1	23	20/3	global	no
KOKEE	1993.5	2011.0	17.5	1444		global	yes
SC-VLBA	1993.5	2007.5	14.0	60		global	yes
HN-VLBA	1993.5	2007.5	14.0	58		global	no
MIZNAO10	1993.5	1994.2	0.6	5		session-wise	no
BR-VLBA	1993.6	2007.5	13.9	65		global	yes
KP-VLBA	1993.9	2007.5	13.6	48		global	no
OV-VLBA	1994.0	2007.5	13.4	59		global	no
MK-VLBA	1994.0	2007.5	13.4	60		global	yes
URUMQI	1994.2	2007.8	13.6	38		global	no
CRIMEA	1994.5	2010.7	16.2	30		global	no
NYALES20	1994.8	2011.0	16.2	873		global	yes
NRAO20	1995.1	2000.5	5.4	298		global	no
MIAMI20	1995.4	1996.4	1.0	18		global	no
YEBES	1997.0	2003.5	6.5	15		global	no
TIGOWTZL	1998.2	2001.0	2.8	9		global	no
TSUKUB32	1998.8	2011.0	12.2	371	3/368	global	no
SYOWA	1999.9	2009.9	10.0	24		global	no
TIGOCONC	2002.4	2011.0	8.6	761	693/68	global	no
CTVASBAY	2002.6	2002.7	0.1	2		session-wise	no
CTVASTJ	2002.9	2005.8	2.9	28		global	no
SVETLOE	2003.2	2011.0	7.8	305		global	no
PARKES	2004.4	2010.1	5.7	9		global	no
METSAHOV	2005.5	2010.4	4.9	4		session-wise	no
ZELENCHK	2006.1	2011.0	4.9	203	64/139	global	no
BADARY	2007.4	2011.0	3.6	115		global	no
YEBES40M	2010.3	2010.7	0.4	10		session-wise	no
HOBART12	2010.8	2010.9	0.1	5		session-wise	no

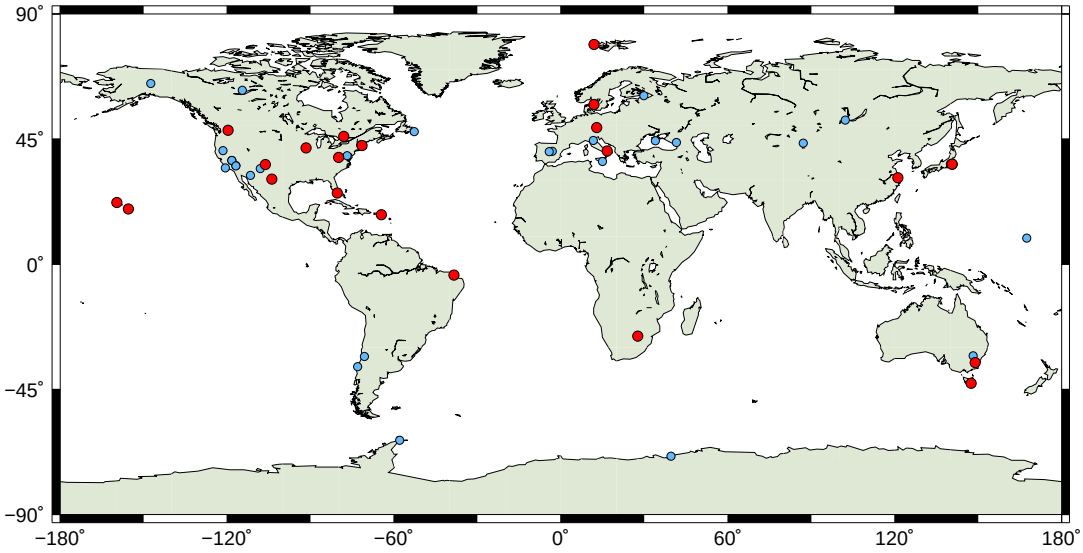

Figure 6.2.: 57 VLBI antennas included in the newly determined TRF VieTRF10a. In red the datum stations are plotted (larger circles), and in light blue the remaining stations are shown.

Figure 6.1 shows the activity of the final 57 stations included in the new TRF (VieTRF10a). Even between these stations large differences concerning their involvement in the observing sessions can be seen. Stations like Wettzell, Westford, 60-ft Onsala or Hartebeesthoek RAO have participated in the observation program right from the beginning and their regular participation in the VLBI sessions during the 27 years gives a homogeneous data coverage of the included time span. The newer stations which only started their observations a few years ago can be seen at the bottom of Figure 6.1. Obviously the number of sessions where they were included is low. Therefore their coordinates and velocities for the new TRF are estimated from significantly fewer measurements compared to the old stations.

For the datum definition 22 stations with a long observation history and a relatively consistent world coverage were chosen. They are marked in the last column of the Table 6.2 and plotted as larger red dots in Figure 6.2. These are Algonquin Park (Canada), Fortaleza (Brazil), Hartebeesthoek RAO (South Africa), 34-m HEF at Tidbinbilla (Australia), 26-m at Hobart (Tasmania), 34-m at Kashima (Japan), Matera (Italy), 85-3 NRAO Green Bank (West Virginia, USA), Ny Alesund (Norway), 26-m at Kashima (Japan), Kokee Park (Hawaii, USA), 60-ft Onsala (Sweden), Richmond (Florida, USA), Shanghai (China), VLBA at Los Alamos (New Mexico, USA), VLBA at Fort Davis (Texas, USA), VLBA at North Liberty (Iowa, USA), VLBA at Saint Croix (Virgin Islands, USA), VLBA at Brewster (Washington, USA), VLBA at

Mauna Kea (Hawaii, USA), Westford (Massachusetts, USA), and Wettzell (Germany).

In the least squares adjustment an additional constraint on the station velocities is applied. At stations where the discontinuity in the position is caused by an antenna repair, the estimated velocities before and after the position discontinuity are forced to be equal. The affected stations are the 32-m at Tsukuba (foundation repair, 1999/05/01), Medicina (repair of azimuth rail, 1996/07/01), GGAO7108 ORION MV3 at Greenbelt (not specified relocation in the vertical, 2003/01/01), DSS65 34-m HEF at Madrid (repair of azimuth rail, 1997/04/15), and Zelenchukskaya (rail replacement, 2007/07/01). Additionally, this condition was also applied at two stations (DSS15 34-m HEF at Goldstone, and 12-m Mojave at Goldstone) where the displacement occurred because of the Landers earthquake (1992/06/27). The reason being that there was only a small number of sessions containing these stations in the individual intervals, which doesn't make it possible to form an independent estimation of velocity for both intervals. Furthermore, a condition for equal velocity was applied to stations located in the same area. Stations, which are new or observe only sporadically for purposes of geodetic VLBI, but are built in the vicinity of an old stable station, profit from this requirement. In this adjustment

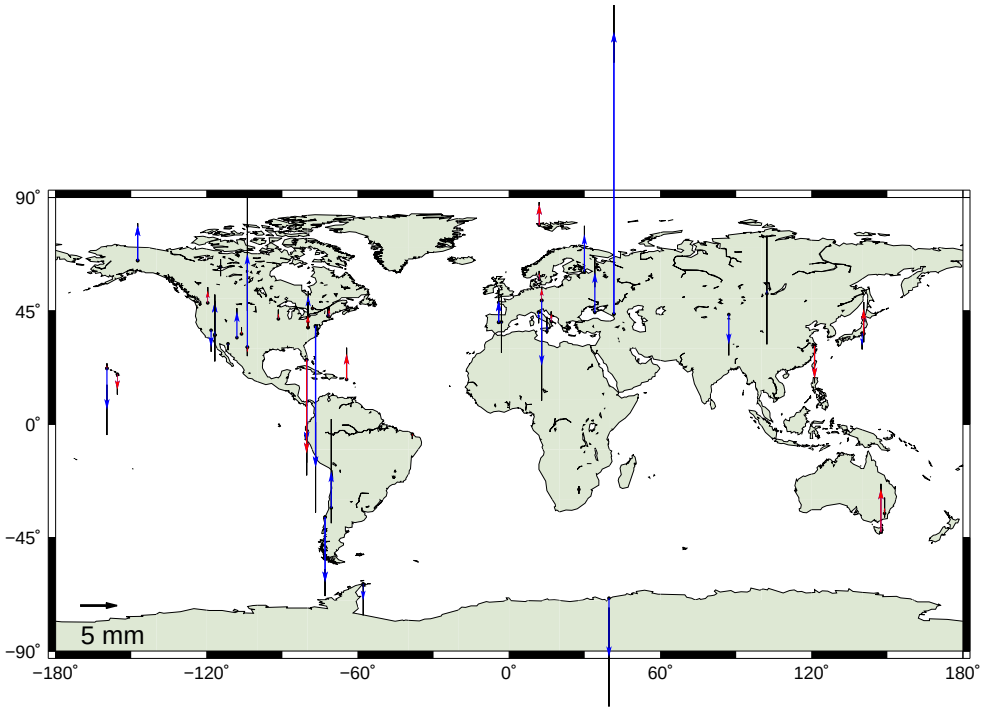

Figure 6.3.: Vertical position differences at epoch 2000.0 between VieTRF10a and VTRF2008. The only differences for stations with a mean coordinate error lower than 0.5 cm are plotted. Red arrows denote the datum stations and blue ones the remaining stations. The bars represent the formal errors.

the pairs of affected stations are 34-m and 26-m at Kashima, TIGO at Wettzell and Wettzell, Richmond and Miami at Florida.

6.2.1. Comparison of VieTRF10a with VTRF2008

The globally estimated differences between VieTRF10a and VTRF2008 are shown in Table A.1.1 (see Appendix A.1). These are the corrections of coordinates and velocities and their formal errors for the 57 stations (described in Table 6.2) to the a priori terrestrial reference frame VTRF2008. In Figures 6.3 and 6.4 the coordinate corrections w.r.t. VTRF2008 for vertical and horizontal components, respectively, are plotted. The velocities of the stations estimated in these two frames can be seen in Figure 6.5. I provide a comparison of VieTRF10a with VTRF2008 in terms of a 14-parameter Helmert transformation (Table 6.3), where the positions and velocities are weighted according to the formal errors derived in the new TRF solution. Three groups of stations were set up. The datum stations, stations with estimated mean coordinate error m_{xyz} lower than 5 mm, and all stations. A good agreement between the frames can be seen for all three sets of the stations realizing that most of the transformation parameters are below their standard deviations. The mean coordinate error m_{xyz} was computed according to

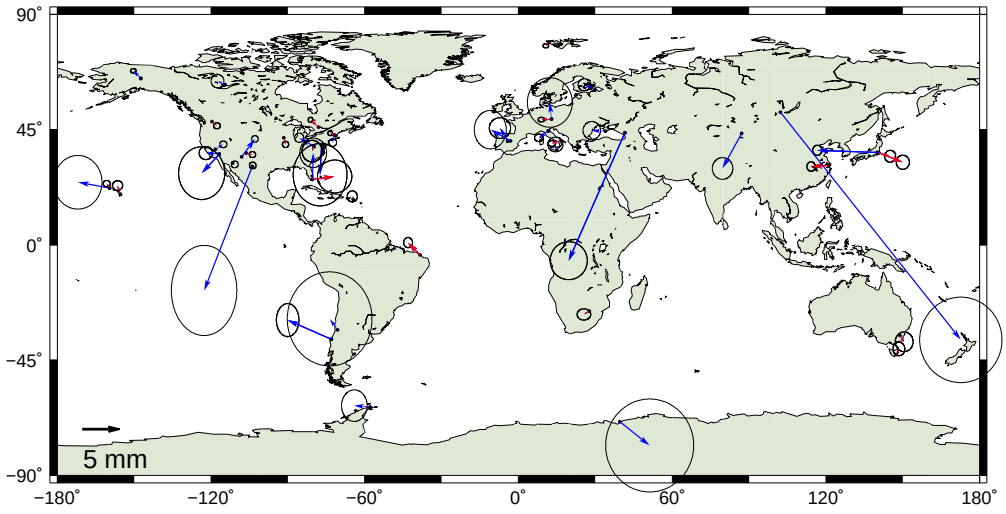

Figure 6.4.: Horizontal position differences at epoch 2000.0 between VieTRF10a and VTRF2008. Only differences for stations with the mean coordinate error lower than 0.5 cm are plotted. Red arrows denote the datum stations and blue ones the remaining stations. The ellipses display the 95% confidence ellipses.

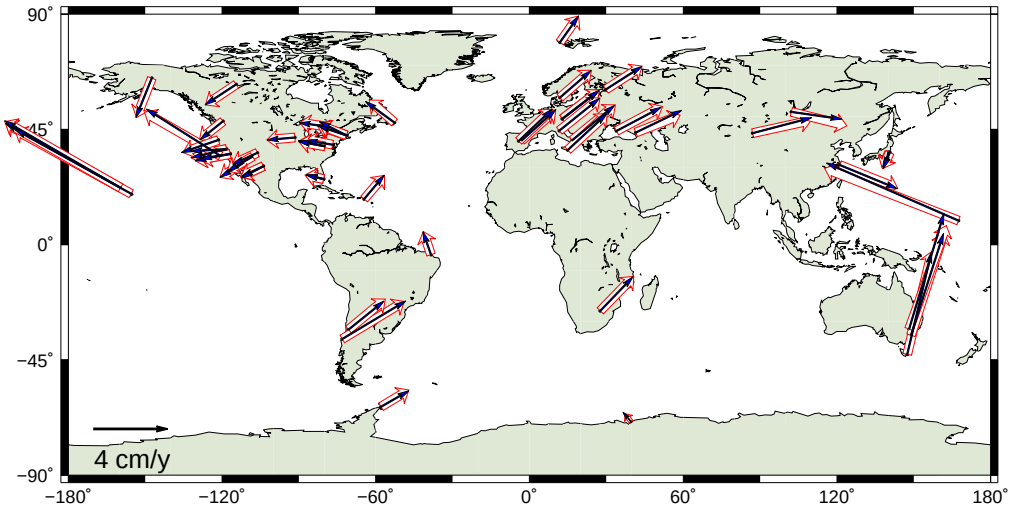

Figure 6.5.: Station horizontal velocities of VTRF2008 (white arrows in the background) and VieTRF10a (black arrows).

Table 6.3.: Helmert parameters (weighted) for the transformation between VTRF2008 and VieTRF10a (VieTRF10a minus VTRF2008) computed for three sets of stations.

Helmert parameters	**stations**		
	used for datum (22 stations)	**with m_{xyz} < 0.5 cm (50 stations)**	**all (57 stations)**
Tx [mm]	0.5 ± 0.4	0.4 ± 0.5	0.3 ± 0.4
Ty [mm]	−0.1 ± 0.4	−0.2 ± 0.5	−0.1 ± 0.5
Tz [mm]	0.7 ± 0.4	0.4 ± 0.5	0.2 ± 0.4
Rx [μas]	4.9 ± 17	18 ± 18	13 ± 18
Ry [μas]	26.1 ± 17	−5 ± 17	−8 ± 17
Rz [μas]	4.7 ± 14	32 ± 15	36 ± 14
$Scale$ [ppb]	0.05 ± 0.06	0.05 ± 0.07	0.09 ± 0.07
δTx [mm/yr]	−0.1 ± 0.1	0.0 ± 0.2	−0.0 ± 0.2
δTy [mm/yr]	−0.1 ± 0.2	−0.1 ± 0.2	−0.1 ± 0.2
δTz [mm/yr]	−0.1 ± 0.2	−0.1 ± 0.2	−0.1 ± 0.2
δRx [μas/yr]	3 ± 6	−0 ± 7	−0 ± 7
δRy [μas/yr]	−0 ± 6	0 ± 7	1 ± 7
δRz [μas/yr]	2 ± 5	1 ± 6	−0 ± 5
$\delta Scale$ [ppb/yr]	−0.01 ± 0.02	0.00 ± 0.03	0.00 ± 0.03

equation (6.1) and is given in the eighth column of Table A.1.1 in appendix A.1.

$$m_{xyz} = \sqrt{\frac{(m_x^2 + m_y^2 + m_z^2)}{3}}, \tag{6.1}$$

where m_x^2, m_y^2, and m_z^2 are variances of the respective coordinates.
The mean velocity error was computed in a similar way and can be found in column fifteen of the afore-mentioned table.

6.3. Celestial Reference Frame

The celestial reference frame VieCRF10a has been estimated in a common global adjustment together with the terrestrial reference frame VieTRF10a. It includes the coordinates of 822 sources. The purely astrometric VCS (Very Long Baseline Array Calibrator Survey, (Beasley et al., 2002)) sessions which would considerably increase the total number of observed sources

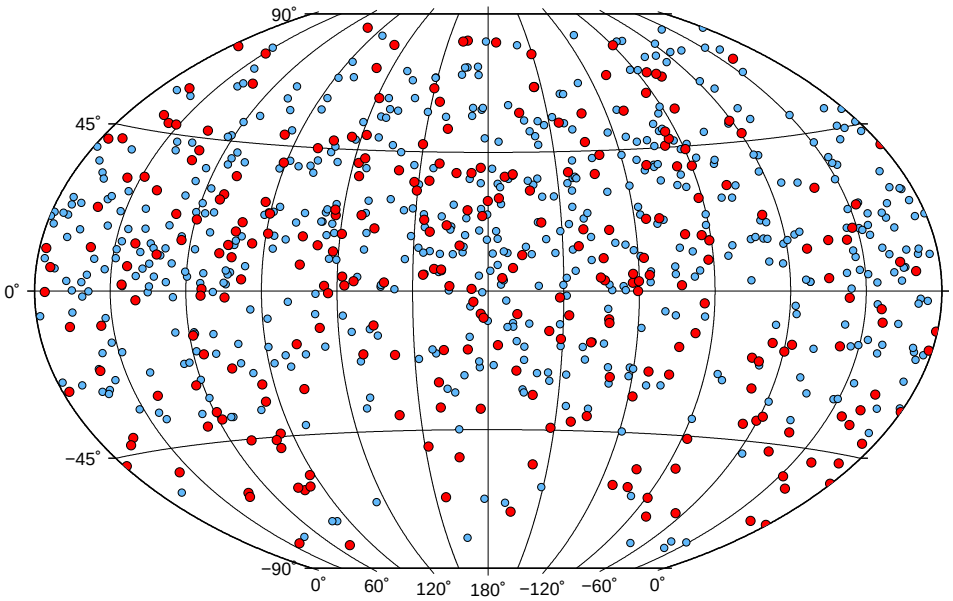

Figure 6.6.: Distribution of sources in the VieCRF10a catalogue. Red circles (larger) denote the datum sources. Remaining sources are plotted in light blue.

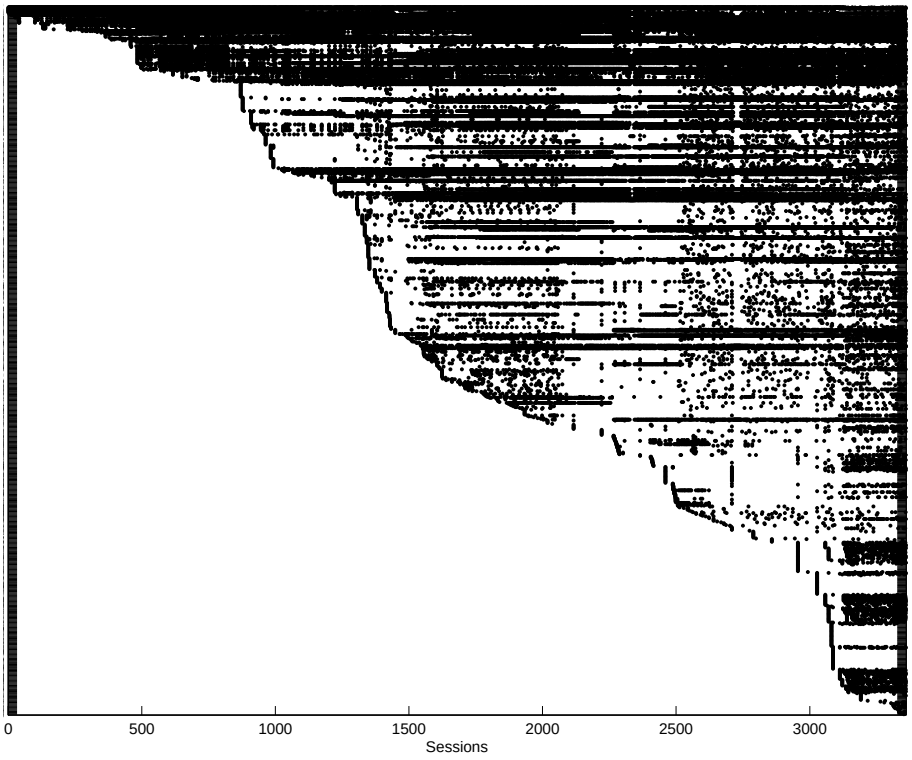

Figure 6.7.: Overview of observed sources in each session.

(for more than 2000 sources) were not included in the processing. In Figure 6.6 the distribution of all estimated sources is shown and sources used for datum definition are plotted as larger red dots. The datum definition was realized with a no-net-rotation condition on 276 so-called defining sources of the source catalogue ICRF2 (Fey et al., 2009) which were available in my data set. In Figures 6.7 and 6.8 (left plot) the number of observing sessions per source can be seen. More than one quarter (27%) of all sources was observed in only two sessions at most. In the analysis 43 sources were fixed to their a priori catalogue coordinates because the total

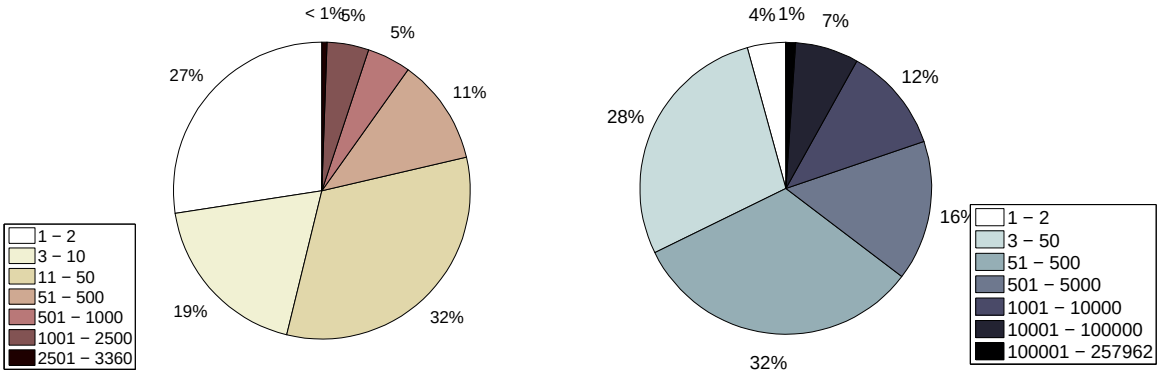

Figure 6.8.: Left-hand side: Distribution of the number of observing sessions per source. Right-hand side: Distribution of the number of observations per sources. Sources with less than three observations were fixed to their a priori coordinates in the analysis.

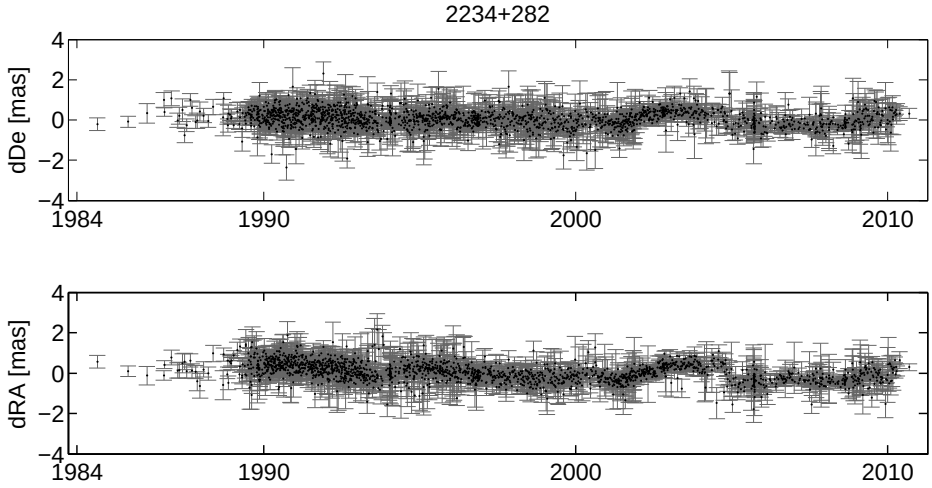

Figure 6.9.: Session-wise estimated position of a special handling source 2234+282.

number of group delay observations for each of these sources during the whole time span was less than three which is insufficient to derive a reliable position. This number corresponds to 4% of all available sources. In Figure 6.8 sources are divided according to the number of observations (right plot) and to the number of sessions in which they were observed (left plot). The highest number of observations per source was nearly 258 000. In the group that includes sources with higher than 100 000 observations is placed 1% of all available sources.

The observed radio sources are, in general, for the purposes of geodetic VLBI considered to be distant compact objects without any changes in their structure or position. However, 39 radio sources have already been detected as sources with systematic position variations (Fey et al., 2009). These are so-called special handling sources and during the determination of a celestial reference frame they have to be excluded from the globally estimated parameters. During the VieCRF10a computation their positions were estimated session-wise to avoid a distortion of the globally estimated frame using the session-wise reduction of their positions from the normal equation system and receiving their position time series with the backward solution. As an example the estimated time series of the source 2234+282 is plotted in Figure 6.9.

The formal errors of the estimated source positions in the catalogue VieCRF10a are discussed in Figures 6.10 - 6.12. Figure 6.10 shows the formal errors of declination (upper plot) and right ascension (lower plot) of sources used for datum definition. The decreasing accuracy of coordinate estimates towards the South Pole is clearly visible which is caused by the sparse network of stations in this region which would be capable of observing sources at these declinations. Coordinates of most of the datum sources (232 for declination and 218 for right ascension) were estimated within a formal error lower than 0.1 mas as can be seen in histograms of the

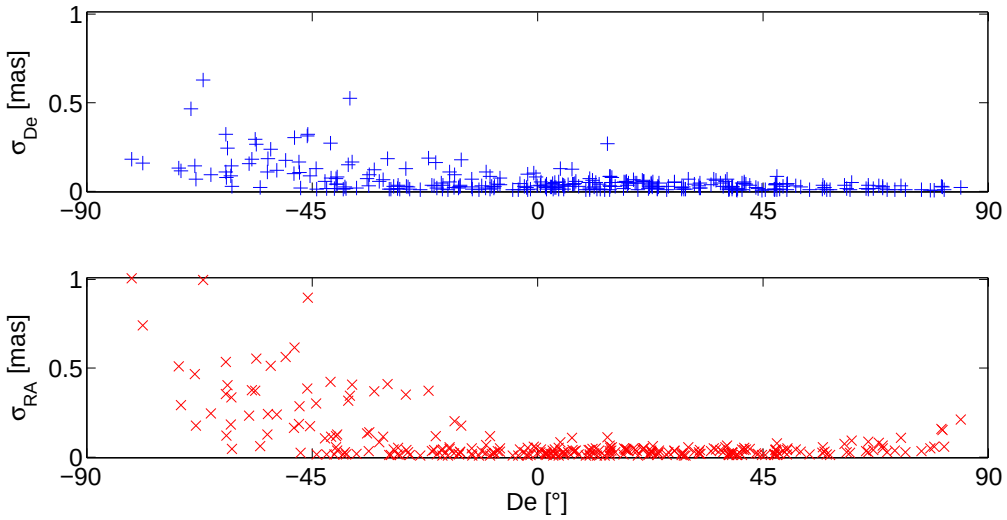

Figure 6.10.: Distribution of formal errors of datum sources in declination (upper plot) and right ascension (lower plot).

formal errors of declination and right ascension estimates of the datum sources in Figure 6.11. According to the six groups of sources in the right plot in Figure 6.8, the formal errors for all six groups were visualized separately (see Figure 6.12) where the groups differ in the number of measurements carried out on the sources. It is obvious that in the first group where the number of time delay measurements per source lies in an interval from three to fifty, it comes to outliers reaching up to 30 mas in the formal errors of the position estimates. It can be clearly seen that with the increasing number of measurements to the sources the formal errors of their estimated coordinates are decreasing considerably. In the sixth group which includes the most observed sources, i.e. where the number of observations is larger than 100 000, the formal errors of declination do not exceed 0.02 mas. For all groups of sources the increasing formal errors of

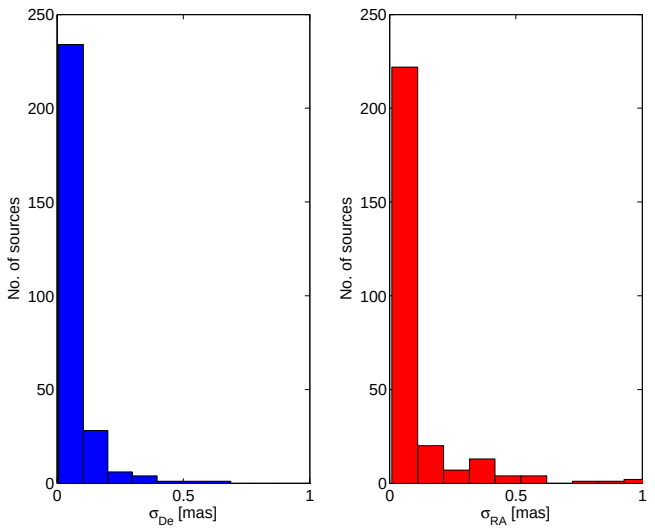

Figure 6.11: Histogram of distribution of formal errors of datum sources in declination (left plot) and right ascension (right plot). The formal errors of most of the sources (more than 200) do not exceed 0.1 mas.

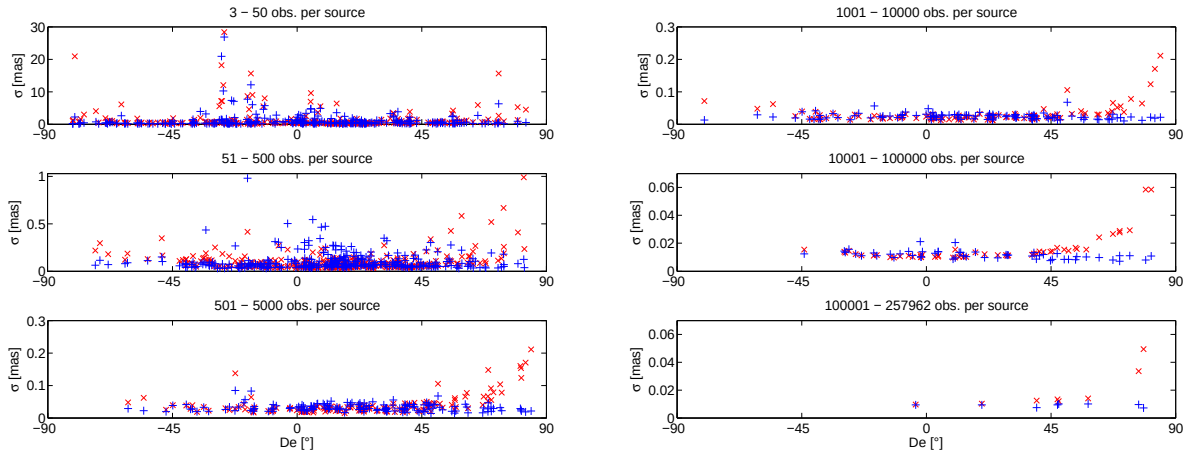

Figure 6.12.: Formal errors of declination (blue "+") and right ascension (light red "x"). Sources are divided into six groups according to the right plot in Figure 6.8. Note the different scales on the y-axis of each plot.

right ascension in higher latitudes can be seen. This is caused by the convergence of meridians which makes the resolution in the right ascension near the poles inaccurate.

6.3.1. Comparison of VieCRF10a with ICRF2 and other CRF catalogues

The newly estimated positions of the radio sources in VieCRF10a are compared to the catalogue ICRF2 which was taken as a priori information about the source positions in the analysis. The comparison is done by three rotation parameters (A_1, A_2, A_3) weighted according to the formal errors of coordinates. The rotation parameters are computed for three sets of sources: 1) sources

Table 6.4.: Rotation parameters (weighted) for the transformation between ICRF2 and VieCRF10a (VieCRF10a minus ICRF2) for three sets of sources.

Rotation parameters	sources used for datum (276 sources)	sources with $m_{RADe} < 100$ μas (443 sources)	sources all (822 sources)
A_1 [μas]	-1 ± 4	6 ± 4	4 ± 12
A_2 [μas]	4 ± 4	11 ± 5	31 ± 12
A_3 [μas]	-18 ± 5	-21 ± 5	-20 ± 12

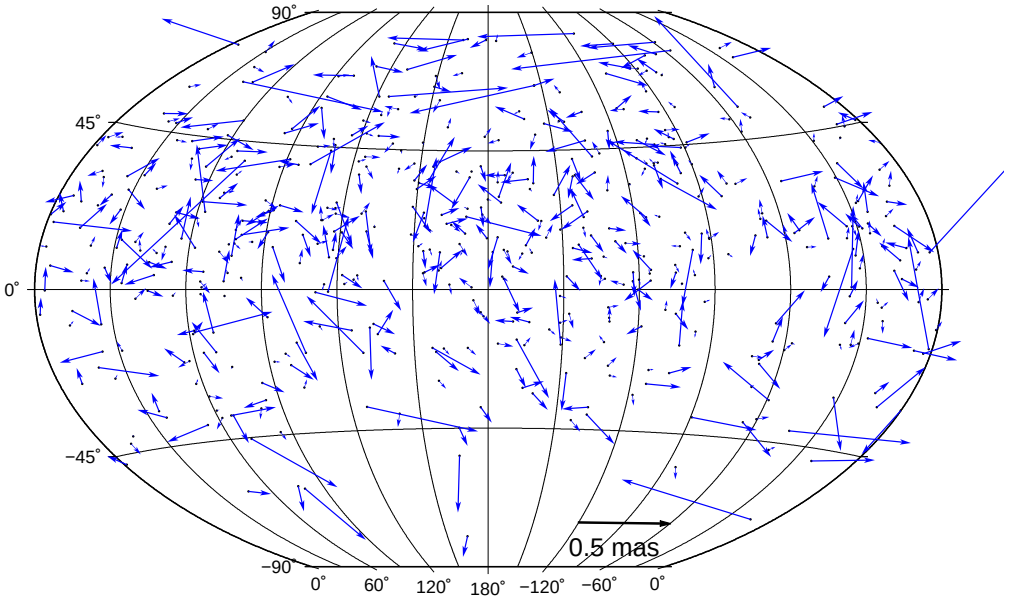

Figure 6.13.: Estimates of source positions in VieCRF10a w.r.t. ICRF2. Only corrections for sources with a formal error lower than 200 μas in both coordinates are plotted.

used for datum definition, 2) sources with mean coordinate errors lower than 0.1 mas, and 3) all sources. The results of least squares estimation of the three rotation angles are presented in Table 6.4. A good alignment is found for all three sets of sources. The estimated rotation parameters exceed only a few microarcseconds with the formal errors of the first two data sets about 5 μas. The slightly higher values of the formal errors (12 μas) computed for the last group are probably caused by fewer observations to several sources and by the sources' instability as noted above. In Figure 6.13 the differences in source positions between VieCRF10a and ICRF2 are shown, where only sources with formal errors in both coordinate estimates which do not exceed 200 μas are plotted.

For an external validation of VieCRF10a a comparison with several other CRF solutions was done. These catalogues were submitted as contributions for investigations during the work on the ICRF2 catalogue. The contributing IVS analysis centres were: Geoscience Australia (GA), Bundesamt für Kartographie und Geodäsie (BKG), NASA Goddard Space Flight Center (GSFC), Institute of Applied Astronomy of the Russian Academy of Sciences in St. Petersburg (IAA), Main Astronomical Observatory of the National Academy of Sciences of Ukraine (MAO), Paris Observatory (OPAR), and U.S. Naval Observatory (USNO). The description of the catalogues such as the number of included sessions and sources, time spans of data, analysis software and

Table 6.5.: Description of contributed catalogues for investigations on ICRF2 and of VieCRF10a catalogue. Adapted from Fey et al. (2009).

catalogue	No. of sessions	No. of sources	time range	analysis software	analysis centre
aus009a	3774	537	1979.7 - 2008.7	OCCAM 6.2	GA
bkg001a	3823	3039	1984.0 - 2009.2	CALC 10, SOLVE 07.10.31	BKG
gsf007b	4540	3414	1979.7 - 2009.2	CALC 10, SOLVE 08.12.05	GSFC
iaa008c	...	3009	1980.0 - 2009.2	QUASAR	IAA
mao008a	4541	3555	1979.7 - 2009.3	SteelBreeze	MAO
opa008b	4528	3244	1979.7 - 2009.2	CALC 10, SOLVE 08.12.05	OPAR
usn010b	4465	3414	1979.7 - 2009.2	CALC 10, SOLVE 07.11.08	USNO
VieCRF10a	3360	822	1984.0 - 2011.0	VieVS	IGG

abbreviations of the analysis centres are given in Table 6.5. In the last line of Table 6.5 the description of VieCRF10a is given. As noted above, VieCRF10a does not include sources from VCS sessions which were carried out to densify the source's network. This explains the lower number of sources contained in VieCRF10a catalogue. In aus009a solution only radio sources with the number of observations higher than 100 were included in the catalogue. It was later decided that the ICRF2 catalogue will be based only on a single solution provided by the GSFC to keep certain information, such as the full covariance matrix, and the links to EOP and the TRF solutions (Fey et al., 2009).

For a comparison of, and evaluation of systematic effects between VieCRF10a and the other catalogues a transformation model is applied. The model assumes three rotations (A_1, A_2, A_3) of one catalogue relative to another and a bias in declination (d_z). The differences in declination $(\Delta\delta)$ and right ascension $(\Delta\alpha)$ can be written as:

$$\Delta\delta = -A_1 \sin\alpha + A_2 \cos\alpha + d_z, \tag{6.2}$$

$$\Delta\alpha = A_1 \tan\delta \cos\alpha + A_2 \tan\delta \sin\alpha - A_3. \tag{6.3}$$

To calculate the parameters of the model, coordinates of ICRF1 (Ma and Feissel, 1997) defining sources were used (without sources which were in Fey et al. (2009) designed as the special

Table 6.6.: 3 rotation parameters and one bias in declination for the transformation between VieCRF10a and other CRF catalogues, submitted by analysis centres during investigations on ICRF2 catalogue.

catalogues	A_1 [μas]	A_2 [μas]	A_3 [μas]	d_z [μas]
VieCRF10a - aus009a	49.6 ± 10.2	11.8 ± 9.3	-22.5 ± 14.8	22.5 ± 14.8
VieCRF10a - bkg001a	-36.4 ± 25.4	-12.1 ± 23.4	16.2 ± 39.5	-13.2 ± 39.1
VieCRF10a - gsf007b	21.9 ± 21.9	-3.7 ± 20.1	3.7 ± 34.0	-3.7 ± 33.6
VieCRF10a - iaa008c	35.5 ± 21.3	-6.6 ± 19.6	18.5 ± 33.2	9.8 ± 32.8
VieCRF10a - mao008a	56.0 ± 21.1	-15.1 ± 19.4	1.9 ± 32.8	31.5 ± 32.4
VieCRF10a - opa008b	17.4 ± 22.9	0.9 ± 21.1	0.4 ± 35.6	-16.7 ± 35.2
VieCRF10a - usn010b	23.4 ± 23.0	19.5 ± 21.1	8.3 ± 35.7	-13.6 ± 35.3

handling ones). In the least squares adjustment obtained rotation angles and the declination bias (see Table 6.6) show that all catalogues lay very close to each other. Most of the parameters stay within their formal errors. The formal errors of rotation angles around the x and y axis are at the level of 20 μas. Rotation around the z axis and the declination bias is estimated with a formal error of around 35 μas between VieCRF10a and nearly all catalogues. The only exception is the comparison with solution aus009a whose formal errors are about one half lower than by the remaining catalogues. The reason for this being the choice of only well observed sources. Considering the fact that the CRF solutions were estimated with five independent analysis software packages using non-identical a priori models and different data sets, the agreement between them and the VieCRF10a catalogue is very good. This proves the comparable quality of VieCRF10a to the other present CRF solutions.

6.4. Annual and semi-annual harmonic signal in TRF

In this work the VLBI measurements are used to estimate certain geophysical parameters (Love and Shida numbers, see especially section 7.2) which are connected to station displacement. To get an impression of how good the estimates of such parameters can be, it is important to know the remaining unmodelled signal which is absorbed by the estimates of station coordinates during the global adjustment. As reported e.g. by Collilieux et al. (2007) and Tesmer et al. (2009) there are still deficiencies in the modelling of station movements over long periods. Therefore I implemented the option to determine amplitudes of harmonic station movements at the annual and semi-annual period in the global solution, as it is already a standard case for some other VLBI analysis software packages, e.g. CALC/SOLVE.
The sine (As) and cosine (Ac) amplitudes are derived from the topocentric station displacement Δd_{REN} with zero a priori values:

$$\Delta d_{REN} = Ac_{REN} \cdot \cos\left(\frac{mjd - mjd_0}{2\pi \cdot P}\right) + As_{REN} \cdot \sin\left(\frac{mjd - mjd_0}{2\pi \cdot P}\right), \tag{6.4}$$

where P is the period of station movement in solar days (i.e., 365.25 and 182.625 solar days for annual and semi-annual term, respectively), reference time epoch mjd_0 is set to 2000.0, and mjd stands for the time of the observation. The components of the amplitude A_{REN} in the local system are obtained as:

$$A_{REN} = \sqrt{Ac_{REN}^2 + As_{REN}^2}, \tag{6.5}$$

with the corresponding phase again for all three components:

$$\phi_{REN} = \arctan\left(\frac{As_{REN}}{Ac_{REN}}\right). \tag{6.6}$$

In the following two solutions sine and cosine amplitudes of the harmonic station displacement are estimated as additional parameters to the default solution where station coordinates and velocities were computed. The estimation is done for all stations which were included in more than 50 sessions with the exception of station O'Higgins. This station is situated in Antarctica and due to the climatic conditions it is only possible to gain measurements at the site during Antarctic summer months. This temporal distribution of data does not allow investigation of a yearly signal contained in the data. In the first solution S1 the sine and cosine amplitudes for annual and semi-annual period are determined. In the second solution S2 only the changes at the annual period are investigated in the global adjustment. The determined amplitudes and

phases of the harmonic signals in the vertical direction are summarized in Table 6.7. In the first four columns the vertical amplitude and phase from solution S1 is given, in the last two columns results from solution S2 are shown. The formal errors reflect the amount and temporal distribution of the measurements over the years at particular sites.

Table 6.7.: Amplitudes and phases of radial displacement at annual and semi-annual periods estimated for stations observing in more than 50 sessions.

	solution S1				solution S2	
	A_R [cm]	ϕ_R [deg]	A_R [cm]	ϕ_R [deg]	A_R [cm]	ϕ_R [deg]
station	annual signal		semi-annual signal		annual signal	
ALGOPARK	0.35 ± 0.05	-73.0 ± 8.2	0.11 ± 0.05	122.7 ± 24.9	0.35 ± 0.05	-68.4 ± 8.0
BADARY	0.34 ± 0.10	-113.6 ± 18.3	0.19 ± 0.10	70.8 ± 31.1	0.42 ± 0.10	-129.3 ± 14.2
BR-VLBA	0.81 ± 0.08	-86.3 ± 4.3	0.22 ± 0.06	97.7 ± 21.2	0.68 ± 0.07	-89.3 ± 4.9
DSS45	0.93 ± 0.13	91.5 ± 9.8	0.31 ± 0.16	-113.9 ± 25.7	0.94 ± 0.13	94.2 ± 9.3
FD-VLBA	0.24 ± 0.06	37.7 ± 14.2	0.23 ± 0.05	-64.4 ± 15.6	0.28 ± 0.05	29.0 ± 11.7
FORTLEZA	0.35 ± 0.06	-62.0 ± 10.9	0.15 ± 0.06	17.5 ± 21.0	0.40 ± 0.06	-45.6 ± 8.5
GILCREEK	0.26 ± 0.03	-92.4 ± 8.9	0.27 ± 0.04	131.7 ± 7.6	0.27 ± 0.03	-103.9 ± 8.0
HARTRAO	0.19 ± 0.08	-167.0 ± 21.6	0.23 ± 0.07	19.1 ± 17.0	0.19 ± 0.08	169.4 ± 20.4
HN-VLBA	0.29 ± 0.10	-133.1 ± 19.3	0.31 ± 0.10	28.8 ± 16.9	0.28 ± 0.08	-157.6 ± 18.7
HOBART26	0.43 ± 0.07	51.6 ± 9.8	0.14 ± 0.07	-54.9 ± 29.4	0.39 ± 0.07	52.5 ± 10.5
HRAS 085	0.51 ± 0.16	128.5 ± 18.8	0.19 ± 0.16	-65.4 ± 49.7	0.42 ± 0.16	133.8 ± 21.9
KASHIM34	0.29 ± 0.14	-46.9 ± 27.1	0.81 ± 0.14	115.6 ± 10.2	0.36 ± 0.12	-99.5 ± 21.9
KASHIMA	0.45 ± 0.13	-137.7 ± 16.0	1.02 ± 0.12	136.0 ± 7.0	0.53 ± 0.12	-152.0 ± 13.1
KAUAI	0.58 ± 0.11	141.6 ± 11.2	0.08 ± 0.11	62.0 ± 79.5	0.61 ± 0.11	149.4 ± 10.5
KOKEE	0.06 ± 0.04	95.1 ± 50.1	0.14 ± 0.05	175.0 ± 16.9	0.04 ± 0.05	-172.2 ± 52.8
LA-VLBA	0.40 ± 0.05	0.4 ± 8.3	0.26 ± 0.05	77.6 ± 12.6	0.36 ± 0.05	13.2 ± 8.2
MATERA	0.60 ± 0.05	-140.9 ± 4.7	0.23 ± 0.05	121.2 ± 11.9	0.56 ± 0.05	-148.6 ± 4.6
MEDICINA	0.45 ± 0.06	-126.8 ± 7.6	0.08 ± 0.06	72.5 ± 43.0	0.39 ± 0.05	-132.5 ± 8.0
MK-VLBA	0.43 ± 0.10	13.8 ± 16.3	0.11 ± 0.12	27.7 ± 55.1	0.40 ± 0.10	23.9 ± 14.8
MOJAVE12	0.13 ± 0.08	-161.7 ± 34.7	0.13 ± 0.08	-58.7 ± 34.6	0.16 ± 0.08	-143.0 ± 27.0
NL-VLBA	0.18 ± 0.07	22.4 ± 29.9	0.38 ± 0.09	-178.6 ± 10.7	0.25 ± 0.07	-19.2 ± 16.9
NRAO20	0.40 ± 0.05	-148.5 ± 7.6	0.15 ± 0.05	-172.7 ± 18.8	0.37 ± 0.05	-141.6 ± 7.8
NRAO85 3	0.38 ± 0.07	-122.7 ± 11.3	0.19 ± 0.07	-164.3 ± 21.2	0.38 ± 0.07	-113.5 ± 11.2
NYALES20	0.31 ± 0.03	-86.0 ± 7.4	0.43 ± 0.03	143.6 ± 4.5	0.30 ± 0.03	-97.7 ± 7.4
ONSALA60	0.57 ± 0.05	-173.6 ± 4.1	0.19 ± 0.04	101.6 ± 13.3	0.59 ± 0.05	177.5 ± 3.7
OV-VLBA	0.45 ± 0.06	-8.1 ± 11.6	0.27 ± 0.07	127.3 ± 17.0	0.44 ± 0.06	-1.4 ± 9.6

Continued on next page...

Table 6.7 – Continued

	solution S1				solution S2	
	A_R [cm]	ϕ_R [deg]	A_R [cm]	ϕ_R [deg]	A_R [cm]	ϕ_R [deg]
station	annual signal		semi-annual signal		annual signal	
PIETOWN	0.50 ± 0.06	-64.0 ± 6.4	0.33 ± 0.06	-139.8 ± 10.0	0.71 ± 0.06	-63.5 ± 4.3
RICHMOND	0.23 ± 0.09	90.3 ± 22.6	0.36 ± 0.09	-126.4 ± 14.7	0.18 ± 0.09	75.7 ± 29.0
SANTIA12	0.33 ± 0.31	51.5 ± 53.9	0.51 ± 0.31	-26.6 ± 33.2	0.34 ± 0.28	53.0 ± 47.6
SC-VLBA	0.46 ± 0.11	-172.5 ± 20.3	0.30 ± 0.12	116.9 ± 30.5	0.34 ± 0.11	170.6 ± 21.1
SESHAN25	1.03 ± 0.08	7.8 ± 4.0	0.50 ± 0.08	119.9 ± 8.5	0.89 ± 0.08	10.1 ± 4.3
SVETLOE	0.52 ± 0.05	-81.6 ± 7.0	0.30 ± 0.06	157.2 ± 10.1	0.46 ± 0.05	-84.8 ± 7.8
TIGOCONC	0.34 ± 0.08	71.4 ± 14.9	0.37 ± 0.08	-43.7 ± 12.7	0.38 ± 0.08	51.6 ± 12.6
TSUKUB32	0.66 ± 0.05	42.4 ± 4.6	0.21 ± 0.05	161.5 ± 12.1	0.58 ± 0.05	51.3 ± 5.0
WESTFORD	0.26 ± 0.03	-83.6 ± 8.2	0.20 ± 0.04	179.3 ± 9.4	0.28 ± 0.03	-74.1 ± 7.4
WETTZELL	0.52 ± 0.04	-133.9 ± 4.4	0.16 ± 0.04	135.5 ± 13.4	0.48 ± 0.04	-141.7 ± 4.3
ZELENCHK	0.67 ± 0.08	-120.9 ± 7.1	0.15 ± 0.08	74.4 ± 31.5	0.65 ± 0.08	-126.6 ± 7.1

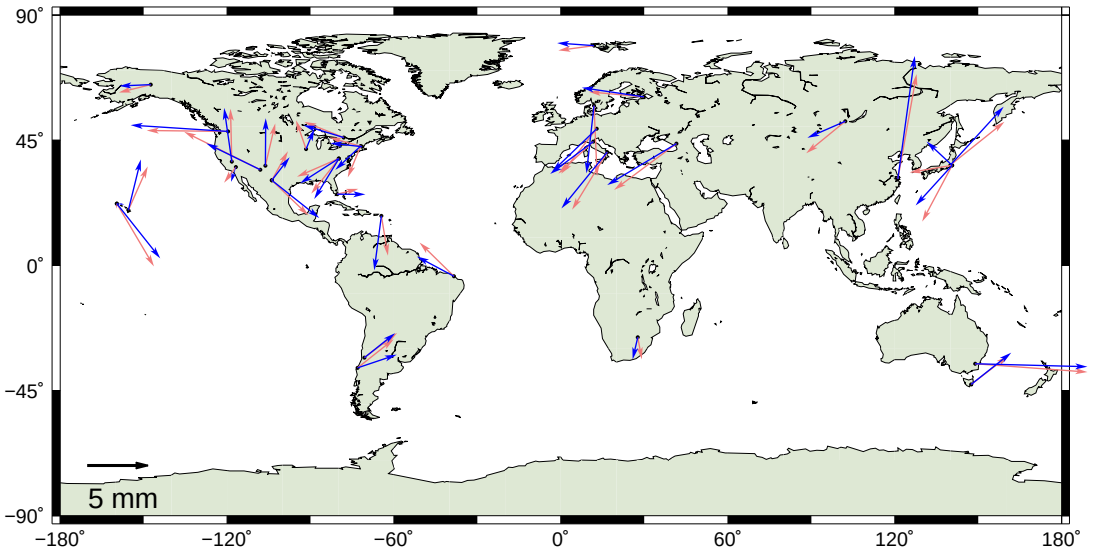

Figure 6.14.: Vertical amplitude of harmonic annual signal at stations which observed in more than 50 sessions. In blue the signal from solution S1 and in light red from solution S2 is plotted. If the arrow points towards north, the maximum annual displacement appears in January and it continues clockwise further.

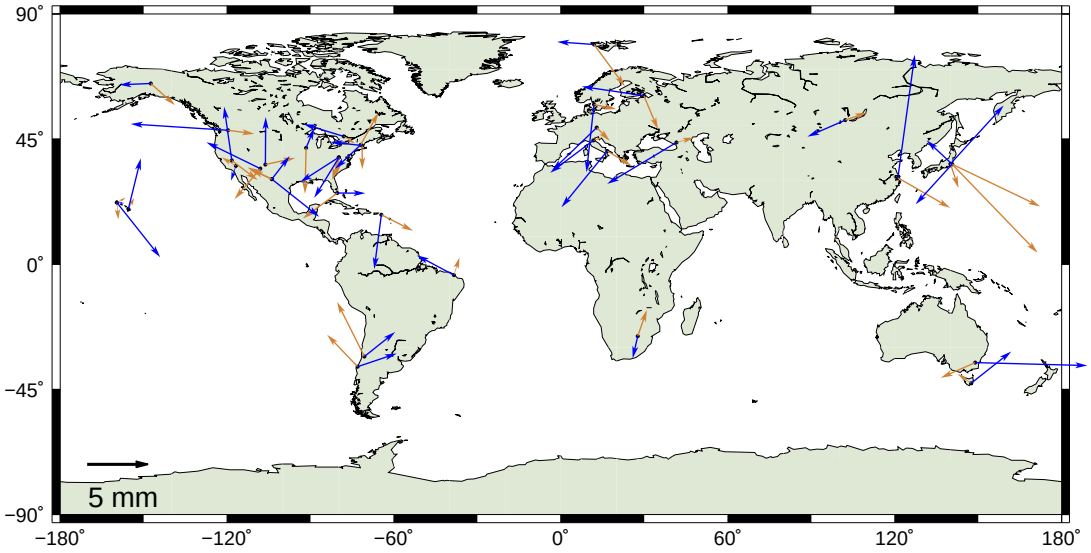

Figure 6.15.: Vertical amplitude of harmonic signals from solution S1 at stations which observed in more than 50 sessions. The annual signal is shown in blue and the semi-annual signal in light orange.

The vertical amplitudes of the annual signal, shown in the form of arrows, are plotted in Figure 6.14 in blue colour for solution S1 and in light red colour for solution S2. The phase indicates the maximum annual displacement within a year. If the arrow points towards north, the maximum appears in January, and it continues clockwise further. E.g. for stations in Europe it is seen that the annual signal of the displacement shows its maximum reading (crust goes up) in the summer months (July, August) which can be explained by the minimal water content in the ground and no snow load. (Related investigation on hydrology loading model is done in chapter 4.6.) The phase difference between the annual signals determined in solutions S1 and S2 is in the range of their formal errors. At most of the stations the amplitude of the height displacement is below 1 cm. The deformation in the horizontal plane exceeds a few millimetres (not shown here). Estimates from my solutions confirm the findings done by Tesmer et al. (2009) who got very similar results for the annual harmonic amplitudes using the VLBI data from 1994 to 2007 and analyzing them with software OCCAM 6.1 (Titov et al., 2004).

The semi-annual (light orange) and annual (blue) signals in vertical direction estimated simultaneously in solution S1 are plotted in Figure 6.15. At most of the stations a phase difference between these two signals is about 90 degrees. This means that the estimated semi-annual signal has its minimum during the time when the maximum displacement caused by the annual term

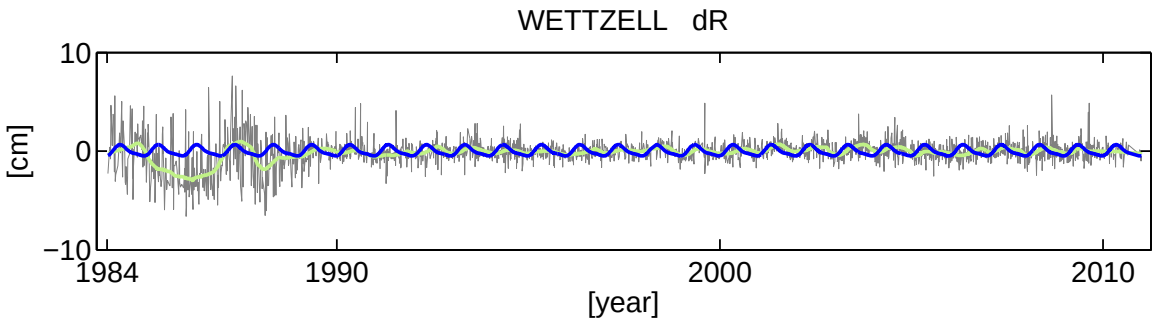

Figure 6.16.: Time series of the estimated height corrections at station Wettzell, smoothed over 50 days (light green line). In blue the sum of two harmonic functions with the estimated amplitudes at semi-annual and annual period is plotted.

appears.

In Figure 6.16 time series of the height component for the station Wettzell is shown together with the sum of the semi-annual and annual remaining seasonal signal (in blue colour). In light green the smoothed estimates over 50 days are shown. In general there is a good agreement between the smoothed line of the session-wise estimated height corrections and the sum of the two harmonic functions, especially in terms of the amplitude size. But it is obvious that the modelling of the remaining signal as an approximation with harmonic functions at semi-annual and annual period does not exactly reflect the reality.

7. Love and Shida numbers

IERS Conventions 2010 (Petit and Luzum, 2010) recommend the representation of Love and Shida numbers employed by Mathews et al. (1995). Love and Shida numbers are introduced there as multiple h and l parameters, where the parameters $h^{(0)}$ and $l^{(0)}$ mentioned in the text below have the role of h_{2m} and l_{2m}.

The displacement Δd_f due to a tidal term of frequency f given in Petit and Luzum (2010) follows Mathews et al. (1995).

Displacement caused by semi-diurnal tides reads:

$$\begin{aligned}\Delta d_f = \sqrt{\frac{5}{96\pi}} H_f \Bigg\{ & h_f(\Phi) 3 \cos^2\Phi \cos(\theta_f + 2\Lambda)\ \hat{r} \\ & - 6\cos\Phi \Big[l_f(\Phi) + l^{(1)} \sin^2\Phi \Big] \sin(\theta_f + 2\Lambda)\ \hat{e} \\ & - 6 \sin\Phi \cos\Phi \Big[l_f(\Phi) + l^{(1)} \Big] \cos(\theta_f + 2\Lambda)\ \hat{n} \Bigg\},\end{aligned} \tag{7.1}$$

by diurnal tides:

$$\begin{aligned}\Delta d_f = -\sqrt{\frac{5}{24\pi}} H_f \Bigg\{ & h_f(\Phi) 3 \sin\Phi \cos\Phi \sin(\theta_f + \Lambda)\ \hat{r} \\ & + \left[\left(3 l_f(\Phi) - \sqrt{\frac{24\pi}{5}} l' \right) \sin\Phi - 3 l^{(1)} \sin\Phi \cos 2\Phi \right] \cos(\theta_f + \Lambda)\ \hat{e} \\ & + \left[3 l_f(\Phi) \cos 2\Phi - 3 l^{(1)} \sin^2\Phi + \sqrt{\frac{24\pi}{5}} l' \right] \sin(\theta_f + \Lambda)\ \hat{n} \Bigg\},\end{aligned} \tag{7.2}$$

and by long-period tides:

$$\begin{aligned}\Delta d_f = \sqrt{\frac{5}{4\pi}} H_f \Bigg\{ & \left[h_f(\Phi) \Big(\frac{3}{2} \sin^2\Phi - \frac{1}{2} \Big) + \sqrt{\frac{4\pi}{5}} h' \right] \cos\theta_f\ \hat{r} \\ & + \cos\Phi \left[3 l^{(1)} \sin^2\Phi - \sqrt{\frac{4\pi}{5}} l' \right] \sin\theta_f\ \hat{e} \\ & + 3 l(\Phi) \sin\Phi \cos\Phi \cos\theta_f\ \hat{n} \Bigg\}.\end{aligned} \tag{7.3}$$

Where

H_f	is Cartwright-Tayler amplitude (Cartwright and Tayler, 1971) of the tidal term with frequency f,
Φ, Λ	are geocentric latitude and longitude of station,
θ_f	is tide argument for tidal constituent with frequency f,
$\hat{r}, \hat{e}, \hat{n}$	are unit vectors in radial, east and north direction respectively.

The latitude dependence of the Love number is considered mainly through the $h_f(\Phi)$ which is expressed as a sum of $h_f^{(0)}$ and a Legendre polynomial of second degree for $\sin\Phi$ multiplied with the parameter $h^{(2)}$. The latitude dependence of the Shida number is expressed identically:

$$\begin{aligned} h_f(\Phi) &= h_f^{(0)} + h^{(2)}\left(\tfrac{3}{2}\sin^2\Phi - \tfrac{1}{2}\right), \\ l_f(\Phi) &= l_f^{(0)} + l^{(2)}\left(\tfrac{3}{2}\sin^2\Phi - \tfrac{1}{2}\right). \end{aligned} \tag{7.4}$$

7.1. Love and Shida numbers for the diurnal tides

Love and Shida numbers in the diurnal band can be represented by a resonance formula as a function of the tidal excitation frequencies with the Chandler wobble (σ_{CW}), the nearly diurnal free wobble (retrograde free core nutation in celestial frame) (σ_{NDFW}) and the free inner core nutation (σ_{FICN}) frequency.

The resonance formula for the complex Love and Shida numbers in the diurnal band is taken from Petit and Luzum (2010)

$$L_f = L_0 + \frac{L_{CW}}{\sigma_f - \sigma_{CW}} + \frac{L_{NDFW}}{\sigma_f - \sigma_{NDFW}} + \frac{L_{FICN}}{\sigma_f - \sigma_{FICN}}, \tag{7.5}$$

where L_f is a generic symbol for the frequency-dependent Love (h) and Shida (l) numbers. The numerical values for the resonance frequencies in equation (7.5) given in terrestrial reference

Table 7.1.: Parameters in the resonance formula (Petit and Luzum, 2010).

	$h_2^{(0)}$		$l_2^{(0)}$	
	Re	Im	Re	Im
L_0	0.60671×10^{0}	-0.2420×10^{-2}	0.84963×10^{-1}	-0.7395×10^{-3}
L_{CW}	-0.15777×10^{-2}	-0.7630×10^{-4}	-0.22107×10^{-3}	-0.9646×10^{-5}
L_{NDFW}	0.18053×10^{-3}	-0.6292×10^{-5}	-0.54710×10^{-5}	-0.2990×10^{-6}
L_{FICN}	-0.18616×10^{-5}	0.1379×10^{-6}	-0.29904×10^{-7}	-0.7717×10^{-8}

Table 7.2.: Parameters $h_f^{(0)}$ and $l_f^{(0)}$ computed from the resonance formula (7.5) for diurnal tidal waves.

Name	Doodson number	Frequency [cpsd]	Cartwright-Tayler amplitude [mm]	$h_f^{(0)}$	$l_f^{(0)}$
Q_1	135.655	0.890804	-50.21	$0.6033 - 0.0024i$	$0.0848 - 0.0007i$
O_1	145.555	0.926996	-262.25	$0.6026 - 0.0024i$	$0.0848 - 0.0007i$
M_1	155.655	0.963806	20.62	$0.6004 - 0.0023i$	$0.0849 - 0.0007i$
π_1	162.556	0.991807	-7.16	$0.5882 - 0.0019i$	$0.0853 - 0.0007i$
P_1	163.555	0.994537	-122.35	$0.5823 - 0.0017i$	$0.0855 - 0.0007i$
K_1	165.555	0.999998	369.14	$0.5261 + 0.0002i$	$0.0871 - 0.0007i$
K_1'	165.565	1.000145	49.97	$0.5209 + 0.0007i$	$0.0872 - 0.0007i$
ψ_1	166.554	1.002728	2.94	$1.0439 + 0.0089i$	$0.0715 - 0.0023i$
ϕ_1	167.555	1.005459	5.26	$0.6623 - 0.0041i$	$0.0830 - 0.0009i$
θ_1	173.655	1.031347	3.94	$0.6113 - 0.0027i$	$0.0846 - 0.0008i$
J_1	175.455	1.036191	20.62	$0.6105 - 0.0027i$	$0.0846 - 0.0008i$
Oo_1	185.555	1.073000	11.29	$0.6078 - 0.0026i$	$0.0847 - 0.0008i$

frame as cycles per sidereal day [cpsd] are listed in Petit and Luzum (2010) and taken from Mathews et al. (2002):

$$\begin{aligned} \sigma_{CW} &= -0.0026010 - 0.0001361i, \\ \sigma_{NDFW} &= 1.0023181 + 0.000025i, \\ \sigma_{FICN} &= 0.999026 + 0.000780i. \end{aligned} \tag{7.6}$$

They were estimated from a fit of nutation theory to nutation amplitude and precession rate estimated from the VLBI data analysis. The parameter L_0 and the resonance coefficients L_{CW}, L_{NDFW}, L_{FICN} are listed in Table 7.1. The resulting parameters $h_f^{(0)}$ and $l_f^{(0)}$ from the resonance formula (7.5) computed for twelve diurnal tidal waves are given in Table 7.2.

Concentrating now only on the frequency dependence of the Love and Shida numbers in the diurnal band, the respective terms can be separated from the general equation (7.2) and the

frequency-dependent corrections to the displacement vector can be written as:

$$\begin{aligned}\delta d_f = -3\sqrt{\frac{5}{24\pi}}H_f\Big\{ & \delta h_f \frac{1}{2}\sin 2\Phi \sin(\theta_f+\Lambda)\ \hat{r} \\ & + \delta l_f \sin\Phi\cos(\theta_f+\Lambda)\ \hat{e} \\ & + \delta l_f \cos 2\Phi \sin(\theta_f+\Lambda)\ \hat{n}\Big\}.\end{aligned} \tag{7.7}$$

δh_f and δl_f are the corrections to the constant nominal values of Love and Shida numbers h_2 and l_2, which equal according to Petit and Luzum (2010) to 0.6078 and 0.0847 respectively.

$$\begin{aligned}\delta h_f &= h_f^{(0)} - h_2, \\ \delta l_f &= l_f^{(0)} - l_2.\end{aligned} \tag{7.8}$$

Generalization to the complex parameters is done by the following replacement:

$$\begin{aligned}L\cos(\theta_f+\Lambda) &\longrightarrow L^R\cos(\theta_f+\Lambda) - L^I\sin(\theta_f+\Lambda), \\ L\sin(\theta_f+\Lambda) &\longrightarrow L^R\sin(\theta_f+\Lambda) + L^I\cos(\theta_f+\Lambda),\end{aligned} \tag{7.9}$$

leading to a complex form of equation (7.7):

$$\begin{aligned}\delta d_f = & -\frac{3}{2}\sqrt{\frac{5}{24\pi}}H_f\left[\delta h_f^R\sin(\theta_f+\Lambda) + \delta h_f^I\cos(\theta_f+\Lambda)\right]\sin 2\Phi\ \hat{r} \\ & - 3\sqrt{\frac{5}{24\pi}}H_f\left[\delta l_f^R\cos(\theta_f+\Lambda) - \delta l_f^I\sin(\theta_f+\Lambda)\right]\sin\Phi\ \hat{e} \\ & - 3\sqrt{\frac{5}{24\pi}}H_f\left[\delta l_f^R\sin(\theta_f+\Lambda) + \delta l_f^I\cos(\theta_f+\Lambda)\right]\cos 2\Phi\ \hat{n}\end{aligned} \tag{7.10}$$

which can easily be used for creating the partial derivatives with respect to the frequency-dependent Love and Shida numbers or the FCN period.

7.1.1. Estimates of Love and Shida numbers for the diurnal tides

Frequency-dependent Love and Shida numbers for twelve diurnal tides were estimated. Aside from the three strongest diurnal waves ($K_1, O_1,\ P_1$) four tides ($Q_1,\ M_1,\ \pi_1,\ K_1'$) with a lower frequency than the resonance of the NDFW has, were included and five tides ($\psi_1,\ \phi_1,\ \theta_1,\ J_1,\ Oo_1$) with a higher frequency. The complex Love and Shida numbers were estimated within a global adjustment of the VLBI data from the time span 1984.0 - 2011.0, following the parameterisation and a priori modelling described in chapter 6. The results have already been published in Krásná et al. (2012a). In the following tables the estimates of real parts (Table 7.3)

Table 7.3.: Real part of the complex Love number for the diurnal tides computed by the software VieVS from the VLBI data (1984.0 - 2011.0).

Name	Doodson number	$h_f^{(0)R}$ Haas and Schuh (1997)	$h_f^{(0)R}$ this work	$\Delta\delta R_f^{ip}$ [mm] this work
Q_1	135.655	0.559 ± 0.012	0.6147 ± 0.0043	0.22 ± 0.08
O_1	145.555	0.612 ± 0.002	0.6026 ± 0.0009	0.00 ± 0.09
M_1	155.655	0.422 ± 0.031	0.5888 ± 0.0101	0.09 ± 0.08
π_1	162.556	0.484 ± 0.093	0.5083 ± 0.0289	−0.22 ± 0.08
P_1	163.555	0.567 ± 0.005	0.5816 ± 0.0017	−0.03 ± 0.08
K_1	165.555	0.512 ± 0.003	0.5267 ± 0.0007	−0.08 ± 0.10
K_1'	165.565	0.429 ± 0.019	0.5294 ± 0.0043	−0.16 ± 0.08
ψ_1	166.554	−0.277 ± 0.234	1.1224 ± 0.0701	−0.09 ± 0.08
ϕ_1	167.555	0.764 ± 0.126	0.7707 ± 0.0392	−0.22 ± 0.08
θ_1	173.655	0.705 ± 0.161	0.8093 ± 0.0515	−0.30 ± 0.08
J_1	175.455	0.542 ± 0.031	0.5988 ± 0.0098	0.09 ± 0.08
Oo_1	185.555	0.495 ± 0.054	0.6594 ± 0.0176	−0.23 ± 0.08

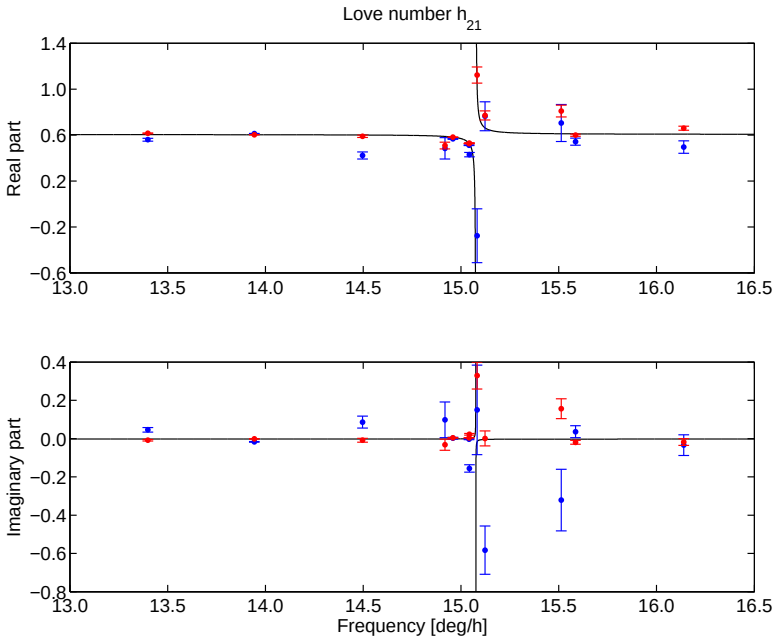

Figure 7.1.: Real (upper plot) and imaginary (lower plot) parts of the Love numbers for twelve diurnal tides. In red are the results from this work, in blue the estimates from Haas and Schuh (1997).

Table 7.4.: Imaginary part of the complex Love number for the diurnal tides computed by the software VieVS from the VLBI data (1984.0 - 2011.0).

Name	Doodson number	$h_f^{(0)I}$ Haas and Schuh (1997)	$h_f^{(0)I}$ this work	$\Delta\delta R_f^{op}$ [mm] this work
Q_1	135.655	0.046 ± 0.012	−0.0087 ± 0.0043	−0.12 ± 0.08
O_1	145.555	−0.017 ± 0.002	−0.0013 ± 0.0008	0.11 ± 0.08
M_1	155.655	0.086 ± 0.031	−0.0084 ± 0.0101	0.05 ± 0.08
π_1	162.556	0.098 ± 0.093	−0.0321 ± 0.0290	−0.08 ± 0.08
P_1	163.555	0.002 ± 0.005	0.0037 ± 0.0017	0.26 ± 0.08
K_1	165.555	−0.003 ± 0.003	0.0041 ± 0.0007	−0.56 ± 0.10
K_1'	165.565	−0.156 ± 0.019	0.0223 ± 0.0043	−0.42 ± 0.08
ψ_1	166.554	0.150 ± 0.234	0.3291 ± 0.0704	−0.36 ± 0.08
ϕ_1	167.555	−0.583 ± 0.126	0.0007 ± 0.0392	−0.01 ± 0.08
θ_1	173.655	−0.321 ± 0.161	0.1562 ± 0.0515	−0.24 ± 0.08
J_1	175.455	0.036 ± 0.031	−0.0194 ± 0.0098	0.13 ± 0.08
Oo_1	185.555	−0.034 ± 0.054	−0.0182 ± 0.0176	0.07 ± 0.08

and imaginary parts (Table 7.4) of the Love numbers are listed. The real and imaginary parts of Shida numbers are given in Tables 7.5 and 7.6, respectively. Summarized and displayed in the third column of these four tables are results obtained by Haas and Schuh (1997), who analysed the VLBI sessions from 1979 to 1996 with the CALC/SOLVE software package, also using a common global least squares adjustment. In the fourth column are the estimates obtained in this work. In the fifth column are the differences between the Love and Shida numbers obtained from my estimates and those computed from the model. They are expressed as differences in the amplitude of the radial and transverse displacement, which follows from the equation (7.10):

$$\begin{pmatrix} \delta R_f^{ip} \\ \delta R_f^{op} \end{pmatrix} = -\frac{3}{2}\sqrt{\frac{5}{24\pi}} H_f \begin{pmatrix} \delta h_f^R \\ \delta h_f^I \end{pmatrix}, \tag{7.11}$$

$$\begin{pmatrix} \delta T_f^{ip} \\ \delta T_f^{op} \end{pmatrix} = -3\sqrt{\frac{5}{24\pi}} H_f \begin{pmatrix} \delta l_f^R \\ \delta l_f^I \end{pmatrix}. \tag{7.12}$$

In Figures 7.1 and 7.2 the Love and Shida numbers from Haas and Schuh (1997) are plotted in blue and results from this work in red. The solid black line represents the theoretical values calculated from the equation (7.5). It can be seen that the newly estimated Love and Shida

Table 7.5.: Real part of the complex Shida number for the diurnal tides computed by the software VieVS from the VLBI data (1984.0 - 2011.0).

Name	Doodson number	$l_f^{(0)R}$ Haas and Schuh (1997)	$l_f^{(0)R}$ this work	$\Delta\delta T_f^{ip}$ [mm] this work
Q_1	135.655	0.076 ± 0.003	0.0870 ± 0.0010	0.09 ± 0.04
O_1	145.555	0.083 ± 0.001	0.0858 ± 0.0002	0.20 ± 0.04
M_1	155.655	0.072 ± 0.008	0.0815 ± 0.0025	0.05 ± 0.04
π_1	162.556	0.054 ± 0.023	0.0827 ± 0.0072	−0.01 ± 0.04
P_1	163.555	0.083 ± 0.001	0.0864 ± 0.0004	0.08 ± 0.04
K_1	165.555	0.090 ± 0.001	0.0881 ± 0.0003	−0.27 ± 0.08
K_1'	165.565	0.060 ± 0.006	0.0912 ± 0.0011	−0.15 ± 0.04
ψ_1	166.554	−0.460 ± 0.058	0.0832 ± 0.0175	−0.03 ± 0.04
ϕ_1	167.555	0.081 ± 0.031	0.1052 ± 0.0098	−0.09 ± 0.04
θ_1	173.655	0.047 ± 0.040	0.1352 ± 0.0129	−0.15 ± 0.04
J_1	175.455	0.076 ± 0.008	0.0833 ± 0.0025	0.02 ± 0.04
Oo_1	185.555	0.058 ± 0.013	0.0856 ± 0.0045	−0.01 ± 0.04

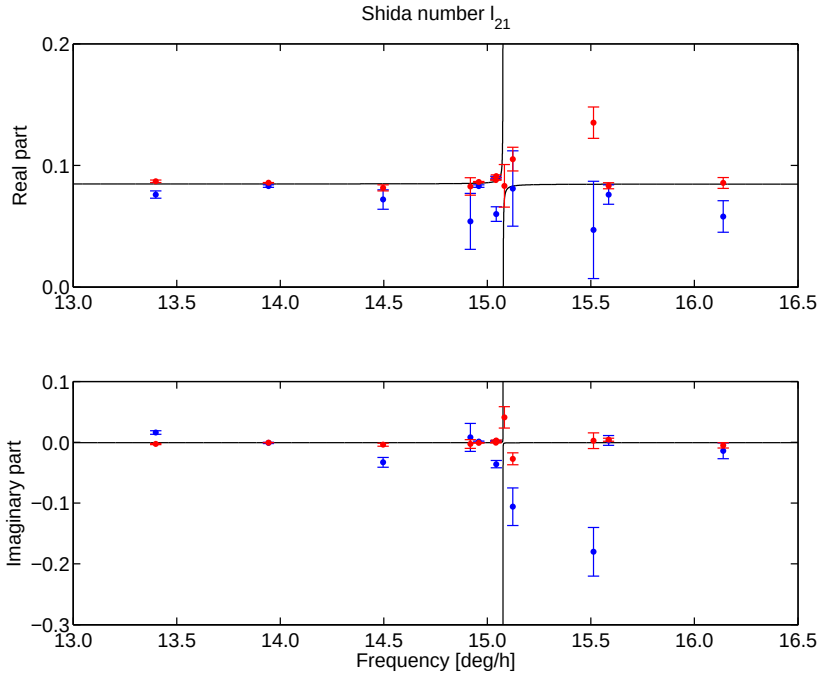

Figure 7.2.: Real and imaginary parts of the Shida numbers for twelve diurnal tides. In red the results from this work are plotted, in blue the estimates from Haas and Schuh (1997).

Table 7.6.: Imaginary part of the complex Shida number for the diurnal tides computed by the software VieVS from the VLBI data (1984.0 - 2011.0).

Name	Doodson number	$l_f^{(0)I}$ Haas and Schuh (1997)	$l_f^{(0)I}$ this work	$\Delta\delta T_f^{op}$ [mm] this work
Q_1	135.655	0.016 ± 0.003	−0.0027 ± 0.0010	−0.08 ± 0.04
O_1	145.555	−0.001 ± 0.001	−0.0006 ± 0.0002	0.02 ± 0.04
M_1	155.655	−0.033 ± 0.008	−0.0040 ± 0.0025	0.05 ± 0.04
π_1	162.556	0.008 ± 0.023	−0.0028 ± 0.0072	−0.01 ± 0.04
P_1	163.555	0.001 ± 0.001	−0.0009 ± 0.0004	−0.02 ± 0.04
K_1	165.555	0.002 ± 0.001	−0.0008 ± 0.0003	0.02 ± 0.08
K_1'	165.565	−0.036 ± 0.006	0.0027 ± 0.0011	−0.13 ± 0.04
ψ_1	166.554	0.234 ± 0.059	0.0409 ± 0.0175	−0.10 ± 0.04
ϕ_1	167.555	−0.106 ± 0.031	−0.0273 ± 0.0098	0.11 ± 0.04
θ_1	173.655	−0.180 ± 0.040	0.0026 ± 0.0129	−0.01 ± 0.04
J_1	175.455	0.003 ± 0.008	0.0043 ± 0.0025	−0.08 ± 0.04
Oo_1	185.555	−0.014 ± 0.013	−0.0050 ± 0.0044	0.04 ± 0.04

numbers lay very close to their theoretical values. A slightly larger deviation from its theoretical value is by the tide θ_1 of about 0.20 in the real part and about 0.15 in the imaginary part of the Love number. The estimated Shida number for this tide differs by about 0.05 in real part from the theory, whereas the imaginary part fits very well to the model. The inaccuracy of this tide may have been caused by the weak amplitude, which obstructs an accurate estimation. But on the other hand it can be seen that the differences in $\delta R_{\theta_1}^{ip}$, $\delta R_{\theta_1}^{op}$ and $\delta T_{\theta_1}^{ip}$ are still small values in sub-millimetre range: -0.3 ± 0.1 mm, -0.2 ± 0.1 mm and -0.2 ± 0.0 mm, respectively. The total difference to the theoretical displacement summed over the absolute values of all twelve diurnal waves reaches 1.73 ± 0.29 mm in vertical direction and 1.15 ± 0.15 mm in horizontal direction.

The correlation coefficients r_{p1p2} between all estimated frequency-dependent Love and Shida numbers in the diurnal band were computed following the basic formula:

$$r_{p1p2} = \frac{\sigma_{p1p2}}{\sqrt{\sigma_{p1p1} \cdot \sigma_{p2p2}}}, \tag{7.13}$$

where σ_{p1p2} is the covariance between the parameter $p1$ and parameter $p2$, and σ_{p1p1}, σ_{p2p2}

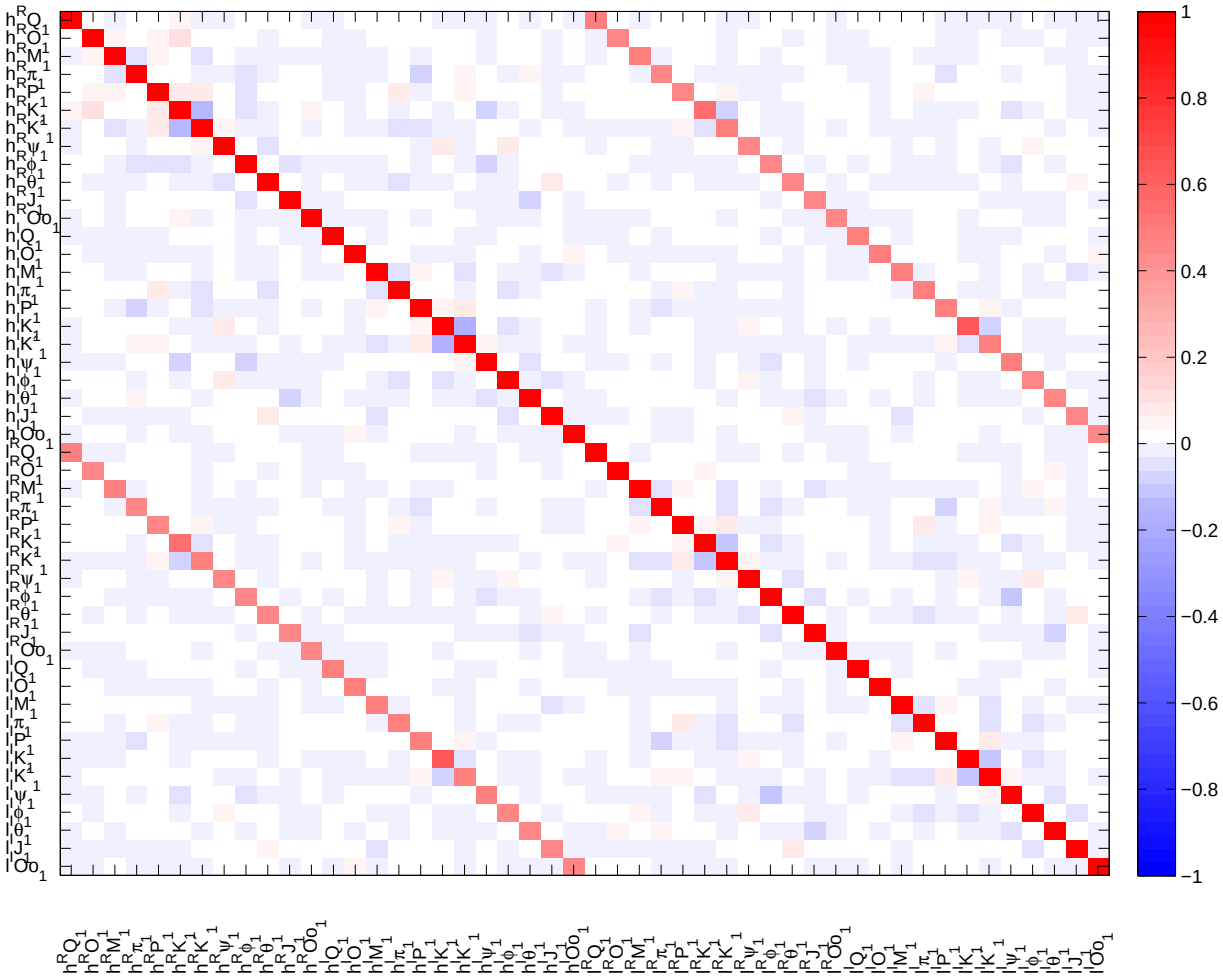

Figure 7.3.: Correlation coefficients between the estimated real and imaginary parts of the Love and Shida numbers of the diurnal tides.

are the variances. In Figure 7.3 the correlation coefficients for all combinations of the real and imaginary parts of the Love and Shida numbers are plotted. The correlations between the Love and Shida numbers of the same tide are clearly visible. They range from 0.44 to 0.48. The only exception is the correlation coefficient for the tide K_1 which exceeds 0.56 between the real parts of Love and Shida number, and 0.64 between their imaginary parts. The correlation between the estimates of Love and Shida numbers can be explained by the common information, which is included in the VLBI measurement. The primary observable (the time delay) is computed among others from the location of the stations, i.e. from the baseline vector between the two stations. Because in the baseline vector both components (radial and transverse) of the station positions are included, the estimates of Love and Shida numbers of the same tide cannot be fully independent.

The maximum correlation between only the real parts of Love numbers is between tides K_1 and K_1' with the correlation coefficient of 0.14 (considering the absolute value), between the imaginary parts is a maximal correlation of 0.18 again found between these two tides. Accordingly between the Shida numbers of the tides K_1 and K_1' the correlation exceeds 0.09 and 0.11 for the real and imaginary parts, respectively. All other correlations do not exceed 0.9 and 89% of all correlation combinations lay below 0.03.

7.1.2. Two models for ocean tidal loading

The parameterisation of the VLBI analysis presented above followed the standard procedure described in chapter 6 where the ocean tide model FES2004 (Letellier, 2004) for the a priori correction of ocean tidal loading at station coordinates was applied. An investigation into the influence of the chosen a priori ocean tide model on the estimated Love and Shida numbers (in the diurnal band) is done. A second solution is computed similar to the default one, using the AG06a (Andersen, 2006) ocean tide model for the correction of ocean tidal loading. In chapter 4 it is shown that the modelled a priori correction of the station displacement in the height component varies in the range of a few millimetres. The model FES2004 is a numerical hydrodynamic model with assimilated altimetry data from TOPEX/Poseidon with a 0.125° resolution. The model AG06a is based on the theoretical model FES94.1 (Le Provost et al., 1994) but adjusted to multi-mission altimetry measurements (TOPEX/Poseidon, Jason-1, ERS/ENVISAT, GFO) (Andersen, 2006).

In Tables 7.7 and 7.8 the estimated complex Love and Shida numbers for the diurnal tides obtained from the "AG06a solution" are listed. In the second and fifth columns the estimates of the real and imaginary part, respectively, are given. In the third and sixth column the difference between the estimates from both solutions in the sense AG06a minus FES2004 is computed. These values are recomputed to show the differences between the respective amplitudes of the station displacement (columns four and seven), similar to the previous section.

The ocean tidal loading is modelled at four diurnal waves: K_1, O_1, P_1, and Q_1. Therefore a change in the estimated Love and Shida numbers is primarily expected for these tides. That is confirmed by the values in Tables 7.7 and 7.8 where the largest differences in $\Delta\delta R_f^{ip}$ can be found by tide K_1 and Q_1, -0.26 ± 0.14 mm and -0.21 ± 0.11 mm, respectively. The values for the tides O_1 and P_1 lay in the range of their formal errors. Similar behaviour can be seen for the imaginary parts and horizontal displacement, where again most of the estimated values

Table 7.7.: Diurnal Love numbers estimated with a priori ocean tidal model AG06a compared to the Love numbers obtained by the default solution (a priori ocean tidal model FES2004).

Name	$h_f^{(0)R}$	$\Delta h_f^{(0)R}$	$\Delta\delta R_f^{ip}$ [mm]	$h_f^{(0)I}$	$\Delta h_f^{(0)I}$	$\Delta\delta R_f^{op}$ [mm]
	AG06a	"AG06a − FES2004"		AG06a	"AG06a − FES2004"	
Q_1	0.6038 ± 0.0040	−0.0109	−0.21 ± 0.11	−0.0117 ± 0.0040	−0.0029	−0.06 ± 0.11
O_1	0.6038 ± 0.0008	0.0012	0.12 ± 0.12	−0.0035 ± 0.0008	−0.0022	−0.22 ± 0.11
M_1	0.5789 ± 0.0095	−0.0099	0.08 ± 0.11	−0.0117 ± 0.0095	−0.0033	0.03 ± 0.11
π_1	0.5218 ± 0.0273	0.0135	0.04 ± 0.11	−0.0396 ± 0.0273	−0.0075	−0.02 ± 0.11
P_1	0.5839 ± 0.0016	0.0022	0.11 ± 0.11	0.0024 ± 0.0016	−0.0014	−0.07 ± 0.11
K_1	0.5285 ± 0.0007	0.0019	−0.26 ± 0.14	0.0026 ± 0.0007	−0.0015	0.21 ± 0.14
K_1'	0.5349 ± 0.0041	0.0055	−0.11 ± 0.11	0.0241 ± 0.0040	0.0018	−0.04 ± 0.11
ψ_1	1.0741 ± 0.0660	−0.0483	0.05 ± 0.11	0.3384 ± 0.0663	0.0092	−0.01 ± 0.11
ϕ_1	0.7650 ± 0.0369	−0.0057	0.01 ± 0.11	0.0165 ± 0.0369	0.0158	−0.03 ± 0.11
θ_1	0.8154 ± 0.0484	0.0061	−0.01 ± 0.11	0.1427 ± 0.0485	−0.0135	0.02 ± 0.11
J_1	0.6022 ± 0.0092	0.0033	−0.03 ± 0.11	−0.0161 ± 0.0092	0.0033	−0.03 ± 0.11
Oo_1	0.6567 ± 0.0165	−0.0027	0.01 ± 0.11	−0.0071 ± 0.0165	0.0111	−0.05 ± 0.11

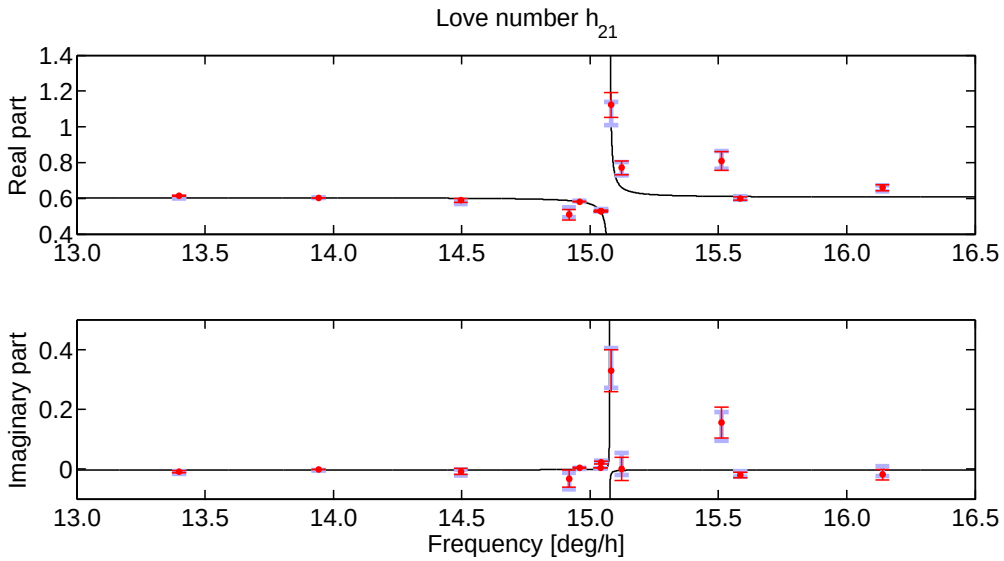

Figure 7.4.: Real and imaginary part of the diurnal Love numbers estimated from the "FES2004 solution" in red and from the "AG06a solution" in light blue.

Table 7.8.: Diurnal Shida numbers estimated with a priori ocean tidal model AG06a compared to the Shida numbers obtained by the default solution (a priori ocean tidal model FES2004).

Name	$l_f^{(0)R}$	$\Delta l_f^{(0)R}$	$\Delta\delta T_f^{ip}$ [mm]	$l_f^{(0)I}$	$\Delta l_f^{(0)I}$	$\Delta\delta T_f^{op}$ [mm]
	AG06a	"AG06a − FES2004"		AG06a	"AG06a − FES2004"	
Q_1	0.0866 ± 0.0010	−0.0004	−0.01 ± 0.03	−0.0030 ± 0.0010	−0.0003	−0.01 ± 0.03
O_1	0.0861 ± 0.0002	0.0003	0.03 ± 0.03	−0.0009 ± 0.0002	−0.0003	−0.03 ± 0.03
M_1	0.0807 ± 0.0023	−0.0008	0.01 ± 0.03	−0.0010 ± 0.0023	0.0030	−0.02 ± 0.03
π_1	0.0820 ± 0.0068	−0.0007	−0.00 ± 0.03	−0.0068 ± 0.0068	−0.0039	−0.01 ± 0.03
P_1	0.0863 ± 0.0004	−0.0001	−0.00 ± 0.03	−0.0002 ± 0.0004	0.0008	0.04 ± 0.03
K_1	0.0881 ± 0.0003	0.0001	−0.01 ± 0.05	−0.0003 ± 0.0003	0.0005	−0.07 ± 0.06
K_1'	0.0915 ± 0.0010	0.0004	−0.01 ± 0.03	0.0043 ± 0.0010	0.0016	−0.03 ± 0.03
ψ_1	0.0778 ± 0.0165	−0.0054	0.01 ± 0.03	0.0575 ± 0.0165	0.0166	−0.02 ± 0.03
ϕ_1	0.1014 ± 0.0092	−0.0038	0.01 ± 0.03	−0.0274 ± 0.0092	−0.0001	0.00 ± 0.03
θ_1	0.1557 ± 0.0122	0.0205	−0.03 ± 0.03	0.0157 ± 0.0122	0.0132	−0.02 ± 0.03
J_1	0.0828 ± 0.0023	−0.0005	0.00 ± 0.03	0.0045 ± 0.0023	0.0002	−0.00 ± 0.03
Oo_1	0.0867 ± 0.0042	0.0011	−0.00 ± 0.03	−0.0046 ± 0.0042	0.0004	−0.00 ± 0.03

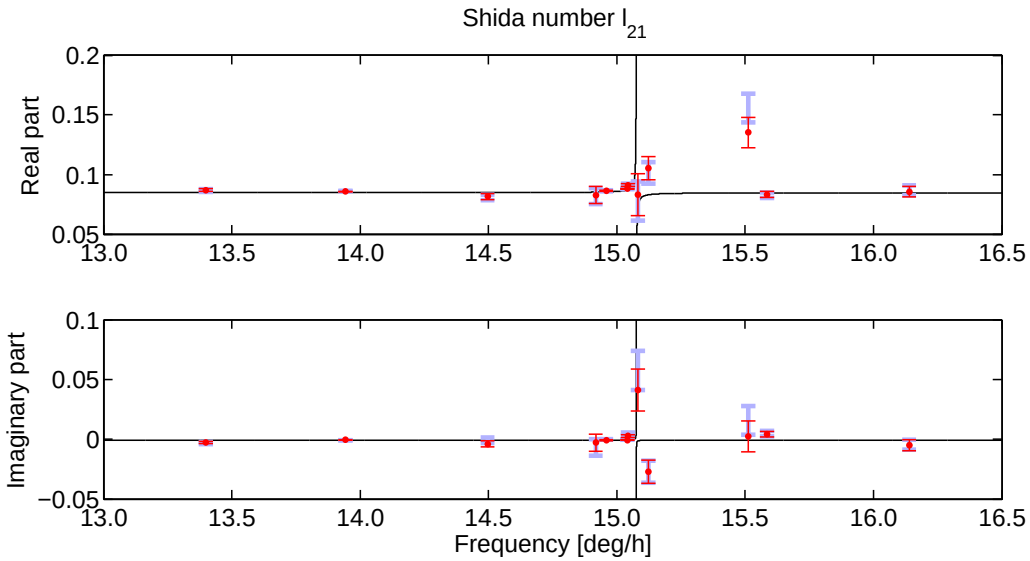

Figure 7.5.: Real and imaginary part of the diurnal Shida numbers estimated from the "FES2004 solution" in red and from the "AG06a solution" in light blue.

are between their formal errors. From this investigation it is evident that the use of an a priori tide model for ocean loading corrections to station coordinates causes a difference in the $\Delta\delta R_f^{ip}$ for the strongest tides at the sub-millimeter level.

7.2. Love and Shida numbers for the long-period tides

The frequency dependence of Love and Shida numbers in the long-period tidal band arises mainly from mantle anelasticity (Petit and Luzum, 2010). The anelasticity model adopted in Petit and Luzum (2010) is the one from Widmer et al. (1991). The variation of $h_{20}^{(0)}$ and $l_{20}^{(0)}$ across the zonal tidal band is described by equations (7.14) and (7.15) (formula (7.4) in Petit and Luzum (2010)). Love and Shida numbers from these equations are also tabulated in the IERS Conventions 2010 and I used them as a priori values for their estimation in the global adjustment.

$$h_{20}^{(0)} = 0.5998 - 9.96 \times 10^{-4}\left\{ \cot\frac{\alpha\pi}{2}\left[1 - \left(\frac{f_m}{f}\right)^{\alpha}\right] + i\left(\frac{f_m}{f}\right)^{\alpha}\right\}, \tag{7.14}$$

$$l_{20}^{(0)} = 0.0831 - 3.01 \times 10^{-4}\left\{ \cot\frac{\alpha\pi}{2}\left[1 - \left(\frac{f_m}{f}\right)^{\alpha}\right] + i\left(\frac{f_m}{f}\right)^{\alpha}\right\}. \tag{7.15}$$

f is the frequency of the zonal tidal constituent, f_m is a reference frequency equivalent to a period of 200 s, and the power law index $\alpha = 15$. To ensure 1 mm accuracy by the computed displacement of the crust five tidal waves has to be taken into account (Petit and Luzum, 2010). In addition for purpose of this work, the annual tidal wave S_a was added to this group. The tidal waves are described in Table 7.9. Deformation of the crust due to the zonal tidal terms

Table 7.9.: Frequency and amplitude of six zonal tides for which the Love and Shida numbers were estimated.

Name	Doodson number	Frequency [cpsd]	Period [solar days]	Cartwright-Tayler amplitude [mm]
Ω_1	55.565	0.000147	6797.38 (= 18.6 yr)	27.9
S_a	56.554	0.002731	365.25	−4.9
S_{sa}	57.555	0.005461	182.62	−30.9
M_m	65.455	0.036193	27.55	−35.2
M_f	75.555	0.073002	13.66	−66.7
M_f'	75.565	0.073149	13.63	−27.6

Table 7.10.: Parameters $h_f^{(0)R}$ for the long-period tides estimated from the VLBI data (1984.0 - 2011.0) within three different solutions and those obtained by Petrov et al. (2004). $\Delta\delta R_f^{ip}$ shows the difference between solution 3 and values given in IERS Conventions 2010.

Name	Doodson number	$h_f^{(0)R}$ from (7.14)	$h_f^{(0)R}$ Petrov et al. (2004)	$h_f^{(0)R}$ this work S1	$h_f^{(0)R}$ this work S2	$h_f^{(0)R}$ this work S3	$\Delta\delta R_f^{ip}$ from S3 [mm]
Ω_1	55.565	0.6344	-	0.7071 ± 0.0188	0.6372 ± 0.0199	0.6372 ± 0.0199	0.05 ± 0.35
S_a	56.554	0.6207	-	-	-	0.5708 ± 0.0612	0.15 ± 0.19
S_{sa}	57.555	0.6182	0.57 ± 0.02	0.5405 ± 0.0090	0.5531 ± 0.0094	0.5635 ± 0.0095	1.07 ± 0.19
M_m	65.455	0.6126	0.622 ± 0.009	0.5965 ± 0.0076	0.5887 ± 0.0079	0.5905 ± 0.0079	0.49 ± 0.18
M_f	75.555	0.6109	0.620 ± 0.005	0.6036 ± 0.0042	0.6052 ± 0.0043	0.6049 ± 0.0043	0.25 ± 0.18
M_f'	75.565	0.6109	-	0.6024 ± 0.0100	0.5878 ± 0.0105	0.5893 ± 0.0105	0.38 ± 0.18

Table 7.11.: Parameters $h_f^{(0)I}$ for the long-period tides estimated from the VLBI data (1984.0 - 2011.0) within three different solutions. $\Delta\delta R_f^{op}$ shows the difference between solution 3 and values given in IERS Conventions 2010.

Name	Doodson number	$h_f^{(0)I}$ from (7.14)	$h_f^{(0)I}$ this work S1	$h_f^{(0)I}$ this work S2	$h_f^{(0)I}$ this work S3	$\Delta\delta R_f^{op}$ from S3 [mm]
Ω_1	55.565	−0.0093	−0.2598 ± 0.0146	−0.2732 ± 0.0154	−0.2710 ± 0.0154	4.61 ± 0.27
S_a	56.554	−0.0060	-	-	−0.5137 ± 0.0583	−1.57 ± 0.18
S_{sa}	57.555	−0.0054	−0.0648 ± 0.0089	−0.0117 ± 0.0093	−0.0145 ± 0.0093	−0.18 ± 0.18
M_m	65.455	−0.0041	0.0217 ± 0.0079	0.0357 ± 0.0083	0.0357 ± 0.0083	0.88 ± 0.18
M_f	75.555	−0.0037	0.0097 ± 0.0042	0.0143 ± 0.0044	0.0137 ± 0.0044	0.73 ± 0.19
M_f'	75.565	−0.0037	0.0103 ± 0.0102	−0.0067 ± 0.0107	−0.0090 ± 0.0107	−0.09 ± 0.19

Table 7.12.: Parameters $l_f^{(0)R}$ for the long-period tides estimated from the VLBI data (1984.0 - 2011.0) within three different solutions and those obtained by Petrov et al. (2004). $\Delta\delta T_f^{ip}$ shows the difference between solution 3 and values given in IERS Conventions 2010.

Name	Doodson number	$l_f^{(0)R}$ from (7.15)	$l_f^{(0)R}$ Petrov et al. (2004)	$l_f^{(0)R}$ this work S1	$l_f^{(0)R}$ this work S2	$l_f^{(0)R}$ this work S3	$\Delta\delta T_f^{ip}$ from S3 [mm]
Ω_1	55.565	0.0936	-	0.1147 ± 0.0044	0.1079 ± 0.0047	0.1078 ± 0.0047	0.37 ± 0.12
S_a	56.554	0.0894	-	-	-	0.1079 ± 0.0146	−0.09 ± 0.07
S_{sa}	57.555	0.0886	0.104 ± 0.003	0.0955 ± 0.0021	0.0954 ± 0.0022	0.0984 ± 0.0023	−0.28 ± 0.07
M_m	65.455	0.0870	0.083 ± 0.002	0.0851 ± 0.0018	0.0819 ± 0.0019	0.0825 ± 0.0019	0.15 ± 0.06
M_f	75.555	0.0864	0.091 ± 0.001	0.0855 ± 0.0010	0.0865 ± 0.0010	0.0864 ± 0.0010	0.01 ± 0.06
M'_f	75.565	0.0864	-	0.0842 ± 0.0024	0.0771 ± 0.0025	0.0772 ± 0.0025	0.24 ± 0.07

Table 7.13.: Parameters $l_f^{(0)I}$ for the long-period tides estimated from the VLBI data (1984.0 - 2011.0) within three different solutions. $\Delta\delta T_f^{op}$ shows the difference between solution 3 and values given in IERS Conventions 2010.

Name	Doodson number	$l_f^{(0)I}$ from (7.15)	$l_f^{(0)I}$ this work S1	$l_f^{(0)I}$ this work S2	$l_f^{(0)I}$ this work S3	$\Delta\delta T_f^{op}$ from S3 [mm]
Ω_1	55.565	−0.0028	−0.0648 ± 0.0033	−0.0613 ± 0.0035	−0.0603 ± 0.0035	1.52 ± 0.09
S_a	56.554	−0.0018	-	-	−0.1562 ± 0.0139	−0.72 ± 0.06
S_{sa}	57.555	−0.0016	−0.0013 ± 0.0021	0.0062± 0.0022	0.0057 ± 0.0022	0.21 ± 0.06
M_m	65.455	−0.0012	0.0035 ± 0.0018	0.0029 ± 0.0020	0.0027 ± 0.0020	0.13 ± 0.07
M_f	75.555	−0.0011	0.0005 ± 0.0010	0.0019 ± 0.0011	0.0018 ± 0.0011	0.18 ± 0.07
M'_f	75.565	−0.0011	−0.0043 ± 0.0024	−0.0060 ± 0.0025	−0.0064 ± 0.0025	−0.14 ± 0.07

(equation (7.16)) follows from equation (7.3). These expressions are taken for building the partial derivatives of the time delay with respect to the long-period Love and Shida numbers in the VLBI analysis.

$$\begin{aligned}\delta d_f =& \sqrt{\frac{5}{4\pi}} H_f \left(\frac{3}{2}\sin^2\Phi - \frac{1}{2}\right)\left(\delta h_f^R \cos\theta_f - \delta h_f^I \sin\theta_f\right)\hat{r} \\ &+ \frac{3}{2}\sqrt{\frac{5}{4\pi}} H_f \sin 2\Phi \left(\delta l_f^R \cos\theta_f - \delta l_f^I \sin\theta_f\right)\hat{n}.\end{aligned} \tag{7.16}$$

Three solutions for estimation of the zonal Love and Shida numbers are performed. In all solutions the estimates of complex Love and Shida numbers together with a constant nominal value of Love and Shida numbers of degree two are obtained from the global adjustment of the VLBI sessions (1984.0 - 2011.0).

- S1 - default parameterisation described in chapter 6, Love and Shida numbers for five main zonal tidal waves are estimated,
- S2 - as S1 but hydrology loading corrections are applied a priori on the station coordinates,
- S3 - as S2 but Love and Shida numbers for six main zonal tidal waves are estimated (the annual tidal wave S_a is added).

The a priori and estimated complex Love and Shida numbers are summarized in Tables 7.10 to 7.13. In the third column of each table there are theoretical real and imaginary parts of the Love and Shida numbers computed from the equations (7.14) and (7.15). The fourth column of the tables summarizing the real part of Love and Shida numbers shows the estimates obtained by Petrov et al. (2004). In the next columns described as "this work" Love and Shida numbers obtained from the solutions S1, S2 and S3 are given. In the last column the differences in the a priori and estimated Love and Shida numbers from solution S3 converted into the difference in amplitude of the tidal term in millimetres are shown.
The conversion is given by equations (7.17) and (7.18) (Petit and Luzum, 2010) which follow from equation (7.16):

$$\begin{pmatrix} \delta R_f^{ip} \\ \delta R_f^{op} \end{pmatrix} = \sqrt{\frac{5}{4\pi}} H_f \begin{pmatrix} \delta h_f^R \\ -\delta h_f^I \end{pmatrix}, \tag{7.17}$$

$$\begin{pmatrix} \delta T_f^{ip} \\ \delta T_f^{op} \end{pmatrix} = \frac{3}{2}\sqrt{\frac{5}{4\pi}} H_f \begin{pmatrix} \delta l_f^R \\ -\delta l_f^I \end{pmatrix}. \tag{7.18}$$

The estimates of Love and Shida numbers from all three solutions can also be found in Figures 7.6

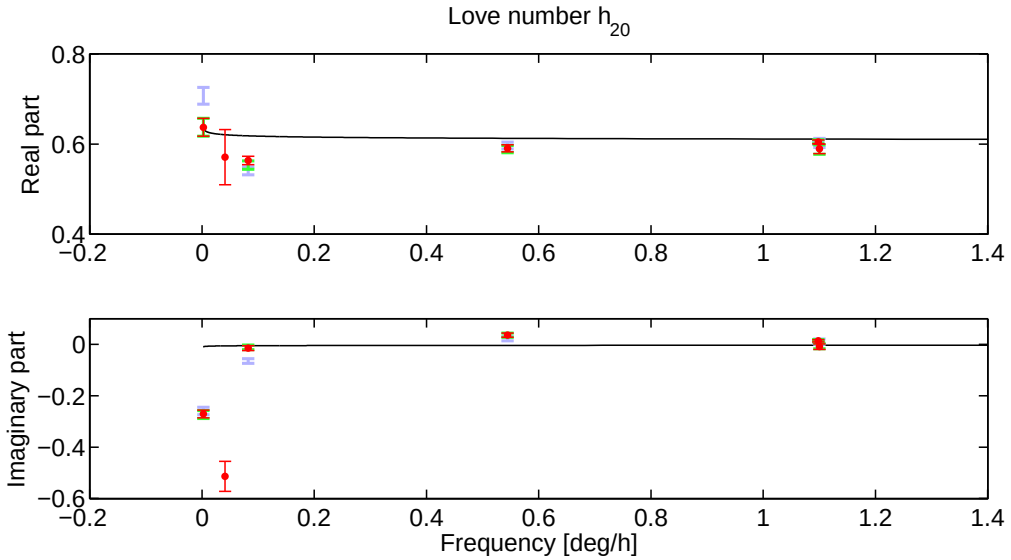

Figure 7.6.: Real and imaginary part of the zonal Love numbers estimated from solution S1 (light blue), S2 (light green), and S3 (red).

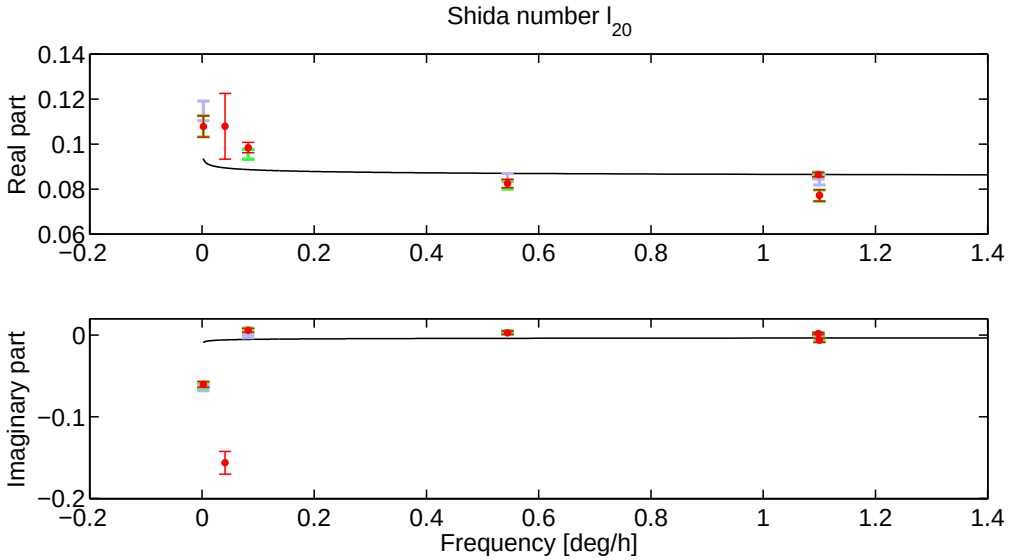

Figure 7.7.: Real and imaginary part of the zonal Shida numbers estimated from solution S1 (light blue), S2 (light green), and S3 (red).

and 7.7. Estimates of the real part of Love numbers from solution S1 (light blue) for the tides Ω_1 and S_{sa} show a relatively large difference of about -0.073 and 0.078 with respect to their theoretical values. The application of hydrology loading corrections on station coordinates (solution S2 - light green) which contain mainly the annual and semi-annual signal (see chapter 4.6) leads surprisingly to a decrease of the difference between the theoretical and estimated value of the Love number for the Ω_1 tide (-0.003). The expected improvement of the estimated Love number of the semi-annual tide S_{sa} appeared only very slightly (the difference to the theoretical value is now 0.065). In the third solution S3 (red colour) the additional estimation of the Love number for the annual tide S_a causes another slight decrease of the difference between estimated and theoretical Love number for the semi-annual term (0.055). The larger formal error of the estimated Love number for the annual tide S_a is related to its weak amplitude. The estimated Love number of the semi-annual tide S_{sa} which represents a 1.1 mm difference in the vertical amplitude of the crust displacement with respect to the theoretical value can reflect some deficiencies in the a priori station displacement modelling of the long-period signals. The estimated Shida numbers are all below a difference in the horizontal amplitude of 0.4 mm. The largest difference is obtained for the tide Ω_1 which can be caused by the fact that the interval of observations could still not be sufficiently long. The difference in the horizontal amplitude for the semi-annual term S_{sa} is 0.3 mm.

7.3. Love and Shida number for the pole tide

Similar to the deformation of the solid Earth due to the tidal potential, there is deformation of the crust caused by variations in centrifugal potential. This change of centrifugal potential arises from variations in orientation of the rotation axis, i.e. from variations in the pole position. The direct response of the crust is called the pole tide and it's maximum in radial direction can reach 25 mm, with a maximum horizontal displacement of about 7 mm (Petit and Luzum, 2010).
The perturbation in the centrifugal potential $\triangle V$ caused by the changes in position of the rotation axis can be written as (Wahr, 1985; Petit and Luzum, 2010):

$$\triangle V(\Theta, \Lambda) = -\frac{\Omega^2 r_{\oplus}^2}{2} \sin 2\Theta (m_1 \cos\Lambda + m_2 \sin\Lambda), \tag{7.19}$$

where $r_{\oplus}$ is the geocentric distance to the station (6378000 m), Θ and Λ geocentric co-latitude and longitude of the station. Ω is the mean angular velocity of the Earth rotation (7.292115e-5 rad/s) and m_1 with m_2 (in arcseconds) describe the time-dependent offset of the instantaneous

rotation pole from the mean rotation pole.

Basic formulation of the displacement vector Δd due to a perturbing potential in a local REN system (see also section 5.4) (Munk and MacDonald, 1960) reads:

$$\Delta d_r = h_2 \frac{\Delta V}{g}, \qquad \Delta d_e = \frac{l_2}{g \sin\Theta} \frac{\partial \Delta V}{\partial \Lambda}, \qquad \Delta d_n = -\frac{l_2}{g} \frac{\partial \Delta V}{\partial \Theta}. \tag{7.20}$$

After a rearrangement of equation (7.20) the final expression for the pole tide at a particular station (Θ, Λ) follows as:

$$\begin{aligned} \Delta d_r &= dR \sin 2\Theta (m_1 \cos\Lambda + m_2 \sin\Lambda), \\ \Delta d_e &= -dT \cos\Theta (m_1 \sin\Lambda - m_2 \cos\Lambda), \\ \Delta d_n &= -dT \cos 2\Theta (m_1 \cos\Lambda + m_2 \sin\Lambda), \end{aligned} \tag{7.21}$$

where dR and dT are given in [m/as]:

$$\begin{aligned} dR &= h_2 \frac{-\Omega^2 r_\oplus^2}{2g} \cdot \pi/180/3600, \\ dT &= l_2 \frac{-\Omega^2 r_\oplus^2}{g} \cdot \pi/180/3600. \end{aligned} \tag{7.22}$$

The nominal values for the Love and Shida numbers are computed following the equation (7.14) and (7.15) for the frequency appropriate to the pole tide, where I used the frequency of Chandler wobble. For the respective period of 433 days, the f in equations (7.14), (7.15) equals to 0.002309 cpsd. The theoretical Love number is then 0.6206 and the Shida number 0.0894.

Several solutions are computed where the Love and Shida numbers for the polar motion are estimated. As the IERS Conventions 2010 do not include the effect of anelasticity, only the real parts of the parameters are determined as additional parameters to the TRF and CRF in a standard global adjustment. The analysis of VLBI data is done according to the default parameterisation with the following differences between the solutions:

- S1 - default parameterisation (cubic function for mean pole (IERS Conventions 2010)),
- S2 - amplitudes of annual and semi-annual station position variations are estimated as additional parameters in the global solution and cubic function for mean pole is applied,
- S3 - as S2 but mean pole is modelled by a linear approximation,
- S4 - as S2 but mean pole is set to zero,
- S5 - as S1 but hydrology loading corrections are applied a priori on the station coordinates, amplitudes of annual station position variations are estimated as additional parameters in the global solution together with the complex Love and Shida numbers for the five main zonal tidal waves.

Table 7.14.: Pole tide Love and Shida number at the zonal frequency of Chandler period.

solutions	h_2 - pole tide	l_2 - pole tide
theoretical value	0.6206	0.0894
S1	0.4638 ± 0.0092	0.1038 ± 0.0023
S2	0.5354 ± 0.0118	0.0943 ± 0.0029
S3	0.5353 ± 0.0118	0.0946 ± 0.0029
S4	0.5353 ± 0.0118	0.0956 ± 0.0029
S5	0.5495 ± 0.0109	0.0953 ± 0.0028
(Petrov, 1998)	0.65 ± 0.20	0.11 ± 0.05
(Gipson and Ma, 1998)	0.636 ± 0.025	0.0868 ± 0.007

In Table 7.14 results of the estimated Love and Shida numbers from the five solutions are summarized. There is a relatively significant difference between the Love number obtained from solution S1 and S2. By determination of the remaining annual and semi-annual signals in the station coordinates (especially height) within the global adjustment, parts of the unmodelled displacement are absorbed which do not then propagate further into the estimates of the pole tide Love number, even if the periods are not exactly the same. The Love numbers obtained from solutions S2, S3 and S4 are identical. This shows that the modelling of the mean pole (cubic, linear, or a total omission) does not have any influence on the Love and Shida numbers estimates. In solution S5 the hydrology loading corrections were applied a priori on the station coordinates and in the global adjustment the complex Love and Shida for the five zonal tidal waves (Ω_1, S_{sa}, M_m, M_f, M'_f (see chapter 7.2)) together with the remaining annual signal in the station coordinates were estimated. This approach gives the best agreement between the

Table 7.15.: Love and Shida numbers for the five zonal tidal waves estimated in solution S5.

Name	$h_f^{(0)R}$ from (7.15)	$h_f^{(0)I}$ this work S1	$l_f^{(0)R}$ this work S2	$l_f^{(0)I}$ this work S3
Ω_1	0.6295 ± 0.0200	−0.2693 ± 0.0155	0.1052 ± 0.0047	−0.0609 ± 0.0036
S_{sa}	0.5584 ± 0.0095	−0.0109 ± 0.0094	0.0971 ± 0.0023	0.0038 ± 0.0023
M_m	0.5896 ± 0.0080	0.0398 ± 0.0083	0.0819 ± 0.0019	0.0029 ± 0.0020
M_f	0.6063 ± 0.0043	0.0136 ± 0.0044	0.0867 ± 0.0010	0.0020 ± 0.0011
M'_f	0.5865 ± 0.0105	−0.0076 ± 0.0107	0.0771 ± 0.0025	−0.0067 ± 0.0025

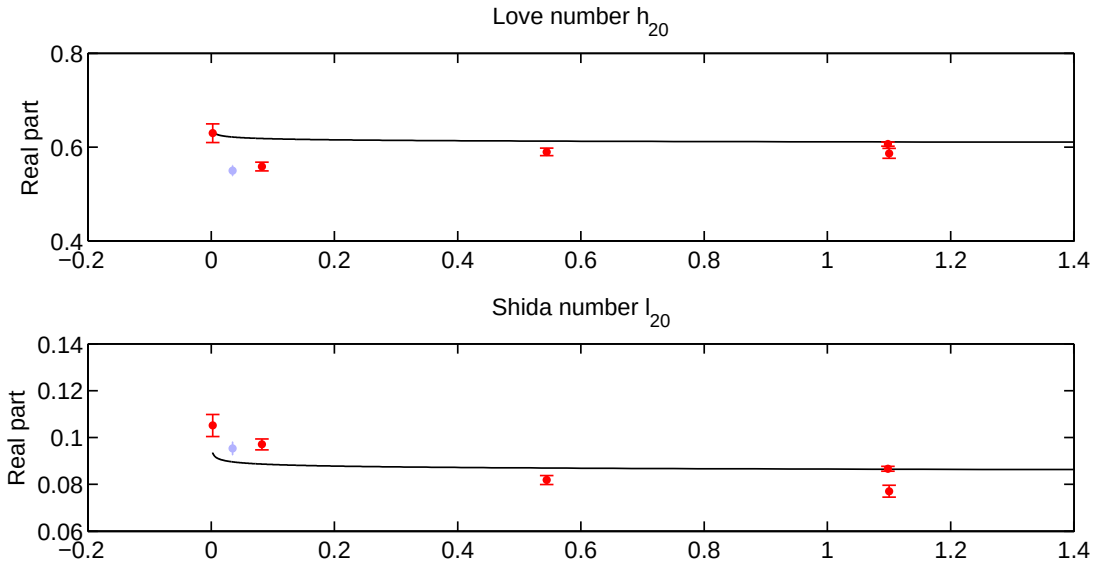

Figure 7.8.: Real parts of the five zonal Love and Shida numbers (red colour) estimated together with the Love and Shida number for the pole tide (light blue colour) in solution S5.

estimated and theoretical pole tide Love number from all five solutions which were carried out. In the last two rows of Table 7.14 results obtained by Petrov (1998) and Gipson and Ma (1998) are shown. Petrov (1998) used only early VLBI data from a time span of 4 years (from 1984 to 1987) for his computation. Even though his Love number estimate (0.65) lies close to the theoretical value (0.62) its large formal error of 0.20 reflects the high uncertainty of the result. Gipson and Ma (1998) included VLBI sessions from 1979 to 1996 and in their modelling they considered the Earth's anelasticity by determining the complex Love and Shida pole number. As visible from the Table 7.14 their estimates agree with the theoretical values.

Figure 7.8 shows the estimated Love and Shida numbers from solution S5. The consistence between the estimated Love number corresponding to the semi-annual tide S_{sa} (0.5584 ± 0.0095) (which is from the estimated Love numbers for solid Earth tides in the zonal band closest to the Chandler period) and the pole tide Love number (0.5495 ± 0.0109) is clearly visible. Rather than doubting the theoretical values of the Love numbers I draw the conclusion that a priori models of station displacement at zonal frequencies are still not sufficiently accurate, and in a global solution the errors propagate into other parameters estimated at those periods.

8. Free Core Nutation

The rotating Earth has five known free rotational modes: the Tilt-Over Mode (TOM), the Free Inner Core Nutation (FICN), the Free Core Nutation (FCN), the Chandler Wobble (CW) and the Inner Core Wobble (ICW). Their resonance periods are dependent on the dynamic ellipticity of a corresponding part of the Earth. The free inner core nutation and inner core wobble are dependent on the inner core, the free core nutation on the outer core and the Chandler wobble is caused by the dynamic flattening of the Earth's mantle. The tilt-over mode is a pure wobble of the whole Earth which does not affect the solid Earth tidal displacement. It depends on the angle between the Earth instantaneous rotation axis and the axis of the terrestrial reference frame. See e.g. Rogister and Valette (2005) or Dehant and Capitaine (1997). In Figure 8.1 the resonance periods in the terrestrial reference frame of these five rotation modes are shown as determined by Mathews et al. (2002).

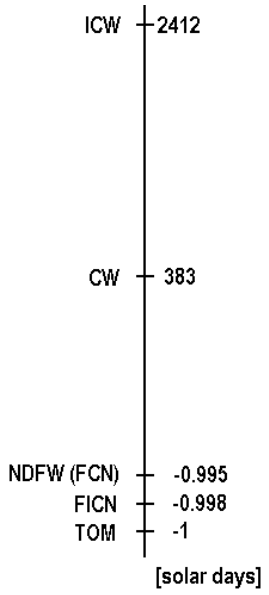

Figure 8.1.: Periods of the Earth's five free rotation modes in the terrestrial frame determined by Mathews et al. (2002). The units are solar days.

The FCN is caused by the fact, that the ellipsoidal liquid core inside the visco-elastic Earth's mantle rotates around an axis which is slightly misaligned with the axis of the mantle. In the celestial reference frame it is visible as a retrograde motion of the Earth figure axis with a period of about 431 days and has an amplitude of about one hundred microarcseconds. Up to now,

there are no models which could predict this motion in a rigorous way, so it is not included in the a priori precession-nutation model of the Earth axis. The motion is a major part of the VLBI residuals between the observed direction of the Celestial Intermediate Pole (CIP) in the celestial reference frame and the direction modelled by the precession-nutation model adopted in the current IERS Conventions 2010. These differences i.e. Celestial Pole Offsets (CPO) are monitored and published by the International Earth Rotation and Reference Systems Service (IERS). In the terrestrial reference frame the motion is observed with a period of about one day and designed as Nearly Diurnal Free Wobble (NDFW). At this frequency it comes to a resonant behaviour of Love and Shida numbers within the diurnal band. The frequency dependence in the diurnal tidal response of the solid Earth allows the estimation of the FCN period directly also from the displacement of the stations in the VLBI data analysis.

8.1. FCN in solid Earth tides

The NDFW affects the solid Earth tides in their diurnal band, where it comes to a strong resonance effect. The Love and Shida numbers for the tides in the vicinity of the NDFW period are strongly frequency-dependent. On the other hand, this resonance effect at these tides can be used for the determination of the FCN period directly during the VLBI analysis. The frequency dependence of the Love and Shida numbers was detailed in chapter 7.1 and the partial derivative of the station displacement in the local coordinate system with respect to the NDFW frequency follows from equation (7.10), where the base is the partial derivative of the resonance formula for the Love and Shida numbers (equation (7.5)):

$$\frac{\partial L_f}{\partial \sigma_{NDFW}} = -\frac{L_{NDFW}}{(\sigma_f - \sigma_{NDFW})^2}, \tag{8.1}$$

where L_{NDFW} is defined in Table 7.1 and σ_f is the frequency of the chosen diurnal tide.

Partial derivative of the basic VLBI model with respect to the NDFW frequency contained in the solid Earth tides, i.e. in the displacement of the baseline $\boldsymbol{b}$ between two stations, is given

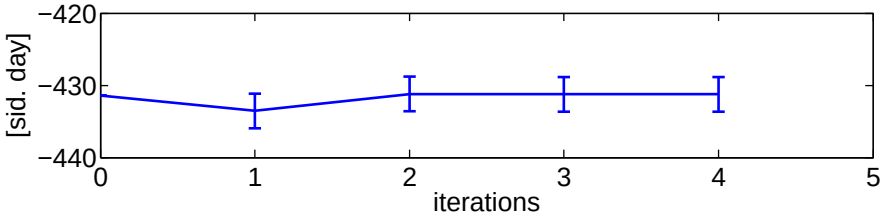

Figure 8.2.: FCN period estimated from the resonance in the solid Earth tides. After four iterations the FCN period converged to -431.23 ± 2.44 sidereal days.

by equation (8.2):

$$\begin{aligned} \frac{\partial \tau}{\partial \sigma_{NDFW}} &= \boldsymbol{k}(t) \cdot \boldsymbol{Q}(t) \cdot \boldsymbol{R}(t) \cdot \boldsymbol{W}(t) \cdot \frac{\partial \boldsymbol{b}(t)}{\partial \sigma_{NDFW}} \\ &= \boldsymbol{k}(t) \cdot \boldsymbol{Q}(t) \cdot \boldsymbol{R}(t) \cdot \boldsymbol{W}(t) \cdot \left(\frac{\partial \boldsymbol{x_2}(t)}{\partial \sigma_{NDFW}} - \frac{\partial \boldsymbol{x_1}(t)}{\partial \sigma_{NDFW}} \right). \end{aligned} \tag{8.2}$$

$\boldsymbol{k}$ is the source vector defined in BCRS, $\boldsymbol{Q}$, $\boldsymbol{R}$ and $\boldsymbol{W}$ are the transformation matrices between the celestial and terrestrial reference frame, and $\boldsymbol{x_1}$, $\boldsymbol{x_2}$ are the position vectors of station 1 and 2 in the ITRS. Because of the non-linear relation in the partial derivative (equation (8.1)) the estimation of the FCN period was done by few iterations. Already after the second iteration (see Figure 8.2) the FCN period stayed stable at -431.23 ± 2.44 sidereal days (-430.05 ± 2.43 solar days).

8.2. FICN in solid Earth tides

As shown in section 7.1 the resonance formula (7.5) of the frequency-dependent Love and Shida numbers in the diurnal band contains the resonance frequencies of the Chandler wobble, NDFW and FICN. Therefore, similar to the estimation of NDFW period from the solid Earth tidal displacement, it should be possible to estimate the period of the free inner core nutation.

The needed partial derivative with respect to the FICN frequency obtained from the resonance equation for the diurnal Love and Shida numbers (equation (7.5)) reads:

$$\frac{\partial L_f}{\partial \sigma_{FICN}} = -\frac{L_{FICN}}{(\sigma_f - \sigma_{FICN})^2}, \tag{8.3}$$

with L_{FICN} defined in Table 7.1 and σ_f which is the frequency of the chosen diurnal tide.
In the equation of VLBI observations the station position vectors of station 1 ($\boldsymbol{x_1}$) and 2 ($\boldsymbol{x_2}$)

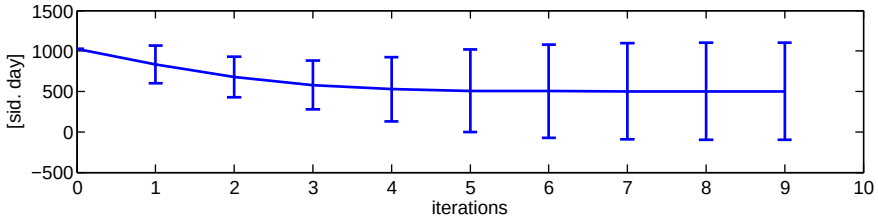

Figure 8.3.: FICN period estimated from the resonance in the solid Earth tides. After nine iterations the FICN period converged to 502.42 ± 601.06 sidereal days.

are derived with respect to the FICN frequency as follows:

$$\frac{\partial \tau}{\partial \sigma_{FICN}} = \boldsymbol{k}(t) \cdot \boldsymbol{Q}(t) \cdot \boldsymbol{R}(t) \cdot \boldsymbol{W}(t) \cdot \left(\frac{\partial \boldsymbol{x_2}(t)}{\partial \sigma_{FICN}} - \frac{\partial \boldsymbol{x_1}(t)}{\partial \sigma_{FICN}} \right). \tag{8.4}$$

Nine iterations were carried out to determine the FICN period starting with the a priori value of 1026.69 sidereal days as given by Mathews et al. (2002). As visible from Figure 8.3 the estimates of the period were getting lower during the first five runs and then they converged to the value of 502.42 ± 601.06 sidereal days which is of factor two shorter then the a priori value. Taking a look at the Table 7.1 one can see that the resonance strength factor for the FICN is about one hundred times smaller than the resonance strength factor for the FCN. This could be the reason why the partial derivative of the resonance formula for the solid Earth tidal displacement is not sufficiently sensitive to the FICN period. It should be mentioned that the theoretical Earth model PREM (Dziewonski and Anderson, 1981) predicts the FICN period to be 476 days. However, because of the large formal error of my estimate no further conclusion about the FICN period can be taken.

8.3. FCN in celestial pole offsets

8.3.1. Motion of CIP in celestial reference system

The CIP separates the motion of the ITRS pole in the GCRS into a celestial part and a terrestrial part. It is done purely by a convention which states that the celestial motion of the CIP includes all the terms with periods greater than 2 days in the GCRS (= precession-nutation) and the

terrestrial motion of the CIP includes all the terms outside the retrograde diurnal band in the ITRS (= polar motion) (Petit and Luzum, 2010). Concentrating on the celestial motion of the CIP the transformation matrix $\boldsymbol{Q}$ can be specified as

$$\boldsymbol{Q}(t) = \boldsymbol{R_z}(-E) \cdot \boldsymbol{R_y}(-d) \cdot \boldsymbol{R_z}(E) \cdot \boldsymbol{R_z}(s), \tag{8.5}$$

with d and E being polar coordinates of the CIP in the GCRS and s being a so-called CIO locator. Following Capitaine and Wallace (2006) and Chapter 5 in Petit and Luzum (2010) the transformation matrix $\boldsymbol{Q}$ can be given in an equivalent form directly involving the celestial pole coordinates X and Y which will lead to a simple expression of the partial derivatives of observables with respect to the Earth orientation parameters. X and Y are the cartesian expression of the CIP unit vector in the GCRS (Figure 8.4):

$$\begin{aligned} X &= \sin d \cos E, \\ Y &= \sin d \sin E, \\ Z &= \cos d, \end{aligned} \tag{8.6}$$

and after combining of the first three rotation matrices in equation (8.5) into one, the matrix $\boldsymbol{Q}$ can be written as:

$$\boldsymbol{Q}(t) = \boldsymbol{M}_{CIO} \cdot \boldsymbol{R_z}(s) = \begin{bmatrix} 1 - aX^2 & -aXY & X \\ -aXY & 1 - aY^2 & Y \\ -X & -Y & 1 - a(X^2 + Y^2) \end{bmatrix} \cdot \boldsymbol{R_z}(s), \tag{8.7}$$

with

$$a = \frac{1}{1 + \cos d} = \frac{1}{1 + Z} = \frac{1}{1 + \sqrt{1 - X^2 - Y^2}}. \tag{8.8}$$

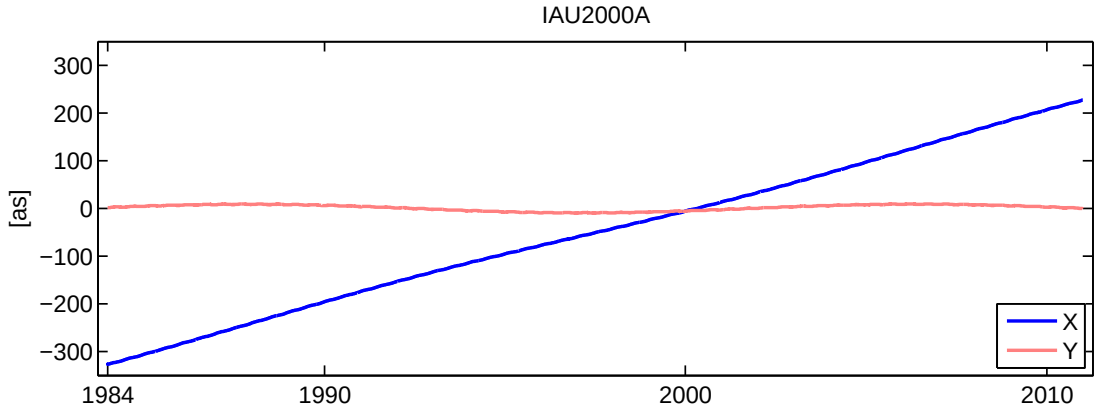

Figure 8.4.: Motion of the CIP in the GCRS modelled by the precession-nutation model IAU2000A.

Following Petit and Luzum (2010) the a in equation (8.8) can be expressed with an accuracy better than 1 μas as

$$a = \frac{1}{2} + \frac{1}{8}(X^2 + Y^2). \tag{8.9}$$

The motion of the CIP in the celestial frame can be determined from VLBI observations as estimates with respect to the a priori IAU precession-nutation model. The partial derivatives of the matrix $\boldsymbol{Q}$ with respect to the CIP coordinates X and Y are listed in equations (8.10) and (8.13). They are obtained from equation (8.7) and a detailed description of the derivation is given e.g. in Gontier (2009).

$$\frac{\partial \boldsymbol{Q}(t)}{\partial X} = \frac{\partial \boldsymbol{M}_{CIO}}{\partial X} \cdot \boldsymbol{R_z}(s) + \boldsymbol{M}_{CIO} \cdot \frac{\partial \boldsymbol{R_z}(s)}{\partial X}, \tag{8.10}$$

where

$$\frac{\partial \boldsymbol{M}_{CIO}}{\partial X} = \begin{bmatrix} -X - X^3/2 - XY^2/4 & -Y/2 - 3X^2Y/8 - Y^3/8 & 1 \\ -Y/2 - 3X^2Y/8 - Y^3/8 & -XY^2/4 & 0 \\ -1 & 0 & -X - X^3/2 - XY^2/2 \end{bmatrix}, \tag{8.11}$$

and

$$\frac{\partial \boldsymbol{R_z}(s)}{\partial X} = -\frac{Y}{2} \cdot \frac{\partial \boldsymbol{R_z}(s)}{s} = -\frac{Y}{2} \cdot \begin{bmatrix} -\sin s & \cos s & 0 \\ -\cos s & -\sin s & 0 \\ 0 & 0 & 0 \end{bmatrix}. \tag{8.12}$$

$$\frac{\partial \boldsymbol{Q}(t)}{\partial Y} = \frac{\partial \boldsymbol{M}_{CIO}}{\partial Y} \cdot \boldsymbol{R_z}(s) + \boldsymbol{M}_{CIO} \cdot \frac{\partial \boldsymbol{R_z}(s)}{\partial Y}, \tag{8.13}$$

where

$$\frac{\partial \boldsymbol{M}_{CIO}}{\partial Y} = \begin{bmatrix} -X^2Y/4 & -X/2 - 3XY^2/8 - X^3/8 & 1 \\ -X/2 - 3XY^2/8 - X^3/8 & -Y - Y^3/2 - X^2Y/4 & 1 \\ 0 & -1 & -Y - Y^3/2 - X^2Y/2 \end{bmatrix}, \tag{8.14}$$

and

$$\frac{\partial \boldsymbol{R_z}(s)}{\partial Y} = -\frac{X}{2} \cdot \frac{\partial \boldsymbol{R_z}(s)}{s} = -\frac{X}{2} \cdot \begin{bmatrix} -\sin s & \cos s & 0 \\ -\cos s & -\sin s & 0 \\ 0 & 0 & 0 \end{bmatrix}. \tag{8.15}$$

8.3.2. Description of FCN in celestial pole offsets

The IAU 2006/2000A precession-nutation model does not contain the nutation offsets caused by free core nutation. Petit and Luzum (2010) refer to an empirical model from Lambert (2007) which is assigned as model of class 3, i.e. "useful but not required". It consists of a constant FCN frequency and a time-varying complex amplitude (Figure 8.5). The FCN offsets in the model of Lambert (2007) are given by:

$$\begin{aligned} X_{FCN} &= A_C \cos(\sigma_{FCN} t) - A_S \sin(\sigma_{FCN} t), \\ Y_{FCN} &= A_S \cos(\sigma_{FCN} t) + A_C \sin(\sigma_{FCN} t), \end{aligned} \tag{8.16}$$

where A_C and A_S are the amplitudes of the cosine and sine term. They are empirically determined from IERS EOP05 C04 combined series by fitting the nutation series and are tabulated in yearly steps. The amplitudes during the year are obtained by a linear interpolation. t is the time given in days since J2000.0 and σ_{FCN} is the frequency of FCN in celestial reference frame.

Equation (8.19) shows how to express σ_{FCN} using the frequency of FCN in terrestrial reference frame, i.e. frequency of nearly diurnal free wobble σ_{NDFW}. The adopted value of 1.0023181 cpsd for σ_{NDFW} in Petit and Luzum (2010) comes from Mathews et al. (2002) and is also used in

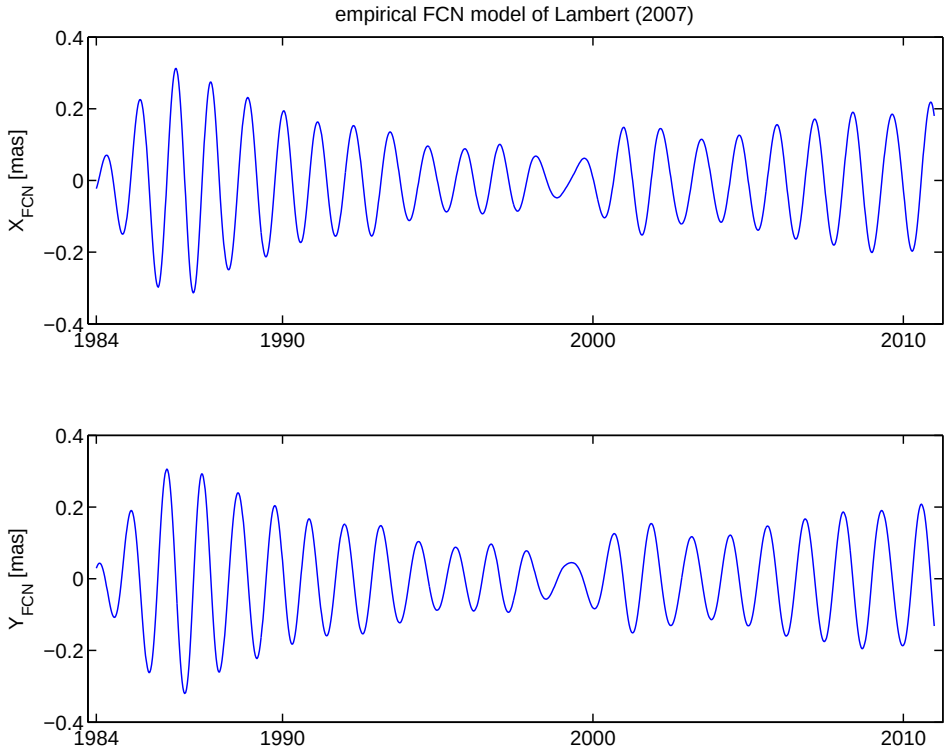

Figure 8.5.: FCN model of Lambert (2007). The coefficients of the amplitude can be found at http://syrte.obspm.fr/∼lambert/fcn/table.txt and are updated regularly.

the model of Lambert (2007). It corresponds to the FCN period P_{FCN} of -430.21 solar days $=$ -431.39 sidereal days.

From the basic relation between frequency and period:

$$\sigma_{FCN} = \frac{2\pi}{P_{FCN}}, \tag{8.17}$$

and from the relationship between frequencies in terrestrial and celestial reference systems:

$$P_{FCN} = \frac{1}{1 - \sigma_{NDFW}} \cdot \frac{1}{sd}, \tag{8.18}$$

follows for σ_{FCN}:

$$\sigma_{FCN} = 2\pi \cdot sd(1 - \sigma_{NDFW}), \tag{8.19}$$

with $sd = 1.002737909$ giving the number of sidereal days per one solar day.

In order to obtain the partial derivatives of the VLBI observable with respect to the FCN period and amplitude, the equations (8.16) for FCN offsets are implemented into the description of the celestial motion of the CIP. The FCN offsets from equation (8.16) are simply added to the X and Y following from the IAU 2006/2000A precession-nutation model:

$$\begin{aligned} X &= X_{FCN} + X_{(IAU)}, \\ Y &= Y_{FCN} + Y_{(IAU)}. \end{aligned} \tag{8.20}$$

According to Petit and Luzum (2010) this addition is practically equivalent to a following multiplication of the transformation matrix $\boldsymbol{Q}_{(IAU)}$:

$$\boldsymbol{Q}(t) = \boldsymbol{dQ}(t) \cdot \boldsymbol{Q}(t)_{(IAU)} = \begin{bmatrix} 1 & 0 & X_{FCN} \\ 0 & 1 & Y_{FCN} \\ -X_{FCN} & -Y_{FCN} & 1 \end{bmatrix} \cdot \boldsymbol{Q}(t)_{(IAU)}. \tag{8.21}$$

The concrete expression of the partial derivatives of $\boldsymbol{dQ}$ with respect to the NDFW frequency σ_{NDFW} then reads

$$\frac{\partial \boldsymbol{dQ}(t)}{\partial \sigma_{NDFW}} = \begin{bmatrix} 0 & 0 & -2\pi \cdot sd \cdot t \cdot \Upsilon_x \\ 0 & 0 & -2\pi \cdot sd \cdot t \cdot \Upsilon_y \\ 2\pi \cdot sd \cdot t \cdot \Upsilon_x & 2\pi \cdot sd \cdot t \cdot \Upsilon_y & 0 \end{bmatrix}, \tag{8.22}$$

where Υ_x and Υ_y denote

$$\begin{aligned} \Upsilon_x &= -A_C \sin(\sigma_{FCN} t) - A_S \cos(\sigma_{FCN} t), \\ \Upsilon_y &= -A_S \sin(\sigma_{FCN} t) + A_C \cos(\sigma_{FCN} t). \end{aligned} \tag{8.23}$$

Partial derivatives of $\boldsymbol{dQ}$ with respect to the amplitude of the cosine term A_C is easily created as:

$$\frac{\partial \boldsymbol{dQ}(t)}{\partial A_C} = \begin{bmatrix} 0 & 0 & \cos(\sigma_{FCN} t) \\ 0 & 0 & \sin(\sigma_{FCN} t) \\ -\cos(\sigma_{FCN} t) & -\sin(\sigma_{FCN} t) & 0 \end{bmatrix}, \tag{8.24}$$

and partial derivatives of $\boldsymbol{dQ}$ with respect to the amplitude of the sine term A_S reads:

$$\frac{\partial \boldsymbol{dQ}(t)}{\partial A_S} = \begin{bmatrix} 0 & 0 & -\sin(\sigma_{FCN} t) \\ 0 & 0 & \cos(\sigma_{FCN} t) \\ \sin(\sigma_{FCN} t) & -\cos(\sigma_{FCN} t) & 0 \end{bmatrix}. \tag{8.25}$$

The incorporation of the partial derivatives of the $\boldsymbol{dQ}$ into the partial derivative of the whole basic VLBI model follows as:

$$\frac{\partial \tau}{\partial \sigma_{NDFW}} = \boldsymbol{k}(t) \cdot \frac{\partial \boldsymbol{dQ}(t)}{\partial \sigma_{NDFW}} \cdot \boldsymbol{Q}(t)_{(IAU)} \cdot \boldsymbol{R}(t) \cdot \boldsymbol{W}(t) \cdot \boldsymbol{b}(t), \tag{8.26}$$

for the partial derivative with respect to the NDFW frequency contained in the celestial pole offsets, where $\boldsymbol{k}$ is again source vector defined in BCRS and $\boldsymbol{b}$ is the baseline vector between the two stations expressed in ITRS.

In the same way one gets the partial derivative of the VLBI model with respect to the amplitude of cosine term:

$$\frac{\partial \tau}{\partial A_C} = \boldsymbol{k}(t) \cdot \frac{\partial \boldsymbol{dQ}(t)}{\partial A_C} \cdot \boldsymbol{Q}(t)_{(IAU)} \cdot \boldsymbol{R}(t) \cdot \boldsymbol{W}(t) \cdot \boldsymbol{b}(t), \tag{8.27}$$

and with respect to the amplitude of sine term:

$$\frac{\partial \tau}{\partial A_S} = \boldsymbol{k}(t) \cdot \frac{\partial \boldsymbol{dQ}(t)}{\partial A_S} \cdot \boldsymbol{Q}(t)_{(IAU)} \cdot \boldsymbol{R}(t) \cdot \boldsymbol{W}(t) \cdot \boldsymbol{b}(t). \tag{8.28}$$

8.3.3. Spectral analysis of CPO

The VLBI measurements following the same parameterisation and choice of a priori models as described in chapter 6 were reanalysed. The only difference was that the celestial pole offsets from the C04 08 time series were not taken as a priori information but only the precession-nutation model IAU 2006/2000A for description of the celestial motion of CIP was used. The estimated celestial pole offsets with respect to the IAU 2006/2000A model are shown in Figure 8.6. As a first step to analyze these estimates a spectral analysis was applied. From Figure 8.6 the increasing precision of the VLBI observations is evident. The spectral analysis was therefore applied to two sets of data. The first set (DS1) was the entire data since 1984.0 (blue line in Figures 8.7 and 8.8), while the second data set (DS2) began in 1990.0 where the observation improvement is visible (light red line in Figures 8.7 and 8.8). First, I applied the Fast Fourier Transform (FFT) algorithm to the complex time series $dX + idY$ in order to solve for prograde as well as for retrograde frequency terms. FFT needs evenly spaced data input, therefore I interpolated the data to three-days intervals using Lagrange interpolation. Spectrum of the DS2 (Figure 8.7) shows a broad peak near the expected FCN period around -460 days, in the spectrum of DS1 even a double peak appears around -410 days and -470 days. The

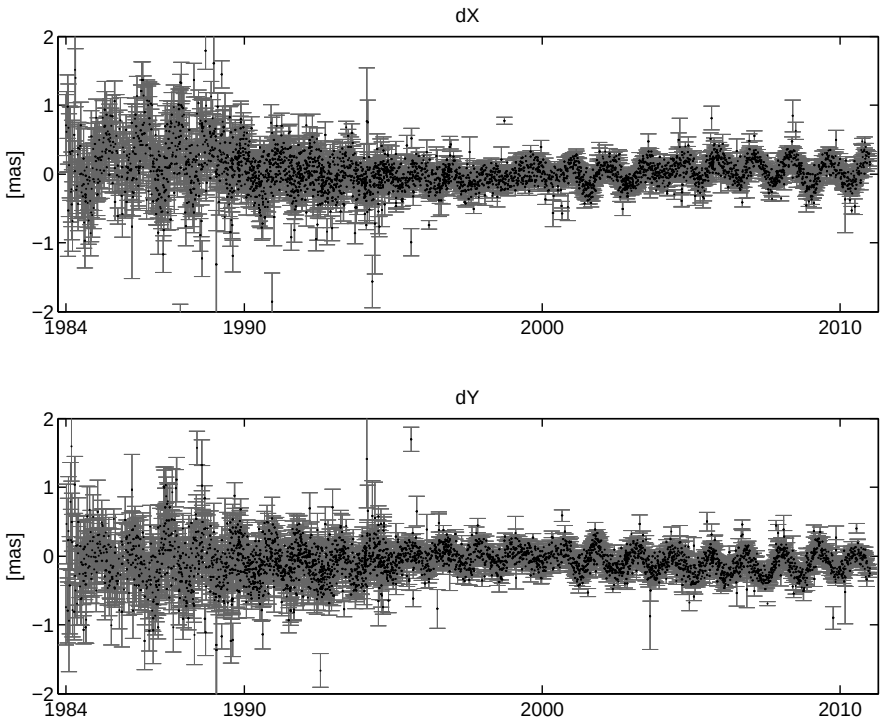

Figure 8.6.: Celestial pole offsets w.r.t. the IAU 2006/2000A precession-nutation model estimated with software VieVS.

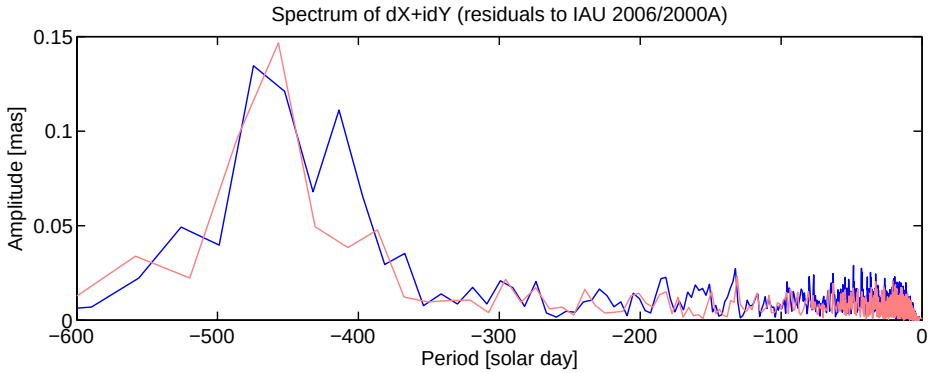

Figure 8.7.: Fourier spectrum for celestial pole offsets estimated with software VieVS w.r.t. the IAU 2006/2000A precession-nutation model. The spectrum for data from 1984.0 to 2011.0 is in blue and for data from 1990.0 to 2011.0 is in light red.

spectral analysis of the celestial pole offsets was also done by a CLEAN algorithm (Baisch and Bokelmann, 1999). This procedure allows analysis of non-equidistantly spaced time series even with larger gaps, so the interpolation of the time series is avoided. However, the series for dX and for dY have to be analysed separately. In the upper part of Figure 8.8 the spectra for dX

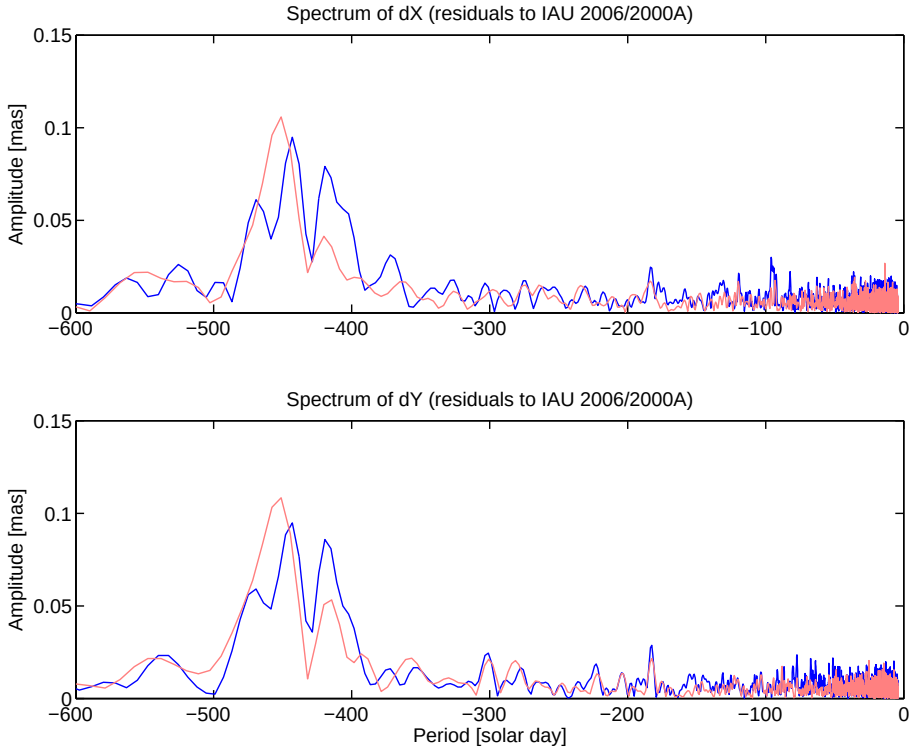

Figure 8.8.: Frequency spectrum obtained by the CLEAN algorithm for celestial pole offsets estimated with software VieVS w.r.t. the IAU 2006/2000A precession-nutation model. Blue displays the spectrum for data from 1984.0 to 2011.0 and light red shows data from 1990.0 to 2011.0.

from DS1 and DS2 are plotted, in the lower part for dY. The resulting spectra for the X and Y coordinate of the celestial pole offsets are in a very good agreement. For DS1 now even three broad peeks in the frequency spectrum are visible between periods of −400 and −500 days. For the data set DS2 the peak appears around −460 days. This shows that the resulting spectrum is strongly dependent on the time interval of the input time series and also on the transformation algorithm.

In the following sections two different explanations and theories about the double peak around the FCN period in the frequency spectrum will be discussed. One theory states that there are two different rotational modes of the Earth. The second one predicts one strong oscillation with a stable period where the apparent change of the period is explained with a variable phase and amplitude of the rotation.

8.3.4. Model for CPO with two periods

One theory works with the presumption that Earth has a fluid core containing an inner core within. The existence of the two layer fluid core would cause two rotational modes and the beating between them would be responsible for the apparent oscillation and damping of the FCN amplitude, which can be observed in the celestial pole offset time series. This theory is included for example in the numerical model for Earth rotation variations, called ERA-2005 (Krasinsky, 2006; Krasinsky and Vasilyev, 2006). In this model preliminary value for the FCN period of −430 days is taken (given as frequency of 0.0146 rad/day in Krasinsky (2006)) together with the value of −422 days for the period of the inner fluid core (corresponding to the frequency of 0.0149 rad/day in Krasinsky (2006)). The periods of these free oscillations are then further adjusted together with other geophysical parameters during the fitting of the constructed model to the VLBI data. Schmidt et al. (2005) analysed two time series of nutation offsets from 1984.0 to 2004.2 by means of a wavelet technique using the Morlet function. The time series were computed independently using two different software packages: OCCAM (Titov et al., 2004) and CALC/SOLVE developed at Goddard Space Flight Center. From this investigation they obtained a FCN period which varied between −425 to −450 days. Thereafter they applied a more constrained wavelet transform on the nutation data and from the results they concluded that two close-by retrograde oscillations with periods of about −410 and −435 days superimpose each other. Malkin and Miller (2007) investigated the IVS time series of celestial pole offsets and also concluded that two harmonic components with periods of about −410 and −452 solar days

are present. They used three statistical tools: discrete Fourier transform, principal component analysis (singular spectrum analysis) and wavelet analysis, where all the methods provided very similar results. Although results in the afore-mentioned papers show very similar oscillations on two frequencies in the frequency domain, there does not exist any seismological or geophysical Earth model which would confirm these findings or provide any explanation for them yet.
Nevertheless, following the authors mentioned above, I calculated a model for the celestial pole offsets as a superposition of two harmonic waves with a constant amplitude and period (equation (8.29) which results from the equation (8.16)). The values for the two periods I chose from the frequency spectrum obtained by the CLEAN algorithm using the data from 1984.0 to 2011.0, i.e. P1 = −415 solar days and P2 = −451 solar days (see Figure 8.8). Following the equations (8.17) and (8.18) the periods were transformed into the frequencies in terrestrial reference frame, i.e. $\sigma_1 = 1.0024031$ cpsd and $\sigma_2 = 1.0022112$ cpsd, and t is again time given in days since J2000.0,

$$\begin{aligned} dX &= A_{C1}\cos(\sigma_1 t) - A_{S1}\sin(\sigma_1 t) + A_{C2}\cos(\sigma_2 t) - A_{S2}\sin(\sigma_2 t), \\ dY &= A_{S1}\cos(\sigma_1 t) + A_{C1}\sin(\sigma_1 t) + A_{S2}\cos(\sigma_2 t) + A_{C2}\sin(\sigma_2 t). \end{aligned} \tag{8.29}$$

The partial derivatives of the model for celestial pole offsets with respect to a constant amplitude (divided into amplitudes for sine and cosine term) are given in equations (8.24) and (8.25), and the partial derivatives of the time delay with respect to the cosine and sine amplitude are presented in equations (8.27) and (8.28). I solved for these four unknown parameters together with TRF, CRF and ERP in a common global adjustment of VLBI data from 1984.0 to 2011.0. The cosine and sine amplitudes are expressed in the usual way with amplitude A and phase Φ (equations (8.30) and (8.31)) in Table (8.1),

$$A = \sqrt{(A_C^2 + A_S^2)}, \tag{8.30}$$

$$\Phi = \arctan\left(\frac{A_S}{A_C}\right). \tag{8.31}$$

Figure 8.9 shows the estimated model (yellow line) in comparison to the celestial pole offsets w.r.t. the IAU 2006/2000A precession-nutation model. Although the geophysical interpretation

Table 8.1.: Amplitudes belonging to periods of −415 and −451 solar days of the signal in celestial pole offsets estimated from the global adjustment by software VieVS.

P [solar days]	A_C [mas]	A_S [mas]	A [mas]	Φ [deg]
−415	−0.0120 ± 0.0011	0.0386 ± 0.0011	0.0404 ± 0.0011	107.27 ± 1.81
−451	0.0165 ± 0.0011	−0.1264 ± 0.0011	0.1275 ± 0.0011	−82.56 ± 0.49

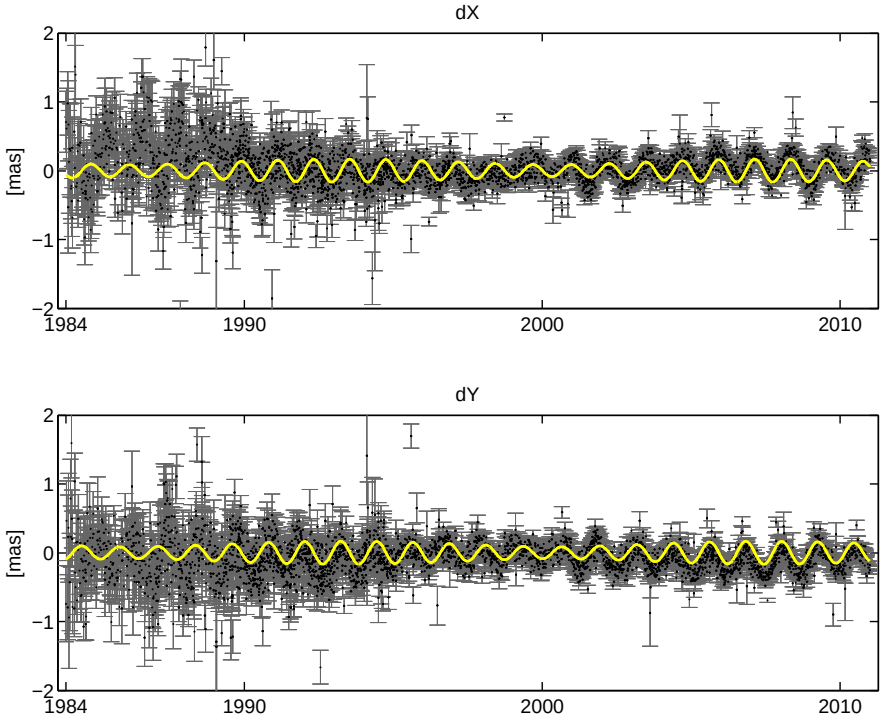

Figure 8.9.: Model with two frequencies for the remaining signal in celestial pole offsets w.r.t. the IAU 2006/2000A precession-nutation model by estimating the amplitudes as global parameters.

of such a model with two retrograde oscillations at periods of about −415 and −451 solar days is questionable, a good agreement can be seen with the residuals to the IAU model (concentrating mainly on data after 1990 where the VLBI data started to be less noisy).

8.3.5. Estimation of a constant FCN period

Earth rotation theory, which is nowadays widely accepted, predicts only one strong oscillation with a stable period in the retrograde band between the periods −400 and −500 days. The non-rigid Earth nutation model of Mathews et al. (2002) is a base for the current IAU 2000A nutation model. It expects a FCN period between −429.93 and −430.48 solar days. The apparent change of the period which is seen in the spectral analysis of celestial pole offsets or even the existence of two oscillations is explained with a variable phase and amplitude.
The time stability of the FCN period has been examined firstly by Roosbeek et al. (1999). They used a transfer function given in Wahr (1979), which expresses the ratio between rigid and non-rigid amplitudes of nutation terms at their frequencies, and which accounts for a resonance effect of the FCN at forced nutations. They determined the amplitudes for five nutation waves

(annual, semi-annual, tri-annual, monthly, and semi-monthly) from VLBI observations (EOP series from GSFC submitted to the IERS in 1998) and then analysed the obtained ratio between the amplitudes in order to estimate the FCN period. This procedure was repeated for thirteen time sub-intervals, where the entire time interval with available VLBI data (1984.0 - 1998.0) was divided with a time step of two years. The determined FCN period from all sub-intervals differs within three days from -431 to -434 sidereal days.

Vondrák et al. (2005) and Vondrák and Ron (2006), parallel to authors mentioned in chapter 8.3.4 started with a direct analysis of celestial pole offsets with the fast Fourier transform. They also found out, that the resulting peak in the frequency spectrum is broad and depends on the time interval of the analysed data. They used the combined IVS solution from 1983.7 - 2004.7 as input data (celestial pole offsets w.r.t. the IAU2000 model of precession-nutation). They divided the data into three different intervals, each seven years long. The spectrum obtained varied for each interval: the amplitude diminished in time and the period grew. For the interval (1983.7 - 1990.7) the peak for the FCN period appeared about -425 days, for the second interval (1990.7 - 1997.7) about -430 days and for the interval (1997.7 - 2004.7) it was about -470 days (Vondrák et al., 2005). They concluded that it is highly improbable, that the FCN period would be so variable because its presence is given by the flattening of the liquid core, which is supposed to be very stable. They followed the proposal of Roosbeek et al. (1999) for an indirect estimation of the FCN period through its resonance effects at the forced nutation terms. They used the transfer function given in Mathews et al. (2002). The non-rigid amplitudes of five selected forced nutations terms (equivalent to those chosen by Roosbeek et al. (1999)) were obtained from the least squares fit to the combined VLBI/GPS solution of celestial pole offsets provided by the Center for Orbit Determination in Europe. The following estimation of the FCN period from the transfer function yielded the value of -430.55 ± 0.11 solar days.

Lambert and Dehant (2007) extended the works of Vondrák et al. (2005) and Vondrák and Ron (2006) by checking the FCN period stability by processing VLBI data sets provided by six different analysis centres (their own data set inclusive), and two combined solutions provided by IVS. They highlighted that each analysis group is using its own strategy for parameterisation, by the use of constraints on reference frames and also for the choice of sessions included in the analysis. They used the same estimation method as Vondrák et al. (2005) and processed the data in two different time spans: the first one from 1984.0 to 2006.0 and the second one from 1990.0 to 2006.0. The results they obtained are summarized in Table (8.2). They concluded that the analysis strategy of VLBI observations has an impact of about half a day on the determination of the FCN period. Considering the time stability (assessed through a 10-years sliding window

Table 8.2.: FCN period estimated from various VLBI series by Lambert and Dehant (2007) using the resonance effect at the forced nutation terms.

Analysis centres	P [solar days] 1984.0 - 2006.0	P [solar days] 1990.0 - 2006.0
GA, Geoscience Australia	-430.13 ± 0.17	-430.56 ± 0.14
BKG, Bundesamt für Kartographie und Geodäsie	-429.84 ± 0.20	-429.50 ± 0.18
GSFC, NASA Goddard Space Flight Center	-430.24 ± 0.07	-430.21 ± 0.10
IVS, midnight epoch	-429.22 ± 0.07	-429.12 ± 0.14
IVS, mid-session epoch	-429.30 ± 0.08	-429.33 ± 0.10
OPAR, Paris Observatory analysis centre	-429.93 ± 0.11	-430.26 ± 0.13
USNO, United States Naval Observatory	-429.89 ± 0.09	-430.16 ± 0.09

displaced by one year), the FCN period is also stable within less than half a day. The averaged value of the FCN period obtained from all data sets is -429.75 ± 0.42 solar days for the time span 1984.0 - 2006.0 and -429.95 ± 0.46 solar days for the time span 1990.0 - 2006.0.
The theory of one constant FCN period and variable phase and amplitude is followed also in the FCN model of Lambert (2007) which was described in chapter 8.3.

8.3.6. Estimation of a constant FCN period from CIP motion

In this section I estimate the FCN period contained in the motion of the CIP in the GCRS as a global parameter in a common adjustment (global solution) of the VLBI sessions. During this analysis a new TRF and a new CRF are estimated as global parameters, whereas the clock parameters, zenith wet delays, tropospheric parameters and ERP are session-wise reduced and estimated from single sessions. The software VieVS was extended with partial derivatives of the measured time delay with respect to the FCN period and the sine and cosine amplitudes as described in chapter 8.3. I compute three solutions with different handlings of FCN amplitudes.

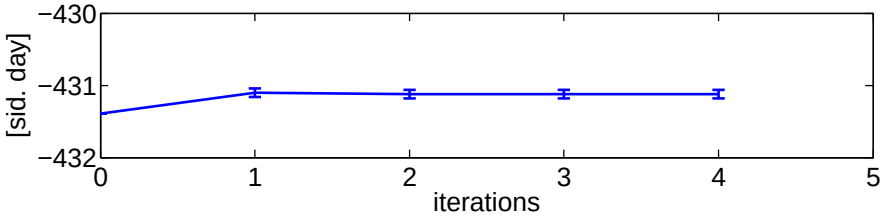

Figure 8.10.: Solution 1 - after four iterations the period converged to -431.12 ± 0.06 sidereal days.

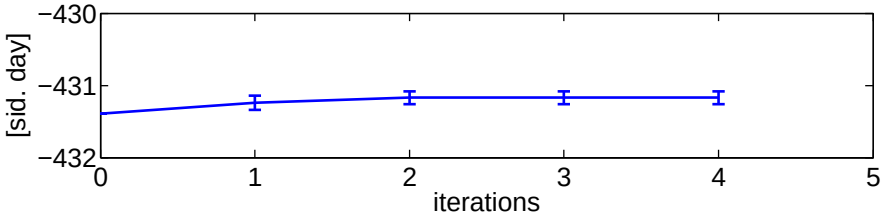

Figure 8.11.: Solution 2 - after four iterations the period converged to -431.17 ± 0.09 sidereal days.

1. In the partial derivatives with respect to the FCN period (equation (8.22)) the values for the amplitudes are taken from FCN model of Lambert (2007). The a priori value of the FCN period in this model is the same as given in the IERS Conventions (Petit and Luzum, 2010), i.e. -431.39 sidereal days.

2. Same as previous solution, but together with the period also the constant corrections to sine and cosine amplitudes of the FCN are estimated.

3. Identical to solution 2, but additional cosine and sine amplitudes of the annual and semi-annual harmonic terms in the nutation are determined.

All solutions are computed in four iteration steps. See Figure 8.10 for solution 1 and Figure 8.11

Table 8.3.: FCN period (P) estimated from motion of the CIP in GCRS within a global solution by the software VieVS.

Solution	P_0 [sid. days]	A_{C0}	A_{S0}	P [sid. days]	A_C [μas]	A_S [μas]
1	-431.39	Lambert (2007)		-431.12 ± 0.06	-	-
2	-431.39	Lambert (2007)		-431.17 ± 0.09	64.6 ± 1.0	34.0 ± 1.2
3	-431.39	Lambert (2007)		-431.18 ± 0.09	64.1 ± 1.0	33.9 ± 1.2

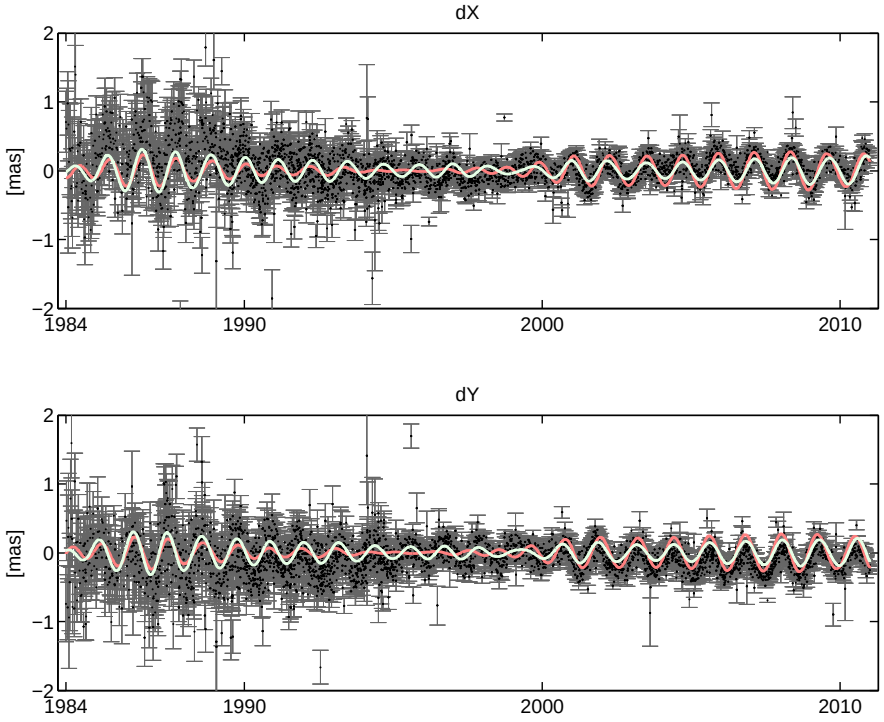

Figure 8.12.: Celestial pole offsets w.r.t. the IAU 2006/2000A precession-nutation model (grey) together with FCN model resulting from solution 1 (period of −431.12 sidereal days and amplitudes taken from Lambert (2007)) plotted in light green, and with model following from solution 2 (period of −431.17 sidereal days and amplitudes from Lambert (2007) corrected for a sine and cosine part of a constant amplitude) in red.

for solution 2. The iteration of solution 3 is not shown here. In solution 1 the period of FCN in the global solution is estimated as -431.12 ± 0.06 sidereal days which equals to -429.94 ± 0.06 solar days. In solution 2 the determined FCN period is equal to -431.17 ± 0.09 sidereal days (-429.99 ± 0.09 solar days) and the amplitude corrections are 64.6 ± 1.0 μas for the cosine term and 34.0 ± 1.2 μas for the sine term. The resulting FCN model from solution 1 is plotted in Figure 8.12 in light green and the one from solution 2 in red. The resulting FCN period obtained from solution 3 (-431.18 ± 0.09 sidereal days, i.e. -430.00 ± 0.09 solar days) is almost identical to the estimates from solution 2. From this the conclusion follows that an additional estimation of corrections to the annual and semi-annual nutation terms does not influence the FCN period determination. The values of the remaining amplitudes of the annual and semi-annual terms (in addition to the values included in the IAU 2000A nutation model) are 15.6 ± 1.0 μas and 21.3 ± 1.0 μas, respectively. These values are estimated from equation (8.30) where the cosine and sine terms equal to -4.6 ± 1.0 μas and 14.9 ± 0.9 μas for annual signal, and -19.3 ± 0.9 μas and -8.9 ± 0.9 μas for semi-annual signal. The FCN model resulting from

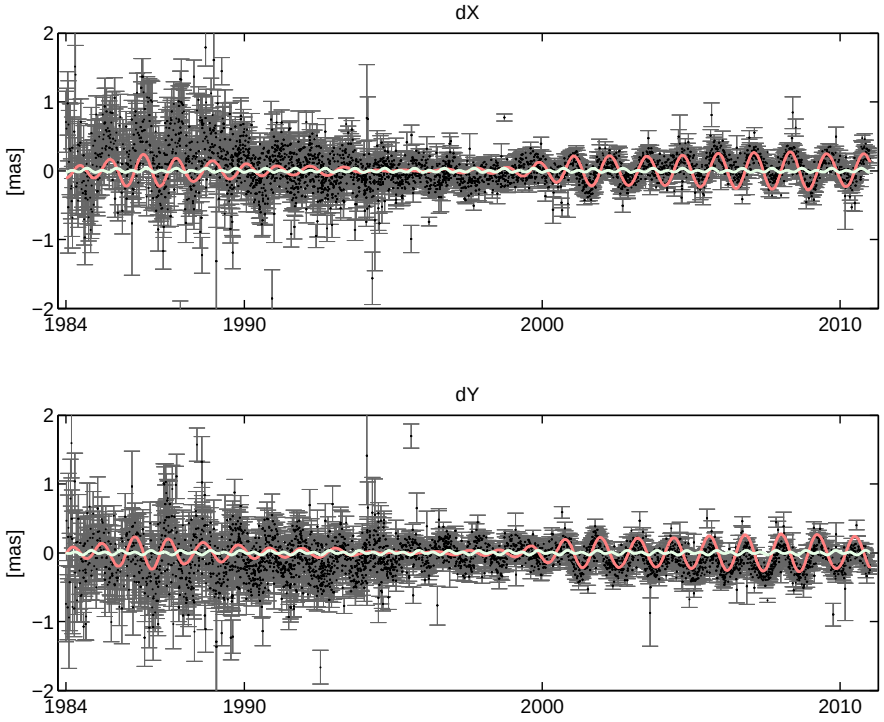

Figure 8.13.: Celestial pole offsets w.r.t. the IAU 2006/2000A precession-nutation model (grey) together with FCN model from solution 3 (red) and the sum of remaining annual and semi-annual signals (light green).

solution 3 (red line) and the sum of annual and semi-annual harmonic terms (light green line) are plotted in Figure 8.13.
The numerical values of the FCN period from all three solutions are summarized in Table 8.3.

8.4. Empirical FCN model with globally estimated varying amplitude

In section 8.3.2 the FCN model created by Lambert (2007) was introduced. The time varying amplitudes (cosine and sine terms) were fitted through the nutation IERS EOP 05 C04 combined series with a sliding window of a length of two years, and displaced by one year. The published tabulated values refer to the middle date, i.e. January 1^{st} of the respective year. The estimates of A_C and A_S designed as fcnnut100701 computed by Lambert (2007) are shown in the second and third column of Table 8.4.
Following this idea of a varying amplitude and phase estimated in a one year step, I determine the A_C and A_S in several global solutions. The data input for each run are VLBI measurements carried out over four years starting in 1984.0. Estimated parameters are constant cosine and

Table 8.4.: Cosine and sine amplitude terms estimated empirically in a one year step by Lambert (2007) (second and third column). Fourth and fifth column show the estimate of A_C and A_S determined with a global solution of VLBI data in this work.

Year	A_C [μas]	A_S [μas]	A_C [μas]	A_S [μas]
	"fcnnut100701" (Lambert, 2007)		this work	
1986.0	-246.6 ± 9.5	-170.2 ± 9.5	-256.6 ± 9.8	-162.6 ± 9.8
1987.0	-281.9 ± 8.6	-159.2 ± 8.6	-261.1 ± 9.1	-104.3 ± 9.1
1988.0	-255.0 ± 8.1	-43.6 ± 8.1	-216.3 ± 9.1	-84.9 ± 9.1
1989.0	-210.5 ± 7.3	-88.6 ± 7.3	-180.5 ± 7.5	-45.6 ± 7.5
1990.0	-187.8 ± 6.4	-57.4 ± 6.4	-166.0 ± 6.1	-6.3 ± 6.1
1991.0	-163.0 ± 5.5	26.3 ± 5.5	-145.3 ± 5.0	19.8 ± 5.0
1992.0	-141.2 ± 4.8	44.6 ± 4.8	-146.3 ± 4.0	26.7 ± 3.9
1993.0	-128.7 ± 4.6	28.6 ± 4.6	-128.7 ± 3.0	23.5 ± 3.0
1994.0	-108.9 ± 3.9	19.5 ± 3.9	-108.3 ± 2.6	19.7 ± 2.6
1995.0	-96.7 ± 3.1	19.7 ± 3.1	-105.2 ± 2.1	17.7 ± 2.2
1996.0	-104.0 ± 2.9	11.9 ± 2.9	-99.4 ± 2.2	18.3 ± 2.2
1997.0	-126.8 ± 2.8	30.4 ± 2.8	-89.9 ± 2.3	16.9 ± 2.3
1998.0	-81.9 ± 2.6	25.0 ± 2.6	-76.0 ± 2.4	2.8 ± 2.4
1999.0	-19.7 ± 2.6	-20.1 ± 2.6	-39.8 ± 2.7	-32.2 ± 2.8
2000.0	10.8 ± 2.7	-76.8 ± 2.7	8.3 ± 2.6	-82.3 ± 2.6
2001.0	65.6 ± 2.5	-137.4 ± 2.5	57.7 ± 2.3	-102.4 ± 2.3
2002.0	78.2 ± 2.3	-127.1 ± 2.3	98.4 ± 2.0	-82.9 ± 2.0
2003.0	108.7 ± 2.1	-42.3 ± 2.1	104.5 ± 1.9	-71.0 ± 1.9
2004.0	117.6 ± 2.2	-1.4 ± 2.2	109.0 ± 1.8	-56.2 ± 1.7
2005.0	115.7 ± 2.9	5.7 ± 2.9	111.9 ± 2.0	-23.0 ± 2.0
2006.0	159.7 ± 4.2	24.2 ± 4.2	121.1 ± 1.8	25.4 ± 1.8
2007.0	154.7 ± 4.5	61.2 ± 4.5	150.3 ± 1.7	75.5 ± 1.7
2008.0	161.1 ± 4.3	98.4 ± 4.3	162.1 ± 1.8	134.0 ± 1.8
2009.0	143.4 ± 4.5	147.0 ± 4.5	145.8 ± 2.2	156.3 ± 2.2

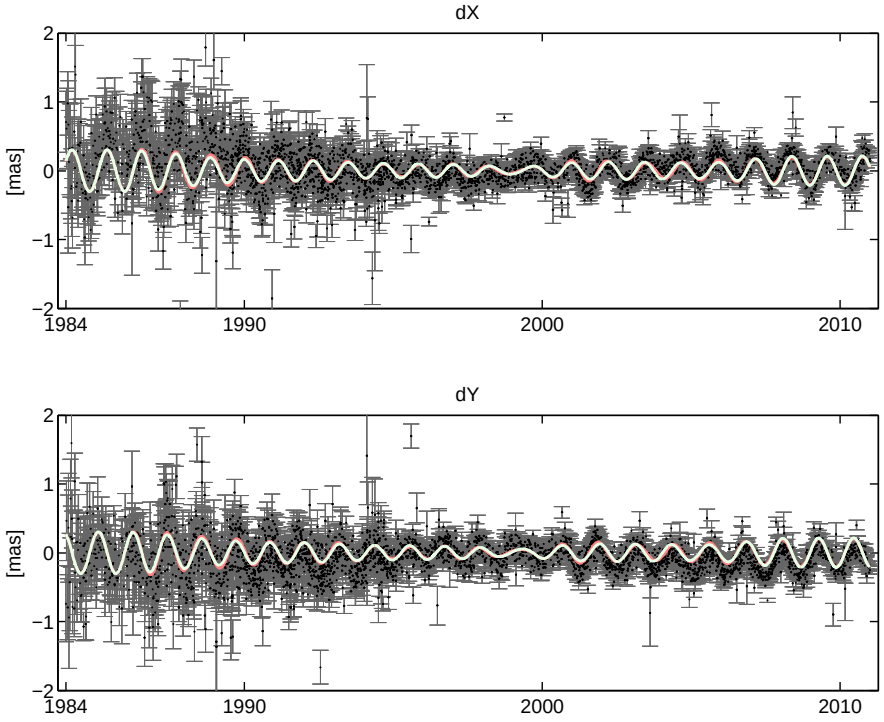

Figure 8.14.: Celestial pole offsets w.r.t. the IAU 2006/2000A precession-nutation model (grey) together with FCN model from Lambert (2007) (red) and a FCN model estimated in this work (light green). Before 1986.0 and after 2009.0 are the models extrapolated.

sine amplitude terms corresponding to the FCN period of −430.00 solar days as estimated in section 8.5. The expressions of the partial derivatives give the equations (8.24) and (8.25) with zero a priori value for the amplitude. Other estimated parameters are the session-wise reduced clock parameters, zenith wet delays, tropospheric gradients, and ERP. The TRF and CRF are fixed to the VieTRF10a and VieCRF10a, respectively. The determined values of the A_C and A_S refer to the middle of the analysed data span. In the first run data from 1984.0 to 1988.0 were involved which gives the middle epoch of 1986.0. The second global solution includes data from 1985.0 till 1989.0, and it continues to the year 2011.0. The estimated values are shown in the fourth and fifth column of Table 8.4. There is a very nice agreement between my solution and the one from Lambert (2007). The determined cosine and sine amplitudes differ maximally by several microarcseconds. The resulting FCN models are plotted in Figure 8.14 where the model computed from my estimates is shown in light green color and the model of Lambert (2007) in red.

8.5. Simultaneous estimation of FCN period from solid Earth tides and nutation

In previous subchapters the presence and effects of the FCN in the solid Earth tides and in the nutation of Earth axis were treated separately. In this section, for a rigorous determination of the FCN period, I created partial derivatives of the nutation matrix $\boldsymbol{dQ}$ and the baseline vector $\boldsymbol{b}$ with respect to the NDFW frequency σ_{NDFW} simultaneously. Partial derivative of the observation equation contains then changes in both parameters (nutation matrix and baseline vector) which are influenced by the presence of free core nutation:

$$\begin{aligned}\frac{\partial \tau}{\partial \sigma_{NDFW}} &= \boldsymbol{k}(t) \cdot \frac{\partial \boldsymbol{dQ}(t)}{\partial \sigma_{NDFW}} \cdot \boldsymbol{Q}(t)_{(IAU)} \cdot \boldsymbol{R}(t) \cdot \boldsymbol{W}(t) \cdot \boldsymbol{b}(t) \\ &+ \boldsymbol{k}(t) \cdot \boldsymbol{Q}(t) \cdot \boldsymbol{R}(t) \cdot \boldsymbol{W}(t) \cdot \frac{\partial \boldsymbol{b}(t)}{\partial \sigma_{NDFW}}.\end{aligned} \tag{8.32}$$

The treatment of the FCN in the CIP motion is parallel to solution 2 in subchapter 8.3.6, i.e. a priori values for the FCN period and amplitudes are taken from the model of Lambert (2007). Constant offsets to the sine and cosine amplitudes over the 27 years of VLBI data are estimated in the global adjustment. Other globally estimated parameters are the terrestrial and celestial reference frames. The determined value of the FCN period is after four iterations -431.18 ± 0.10 sidereal days (-430.00 ± 0.10 solar days). This value lies very close to the result from the "nutation only" solution which is caused by the lower formal error of the estimate resulting from the nutation motion compared to the formal error of the estimate from solid Earth tides.

9. Conclusions

The rapid improvement in space-geodetic techniques and their increasing accuracy allows us nowadays to access parameters of theoretical models describing the changes above, on the surface, as well as inside the Earth. As a fundamental requirement of a reliable estimation of such parameters stable and consistent reference frames are needed. Module Vie_GLOB of the VLBI analysis software VieVS is introduced which is capable of determining a consistent terrestrial and celestial reference frame together with other parameters of interest. Comparison with officially recognized reference frames is provided and the high quality of the provided VieTRF10a and VieCRF10a is presented.

In this work frequency-dependent Love and Shida numbers of degree two are estimated in a global adjustment of VLBI measurements covering the time period of 27 years (1984.0 - 2011.0). The determination is done for twelve diurnal and five long-period tides. The respective differences in the individual displacement amplitudes based on the theoretical and estimated diurnal Love and Shida numbers do not exceed 0.3 mm. The total difference to the theoretical displacement summed over the absolute values of all twelve diurnal waves reaches 1.73 $\pm$ 0.29 mm in vertical direction and 1.15 $\pm$ 0.15 mm in horizontal direction. In the long-period band the differences between the estimated and theoretical Love and Shida numbers exceed larger values. The Love numbers for semi-annual (S_{sa}, 0.6182) and monthly (M_m, 0.6126) tides are estimated as 0.5584 $\pm$ 0.0095 and 0.5896 $\pm$ 0.0080, which correspond to 1.17 $\pm$ 0.19 mm and 0.51 $\pm$ 0.18 mm difference in the vertical amplitudes, respectively. Similarly, lower estimate of the pole tide Love number determined at the Chandler period (i.e. 433 days) (0.5495 $\pm$ 0.0109) than expected from the theory (0.6206) is obtained. The reason for this could be due to deficiencies in the a priori station modelling at longer time periods which then propagate to other parameters.

Free core nutation period is estimated within a global VLBI solution a) from solid Earth tidal displacement as -431.23 $\pm$ 2.44 sidereal days, and b) from the motion of celestial intermediate pole as -431.17 $\pm$ 0.09 sidereal days together with constant sine and cosine amplitude terms. The final value for the FCN period is derived simultaneously from the solid Earth tidal

displacement and from the motion of the CIP. Its estimated value of -431.18 ± 0.10 sidereal days differs slightly from the conventional value -431.39 sidereal days given in Petit and Luzum (2010). Furthermore, an empirical FCN model is introduced. The time varying amplitude and phase are estimated from several global solutions in the form of cosine and sine amplitude parameters in yearly steps. The input data for each run are VLBI measurements divided into groups over four years.

The results of this work confirm the unique characteristics of the VLBI technique. Its measurements to the distant quasi-stellar radio sources from widely spaced antennas on the Earth's surface allow an insight into the Earth's structure. The VLBI technique is perfectly suited for the estimation of Love and Shida numbers which describe the elasticity of the Earth, and also for the estimation of FCN period which depends on the flattening of the Earth's fluid core. In this thesis very precise estimates of the above-mentioned parameters are presented. The advantage is taken from a newly developed analysis software which follows the latest recommendations of the IERS service on a priori observation modelling, and from the long time span of 27 years of all suitable VLBI data which includes the highly accurate measurements from the last years. As a next step, a combination with measurements of Global Navigation Satellite Systems can be carried out, which will assure a better spatial data coverage and will increase the amount of observation data significantly. For the further research the module Vie_GLOB of the VieVS software is a great tool for estimation of other Earth parameters such as e.g. the strength factor for the FCN in the resonance formula for the diurnal Love and Shida numbers or for further investigation of the FICN period.

Bibliography

Andersen, O. B. (2006). The ANDERSEN-2006 global empirical ocean tide model. *http://ebookbrowse.com/andersen-ag06-tide-pdf-d351826746*, : p. 6.

Angermann, D., Drewes, H., Krügel, M., Meisel, B., M., G., Kelm, R., Müller, H., Seemüller, W., and Tesmer, V. (2004). *ITRS Combination Center at DGFI: A Terrestrial Reference Frame Realization 2003*. Verlag der Bayerischen Akademie der Wissenschaften. Reihe B. Heft Nr. 313. ISBN 3-7696-8593-8. p. 141.

Baisch, S. and Bokelmann, G. (1999). Spectral analysis with incomplete time series: an example from seismology. *Computers & Geosciences*, 25: PII: S0095–3004(99)00026–6. pp. 739–750.

Beasley, A. J., Gordon, D., Peck, A. B., Petrov, L., McMillan, D. S., Fomalont, E. B., and Ma, C. (2002). The VLBA Calibrator Survey-VCS1. *Astrophysical Journal Supplement*, 141: pp. 13–21.

Behrend, D. and Baver, K. (2011a). IVS Organization. In Behrend, D. and Baver, K., editors, *International VLBI Service for Geodesy and Astrometry 2010 Annual Report*, NASA/TP-2011-215880. pp. 2-3.

Behrend, D. and Baver, K. (2011b). IVS Terms of Reference. In Behrend, D. and Baver, K., editors, *International VLBI Service for Geodesy and Astrometry 2010 Annual Report*, NASA/TP-2010-215880. pp. 305-314.

Beutler, G. (2005). *Methods of Celestial Mechanics Volume I: Physical, Mathematical, and Numerical Principles*. Springer, ISBN 3-540-40749-9, p. 464.

Böckmann, S., Artz, T., and Nothnagel, A. (2010). VLBI terrestrial reference frame contributions to ITRF2008. *Journal of Geodesy*, 84: doi: 10.1007/s00190–009–0357–7 pp. 201–219.

Böhm, J., Böhm, S., Nilsson, T., Pany, A., Plank, L., Spicakova, H., Teke, K., and Schuh, H.

(2012). The new Vienna VLBI Software VieVS. In Kenyon, S., Pacino, M., and Marti, U., editors, *IAG Symposium 2009, Vol. 136*, ISBN 978-3-642-20337-4. pp. 1007-1012.

Böhm, J., Niell, A., Tregoning, P., and Schuh, H. (2006a). Global Mapping Function (GMF): A new empirical mapping function based on data from numerical weather model data. *Geophysical Research Letters*, 33. L07304: doi: 10.1029/2005GL025546.

Böhm, J., Spicakova, H., Plank, L., Teke, K., Pany, A., Wresnik, J., Englich, S., Nilsson, T., Schuh, H., Hobiger, T., Ichikawa, R., Koyama, Y., Gotoh, T., Kubooka, T., and Otsubo, T. (2009). Plans for the Vienna VLBI Software VieVS. In Bourda, G., Charlot, P., and Collioud, A., editors, *Proceedings of the 19th European VLBI for Geodesy and Astrometry Working Meeting*, pp. 161-164.

Böhm, J., Spicakova, H., Urquhart, L., Steigenberger, P., and Schuh, H. (2011). Impact on A Priori Gradients on VLBI-Derived Terrestrial Reference Frames. In Alef, W., Bernhart, S., and Nothnagel, A., editors, *Proceedings of the 20th European VLBI for Geodesy and Astrometry Working Meeting*, ISSN: 1864-1113. pp. 128-132.

Böhm, J., Werl, B., and Schuh, H. (2006b). Troposphere mapping functions for GPS and very long baseline interferometry from European Centre for Medium-Range Weather Forecasts operational analysis data. *Journal of Geophysical Research*, 11: doi: 10.1029/2005JB003629. pp. 9.

Campbell, J. (2000). From Quasar to Benchmarks: VLBI Links Heaven and Earth. In Vandenberg, N. and Baver, K., editors, *International VLBI Service for Geodesy and Astrometry 2000 General Meeting Proceedings*, NASA/CP-2000-209893. pp. 19-34.

Capitaine, N. and Wallace, P. (2006). Heigh precision methods for locating the celestial intermediate pole and origin. *Astronomy & Astrophysics*, 450: DOI: 10.1051/0004–6361:20054550. pp. 855–872.

Capitaine, N., Wallace, P., and Chapront, J. (2003). Expressions for IAU 2000 precession quantities. *Astronomy & Astrophysics*, 412/2: doi: 10.1051/0004–6361:20031539. pp. 567–586.

Cartwright, D. E. and Tayler, R. J. (1971). New computations of the tide-generating potential. *Geophysical Journal of the Royal Astronomical Society*, 23(1): doi: 10.1111/j.1365–246X. pp. 45–74.

Chen, G. and Herring, T. A. (1997). Effects of atmospheric azimuthal asymmetry on the analysis of space geodetic data. *Journal of Geophysical Research*, 102: pp. 20,489–20,502.

Collilieux, X., Altamimi, Z., Coulot, D., Ray, J., and Sillard, P. (2007). Comparison of very long baseline interferometry, GPS, and satellite laser ranging height residuals from ITRF2005 using spectral and correlation methods. *Journal of Geophysical Research*, 112/B12403: doi: 10.1029/2007JB004933. p. 18.

Dehant, V. and Capitaine, N. (1997). On the precession constant: values and constraints on the dynamical ellipticity; link with Oppolzer terms and tilt-over mode. *Celestial Mechanics and Dynamical Astronomy*, 65: pp. 439–458.

Desai, S. D. (2002). Observing the pole tide with satellite altimetry. *Journal of Geophysical Research*, 107/C11: doi: 10.1029/2001JC001224. p. 13.

Dziewonski, A. M. and Anderson, D. L. (1981). Preliminary reference Earth model. *Physics of the Earth and Planetary Interiors*, 25: pp. 297–356.

Egbert, G. D. and Erofeeva, S. Y. (2002). Efficient inverse modeling of barotropic ocean tides. *Journal of Atmospheric and Oceanic Technology*, 19(2): pp. 183–204.

Eubanks, T. M. (1991). A Consensus Model for Relativistic Effects in Geodetic VLBI. *Proceedings of the USNO workshop on Relativistic Models for Use in Space Geodesy*, : pp. 60–82.

Feissel-Vernier, M., Ma, C., Gontier, A.-M., and Barache, C. (2006). Analysis strategy issues for the maintenance of the ICRF axes. *Astronomy & Astrophysics*, 452: DOI: 10.1051/0004–6361:20054581. pp. 1107–1112.

Fey, A. and Charlot, P. (1997). VLBA observations of radio reference frame sources. II. Astrometric suitability based on observed structure. *The Astrophysical Journal Supplement Series*, 111: pp. 95–142.

Fey, A., Gordon, D., and Jacobs, C. S. (2009). The Second Realization of the International Celestial Reference Frame by Very Long Baseline Interferometry. *IERS Technical Note*, 35: ISBN 3–89888–918–6. p. 204.

Gipson, J. (1998). Ordered Matrix Inversion. *Technical Note, ftp://gemini.gsfc.nasa.gov/pub/misc/jmg/fast_slv.pdf*, : p. 16.

Gipson, J. and Ma, C. (1998). Site displacement due to variation in Earth rotation. *Journal of Geophysical Research*, 103/B4: doi: 0148–0227/98JB–00149. pp. 7337–7350.

Gontier, A.-M. (2009). *Notice for users of the FORTRAN procedure nro_transf.* p. 5.

Haas, R. and Schuh, H. (1997). Determination of Tidal Parameters from VLBI. *Marees Terrestres Bulletin D'Informations*, 127: pp. 9778–9786.

Hampacher, M. and Radouch, V. (2003). *Teorie chyb a vyrovnávací pocet 10.* Vydavatelství CVUT. ISBN 80-01-02833-X. p. 159.

Hase, H., Behrend, D., Ma, C., Petrachenko, W., Schuh, H., and Whitney, A. (2011). The Future Global VLBI2010 Network of IVS. In Alef, W., Bernhart, S., and Nothnagel, A., editors, *Proceedings of the 20th European VLBI for Geodesy and Astrometry Working Meeting*, ISSN: 1864-1113. pp. 78-81.

Herring, T., Davis, J., and Shapiro, I. (1990). Geodesy by Radio Interferometry: The Application of Kalman Filtering to the Analysis of Very Long Baseline Interferometry Data. *Journal of Geophysical Research*, 95/98: pp. 12561–12581.

Herring, T. A. (1992). Modeling atmospheric delays in the analysis of space geodetic data. In DeMunck, J. C. and Spoelstra, T., editors, *Publications on Gedesy. Proceedings of Refraction of Transatmospheric Signals in Geodesy*, pp. 157-164.

Hobson, E. W. (1931). *The Theory of Spherical and Ellipsoidal Harmonics.* Cambridge, University Press, p. 500.

Krasinsky, G. A. (2006). Numerical theory of rotation of the deformable Earth with the two-layer fluid core. Part 1: Mathematical model. *Celestial Mechanics and Dynamical Astronomy*, 96: doi: 10.1007/s10569–006–9038–5. pp. 169–217.

Krasinsky, G. A. and Vasilyev, M. V. (2006). Numerical theory of rotation of the deformable Earth with the two-layer fluid core. Part 2: Fitting to VLBI data. *Celestial Mechanics and Dynamical Astronomy*, 96: doi: 10.1007/s10569–006–9033–x. pp. 219–237.

Krásná, H., Böhm, J., Böhm, S., and Schuh, H. (2012a). Solid earth tide parameters from VLBI measurements and FCN analysis. In Behrend, D. and Baver, K. D., editors, *IVS 2012 General Meeting Proceedings*, NASA/CP-2012-xxxxxx. accepted.

Krásná, H., Böhm, J., Plank, L., Nilsson, T., and Schuh, H. (2012b). Atmospheric effects on VLBI-derived terrestrial and celestial reference frames. In Rizos, C. and Willis, P., editors, *IAG Symposium 2011, Vol. 139*, ISSN 0939-9585. accepted.

Lambert, S. B. (2007). Empirical modeling of the retrograde Free Core Nutation. *Technical Note, ftp://hpiers.obspm.fr/eop-pc/models/fcn/notice.pdf*.

Lambert, S. B. and Dehant, V. (2007). The Earth's core parameters as seen by the VLBI. *Astronomy & Astrophysics*, 469: doi: 10.1051/0004–6361:20077392. pp. 777–781.

Le Provost, C., Genco, M. L., Lyard, F., Vincent, P., and Canceil, P. (1994). Spectroscopy of the world ocean tides from a finite-element hydrodynamic model. *Journal of Geophysical Research*, 99(C12): pp. 24,777–24,797.

Letellier, T. (2004). Etude des ondes de marée sur les plateaux continentaux. *Ph.D. thesis, Université de Toulouse III*, : p. 237.

Love, A. E. H. (1909). The Yielding of the Earth to Disturbing Forces. *Proceedings of the Royal Society of London. Series A, Containing Papers of a Mathematical and Physical Character*, Vol. 82, No. 551: pp. 73–88.

Lyard, F., Lefevre, F., Letellier, T., and Francis, O. (2004). Modelling the global ocean tides: modern insights from FES2004. *Ocean Dynamics*, 56: doi: 10.1007/s10236–006–0086–x. pp. 394–415.

Ma, C. and Feissel, M. (1997). Definition and realization of the International Celestial Reference System by VLBI astrometry of extragalactic objects. *IERS Technical Note*, 23: ISBN p. 282.

MacMillan, D. S. and Ma, C. (1997). Atmospheric gradients and VLBI terrestrial and celestial reference frames. *Geophysical Research Letters*, 24/4: doi: 10.1029/97GL00143 pp. 453–456.

Malkin, Z. and Miller, N. (2007). An analysis of celestial pole offset observations in the free core nutation frequency band. In Böhm, J., Pany, A., and Schuh, H., editors, *Proceedings of 18th EVGA Working Meeting, Vienna, Austria, 12-15 April 2007*, Geowissenschaftliche Mitteilungen. Vol. 79. pp. 93-97.

Mathews, P. M., Buffett, B. A., and Shapiro, I. I. (1995). Love numbers for a rotating spheroidal Earth: New definitions and numerical values. *Geophysical Research Letters*, 22(5): doi: 10.1029/95GL00161. pp. 579–582.

Mathews, P. M., Herring, T. A., and Buffett, B. A. (2002). Modeling of nutation-precession: New nutation series for nonrigid Earth, and insights into the Earth's interior. *Journal of Geophysical Research*, 107(B4): doi: 10.1029/2001JB000390.

McCarthy, D. D. and Petit, G. (2004). *IERS Conventions 2003*. IERS Technical Note No. 32. Verlag des Bundesamts für Kartographie und Geodäsie. Frankfurt am Main, Germany. p. 127.

Melchior, P. (1978). *The tides of the planet Earth*. Pergamon Press. ISBN: 0-08-022047-9 p. 609.

Munk, W. H. and MacDonald, G. J. F. (1960). The rotation of the Earth. *Cambridge Univ. Press. New York*, pages pp. 24–25.

Neidhardt, A., Ettl, M., Rottmann, H., Plötz, C., Mühlbauer, M., Hase, H., Alef, W., Sobarzo, S., Herrera, C., Beaudoin, C., and Himwich, E. (2011). New technical observation strategies with e-control (new name: e-RemoteCtrl). In Alef, W., Bernhart, S., and Nothnagel, A., editors, *Proceedings of the 20th European VLBI for Geodesy and Astrometry Working Meeting*, ISSN: 1864-1113. pp. 26-30.

Niell, A., Whitney, A., Petrachenko, B., Schlütter, W., Vandenberg, N., Hase, H., Koyama, Y., Ma, C., Schuh, H., and Tuccari, G. (2005). VLBI2010: Current and Future Requirements for Geodetic VLBI Systems. *Report of Working Group 3 to the IVS Directing Board*, : p. 21.

Nilsson, T., Böhm, J., Böhm, S., Madzak, M., Nafisi, V., Plank, L., Spicakova, H., Sun, J., Tierno Ros, C., and Schuh, H. (2011). Status and future plans for the Vienna VLBI Software VieVS. In Alef, W., Bernhart, S., and Nothnagel, A., editors, *Proceedings of the 20th European VLBI for Geodesy and Astrometry Working Meeting*, ISSN: 1864-1113. pp. 93-96.

Nilsson, T. and Haas, R. (2010). Impact of atmospheric turbulence on geodetic very long baseline interferometry. *Journal of Geophysical Research*, 115(B03407): doi: 10.1029/2009JB006579. p. 11.

Pany, A., Böhm, J., MacMillan, D., Schuh, H., Nilsson, T., and Wresnik, J. (2011). Monte Carlo simulations of the impact of troposphere, clock and measurement errors on the repeatability of VLBI positions. *Journal of Geodesy*, 85: doi: 10.1007/s00190–010–0415–1. pp 39–50.

Perović, G. (2005). *Least Squares*. University of Belgrade, Faculty of Civil Engineering. ISBN 86-907409-0-2. p. 648.

Petit, G. and Luzum, B. (2010). *IERS Conventions 2010*. IERS Technical Note No. 36. Verlag des Bundesamts für Kartographie und Geodäsie. Frankfurt am Main, Germany. p. 179.

Petrachenko, B., Niell, A., Behrend, D., Corey, B., Böhm, J., Charlot, P., Collioud, A., Gipson, J., Haas, R., Hobiger, T., Koyama, Y., MacMillan, D., Malkin, Z., Nilsson, T., Pany, A., Tuccari, G., Whitney, A., and Wresnik, J. (2009). Design Aspects of the VLBI2010 System. *Progress Report of the IVS VLBI2010 Committee*, : NASA/TM–2009–214180. p. 58.

Petrov, L. (1998). VLBI Measurements of the Crustal Deformation Induced by Polar Motion. *Physics of the Solid Earth*, 34: pp. 228–230.

Petrov, L. and Boy, J.-P. (2004). Study of the atmospheric pressure loading signal in very long baseline interferometry observations. *Journal of Geophysical Research*, 109: doi: 10.1029/2003JB002500.

Petrov, L., Hinderer, J., and Boy, J.-P. (2004). Combined analysis of VLBI and superconducting gravimeter data. *15th Earth tide Symposium in Ottawa on 02-AUG-2004*, page p. 14.

Plag, H.-P. and Pearlman, M. (2009). *GGOS: Meeting the Requirements of a Global Society on a Changing Planet in 2020*. Springer. ISBN 978-3-642-02686-7. p. 332.

Plank, L., Spicakova, H., Böhm, J., Nilsson, T., Pany, A., and Schuh, H. (2013). Systematic errors of a VLBI determined TRF investigated by simulations. In Altamimi, Z. and Collilieux, X., editors, *IAG Symposium REFAG2010, Vol. 138*, ISBN 978-3-642-32997-5. accepted.

Resch, G. (2000). Calibration of Atmospherically Induced Delay Fluctuations due to Water Vapor. In Vandenberg, N. and Baver, K., editors, *International VLBI Service for Geodesy and Astrometry 2000 General Meeting Proceedings*, NASA/CP-2000-209893. pp. 274-279.

Rogister, Y. and Valette, B. (2005). Influence of outer core dynamics on Chandler wobble. In Plag, H., editor, *Forcing of Polar Motion in the Chandler Frequency Band:*

A Contribution to Understanding Interannual Climate Variations, Cahiers du Centre Europeen de Geodynamique et de Seismologie 24. pp. 61-68.

Roosbeek, F., Defraigne, P., Feissel, M., and Dehant, V. (1999). The free core nutation period stays between 431 and 434 sidereal days. *Geophysical Research Letters*, 26/1: doi: 0094–8276/99/1998GL900225. pp. 131–134.

Schlüter, W. (2000). Report of the IVS chair. In Vandenberg, N. and Baver, K., editors, *International VLBI Service for Geodesy and Astrometry 2000 General Meeting Proceedings*, NASA/CP-2000-209893. pp. 11-15.

Schmidt, M., Tesmer, V., and Schuh, H. (2005). Wavelet analysis of vlbi nutation series w.r.t. fcn. *EGU General Assembly, Vienna, Austria, 24-29 April 2005, Geophysical Research Abstracts,*, 7: SRef–ID:1607–7962/gra/EGU05–A–04555.

Schubert, S. D., Pjaendter, J., and Rood, R. (1993). An assimilated data set for earth science applications. *Bulletin of the American Meteorological Society*, 74(12): pp. 2331–2342.

Schuh, H. (1987). Die Radiointerferometrie auf langen Basen zur Bestimmung von Punktverschiebungen und Erdrotationsparametern. *DGK Reihe C, Verlag der Bayerischen Akademie der Wissenschaften*, 328: ISBN: 3–7696–9378–7. p. 124.

Schuh, H. (2000). Geodetic Analysis Overview. In Vandenberg, N. and Baver, K., editors, *International VLBI Service for Geodesy and Astrometry 2000 General Meeting Proceedings*, NASA/CP-2000-209893. pp. 219-229.

Schuh, H. and Behrend, D. (2012). VLBI: A fascinating technique for geodesy and astrometry. *Journal of Geodynamics*, 61: doi: 10.1016/j.jog.2012.07.007. pp. 68–80.

Schuh, H. and Böhm, J. (2013). Very Long Baseline Interferometry for Geodesy and Astrometry. *Science of Geodesy II*, : doi: 10.1007/978–3–642–28000–9–7. pp. 339–376.

Soja, B. (2011). Relativistische Laufzeitverzögerung in der VLBI. *Bachelor thesis, TU Wien*, : p. 34.

Spicakova, H., Böhm, J., Böhm, S., Nilsson, T., Pany, A., Plank, L., Teke, K., and Schuh, H. (2010). Estimation of geodetic and geodynamical parameters with VieVS. In Behrend, D. and Baver, K., editors, *International VLBI Service for Geodesy and Astrometry 2010 General Meeting Proceedings*, NASA/TP-2010-215864. pp. 202-206.

Spicakova, H., Böhm, J., Englich, S., Nilsson, T., Pany, A., Plank, L., Wresnik, J., Teke, K., Schuh, H., Hobiger, T., Ichikawa, R., Koyama, Y., Gotoh, T., Otsubo, T., and Kubooka, T. (2009). The new Vienna VLBI Software VieVS. *Poster PS7-Th32 at IAG Symposium 2009*.

Spicakova, H., Plank, L., Nilsson, T., Böhm, J., and Schuh, H. (2011). Terrestrial reference frame solution with the Vienna VLBI Software VieVS and implication of tropospheric gradient estimation. In Alef, W., Bernhart, S., and Nothnagel, A., editors, *Proceedings of the 20th European VLBI for Geodesy and Astrometry Working Meeting*, ISSN: 1864-1113. pp. 118-122.

Steigenberger, P., Böhm, J., and Tesmer, V. (2009). Comparison of GMF/GPT with VMF1/ECMWF and implications for atmospheric loading. *Journal of Geodesy*, 83: doi: 10.1007/s00190–009–0311–8. pp. 943–951.

Sun, J., Pany, A., Nilsson, T., Böhm, J., and Schuh, H. (2011). Status and future plans for the VieVS scheduling package. In Alef, W., Bernhart, S., and Nothnagel, A., editors, *Proceedings of the 20th European VLBI for Geodesy and Astrometry Working Meeting*, ISSN: 1864-1113. pp. 44-48.

Teke, K., Böhm, J., Spicakova, H., Pany, A., Plank, L., Schuh, H., and Tanir, E. (2009). Piecewise linear offsets for VLBI parameter estimation. In Bourda, G., Charlot, P., and Collioud, A., editors, *Proceedings of the 19th European VLBI for Geodesy and Astrometry Working Meeting*, pp. 63-67.

Tesmer, V., Böhm, J., Heinkelmann, R., and Schuh, H. (2007). Effect of different tropospheric mapping functions on the TRF, CRF and position time-series estimated from VLBI. *Journal of Geodesy*, 81/6-8: doi: 10.1007/s00190–006–0126–9. pp. 409–421.

Tesmer, V., Steigenberger, P., Rothacher, M., Böhm, J., and Meisel, B. (2009). Annual deformation signals from homogeneously reprecessed VLBI and GPS height time series. *Journal of Geodesy*, 83: doi: 10.1007/s00190–009–0316–3. pp. 973–988.

Thomson, W. (1863). On the Rigidity of the Earth. *Philosophical Transactions of the Royal Society of London*, 153: pp. 573–582.

Titov, O., Tesmer, V., and Böhm, J. (2004). OCCAM v.6.0 Software for VLBI Data Analysis. In Vandenberg, N. and Baver, K., editors, *International VLBI Service for Geodesy and Astrometry 2004 General Meeting Proceedings*, NASA/CP-2004-212255.

van Dam, T. (2010). NCEP Derived 6-hourly, global surface displacements at 2.5 x 2.5 degree spacing. *Data set at http://geophy.uni.lu/ncep-loading.html*.

van den Dool, H. M., Saha, S., Schemm, J., and Huang, J. (1997). A temporal interpolation method to obtain hourly atmospheric surface pressure tides in reanalysis 1979-1995. *Journal of Geophysical Research*, 102/D18: 0148–0227/97/97JD–01571. pp. 22.013–22.024.

Vondrák, J. and Ron, C. (2006). Resonant period of free core nutation - its observed changes and excitations. *Acta Geodynamica et Geomaterialia*, 3/3: pp. 53–60.

Vondrák, J., Weber, R., and Ron, C. (2005). Free core nutation: direct observations and resonance effects. *Astronomy & Astrophysics*, 444: doi: 10.1051/0004–6361:20053429. pp. 297–303.

Wahr, J. M. (1979). The tidal motions of a rotating, elliptical, elastic and oceanless Earth. *Ph.D. thesis, University of Colorado Boulder*, : p. 216.

Wahr, J. M. (1981). Body tides on an elliptical, rotating, elastic, and oceanless Earth. *Geophysical Journal of the Royal Astronomical Society*, 64/3: pp. 677–703.

Wahr, J. M. (1985). Deformation induced by polar motion. *Journal of Geophysical Research*, 90(B11): doi: 10.1029/JB090iB11p09363. pp. 9363–9368.

Wahr, J. M. (1995). Earth Tides. *Global Earth Physics, A Handbook of Physical Constants*, : pp. 40–46.

Widmer, R., Masters, G., and Gilbert, F. (1991). Spherically symmetric attenuation within the Earth from normal mode data. *Geophysical Journal International*, 104: pp. 541–553.

Wijaya, D. D., Böhm, J., Spicakova, H., Schindelegger, M., Karbon, M., Salstein, D., and Schuh, H. (2012). Determination of atmospheric pressure loading corrections and a new concept of reference pressure. *Journal of Geodesy*, : In preparation.

List of Figures

2.1 VLBI observation principle. Wavefronts emitted by a quasar from the direction $\boldsymbol{k}$ reach stations No. 1 and No. 2 separated by a baseline $\boldsymbol{b}$. The green line represents the spatial distance which equals the time delay τ multiplied by the velocity of light c. 5

2.2 Schematic flow diagram describing the VLBI data analysis. Based on Schuh (1987). 6

2.3 Deflection of two parallel radio signals near a massive gravitating body. . . . 8

2.4 Symbolic illustration of the transformation of station positions (baseline vector) into GCRS (Step 2) and the following calculation of the time delay in BCRS (Step 4). (Courtesy of Lucia Plank.) 10

2.5 Internal structure of VieVS Version 2.0. Adapted from Spicakova et al. (2009) 12

2.6 One of the graphical user interfaces of VieVS 2.0 controlling the module Vie_GLOB. 13

2.7 Map with the global distribution of IVS components. 15

2.8 Main IVS products with their current accuracies. Based on Schlüter (2000) and Schuh and Böhm (2013). 16

4.1 Maximal vertical crustal deformation that can be caused by these particular phenomena. 28

4.2 Modelled displacement (in local REN system - blue, red, green) at station Wettzell caused by solid Earth tides during August 2008. 29

4.3 Comparison of five ocean tidal models providing ocean loading corrections during one 24-hour VLBI session on September 12, 2005. The upper plot shows the differences at station Kokee Park exceeding 2 mm. On the lower plot the ocean loading corrections for station Wettzell are plotted. 30

4.4 Standard deviations of height time series from three VLBI solutions with different APL corrections: Vienna group (blue), GSFC group (light green) and University of Luxembourg (light pink). The differences are with respect to the solution where no APL corrections were applied. 31

4.5 Baseline length repeatabilities from VLBI solution with applying APL as a priori corrections (black) and from solution without applying APL (light red). The lower plot shows differences in the standard deviation (std) of the baseline length (with minus without APL). The mean std is plotted with the red line. 32

4.6 Standard deviations of the height time series. In the upper figure std from sessions with a pressure difference of more than 10 hPa at one station are plotted. In the lower left and right figures the std are computed from sessions with a pressure difference of more than 20 hPa and 30 hPa respectively. The red lines show the mean std of the height time series. 33

4.7 Models for secular variation of the Earth's mean rotation pole. 35

4.8 Change of the TRF scale caused by disregarding the linear mean pole path model. On the left hand side results arising from R1 networks are plotted and on the right hand side from the R4 networks. The R1 networks (denser and with a large volume) balance the impact on the scale from the mismodelled effect better than R4, where the scale change corresponds to 0.47 mm/yr. . . 36

4.9 Change in the scale of the TRF where the new cubic model, rather than the linear one, was applied. The scale change after 8.5 years exceeds 0.6 mm. . . 36

4.10 Upper plot: ocean pole tide loading in vertical direction at station Wettzell (red) and Kokee Park (blue). In light colour shades the displacement computed with cubic mean pole function is plotted, in dark colour shades the corrections resulting from the linear mean pole approximation. Lower plot: instantaneous rotation pole components (C04 08 time series), x-pole is shown in green and y-pole in dark violet. 37

4.11 Vertical hydrology loading corrections provided by the NASA GSFC VLBI group for station Zelenchukskaya (blue) and Kokee Park (light red). 39

4.12 Fourier spectrum obtained for the vertical hydrology loading corrections at station Zelenchukskaya (blue) and Kokee Park (light red). 39

4.13 Differences between the standard deviations of the height time series (with minus without hydrology loading). 40

4.14 Session-wise station height residuals at Wettzell (upper plot) with applied hydrology loading corrections (red) and without (blue). The lower plot shows the differences between these two solutions (without minus with) and the smoothed values over 50 days which are compared to the modelled values shown in pink. 40

4.15 Differences between the standard deviations of the baseline length (with minus without hydrology loading). 41

5.1 Field of resulting tidal forces 42

5.2 Geometry of the two-body problem needed for the expression of a tidal force produced by the Moon at an Earth-based point O. 43

5.3 Vertical displacement due to degree two (upper plots) and three (lower plots) tides caused by the Moon (left-hand side) and the Sun (right-hand side) on April 14^{th}, 2012 at 12 UT. The thick black lines highlight the equator and the zero meridian. Units of all colour bars are centimetres. 45

5.4 Graphical illustration of second degree spherical harmonics of order zero (zonal, left plot), one (tesseral, middle plot), and two (sectorial, right plot). . 48

5.5 Graphic to Doodson variables (Table 5.3). 49

6.1 Involvement of VLBI antennas in single sessions (1984.0 - 2011.0) included in the global adjustment. 54

6.2 57 VLBI antennas included in the newly determined TRF VieTRF10a. In red the datum stations are plotted (larger circles), and in light blue the remaining stations are shown. 59

6.3 Vertical position differences at epoch 2000.0 between VieTRF10a and VTRF2008. The only differences for stations with a mean coordinate error lower than 0.5 cm are plotted. Red arrows denote the datum stations and blue ones the remaining stations. The bars represent the formal errors. 60

6.4 Horizontal position differences at epoch 2000.0 between VieTRF10a and VTRF2008. Only differences for stations with the mean coordinate error lower than 0.5 cm are plotted. Red arrows denote the datum stations and blue ones the remaining stations. The ellipses display the 95% confidence ellipses. 61

6.5 Station horizontal velocities of VTRF2008 (white arrows in the background) and VieTRF10a (black arrows). 62

6.6 Distribution of sources in the VieCRF10a catalogue. Red circles (larger) denote the datum sources. Remaining sources are plotted in light blue. . . . 63

6.7 Overview of observed sources in each session. 64

6.8 Left-hand side: Distribution of the number of observing sessions per source. Right-hand side: Distribution of the number of observations per sources. Sources with less than three observations were fixed to their a priori coordinates in the analysis. 64

6.9 Session-wise estimated position of a special handling source 2234+282. 65

6.10 Distribution of formal errors of datum sources in declination (upper plot) and right ascension (lower plot). 66

6.11 Histogram of distribution of formal errors of datum sources in declination (left plot) and right ascension (right plot). The formal errors of most of the sources (more than 200) do not exceed 0.1 mas. 66

6.12 Formal errors of declination (blue "+") and right ascension (light red "x"). Sources are divided into six groups according to the right plot in Figure 6.8. Note the different scales on the y-axis of each plot. 67

6.13 Estimates of source positions in VieCRF10a w.r.t. ICRF2. Only corrections for sources with a formal error lower than 200 μas in both coordinates are plotted. 68

6.14 Vertical amplitude of harmonic annual signal at stations which observed in more than 50 sessions. In blue the signal from solution S1 and in light red from solution S2 is plotted. If the arrow points towards north, the maximum annual displacement appears in January and it continues clockwise further. . 73

6.15 Vertical amplitude of harmonic signals from solution S1 at stations which observed in more than 50 sessions. The annual signal is shown in blue and the semi-annual signal in light orange. 74

6.16 Time series of the estimated height corrections at station Wettzell, smoothed over 50 days (light green line). In blue the sum of two harmonic functions with the estimated amplitudes at semi-annual and annual period is plotted. . 75

7.1 Real (upper plot) and imaginary (lower plot) parts of the Love numbers for twelve diurnal tides. In red are the results from this work, in blue the estimates from Haas and Schuh (1997). 80

7.2 Real and imaginary parts of the Shida numbers for twelve diurnal tides. In red the results from this work are plotted, in blue the estimates from Haas and Schuh (1997). 82

7.3 Correlation coefficients between the estimated real and imaginary parts of the Love and Shida numbers of the diurnal tides. 84

7.4 Real and imaginary part of the diurnal Love numbers estimated from the "FES2004 solution" in red and from the "AG06a solution" in light blue. . . . 86

7.5 Real and imaginary part of the diurnal Shida numbers estimated from the "FES2004 solution" in red and from the "AG06a solution" in light blue. . . . 87

7.6 Real and imaginary part of the zonal Love numbers estimated from solution S1 (light blue), S2 (light green), and S3 (red). 92

7.7 Real and imaginary part of the zonal Shida numbers estimated from solution S1 (light blue), S2 (light green), and S3 (red). 92

7.8 Real parts of the five zonal Love and Shida numbers (red colour) estimated together with the Love and Shida number for the pole tide (light blue colour) in solution S5. 96

8.1 Periods of the Earth's five free rotation modes in the terrestrial frame determined by Mathews et al. (2002). The units are solar days. 97

8.2 FCN period estimated from the resonance in the solid Earth tides. After four iterations the FCN period converged to -431.23 ± 2.44 sidereal days. 99

8.3 FICN period estimated from the resonance in the solid Earth tides. After nine iterations the FICN period converged to 502.42 ± 601.06 sidereal days. . 100

8.4 Motion of the CIP in the GCRS modelled by the precession-nutation model IAU2000A. 101

8.5 FCN model of Lambert (2007). The coefficients of the amplitude can be found at http://syrte.obspm.fr/~lambert/fcn/table.txt and are updated regularly. . 103

8.6 Celestial pole offsets w.r.t. the IAU 2006/2000A precession-nutation model estimated with software VieVS. 106

8.7 Fourier spectrum for celestial pole offsets estimated with software VieVS w.r.t. the IAU 2006/2000A precession-nutation model. The spectrum for data from 1984.0 to 2011.0 is in blue and for data from 1990.0 to 2011.0 is in light red. 107

8.8 Frequency spectrum obtained by the CLEAN algorithm for celestial pole offsets estimated with software VieVS w.r.t. the IAU 2006/2000A precession-nutation model. Blue displays the spectrum for data from 1984.0 to 2011.0 and light red shows data from 1990.0 to 2011.0. 107

8.9 Model with two frequencies for the remaining signal in celestial pole offsets w.r.t. the IAU 2006/2000A precession-nutation model by estimating the amplitudes as global parameters. 110

8.10 Solution 1 - after four iterations the period converged to -431.12 ± 0.06 sidereal days. 113

8.11 Solution 2 - after four iterations the period converged to -431.17 ± 0.09 sidereal days. 113

8.12 Celestial pole offsets w.r.t. the IAU 2006/2000A precession-nutation model (grey) together with FCN model resulting from solution 1 (period of -431.12 sidereal days and amplitudes taken from Lambert (2007)) plotted in light green, and with model following from solution 2 (period of -431.17 sidereal days and amplitudes from Lambert (2007) corrected for a sine and cosine part of a constant amplitude) in red. 114

8.13 Celestial pole offsets w.r.t. the IAU 2006/2000A precession-nutation model (grey) together with FCN model from solution 3 (red) and the sum of remaining annual and semi-annual signals (light green). 115

8.14 Celestial pole offsets w.r.t. the IAU 2006/2000A precession-nutation model (grey) together with FCN model from Lambert (2007) (red) and a FCN model estimated in this work (light green). Before 1986.0 and after 2009.0 are the models extrapolated. 117

A.2.1 Atmospheric bulge over equator causes systematic effects in the measured time delay dependent on the azimuth angle. 147

A.2.2 Total session-wise estimated gradients at station Westford. In light grey gradients from solution 2 are plotted, in black from solution 3. Bold lines are smoothed values over 100 days. 149

A.2.3 Difference in station coordinates (height and north component) at station Westford for solution 2 (light grey) and solution 3 (black) w.r.t. solution 1. Bold lines are smoothed values over 100 days. 150

A.2.4 Global map with mean values over 1990.0 - 2011.0 for total tropospheric gradients from solution 2 (light grey) and solution 3 (black). Stations that participated in more than 20 sessions are plotted. 151

A.2.5 Mean values over 1990.0 - 2011.0 for height and north component of stations participating in more than 20 sessions sorted by latitude. Solution 2 (light grey) and solution 3 (black) are plotted w.r.t. solution 1. 152

A.2.6 Differences in stations positions between VieTRF10a (DAO a priori, estimated) minus GS1 (fixed to zero values). The height differences are plotted with coloured triangles (red up-pointing triangles: uplift, blue down-pointing triangles: subsidence). 153

A.2.7 Differences in stations positions between TRF with estimated gradients: VieTRF10a (DAO a priori) minus GS2 (zero gradients a priori). The height differences are plotted with coloured triangles (red up-pointing triangles: uplift, blue down-pointing triangles: subsidence). 154

A.2.8 Difference in declination (upper plot) and right ascension (lower plot) between the VieCRF10a w.r.t. CRF of solution GS1 (red line, black "+") and solution GS2 (blue line, grey "x"). 154

A.2.9 Differences in stations positions between VieTRF10a (VMF1) and the TRF solution with GMF in the sense VMF1 minus GMF. The height differences are plotted with coloured triangles (red up-pointing triangles: uplift, blue down-pointing triangles: subsidence). 156

A.2.10 Difference in declination (upper plot) and right ascension (lower plot) between VieCRF10a (VMF1) minus CRF with GMF. 157

List of Tables

5.1 Geocentric distance R_j and the mass M_j of the Moon, the Sun, Jupiter, and Venus as input parameters for a comparison of second degree tidal potential. 44

5.2 Ratio between the Earth's radius and the geocentric distance to the Moon and the Sun in the second, third, and fourth degree of the tidal potential. . . 44

5.3 Doodson variables and their relation to the fundamental arguments of nutation, i.e. to the Delaunay variables. 49

5.4 Tidal waves selected for this work. The amplitudes are taken from Cartwright and Tayler (1971). 50

6.1 Overview of a priori models and parameterisation options used to analyze VLBI data for estimation of the VieTRF10a and VieCRF10a. 55

6.2 All VLBI antennas in the analysed sessions. 56

6.3 Helmert parameters (weighted) for the transformation between VTRF2008 and VieTRF10a (VieTRF10a minus VTRF2008) computed for three sets of stations. 62

6.4 Rotation parameters (weighted) for the transformation between ICRF2 and VieCRF10a (VieCRF10a minus ICRF2) for three sets of sources. 67

6.5 Description of contributed catalogues for investigations on ICRF2 and of VieCRF10a catalogue. Adapted from Fey et al. (2009). 69

6.6 3 rotation parameters and one bias in declination for the transformation between VieCRF10a and other CRF catalogues, submitted by analysis centres during investigations on ICRF2 catalogue. 70

6.7 Amplitudes and phases of radial displacement at annual and semi-annual periods estimated for stations observing in more than 50 sessions. 72

7.1 Parameters in the resonance formula (Petit and Luzum, 2010). 77

7.2 Parameters $h_f^{(0)}$ and $l_f^{(0)}$ computed from the resonance formula (7.5) for diurnal tidal waves. 78

7.3 Real part of the complex Love number for the diurnal tides computed by the software VieVS from the VLBI data (1984.0 - 2011.0). 80
7.4 Imaginary part of the complex Love number for the diurnal tides computed by the software VieVS from the VLBI data (1984.0 - 2011.0). 81
7.5 Real part of the complex Shida number for the diurnal tides computed by the software VieVS from the VLBI data (1984.0 - 2011.0). 82
7.6 Imaginary part of the complex Shida number for the diurnal tides computed by the software VieVS from the VLBI data (1984.0 - 2011.0). 83
7.7 Diurnal Love numbers estimated with a priori ocean tidal model AG06a compared to the Love numbers obtained by the default solution (a priori ocean tidal model FES2004). 86
7.8 Diurnal Shida numbers estimated with a priori ocean tidal model AG06a compared to the Shida numbers obtained by the default solution (a priori ocean tidal model FES2004). 87
7.9 Frequency and amplitude of six zonal tides for which the Love and Shida numbers were estimated. 88
7.10 Parameters $h_f^{(0)R}$ for the long-period tides estimated from the VLBI data (1984.0 - 2011.0) within three different solutions and those obtained by Petrov et al. (2004). $\Delta\delta R_f^{ip}$ shows the difference between solution 3 and values given in IERS Conventions 2010. 89
7.11 Parameters $h_f^{(0)I}$ for the long-period tides estimated from the VLBI data (1984.0 - 2011.0) within three different solutions. $\Delta\delta R_f^{op}$ shows the difference between solution 3 and values given in IERS Conventions 2010. 89
7.12 Parameters $l_f^{(0)R}$ for the long-period tides estimated from the VLBI data (1984.0 - 2011.0) within three different solutions and those obtained by Petrov et al. (2004). $\Delta\delta T_f^{ip}$ shows the difference between solution 3 and values given in IERS Conventions 2010. 90
7.13 Parameters $l_f^{(0)I}$ for the long-period tides estimated from the VLBI data (1984.0 - 2011.0) within three different solutions. $\Delta\delta T_f^{op}$ shows the difference between solution 3 and values given in IERS Conventions 2010. 90
7.14 Pole tide Love and Shida number at the zonal frequency of Chandler period. 95
7.15 Love and Shida numbers for the five zonal tidal waves estimated in solution S5. 95

8.1 Amplitudes belonging to periods of −415 and −451 solar days of the signal in celestial pole offsets estimated from the global adjustment by software VieVS. 109

8.2 FCN period estimated from various VLBI series by Lambert and Dehant (2007) using the resonance effect at the forced nutation terms. 112

8.3 FCN period (P) estimated from motion of the CIP in GCRS within a global solution by the software VieVS. 113

8.4 Cosine and sine amplitude terms estimated empirically in a one year step by Lambert (2007) (second and third column). Fourth and fifth column show the estimate of A_C and A_S determined with a global solution of VLBI data in this work. 116

A.1.1 VieTRF10a: coordinate and velocity residuals to the a priori catalogue VTRF2008. 143

A.2.1 Overview of three different gradient parameterisation used to a session-wise comparison. 149

A.2.2 Overview of three different gradient parameterisations used for a comparison of TRF and CRF. 153

A.2.3 Helmert parameters for the transformation between different TRF, mean difference and standard deviation of station and source positions. 155

Curriculum vitae

Hana Krásná (née Špičáková)

Personal details

Date of Birth	13 April 1983
Place of Birth	Prague, Czech Republic
Nationality	Czech Republic

Education

since July 2008

Vienna University of Technology, Doctorate programme: Geodesy and Geophysics

Project assistant (since July 2011)

Holder of MONDI Austrian Student Scholarship (July 2008 - June 2011)

March 2007 - June 2008

Vienna University of Technology, Master programme: Geodesy and Geophysics

Graduation degree: Dipl.-Ing. (= M.Sc.)

Holder of MONDI Austrian Student Scholarship

Oct. 2005 - Jan. 2006

semester abroad at Vienna University of Technology

Erasmus programme

Sept. 2002 - June 2008

Czech Technical University in Prague

Diploma programme: Geodesy and Cartography

Area of concentration: Cartography and Remote Sensing

Graduation degree: Ing. (= M.Sc.)

Sept. 1998 - May 2002

secondary school - Johannes Kepler Gymnasium in Prague

A. Appendices

A.1. VieTRF10a - coordinate and velocity residuals

Table A.1.1 gives an overview of coordinate and velocity residuals and their formal errors for 57 stations included in VieTRF10a (discussed in chapter 6.2.1) to the a priori terrestrial reference frame VTRF2008.

Table A.1.1.: VieTRF10a: coordinate and velocity residuals to the a priori catalogue VTRF2008.

VLBI antenna	**coordin. estimates [cm]**			**formal errors [cm]**			m_{xyz} **[cm]**	**veloc. estimates [cm/y]**			**formal errors [cm/y]**			mv_{xyz} **[cm/y]**	**intervals [mjd]**	
	Δx	**Δy**	**Δz**	**mx**	**my**	**mz**		**Δvx**	**Δvy**	**Δvz**	**mvx**	**mvy**	**mvz**		**start**	**end**
ALGOPARK	-0.12	0.04	0.08	0.01	0.02	0.03	0.02	-0.01	-0.02	0.02	0.00	0.01	0.01	0.01	0	99999
BADARY	-2.91	1.88	-1.87	0.22	0.44	0.66	0.47	0.39	-0.24	0.15	0.02	0.05	0.07	0.05	0	99999
BR-VLBA	-0.02	-0.17	0.09	0.02	0.03	0.04	0.03	0.02	-0.00	-0.01	0.00	0.01	0.01	0.01	0	99999
CRIMEA	0.43	0.06	0.39	0.13	0.09	0.15	0.13	0.08	-0.04	-0.02	0.03	0.02	0.04	0.03	0	99999
CTVASTJ	0.62	0.48	-0.02	0.79	1.15	1.39	1.14	-0.11	-0.20	0.13	0.18	0.25	0.31	0.25	0	99999
DSS15	-0.35	0.93	1.32	0.35	0.70	0.83	0.66	-0.05	0.00	0.02	0.01	0.02	0.02	0.02	0	48800
DSS15	-0.32	-0.24	0.28	0.05	0.07	0.07	0.07	-0.05	0.00	0.02	0.01	0.02	0.02	0.02	48800	99999
DSS45	-0.04	-0.04	-0.12	0.10	0.08	0.09	0.09	0.03	0.01	-0.02	0.02	0.01	0.02	0.02	0	99999
DSS65	0.86	-0.36	0.91	0.36	0.16	0.34	0.30	0.07	0.00	0.08	0.05	0.02	0.05	0.04	0	50553
DSS65	0.10	-0.11	0.33	0.13	0.06	0.13	0.11	0.07	0.00	0.08	0.05	0.02	0.05	0.04	50553	99999
FD-VLBA	0.02	0.07	-0.03	0.02	0.04	0.03	0.03	0.02	-0.01	0.02	0.00	0.01	0.01	0.01	0	99999
FORTLEZA	-0.12	-0.11	0.17	0.03	0.03	0.03	0.03	0.02	-0.03	-0.01	0.01	0.01	0.00	0.01	0	99999
GGAO7108	-0.31	1.22	-1.54	0.18	0.50	0.41	0.39	-0.06	0.26	-0.32	0.03	0.10	0.08	0.08	0	52640
GGAO7108	1.02	-2.87	2.93	0.52	1.54	1.31	1.21	-0.06	0.26	-0.32	0.03	0.10	0.08	0.08	52640	99999
GILCREEK	-0.15	0.02	0.48	0.01	0.02	0.03	0.02	-0.03	0.02	0.02	0.00	0.00	0.00	0.00	0	52581
GILCREEK	0.06	0.07	0.65	0.05	0.04	0.10	0.07	-0.06	-0.02	-0.04	0.01	0.01	0.02	0.01	52581	54100
HARTRAO	0.01	-0.08	-0.04	0.05	0.04	0.03	0.04	0.04	-0.02	-0.05	0.01	0.01	0.00	0.01	0	99999
HATCREEK	1.55	3.65	-4.11	0.95	1.33	1.33	1.21	0.12	0.33	-0.39	0.08	0.11	0.11	0.10	0	99999
HAYSTACK	-1.05	2.50	-1.70	0.41	0.80	0.93	0.75	-0.12	0.28	-0.19	0.04	0.08	0.09	0.07	0	99999

Continued on next page...

Table A.1.1 – Continued

VLBI antenna	**coordin. estimates [cm]**			**formal errors [cm]**			**[cm]**	**veloc. estimates [cm/y]**			**formal errors [cm/y]**			**[cm/y]**	**intervals [mjd]**	
	Δx	**Δy**	**Δz**	**mx**	**my**	**mz**	m_{xyz}	**Δvx**	**Δvy**	**Δvz**	**mvx**	**mvy**	**mvz**	mv_{xyz}	**start**	**end**
HN-VLBA	0.02	-0.10	-0.05	0.02	0.05	0.05	0.04	0.01	0.02	-0.02	0.00	0.01	0.01	0.01	0	99999
HOBART26	-0.44	0.23	-0.35	0.05	0.04	0.05	0.05	0.04	0.00	0.00	0.01	0.01	0.01	0.01	0	99999
HRAS 085	-1.11	-1.75	-0.79	0.21	0.67	0.49	0.49	-0.10	-0.18	-0.10	0.02	0.06	0.04	0.04	0	99999
KASHIM34	-0.10	-0.12	-0.06	0.06	0.05	0.06	0.06	-0.09	0.01	0.06	0.01	0.01	0.01	0.01	0	99999
KASHIMA	-0.48	-0.03	0.10	0.07	0.06	0.07	0.06	-0.09	0.01	0.06	0.01	0.01	0.01	0.01	0	55631
KAUAI	0.38	0.60	-0.14	0.28	0.16	0.24	0.23	0.04	0.09	-0.02	0.03	0.02	0.03	0.03	0	99999
KOKEE	-0.03	0.03	0.07	0.02	0.02	0.02	0.02	0.01	0.02	-0.01	0.00	0.00	0.00	0.00	0	99999
KP-VLBA	0.04	0.01	-0.04	0.02	0.04	0.03	0.03	0.01	-0.01	0.01	0.00	0.01	0.01	0.01	0	99999
KWAJAL26	1.05	-3.36	2.02	6.28	1.80	2.44	4.03	0.06	-0.13	0.20	0.46	0.13	0.18	0.29	0	99999
LA-VLBA	0.07	-0.07	0.01	0.02	0.04	0.03	0.03	0.02	-0.01	0.00	0.00	0.01	0.01	0.01	0	99999
MATERA	0.14	-0.09	0.04	0.03	0.02	0.03	0.02	-0.01	-0.03	-0.03	0.00	0.00	0.00	0.00	0	99999
MEDICINA	0.12	-0.05	-0.03	0.11	0.05	0.12	0.10	0.03	-0.01	0.01	0.01	0.00	0.01	0.01	0	50265
MEDICINA	0.02	-0.12	-0.14	0.04	0.02	0.04	0.04	0.03	-0.01	0.01	0.01	0.00	0.01	0.01	50265	99999
MIAMI20	-0.19	1.17	-0.17	0.09	0.25	0.14	0.17	0.02	0.11	-0.06	0.01	0.03	0.02	0.02	0	99999
MK-VLBA	0.20	0.13	0.04	0.05	0.04	0.04	0.04	0.00	-0.02	0.01	0.01	0.01	0.01	0.01	0	99999
MOJAVE12	-0.14	0.51	-0.47	0.14	0.22	0.25	0.21	-0.01	0.06	-0.07	0.01	0.02	0.03	0.02	0	48800
MOJAVE12	-0.30	-0.07	-0.17	0.17	0.30	0.30	0.27	-0.01	0.06	-0.07	0.01	0.02	0.03	0.02	48800	99999
NL-VLBA	0.02	-0.12	-0.02	0.02	0.04	0.04	0.03	0.02	-0.01	0.01	0.00	0.01	0.01	0.01	0	99999
NOTO	0.02	-0.01	0.11	0.09	0.04	0.08	0.08	0.03	-0.02	-0.00	0.02	0.01	0.02	0.02	0	99999

Continued on next page...

Table A.1.1 – Continued

VLBI antenna	**coordin. estimates [cm]**			**formal errors [cm]**			**[cm]**	**veloc. estimates [cm/y]**			**formal errors [cm/y]**			**[cm/y]**	**intervals [mjd]**	
	Δx	**Δy**	**Δz**	**mx**	**my**	**mz**	m_{xyz}	**Δvx**	**Δvy**	**Δvz**	**mvx**	**mvy**	**mvz**	mv_{xyz}	**start**	**end**
NRAO20	-0.15	-0.30	0.37	0.03	0.05	0.05	0.04	-0.03	-0.07	0.06	0.01	0.02	0.02	0.01	0	99999
NRAO85 3	0.01	-0.17	0.05	0.06	0.15	0.12	0.12	-0.01	-0.01	0.02	0.01	0.02	0.02	0.02	0	99999
NYALES20	0.11	-0.02	0.28	0.01	0.02	0.03	0.02	-0.01	0.01	-0.05	0.00	0.00	0.00	0.00	0	99999
OHIGGINS	-0.23	-0.04	0.21	0.09	0.11	0.19	0.14	-0.00	0.01	-0.03	0.01	0.02	0.03	0.02	0	99999
ONSALA60	0.03	-0.02	0.09	0.02	0.02	0.03	0.02	0.01	-0.01	-0.01	0.00	0.00	0.00	0.00	0	99999
OV-VLBA	0.20	0.15	-0.09	0.03	0.04	0.04	0.04	0.04	0.02	-0.02	0.01	0.01	0.01	0.01	0	99999
OVRO 130	2.21	5.70	-2.27	1.58	3.01	2.85	2.56	0.12	0.35	-0.12	0.12	0.23	0.22	0.19	0	99999
PARKES	1.09	-1.94	-0.02	3.78	2.37	2.84	3.05	-0.17	0.31	-0.09	0.49	0.31	0.37	0.39	0	99999
PIETOWN	0.12	-0.21	0.41	0.02	0.04	0.03	0.03	0.02	-0.01	0.01	0.00	0.01	0.01	0.01	0	99999
RICHMOND	0.10	1.21	-0.52	0.11	0.27	0.17	0.19	0.02	0.11	-0.06	0.01	0.03	0.02	0.02	0	99999
SANTIA12	0.07	-0.51	-0.15	0.33	0.58	0.45	0.46	0.01	-0.04	-0.08	0.06	0.11	0.09	0.09	0	99999
SC-VLBA	0.13	-0.30	0.15	0.03	0.07	0.05	0.05	0.02	-0.07	0.05	0.01	0.01	0.01	0.01	0	99999
SESHAN25	0.40	-0.20	-0.25	0.04	0.05	0.04	0.04	-0.01	0.07	0.03	0.01	0.01	0.01	0.01	0	99999
SVETLOE	0.24	-0.03	0.48	0.06	0.04	0.11	0.07	-0.02	-0.01	-0.07	0.01	0.01	0.01	0.01	0	99999
SYOWA	-0.71	-0.07	0.64	0.34	0.31	0.62	0.45	0.21	0.03	-0.27	0.05	0.04	0.09	0.06	0	99999
TIGOCONC	-0.73	0.37	0.75	0.08	0.16	0.13	0.13	0.11	-0.10	-0.08	0.01	0.02	0.02	0.02	0	55253
TIGOCONC	-130.36	-13.14	-30.30	3.39	7.19	5.86	5.70	-12.93	-3.88	0.27	0.32	0.68	0.55	0.54	55253	55604
TIGOWTZL	-0.73	-0.19	-0.53	0.31	0.13	0.39	0.30	-0.01	-0.02	-0.02	0.00	0.00	0.00	0.00	0	99999
TSUKUB32	-0.03	-0.02	-0.36	0.15	0.12	0.15	0.14	-0.09	-0.09	-0.03	0.00	0.00	0.01	0.01	0	51299

Continued on next page...

Table A.1.1 – Continued

VLBI antenna	**coordin. estimates [cm]**			**formal errors [cm]**			**[cm]**	**veloc. estimates [cm/y]**			**formal errors [cm/y]**			**[cm/y]**	**intervals [mjd]**	
	Δx	**Δy**	**Δz**	**mx**	**my**	**mz**	m_{xyz}	**Δvx**	**Δvy**	**Δvz**	**mvx**	**mvy**	**mvz**	mv_{xyz}	**start**	**end**
TSUKUB32	0.64	0.53	-0.08	0.04	0.03	0.04	0.04	-0.09	-0.09	-0.03	0.00	0.00	0.01	0.01	51299	55631
URUMQI	0.26	0.01	-0.63	0.06	0.11	0.12	0.10	-0.03	-0.05	0.14	0.01	0.02	0.02	0.02	0	99999
VNDNBERG	-0.33	-0.74	0.69	0.80	1.12	1.01	0.98	-0.02	-0.04	0.02	0.07	0.09	0.08	0.08	0	99999
WESTFORD	-0.05	-0.08	0.10	0.01	0.02	0.02	0.02	-0.02	0.00	-0.00	0.00	0.00	0.00	0.00	0	99999
WETTZELL	0.14	-0.11	0.12	0.01	0.02	0.02	0.02	-0.01	-0.02	-0.02	0.00	0.00	0.00	0.00	0	99999
YEBES	-0.14	-0.27	0.10	0.32	0.09	0.26	0.24	0.43	-0.03	0.34	0.14	0.04	0.11	0.11	0	99999
YLOW7296	-0.07	0.09	0.01	0.04	0.06	0.10	0.07	-0.01	0.04	-0.07	0.01	0.01	0.02	0.02	0	99999
ZELENCHK	3.51	2.09	1.44	0.24	0.21	0.33	0.26	-0.51	-0.33	-0.23	0.03	0.03	0.05	0.04	0	54282
ZELENCHK	4.40	2.52	1.43	0.32	0.28	0.43	0.35	-0.51	-0.33	-0.23	0.03	0.03	0.05	0.04	54282	99999

A.2. Tropospheric effects on TRF and CRF

The troposphere is the lowest part of the atmosphere which reaches several kilometres above the Earth's surface where most of the weather takes place. The effect of the troposphere (especially the wet component) on the path of the microwave VLBI signal was recognized as the most limiting factor of a precise estimation of TRF and CRF (Pany et al., 2011). Therefore investigations on the handling of tropospheric gradients on the estimated reference frames are shown here, together with a comparison of two different mapping functions. In the computation of VieTRF10a and VieCRF10a the latest recommendations on models used in the data analysis were followed. The tropospheric delays were modelled with Vienna Mapping Functions (VMF1, (Böhm et al., 2006b)) and the horizontal asymmetry was accounted for with Data Assimilation Office (DAO) model (MacMillan and Ma, 1997). A summary of these findings was published by Krásná et al. (2012b).

A.2.1. Impact of tropospheric gradient estimation

The extension of the atmosphere above the equator is larger than in the polar regions (see Figure A.2.1). This atmospheric bulge is responsible for a systematic effect in the measured time delay mainly in a north-south direction (MacMillan and Ma, 1997). The path of the radio wave through the atmosphere is then larger when an antenna in the northern hemisphere observes in a southerly direction than if it observed in a northernly direction. If the azimuthal asymmetric part of the tropospheric delays was neglected, systematic effects would appear in the terrestrial and the celestial reference frames. Investigations of an optimum parameterisation for the gradient estimation in the VLBI analysis are presented here together with the effect on station and source coordinates if this phenomenon was totally

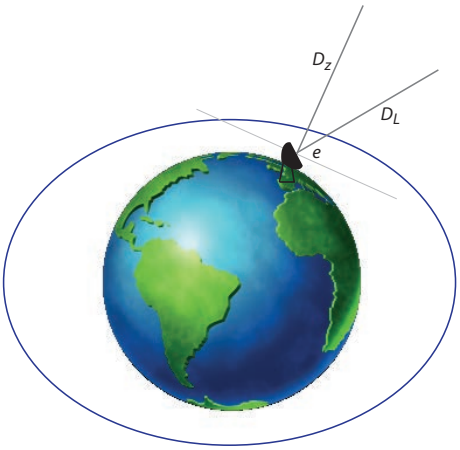

Figure A.2.1.: Atmospheric bulge over equator causes systematic effects in the measured time delay dependent on the azimuth angle.

omitted.

Equation (A.2.1) shows the basic formula of the neutral atmospheric delay recommended by the IERS Conventions 2010. The line-of-sight delay (D_L) is divided into a) a symmetrical part described by elevation-dependent hydrostatic and wet mapping functions ($m_{h,w}(e)$) and the corresponding delays in zenith direction ($D^z_{h,w}$) and b) an azimuth-dependent part described by a gradient vector in north (G_N) and east (G_E) directions, and mapped using the azimuth angle (a) and the gradient mapping function (m_g) into the direction toward the source,

$$\triangle D(a,e) = \triangle D^z_h m_h(e) + \triangle D^z_w m_w(e) + m_g(e) \times [G_N \cdot \cos(a) + G_E \cdot \sin(a)]. \tag{A.2.1}$$

In the VieVS software the formulation of the gradient mapping function suggested by Chen and Herring (1997) is used (equation (A.2.2)). For parameter C the recommended value of 0.0032 (Herring, 1992) is taken, which holds for mapping of the a priori gradients as well as for their estimation (Böhm et al., 2011):

$$m_g(e) = \frac{1}{\tan(e)\sin(e) + C}. \tag{A.2.2}$$

Time series

To test the assumption that tropospheric asymmetry causes a systematic effect on the estimated station coordinates I run three test solutions (Table A.2.1) where I concentrate on the station coordinate time series and the session-wise estimated horizontal gradients on particular stations. Due to the fact that it is the session-wise analysis of the VLBI measurements, the source positions have to be fixed to their catalogue values.

1. In the first solution the asymmetric part is fixed to zero and the tropospheric gradients in the VLBI analysis are omitted.

2. The asymmetric part is a priori set to zero, and the components G_N and G_E of the horizontal gradient vector are estimated in the least squares analysis with relative constraints (0.5 mm after 6 hours) to stabilize the NEQ.

3. The parameterisation is identical to solution 2 with additional absolute constraints (0.5 mm) applied on G_N and G_E.

As an illustrative example the station Westford (Massachusetts, USA) is chosen. In Figure A.2.2 session-wise estimated gradients at station Westford from 1984.0 to 2011.0 are plotted. In light

Table A.2.1.: Overview of three different gradient parameterisation used to a session-wise comparison.

	estimation of gradients	relative constraints	absolute constraints
session-wise solution 1	no	-	-
session-wise solution 2	yes, 6-h offsets	0.5 mm	no
session-wise solution 3	yes, 6-h offsets	0.5 mm	0.5 mm

grey the estimated total gradients from solution 2 are shown and in black the estimates from solution 3. It can be seen, that before 1990 the determined gradients without applying absolute constraints in the least squares analysis are unreliably large. This is most probably due to the poor network geometry in the early VLBI years and the limited number of observations especially to the sources in the southern hemisphere. After 1990 the estimated values for the north gradients are stable and reach systematically negative values, which reflects the atmospheric bulge above the equator since Westford is a station in the northern hemisphere. The corresponding estimates of station positions (height and north component) at station Westford

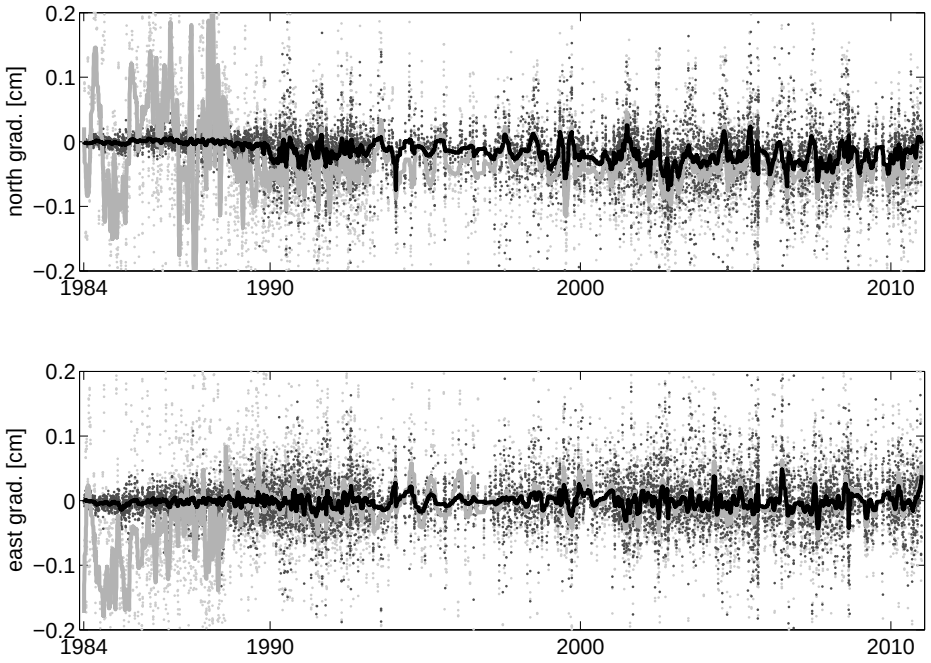

Figure A.2.2.: Total session-wise estimated gradients at station Westford. In light grey gradients from solution 2 are plotted, in black from solution 3. Bold lines are smoothed values over 100 days.

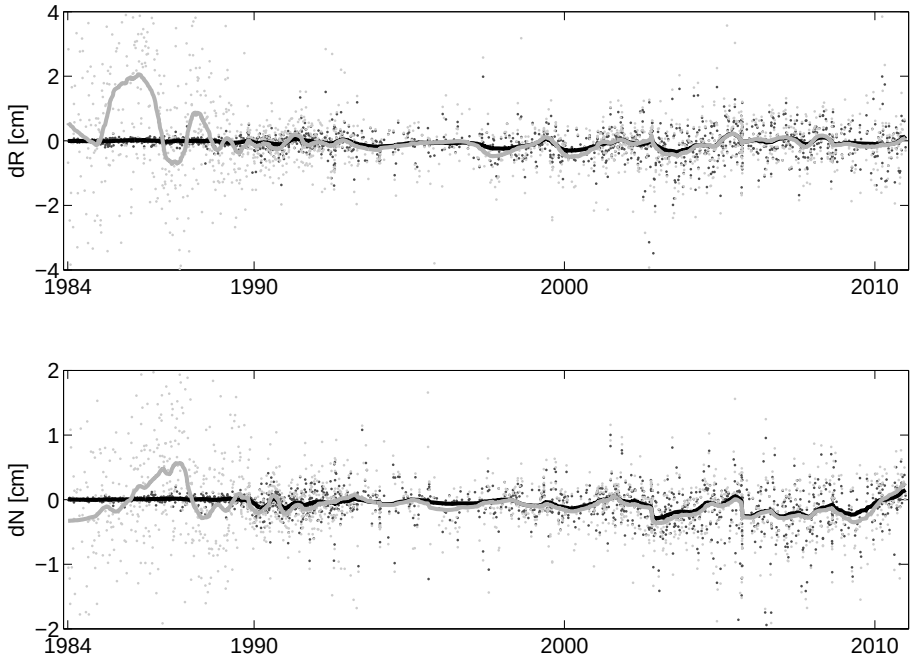

Figure A.2.3.: Difference in station coordinates (height and north component) at station Westford for solution 2 (light grey) and solution 3 (black) w.r.t. solution 1. Bold lines are smoothed values over 100 days.

for solution 2 (light grey) and solution 3 (black) with respect to station positions estimated in solution 1 are shown in Figure A.2.3. The unstable gradient determination in solution 2 in the early years also shows up in the station estimates and can reach a few centimetres. Since 1990 there is a good agreement between the station coordinates if gradients are estimated with or without absolute constraints. The difference to solution 1 (negligence of the tropospheric asymmetry) reaches several millimetres.

For all stations participating in more than 20 sessions during the years 1990.0 - 2011.0 mean values of the session-wise estimated total gradients are calculated. In Figure A.2.4 in the light grey colour the mean gradients from solution 2 are plotted and the gradients from solution 3 as black arrows. At all stations, the north-south component of the tropospheric gradient vectors points towards the equator. The unconstrained gradients from solution 2 are larger at all sites in comparison with solution 3. The largest grey arrows representing the estimated unconstrained gradients appear at stations which observed only in the 90ies, such as 12-m at Santiago (Chile) and 85-3 NRAO Green Bank (West Virginia, USA), or at stations like CTVA 3.6-m at St. Johns (Canada) and Urumqi (China) which show high formal error of their position estimates (see the estimation of VieTRF10a in section 6.2 and Table A.1.1 in appendix A.1) caused probably by

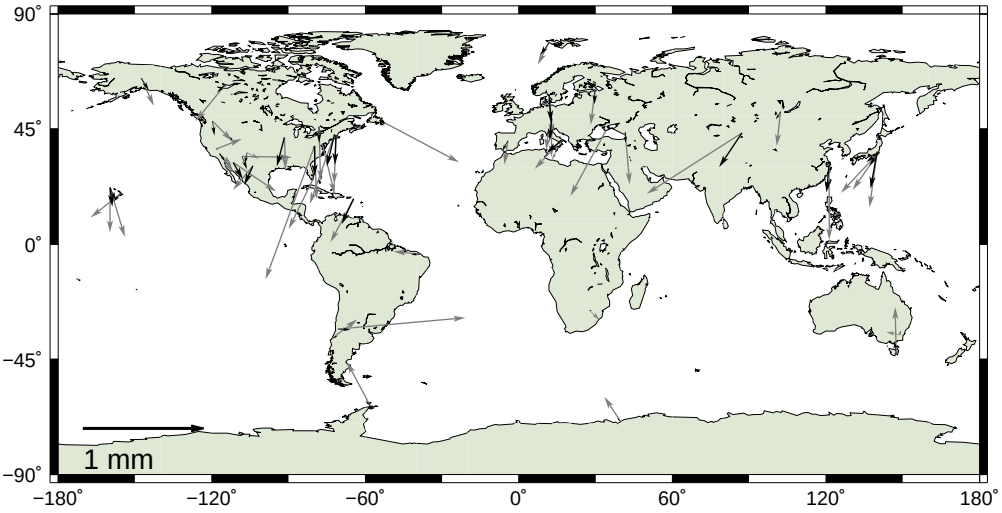

Figure A.2.4.: Global map with mean values over 1990.0 - 2011.0 for total tropospheric gradients from solution 2 (light grey) and solution 3 (black). Stations that participated in more than 20 sessions are plotted.

the small number of observations.

In Figure A.2.5 the mean values of the session-wise estimated station heights and north components for stations participated in more than 20 sessions are plotted. The stations are sorted on the x-axis by latitude. The estimated positions are plotted with respect to the estimates from solution 1. The mean difference in the north component for stations in the southern hemisphere is 2.8 mm between solution 2 and solution 1, and 1.4 mm between solution 3 and solution 1. In the northern hemisphere the mean difference in the north component with respect to solution 1 is -0.6 mm for solution 2, and -0.4 mm for solution 3. In other words if tropospheric asymmetry was ignored, stations would be shifted towards the poles with respect to their real positions. Results of this investigation have been published in Spicakova et al. (2011).

Global reference frames

For the computation of reference frame VieTRF10a a priori gradient model computed by MacMillan and Ma (1997) was used (see Table 6.1) as recommended in Böhm et al. (2011). In the least squares adjustment the residual gradients were estimated with applied relative constraints of

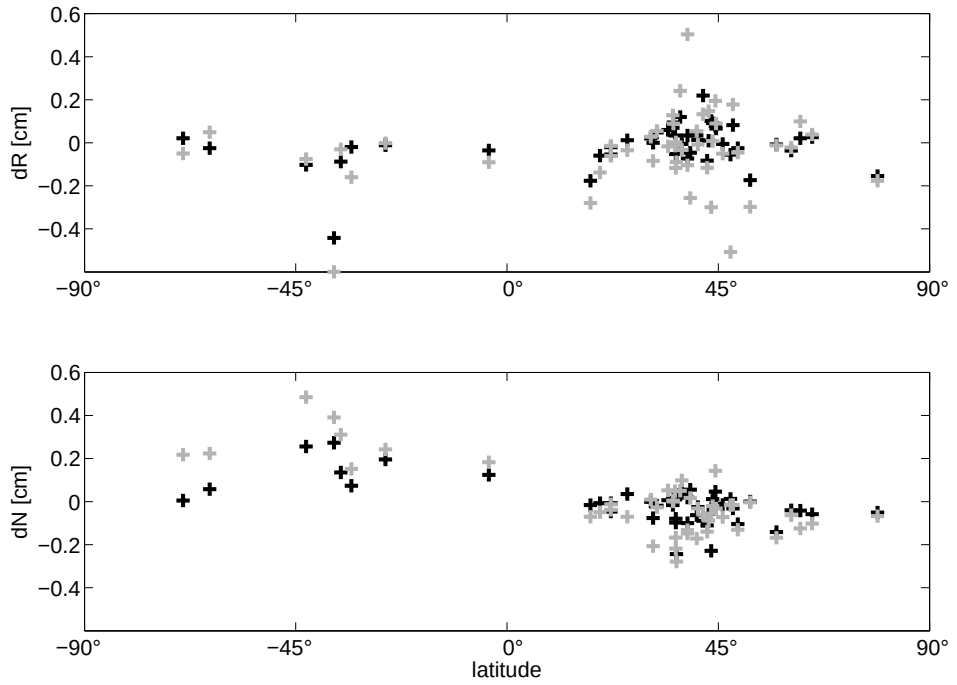

Figure A.2.5.: Mean values over 1990.0 - 2011.0 for height and north component of stations participating in more than 20 sessions sorted by latitude. Solution 2 (light grey) and solution 3 (black) are plotted w.r.t. solution 1.

0.5 mm after 6 hours and absolute constraints of 1 mm. In this model the mean gradients for all VLBI sites are derived from profiles from 1990 till 1995 of the Data Assimilation Office (DAO; (Schubert et al., 1993)) at the NASA Goddard Space Flight Center by vertical integration over horizontal gradients of refractivity. To investigate the influence of tropospheric gradient handling on the globally estimated reference frames (terrestrial and celestial) two further reference frame solutions are computed. The parameterisation of the first one (GS1) is identical to the solution 1 from the previous section, i.e. gradients are fixed in the analysis to zero. The second solution (GS2) is computed without applying a gradient model a priori but the total gradients are estimated in the least squares adjustment with identical constraints as in VieTRF10a. An overview is given in Table A.2.2.

The changes in station position estimates between VieTRF10a w.r.t. GS1 are plotted in Figure A.2.6. It is obvious that the differences in the north component are largest at stations near the South Pole, and these are monotonically decreasing over the equator to the north latitudes. At around 45°N a switch in the direction occurs. The change in the height component between VieTRF10a w.r.t. GS1 also exhibits a variation with latitude. A positive difference in height is observed at stations in the southern hemisphere and a negative difference in the northern

Table A.2.2.: Overview of three different gradient parameterisations used for a comparison of TRF and CRF.

	a priori model	estimation of gradients	relative constraints	absolute constraints
global solution 1 (GS1)	no	no	-	-
global solution 2 (GS2)	no	yes, 6-h offsets	0.5 mm	0.5 mm
global solution 3 (VieTRF10a)	DAO	yes, 6-h offsets	0.5 mm	0.5 mm

hemisphere with a mean value of −3.7 mm. Similar behaviour in the station position differences can be observed between VieTRF10a w.r.t. GS2 (Figure A.2.7) but at a smaller scale. The scale of horizontal differences is of one order magnitude lower than between VieTRF10a and GS1 and the vertical scale bar has the limits eight times lower.

Seven Helmert parameter transformations between VieTRF10a and the two tested TRF (GS1 and GS2) are computed and the parameters are summarized in the upper part of Table A.2.3 (first and second column). Transformation parameters w.r.t. GS1 show that the existence of tropospheric gradients influences the estimation of terrestrial reference frames at millimetre level and causes large uncertainties of the transformation parameters. If the tropospheric gradients

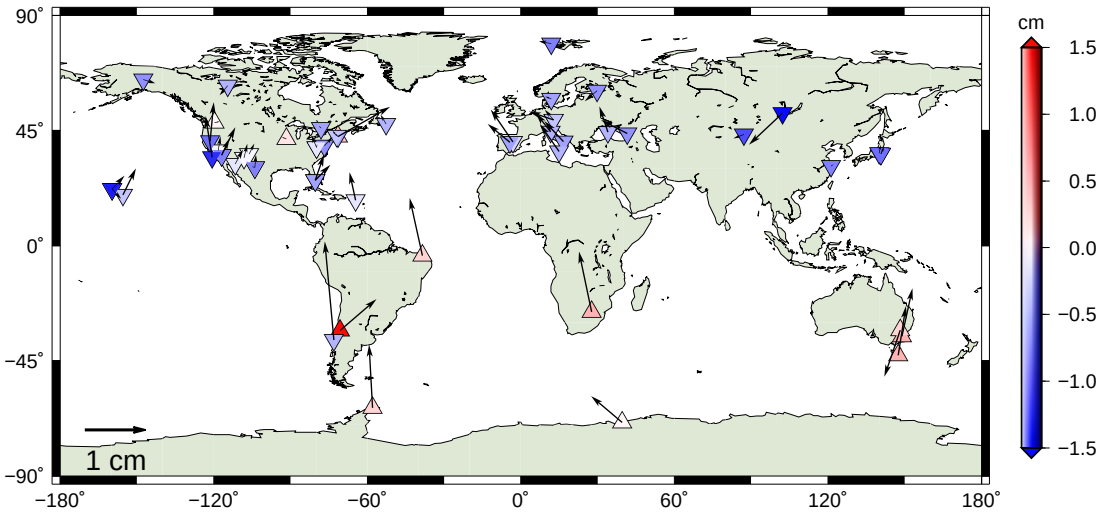

Figure A.2.6.: Differences in stations positions between VieTRF10a (DAO a priori, estimated) minus GS1 (fixed to zero values). The height differences are plotted with coloured triangles (red up-pointing triangles: uplift, blue down-pointing triangles: subsidence).

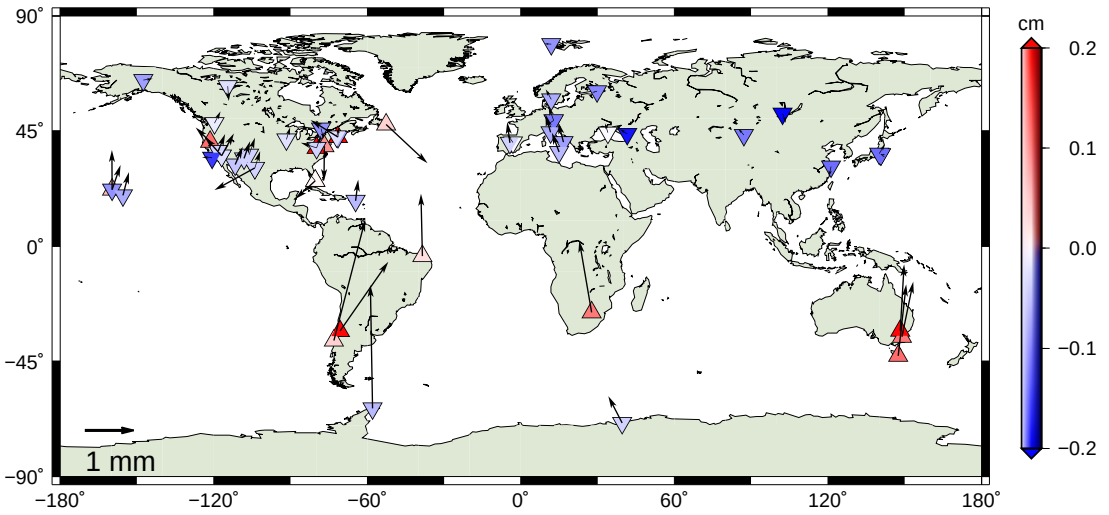

Figure A.2.7.: Differences in stations positions between TRF with estimated gradients: VieTRF10a (DAO a priori) minus GS2 (zero gradients a priori). The height differences are plotted with coloured triangles (red up-pointing triangles: uplift, blue down-pointing triangles: subsidence).

would be omitted in the VLBI analysis, the TRF would have a scale change of 0.65 ppb compared to a TRF with estimated gradients (GS1 w.r.t. VieTRF10a). Similar results (0.7 ppb)

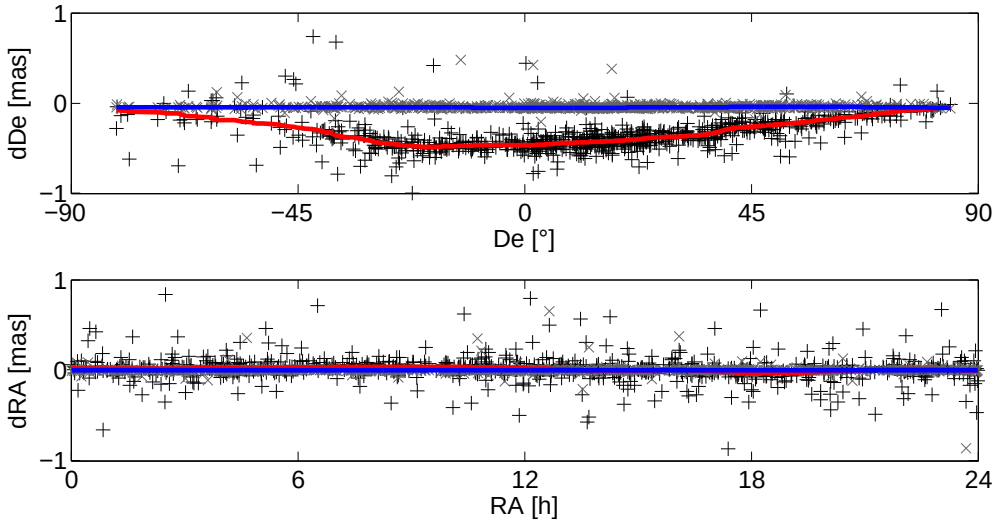

Figure A.2.8.: Difference in declination (upper plot) and right ascension (lower plot) between the VieCRF10a w.r.t. CRF of solution GS1 (red line, black "+") and solution GS2 (blue line, grey "x").

were obtained by MacMillan and Ma (1997). The low values of the transformation parameters between VieTRF10a and GS2 point out that the analysis approach by VieTRF10a (applying a priori gradient model with the estimation of residuals) and the approach in solution GS2 (no a priori model with the estimation of total gradients) are equivalent and differences only show up because of the constraints applied on the gradients.

The influence of tropospheric gradients on the celestial reference frame is investigated for both solutions. Comparisons of declination and right ascension estimates of sources between VieCRF10a w.r.t. GS1 and GS2 are shown in Figure A.2.8. By fixing gradients to zero (GS1, red line) the apparent declination increases and the difference reaches a mean systematic value of -0.36 mas with a maximum of around -0.5 mas near the equator, which was also reported by Fey et al. (2009) and MacMillan and Ma (1997). The agreement between declination estimates in GS2 and VieCRF10a is very good with a mean systematic difference of -0.04 mas lying bellow its standard deviation (see Table A.2.3, second column). The differences appearing in right ascension are very small. The mean systematic difference between VieCRF10a w.r.t. GS1 reaches

Table A.2.3.: Helmert parameters for the transformation between different TRF, mean difference and standard deviation of station and source positions.

	VieTRF10a		VMF1
Helmert parameters between TRF	w.r.t. GS1	w.r.t. GS2	w.r.t. GMF
Tx [mm]	1.7 ± 0.6	0.1 ± 0.1	-0.3 ± 0.1
Ty [mm]	-2.4 ± 0.6	-0.4 ± 0.1	-0.0 ± 0.1
Tz [mm]	0.4 ± 0.6	-0.0 ± 0.1	0.1 ± 0.1
Rx [μas]	80 ± 24	11 ± 5	-1 ± 4
Ry [μas]	51 ± 25	3 ± 5	-6 ± 4
Rz [μas]	21 ± 24	-1 ± 5	-2 ± 4
$Scale$ [ppb]	-0.65 ± 0.10	-0.05 ± 0.02	-0.08 ± 0.02
Mean difference of station positions			
dH [mm]	-3.7 ± 5.2	-0.2 ± 1.2	-0.5 ± 1.1
dE [mm]	-0.4 ± 2.5	-0.0 ± 0.2	-0.0 ± 0.2
dN [mm]	2.7 ± 3.9	0.4 ± 0.6	0.2 ± 0.3
Mean difference of source positions			
De [μas]	-356 ± 175	-43 ± 72	-1 ± 12
RA [μas]	13 ± 173	2 ± 51	-0 ± 16

0.01 mas but with a large scatter of the estimates and a corresponding large standard deviation of 0.17 mas (similar to the standard deviation of declination estimates). Differences between VieCRF10a and GS2 are in right ascension negligible (0.00 mas with standard deviation of 0.05 mas).

A.2.2. Impact of two different mapping functions

The Vienna Mapping Functions (VMF1, (Böhm et al., 2006b)) are elevation-dependent functions based on ray-traces through a numerical weather model provided with a time resolution of typically 6 hours. This allows to reflect changing weather conditions on VLBI sites. However it requires access to the external time series of the weather data or to the provider of the already computed mapping functions. The Global Mapping Functions (GMF, Böhm et al. (2006a)) were determined as a backup and average of the VMF1. GMF are analytical functions using station position (latitude, longitude, height) and day of year as input for computation of the coefficients. These are obtained as an expansion of the VMF1 parameters into spherical harmonics allowing only an annual variability. Comparisons between these two mapping functions and their effect

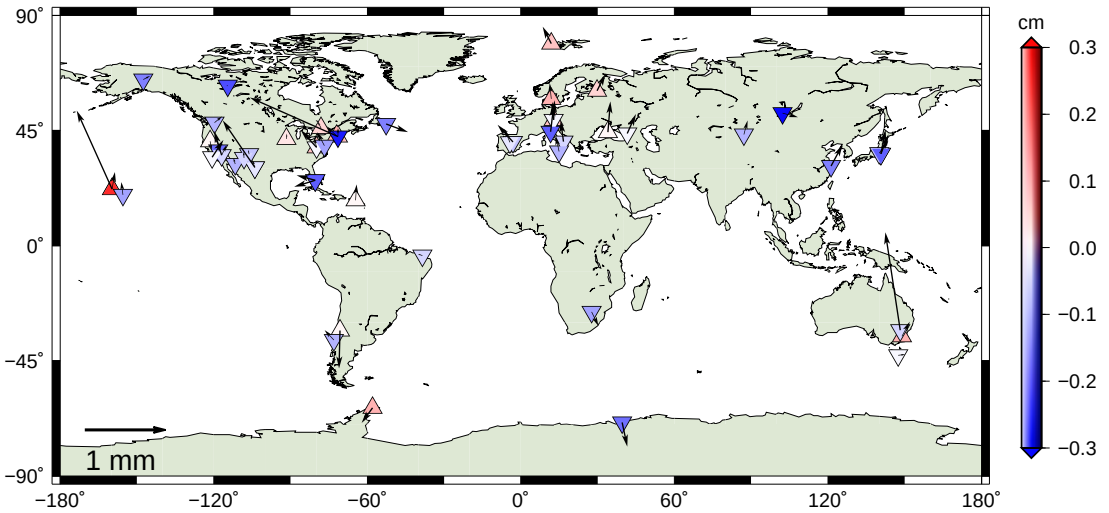

Figure A.2.9.: Differences in stations positions between VieTRF10a (VMF1) and the TRF solution with GMF in the sense VMF1 minus GMF. The height differences are plotted with coloured triangles (red up-pointing triangles: uplift, blue down-pointing triangles: subsidence).

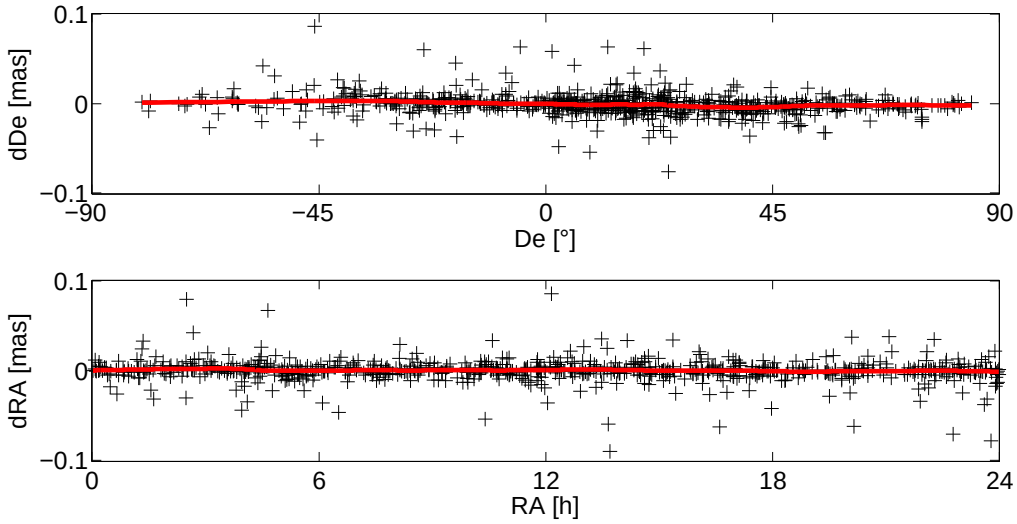

Figure A.2.10.: Difference in declination (upper plot) and right ascension (lower plot) between VieCRF10a (VMF1) minus CRF with GMF.

on the TRF and CRF determined by VLBI were done e.g. by Tesmer et al. (2007) and the effect on the TRF determined from GPS data was examined e.g. by Steigenberger et al. (2009). Here I show the performance of the newly developed software VieVS with the analysis of 27 years of VLBI data which was published in Krásná et al. (2012b).

The parameterisation of the investigated solution is identical to the parameterisation of VieTRF10a and VieCRF10a except of using GMF instead of VMF1. In Figure A.2.9 the differences between station positions in local coordinate systems at epoch 2000.0 are shown. At most of the stations the positional changes are below 1 mm. Higher difference between these two solutions appears at stations with a higher formal error of the estimated position from the global adjustment, these are 9-m Kauai at Kokee Park (Hawaii, USA), Haystack at Westford (Massachusetts, USA), and Parkes (Australia). The mean height difference between all stations is -0.5 mm, and the change in horizontal components reaches 0.0 mm and 0.2 mm for east and north components respectively, always in the sense VMF1 solution minus GMF solution (see also the lower part of the third column in Table A.2.3). The seven Helmert parameters computed for the transformation between these two TRF obtained with different mapping functions are listed in the upper part of Table A.2.3 (third column). The consistency between the mean height coordinate difference and the scale change (-0.08 ppb $\sim$ -0.5 mm) is evident. Tesmer et al. (2007) obtained a scale change of -0.03 ppb between the two TRF solutions. This slightly better agreement between the TRF can be explained with the choice of stations for the computation of transformation parameters, because Tesmer et al. (2007) included only 25 well-determined stations, which were also used for the datum realization. In this solution I included all available

stations into the transformation.

The differences between the two estimated celestial reference frames are plotted in Figure A.2.10. Neither in declination (upper plot) nor in right ascension (lower plot) a bias can be seen. The computed mean differences in declination and right ascension (Table A.2.3, third column) equal to -0.00 mas for both coordinates with standard deviations of 0.01 mas and 0.02 mas, respectively.

GEOWISSENSCHAFTLICHE MITTEILUNGEN

Bisher erschienen:

Heft 1 Kolloquium der Assistenten der Studienrichtung Vermessungswesen. 1970 - 1973, Dezember 1973.

Heft 2 EGGER-PERDICH-PLACH-WAGENSOMMERER, Taschenrechner HP 45 und HP 65, Programme und Anwendungen im Vermessungswesen. 1. Auflage, März 1974, Special Edition in English, Juli 1974, 2. verbesserte Auflage, November 1974.

Heft 3 Kolloquium der Assistenten der Studienrichtung Vermessungswesen 1973 - 1974, September 1974.

Heft 4 EGGER-PALFINGER-PERDICH-PLACH-WAGENSOMMERER, Tektronix-Tischrechner TEK 31, Programmbibliothek für den Einsatz im Vermessungswesen, November 1974.

Heft 5 K. LEDERSTEGER, Die horizontale Isostasie und das isostatische Geoid, Februar 1975.

Heft 6 F. REINHART, Katalog von FK4 Horrebow-Paaren für Breiten von +30 bis +60, Oktober 1975.

Heft 7 Arbeiten aus dem Institut für Höhere Geodäsie, Wien, Dezember 1975.

Heft 8 Veröffentlichungen des Instituts für Photogrammetrie zum XIII. Internationalen Kongreß für Photogrammetrie in Helsinki 1976, Wien, Juli 1976.

Heft 9 W. PILLEWIZER, Felsdarstellung aus Orthophotos, Wien, Juni 1976.

Heft 10 PERDICH-PLACH-WAGENSOMMERER, Der Einsatz des programmierbaren Taschenrechners Texas Instruments SR-52 mit Drucker PC100 in ingenieurgeodätischen Rechentechnik, Wien, Mai 1976.

Heft 11 Kolloquium der Assistenten der Studienrichtung Vermessungswesen 1974 - 1976, November 1976.

Heft 12 Kartographische Vorträge der Geodätischen Informationstage 1976, Wien, Mai 1977.

Heft 13 Veröffentlichung des Instituts für Photogrammetrie anläßlich des 80. Geburtstages von Prof. Dr.h.c. K. Neumaier, Wien, Januar 1978.

Heft 14 L. MOLNAR, Self Checking Analytical Relative Orientation and Strip Formation, Wien, Dezember 1978.

Heft 15 Veröffentlichung des Instituts für Landesvermessung anläßlich des 80. Geburtstages von Prof. Dr. Alois Bavir, Wien, Januar 1979.

Heft 16 Kolloquium der Assistenten der Studienrichtung Vermessungswesen 1976 - 1978, Wien, November 1979.

Heft 17 E. VOZIKIS, Die photographische Differentialumbildung gekrümmter Flächen mit Beispielen aus der Architekturbildmessung, Wien, Dezember 1979.

Heft 18 Veröffentlichung des Instituts für Allgemeine Geodäsie anläßlich des 75. Geburtstages von Prof. Dipl.-Ing. Dr. F. Hauer, Die Höhe des Großglockners, Wien, 1981.

Heft 19 H. KAGER, Bündeltriangulation mit indirekt beobachteten Kreiszentren, Wien, April 1981.

Heft 20 Kartographische Vorträge der Geodätischen Informationstage 1980, Wien, Mai 1982.

Heft 21 Veröffentlichung des Instituts für Kartographie anläßlich des 70. Geburtstages von Prof. Dr. Wolfgang Pillewizer: Glaziologie und Kartographie, Wien, Dezember 1982.

Heft 22 K. TEMPFLI, Genauigkeitsschätzung digitaler Höhenmodelle mittels Spektralanalyse, Wien, Mai 1982.

Heft 23 E. CSAPLOVICS, Interpretation von Farbinfrarotbildern, Wien, November 1982.

Heft 24 J. JANSA, Rektifizierung von Multispektral-Scanneraufnahmen - Entwicklung und Erprobung eines EDV-Programms, Wien, Mai 1983.

Heft 25 Zusammenfassung der Diplomarbeiten, Dissertationen und Habilitationen an den geodätischen Instituten der TU Wien, Wien, November 1984.

Heft 26 T. WUNDERLICH, Die voraussetzungsfreie Bestimmung von Refraktionswinkeln, Wien, August 1985.

Heft 27 G. GERSTBACH (Hrsg.), Geowissenschaftliche/geotechnische Daten in Landinformationssystemen - Bedarf und Möglichkeiten in Österreich, Juni 1986.

Heft 28 K. NOVAK, Orientierung von Amateuraufnahmen ohne Paßpunkte, Wien, August 1986.

Heft 29 Veröffentlichung des Instituts für Landesvermessung und Ingenieurgeodäsie, Abt. Ingenieurgeodäsie, anläßlich des 80. Geburtstages von Prof. Dipl.-Ing. Dr. F. Hauer, Wien, Oktober 1986.

Heft 30 K.-H. ROCH, Über die Bedeutung dynamisch ermittelter Parameter für die Bestimmung von Gesteins- und Gebirgseigenschaften, Wien, Februar 1987.

Heft 31 G. HE, Bildverbesserung mittels digitaler Filterung, Wien, April 1989.

Heft 32 F. SCHLÖGELHOFER, Qualitäts- und Wirtschaftlichkeitsmodelle für die Ingenieurphotogrammetrie, Wien, April 1989.

Heft 33 G. GERSTBACH (Hrsg.), Geowissenschaftliche/geotechnische Daten in Landinformationssystemen - Datenbestände und Datenaustausch in Österreich, Wien, Juni 1989.

Heft 34 F. HOCHSTÖGER, Ein Beitrag zur Anwendung und Visualisierung digitaler Geländemodelle, Wien, Dezember 1989.

Heft 35 R. WEBER, Lokale Schwerefeldmodellierung unter Berücksichtigung spektraler Methoden zur Geländereduktion, Wien, April 1990.

Heft 36 o.Prof. Dr. Hans Schmid zum 70. Geburtstag. Veröffentlichung der Abteilung für Landesvermessung, Wien, Oktober 1990.

Heft 37 G. GERSTBACH, H. P. HÖLLRIEGL und R. WEBER, Geowissenschaftliche Informationsbörse - Eine Nachlese zu GeoLIS II, Wien, Oktober 1990.

Heft 38 R. ECKER, Rastergraphische Visualisierungen mittels digitaler Geländemodelle, Wien, August 1991.

Heft 39 Kartographische Forschungen und Anwendungsorientierte Entwicklungen, herausgegeben von W. Stams und F. Kelnhofer zum 80. Geburtstag von Prof. Dr. W. Pillewizer, Wien, Juli 1991.

Heft 39a W. RIEGER, Hydrologische Anwendungen des digitalen Geländemodelles, Wien, Juli 1992.

Heft 40 K. STEINNOCHER, Methodische Erweiterungen der Landnutzungsklassifikation und Implementierung auf einem Transputernetzwerk, Wien, Juli 1994.

Heft 41 G. FORKERT, Die Lösung photogrammetrischer Orientierungs- und Rekonstruktionsaufgaben mittels allgemeiner kurvenförmiger Elemente, Wien, Juli 1994.

Heft 42 M. SCHÖNER, W. SCHÖNER, Photogrammetrische und glaziologische Untersuchungen am Gàsbre (Ergebnisse der Spitzbergenexpedition 1991), Wien, Mai 1996.

Heft 43 M. ROIC. Erfassung von nicht signalisierten 3D-Strukturen mit Videotheodoliten, Wien, April 1996.

Heft 44 G. RETSCHER, 3D-Gleiserfassung mit einem Multisensorsystem und linearen Filterverfahren, Wien, April 1996.

Heft 45 W. DAXINGER, Astrogravimetrische Geoidbestimmung für Ingenieurprojekte, Wien, Juli 1996.

Heft 46 M. PLONER, CCD-Astrometrie von Objekten des geostationären Ringes, Wien, November 1996.

Heft 47 Zum Gedenken an Karl Killian "Ingenieur" und "Geodät" 1903-1991, Veröffentlichung der Fachgruppe Geowissenschaften, Wien, Februar 1997.

Heft 48 A. SINDHUBER, Ergänzung und Fortführung eines digitalen Landschaftsmodelles mit multispektralen und hochauflösenden Fernerkundungsaufnahmen, Wien, Mai 1998.

Heft 49 W. WAGNER, Soil Moisture Retrieval from ERS Scatterometer Data, Wien, Dezember 1998.

Heft 50 R. WEBER, E. FRAGNER (Editoren),Prof. Bretterbauer, Festschrift zum 70. Geburtstag, Wien, Juli 1999.

Heft 51 Ch. ÖHRENEDER, A Similarity Measure for Global Image Matching Based on The Forward Modeling Principle, Wien, April 1999.

Heft 52 M. LECHTHALER, G. GARTNER, Per Aspera ad Astra, Festschrift für Fritz Kelnhofer zum 60. Geburtstag, Wien, Jänner 2000.

Heft 53 F. KELNHOFER, M. LECHTHALER, Interaktive Karten (Atlanten) und Multimedia – Applikationen, Wien, März 2000.

Heft 54 A. MISCHKE, Entwicklung eines Videotheodlit-Meßsystems zur automatischen Richtungsmessung von nicht signalisierten Objektpunkten, Wien, Mai 2000.

Heft 55 Veröffentlichung des I.P.F. anlässlich der Emeritierung von Prof. Dr. Peter Waldhäusl, Wien.

Heft 56 F. ROTTENSTEINER, Semi-automatic Extraction of Buildings Based on Hybrid Adjustment Using 3D Surface Models and Management of Building Data in a TIS, Wien, Juni 2001.

Heft 57 D. LEGENSTEIN, Objektrekonstruktion aus perspektiven Bildern unter Einbeziehung von Umrisslinien, Wien, Mai 2001.

Heft 58 F. KELNHOFER, M. LECHTHALER und K. BRUNNER (Hrsg.), Telekartographie und Location Based Services, Wien, Jänner 2002.

Heft 59 K. BRETTERBAUER, Die runde Erde eben dargestellt: Abbildungslehre und sphärische Kartennetzentwürfe, Wien, 2002.

Heft 60 G. GARTNER, Maps and the Internet 2002, Wien 2002.

Heft 61 L. DORFFNER, Erzeugung von qualitativ hochwertigen 3D Photomodellen für Internetbasierte Anwendungen mit besonderem Augenmerk auf Objekte der Nahbereichsphotogrammetrie, Wien, Jänner 2002.

Heft 62 K. CHMELINA, Wissensbasierte Analyse von Verschiebungsdaten im Tunnelbau, Wien 2002.

Heft 63 A. NIESSNER, Qualitative Deformationsanalase unter Ausnutzung der Farbinformation, Wien 2002.

Heft 64 K. BRETTERBAUER, R. WEBER, A Primer of Geodesy for GIS-Users, Wien 2003.

Heft 65 N. PFEIFER, 3D Terrain Models on the basis of a triangulation, Wien, Jänner 2002.

Heft 66 G. GARTNER (Hrsg), Lacation Based Services & Telecartography, Wien 2004.

Heft 67 I. KABASHI, Gleichzeitig-gegenseitige Zenitwinkelmessung über größere Entfernungen mit automatischen Zielsystemen, Wien 2004.

Heft 68 J. BÖHM, Troposphärische Laufzeitverzögerungen in der VLBI, Wien 2004.

Heft 69 R. WEBER, W. SCHLÜTER, U. SCHREIBER, O. TITOV Evolving Space Geodesy Techniques (EGS XXVII General Assembly, Nice, France, 2002), Wien 2004.

Heft 70 G. WEINWURM, Amalthea's Gravity Field and its Impact on a Spacecraft Trajectory, Wien 2004.

Heft 71 Forschungsgruppe Ingenieurgeodäsie, Festschrift anlässlich des 65. Geburtstages von Herrn o.Univ. Prof. Dr.-Ing. Heribert Kahmen, Wien 2005.

Heft 72 A. REITERER, A Knowledge-Based Decision System for an On-Line Video-Theodolite-Based Multisensor System, Wien 2005.

Heft 73 M. HABERLER, Einsatz von Fuzzy Methoden zur Detektion konsistenter Punktbewegungen, Wien 2005.

Heft 74 G. GARTNER, Location Based Services & Telecartography, Proceedings of the Symposium 2005, Wien 2005.

Heft 75 Th. HOBIGER, VLBI as a tool to probe the ionosphere, Wien 2006.

Heft 76 E. KLAFFENBÖCK, Troposphärische Laufzeitverzögerung von GNSS-Signalen – Nutzen aktiver Referenzstationsnetze für die Meteorologie, Wien 2006.

Heft 76a P. J. MENDES-CERVEIRA, Tidal and non-tidal contributions to surface loading processes on station coordinates, Wien 2006.

Heft 78 G. KOSTOV, G. BOURDA, L. FERNANDEZ, T. KONDO, Research Projects at IGG Reports, Wien 2007.

Heft 79 J. BÖHM, A. PANY, H. SCHUH (Editors), Proceedings of the 18th European VLBI for Geodesy and Astrometry Working Meeting, 12-13 April 2007, Wien 2007.

Heft 80 J. BÖHM, Tropospheric Delay Modelling at Radio Wavelengths for Space Geodetic Techniques, Wien 2007.

Heft 81 G. Retscher, Mobile Multi-sensor Systems for Personal Navigation and Location-based Services, Wien 2007.

Heft 82 R. HEINKELMANN, Bestimmung des atmosphärischen Wasserdampfes mittels VLBI als Beitrag zur Klimaforschung, Wien 2008.

Heft 83 F. ROTTENSTEINER, Automatic extraction of buildings from airborne laserscanner data and aerial images, Wien 2008.

Heft 84 S. TODOROVA, Kombination geodätischer Weltraumverfahren für globale Karten der Ionosphäre, Wien 2009.

Heft 85 J. WRESNIK, Simulationen für die neue Generation von VLBI-Systemen, Wien 2009.

Heft 86 A. KARABATIC, Precise Point Positioning (PPP). An alternative technique for ground based GNSS troposphere monitoring, Wien 2011.

Heft 87 K. TEKE, Sub-daily Parameter Estimation in VLBI Data Analysis, Wien 2011.

Heft 88 G. THALER, Echtzeit Bahn- und Uhrberechnung der GPS-Satellitenkonstellation basierend auf Beobachtungsdaten des RTIGS-Stationsnetzwerkes, Wien.

Heft 89 P. SWATSCHINA, Dynamic and Reduced-Dynamic Precise Orbit Determination of Satellites in Low Earth Orbits, Wien 2012.

Heft 90 S. BÖHM, Tidal excitation of Earth rotation observed by VLBI and GNSS, Wien 2012.